HAL
open science

Metastable states in model glass-formers

Benjamin Guiselin

To cite this version:

Benjamin Guiselin. Metastable states in model glass-formers. Mechanics [physics]. Université Montpellier, 2021. English. NNT : 2021MONTS030 . tel-03396817

HAL Id: tel-03396817

https://theses.hal.science/tel-03396817v1

Submitted on 22 Oct 2021

HAL is a multi-disciplinary open access archive for the deposit and dissemination of scientific research documents, whether they are published or not. The documents may come from teaching and research institutions in France or abroad, or from public or private research centers.

L'archive ouverte pluridisciplinaire **HAL**, est destinée au dépôt et à la diffusion de documents scientifiques de niveau recherche, publiés ou non, émanant des établissements d'enseignement et de recherche français ou étrangers, des laboratoires publics ou privés.

THÈSE POUR OBTENIR LE GRADE DE DOCTEUR DE L'UNIVERSITÉ DE MONTPELLIER

En Physique

École doctorale : Information, Structures, Systèmes

Unité de recherche Laboratoire Charles Coulomb UMR 5221

Metastable states in model glass-formers

Présentée par Benjamin Guiselin
Le 21 Juin 2021

Sous la direction de Ludovic Berthier et Gilles Tarjus

Devant le jury composé de

Jean-Louis Barrat, Professeur des Universités, Université Grenoble Alpes	Rapporteur
Ludovic Berthier, Directeur de Recherche, Laboratoire Charles Coulomb	Directeur de thèse
Jean-Philippe Bouchaud, Professeur, Collège de France	Président du Jury
Chiara Cammarota, Associate Professor, Sapienza Università di Roma	Examinatrice
Silvio Franz, Professeur des Universités, Université Paris-Saclay	Rapporteur
Gilles Tarjus, Directeur de Recherche, Laboratoire de Physique Théorique de la Matière Condensée	Directeur de thèse
Marco Tarzia, Maître de Conférences, Sorbonne Université	Examinateur

UNIVERSITÉ DE MONTPELLIER

Acknowledgments

I first want to thank my two PhD supervisors Ludovic Berthier and Gilles Tarjus who have guided me for three years in a wonderful way and who have accepted to share their rich experience with me. I have really appreciated their high-standard scientific supervision. Our discussions, their questions, comments or encouragement have undoubtedly improved my thesis by pushing me to think better and to work more. Ludovic and Gilles are two friends and it was a pleasure to work in such a friendly atmosphere. I first met Ludovic when he was teaching the course of advanced Statistical Physics at ENS Lyon. I really appreciated the rigour and the pedagogy of his lectures and I was honoured when he offered to do my Master internship and my PhD in Laboratoire Charles Coulomb at the University of Montpellier, the only requirement being that I had to address him as "tu". I then realised that he was also an impressive researcher. From Ludovic, I have learnt a lot about computer simulations and I estimate his pragmatism and his efficiency regarding technical or coding aspects. I first met Gilles in Bristol for a conference, who is an enthusiast researcher. With Gilles, I had the opportunity to escape simulations for analytical works that I was looking for and I really enjoyed this ambivalence. Working with both of them has also been a source of multiple opportunities. On the one hand, I thank Gilles for hosting me several times in Paris. On the other hand, I am grateful to Ludovic who gave me the opportunity to visit the University of Cambridge as he is a fellow of Churchill College. Besides, as Ludovic and Gilles are both members of the Simons international collaboration "Cracking the Glass problem", I had the chance to attend several conferences all around the world with leading researchers in the field.

Then, I would like to thank the members of my jury. First, I am grateful to Silvio Franz and Jean-Louis Barrat who have accepted to assess my manuscript. Jean-Louis Barrat was my professor of continuum mechanics when I was a student at ENS Lyon and I am proud that he is a member of my jury. The work of Silvio Franz has largely inspired my PhD thesis and its developments (as demonstrated by the number of times his name appears in this thesis) and I am honoured that he has accepted to examine my manuscript. Then, I want to thank Chiara Cammarota, Marco Tarzia and Jean-Philippe Bouchaud for agreeing to take part in my thesis committee. Recent theoretical work of Chiara and Marco have guided several projects of my PhD and I am happy to have the chance to present directly related numerical results to them. Moreover, my PhD thesis has benefited from the generous funding from Fondation CFM which is headed by Jean-Philippe Bouchaud. I have appreciated the few discussions I had with Jean-Philippe Bouchaud during the last three years and his encouragement. Presenting my results to him is therefore a great honour, all the more so that I know that he is busy. Finally, even though he is not a member of the jury, I want to thank Giorgio Parisi whose work since the 80s show through the various topics I have addressed during my PhD.

During the last three years, I had the chance to interact with several researchers during conferences, summer schools or the annual *Comités de Suivi de Thèse*. I thus want to thank them for their scientific advise and encouragement, in particular Giulio Biroli, Daniele Coslovich, Mark Ediger, Lucyna Firlej, Robert Jack and Sidney Nagel. Daniele introduced me to computer simulations and he has always been available for answering my questions. I am thus grateful to

him. I also want to thank Giulio and Chiara, who gave me the opportunity to attend the Beg Rohu summer school. Beyond the great scientific experience, I met nice people and I had the chance to practice sailing.

The work in this thesis has led me to collaborate with former members of Laboratoire Charles Coulomb in Montpellier, namely, Camille Scalliet and Anshul Parmar, and I thank both of them along with Ludovic for these opportunities. First, as a young PhD student, Camille has been a guide through technical and administrative matters. She is also brilliant and kind and I have been more than happy to share my office at the University of Montpellier with her for one year. Developing a scientific collaboration with her when she left Montpellier was thus a pleasure. I also enjoyed working with Anshul and sharing our respective areas of expertise. Even though we did not collaborate formally, I am grateful to Misaki who helped me several times with his numerical skills but also his incredible memory of published works. Finally, I thank the other past and present people of the team *Physique statistique* in Laboratoire Charles Coulomb for scientific discussions, but also for more festive events: Joris, Marouane, Valerio, Yoshihiko, Yann, Murari, Simona, Zhen, Chris, Qinyi. I also acknowledge Klaus and the MESO@LR-Platform for technical support and extra computer resources.

Finally, leaving his comfort zone for an unknown city was not easy. Therefore, I thank my *amis Lyonnais* for their moral support, their hospitality during weekends and holidays, but also for paying me a visit several times: Camille, Clément, Étienne, Louis et Noémie. In particular, I am indebted to Noémie who accompanied me during my first visit of the lab in Montpellier and who helped me make my decision to come here for the three years of my PhD. Last but not least, I thank Martial, living in Montpellier has been far more enjoyable with you.

Table of contents

I. General introduction 3

1. Phenomenology of the glass transition 4
2. The mean-field theory of the glass transition 14
3. Towards a theory of the glass transition in finite dimensions 21
4. Structure of the manuscript 26

II. An introduction to the theoretical Franz-Parisi construction 29

1. Presentation 30
2. Statistical mechanics formulation 33
3. Exact results from mean-field theory: the spherical p-spin 40
4. Statistical field theory beyond mean-field 52
5. Computer studies of glass-formers in the Franz-Parisi construction 59

A. The random-field Ising model 61

III. Phase diagram of finite-dimensional constrained supercooled liquids from computer simulations 66

1. Introduction 67
2. Model and methods 68
3. Mean-field-like behaviour in finite systems 80
4. Contrasting results in two and three dimensions through a finite-size scaling analysis 83
5. Characterisation of the critical point in the three-dimensional system 89
6. Conclusions 93

A. Simulation results for the case of equal temperatures $T = T_0$ 95

IV. Detailed analysis of the definition of the overlap between liquid configurations 97

1. Introduction 98
2. Liquid-state theory in the theoretical Franz-Parisi construction 99
3. Hypernetted chain approximation and the Franz-Parisi potential 104
4. Hypernetted chain results for the critical endpoint 108
5. Confronting the hypernetted chain results with computer simulations 115
6. Discussion 118

A. Analysis of the hypernetted chain equations in the limit of vanishing tolerance length ... 121

V. Local fluctuations of the "self-induced" disorder in glass-forming liquids ... 126

1. Introduction ... 127
2. General formalism ... 130
3. Model and methods ... 132
4. Thermodynamic spatial fluctuations ... 135
5. Conclusions and perspectives ... 139

VI. Escaping "metastable states": watching 1 millisecond of the equilibrium relaxation in supercooled liquids ... 145

1. Introduction ... 146
2. Model and methods ... 148
3. Equilibrium correlation functions towards the glass transition ... 152
4. Short-time relaxation much before the bulk ... 156
5. Dynamic facilitation towards the α-relaxation ... 160
6. Conclusions ... 164

A. Suppression of the "excess wing" in stable glasses ... 166

VII. Article: Stable glassy configurations of the Kob–Andersen model through the swap Monte Carlo algorithm ... 168

1. Introduction ... 169
2. Models ... 169
3. Reweighting equilibrium distributions ... 171
4. Annealing procedures to generate glassy Kob-Andersen configurations ... 174
5. Enhanced stability of the annealed glassy Kob-Andersen configurations ... 175
6. Conclusions ... 179

VIII. Conclusions and perspectives ... 181

1. The thermodynamics of constrained glass-forming liquids ... 181
2. The dynamics of supercooled liquids close to their glass transition ... 183
3. The properties of the non-equilibrium glass phase ... 184

IX. Résumé en français ... 186

1. Motivations ... 186
2. Résumé des résultats obtenus ... 189

References ... 193

I General introduction

Outline

1 Phenomenology of the glass transition 4
  1.1 Dynamic facts 4
  1.2 Properties of the non-equilibrium glass phase 10
  1.3 Thermodynamic features 13
2 The mean-field theory of the glass transition 14
  2.1 From fully-connected spin glasses to liquids in infinite dimensions 14
  2.2 The dynamics in infinite dimensions 14
  2.3 The thermodynamics in infinite dimensions 17
  2.4 Properties of the non-equilibrium glass phase in infinite dimensions 20
3 Towards a theory of the glass transition in finite dimensions 21
  3.1 The fate of the metastable states in finite dimensions 21
  3.2 Spatial definition of the metastable states: the point-to-set length 22
  3.3 Activation and the escape from the metastable states 24
  3.4 Dynamic heterogeneities and dynamic facilitation 25
4 Structure of the manuscript 26

Glasses and liquids are ubiquitous [1]. However, they remain a puzzle and their description represents a great challenge for theoreticians [2], probably "the deepest and most interesting unsolved problem in solid state theory" [3]. In usual statistical mechanics textbooks and courses, we learn the statistical mechanics formulation of two archetypal and unrealistic materials: the ideal gas (in the limit of vanishing density) [4] and the perfect crystal (without defects and at zero temperature) [5, 6]. Properties of more realistic gases or solids can then be deduced from these limits thanks to perturbative expansions with respect to the density for the former and to the temperature for the latter. However, dealing with liquids is far more complex because they are disordered and dense. From a solid perspective, their intrinsic disorder forbids to use the statistical tools which are implemented in order to deal with crystals. From a gas point of view, their high density makes interactions between constituents no longer negligible. This is emphasised by the fact that the liquid is separated from both the gas[1] and the solid phases by thermodynamic first order phase transitions [8, 9].

What is then the good statistical mechanics description of these materials? Can one encompass the thermal and dynamic properties of liquids and glasses within a single theoretical framework? The work which is presented here participates to answering these questions. This introduction poses the main aspects of supercooled liquids and glasses that are relevant for the

[1] This is true only below the liquid-gas critical point. Above, a single fluid phase exists [7].

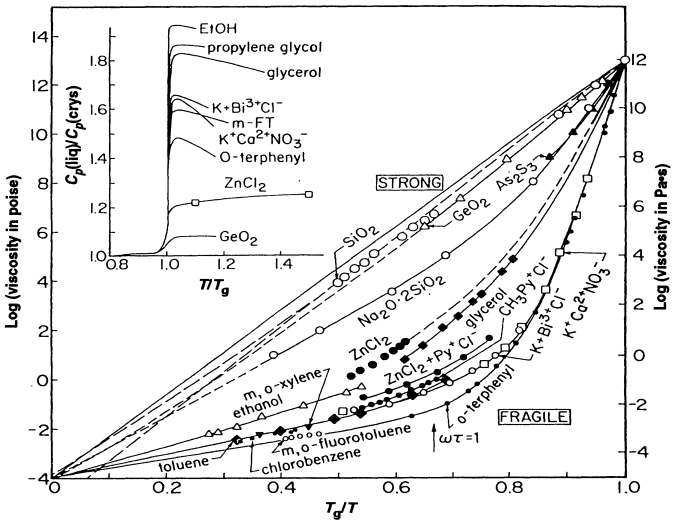

Fig. I.1 | Angell plot which represents the experimental measure of the variation of the bulk viscosity η for several glass-forming liquids. Data are plotted on a logarithmic scale versus T_g/T, where the glass transition temperature T_g is operatively defined when the viscosity reaches 10^{12} Pa.s. A significant slowing down is clearly visible: the bulk viscosity (or equivalently the structural relaxation time) skyrockets with decreasing the temperature on a small window. Strong liquids display an almost Arrhenius behaviour while the increase in viscosity in fragile liquids is more pronounced and follows a super-Arrhenius trend. The inset shows the discontinuous jump in the heat capacity at the glass transition: the heat capacity varies rapidly from its value in the supercooled liquid to its value in the glass phase which is approximately equal to the heat capacity of the crystal at the same temperature. Figure from Ref. [15].

work which is presented in the next chapters. Additive information can be found in several reviews [10–14].

1. Phenomenology of the glass transition

1.1 Dynamic facts

1.1.1 Dynamic slowdown

The glass transition concerns a huge variety of materials, from atomic or polymeric liquids [15, 16] to colloidal systems [17, 18], granular materials [19–21] and even active matter [22, 23] and biological objects [24, 25]. They are all characterised by a significant increase in their microscopic relaxation time (by orders of magnitude) when one control parameter (typically the temperature or the density) is increased or decreased by a small amount. This is a universal behaviour which seems independent of the microscopic details of the materials and which continues to trigger many studies in order to provide a unified description of glassy materials.

In usual statistical mechanics textbooks, we read that when a liquid is cooled below the melting point T_m, it undergoes a first order thermodynamic phase transition and ends up in a solid crystalline phase. However, this statement is only true at the genuine thermodynamic equilibrium, *i.e.*, if the liquid is cooled infinitely slowly. Instead, if the liquid is cooled fast enough, it can avoid crystallisation and enter the supercooled regime which represents a metastable

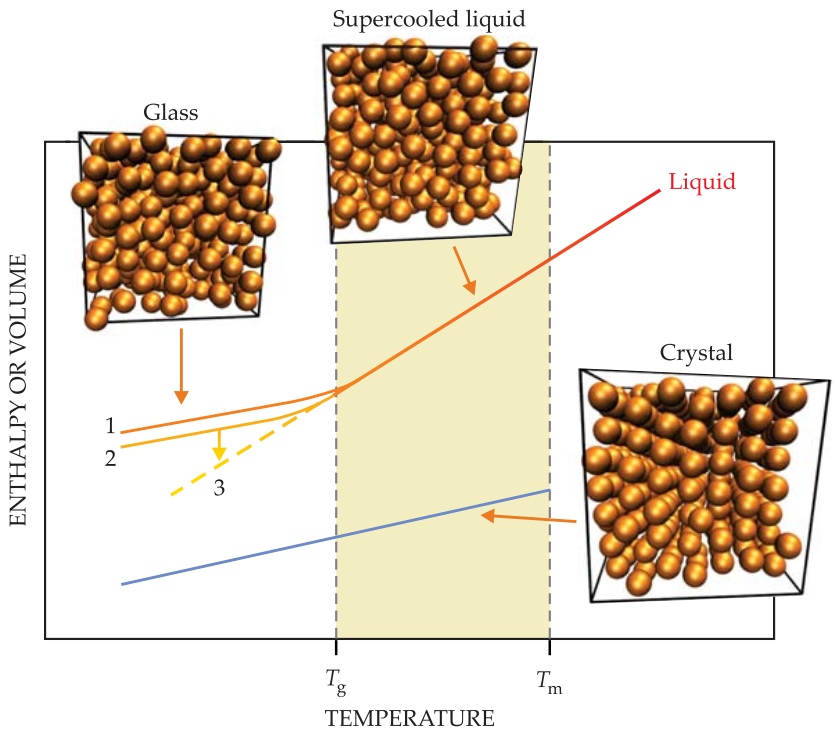

Fig. I.2 | Schematic evolution of the molar enthalpy or the molar volume of the supercooled liquid when it is cooled below the melting point at a constant pressure. The curves 1 and 2 are obtained for two different cooling rates. At high-enough temperatures, they all follow the same master curve which represents the equation of state of the liquid in the supercooled regime. The liquid eventually falls out of equilibrium and freezes into an amorphous solid, *i.e.*, a glass. The lower the cooling rate, the lower temperature at which the liquid vitrifies. We recall that the glass transition temperature T_g is defined by the condition $\eta(T_g) = 10^{12}$ Pa.s with $\eta(T)$ the bulk viscosity. When a glass ages, its thermodynamic properties slowly evolve, for instance it becomes denser and explores lower energies (curve 3). If the glass ages for a very long time, it can eventually reach equilibrium to follow back the equation of state of the supercooled liquid. The blue curve instead represents the equilibrium equation of state of the crystal. Configurations of a $3d$ system from computer simulations are shown for a supercooled liquid, a glass and a crystal. Figure from Ref. [26].

thermodynamic phase[2] with respect to the stable crystal phase. Even though the supercooled liquid is not the thermodynamic equilibrium phase for $T < T_m$, it behaves as such as soon as it does not crystallise. In particular, intensive thermodynamic variables can be defined and the fluctuation-dissipation theorem holds [10].

In the supercooled regime, the equilibrium relaxation time for density fluctuations τ_α (or equivalently the bulk viscosity η) increases significantly by several orders of magnitude when decreasing the temperature in a small interval [15], see Fig. I.1. Therefore, if a liquid is gradually cooled below T_m at a constant rate, typically between 0.1 K.min^{-1} and 100 K.min^{-1}, there is a temperature at which the cooling rate becomes too large to allow for the liquid equilibration. The system falls out of equilibrium and does not flow on a reasonable timescale. The frozen liquid behaves as a disordered solid which is called a glass. The temperature at which the liquid forms a glass corresponds to the glass transition temperature and it is denoted by T_g, see Fig. I.2.

[2]This is very different from the metastable glassy states which are mentioned in the title of this work and which are discussed below.

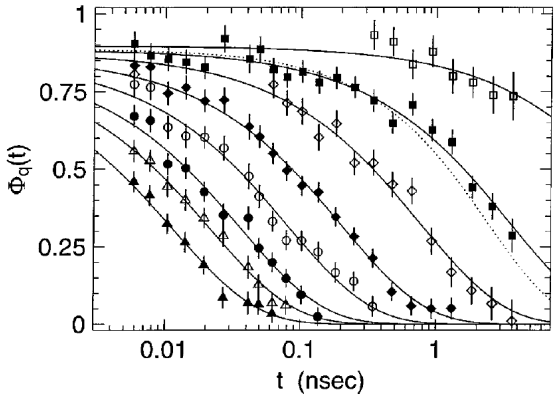

Fig. I.3 | Time evolution of the rescaled intermediate scattering function $\Phi_{\boldsymbol{q}}(t) = F(\boldsymbol{q}, t)/F(\boldsymbol{q}, 0)$ for several temperatures which range from $T = 413$ K (left) to $T = 270$ K (right) from experiments on glycerol. The wave vector is taken at the first maximum in the structure factor. As the temperature is reduced, data shift towards later times (on a logarithmic scale) but they also indicate a crossover from a mere exponential relaxation to a two-step decay with a first relaxation to a plateau which is followed by a stretched exponential relaxation. Figure from Ref. [29].

We must emphasise that the glass transition is not a genuine thermodynamic phase transition. Instead, it is protocol-dependent (a lower cooling rate leads to a lower temperature[3] at which the supercooled liquid falls out of equilibrium) and it is dependent on the timescale over which the experiment is performed [27]. Only an operative definition of the glass transition temperature T_{g} can be given. It is often defined by the condition $\eta(T_{\mathrm{g}}) = 10^{12}$ Pa.s, or equivalently by the relation $\tau_\alpha(T_{\mathrm{g}}) = 10^2$ s. As a matter of comparison, the relaxation time of liquids at the melting point is about 1 ps, and the bulk viscosity is about 10^{-2} Pa.s. In other words, on a small temperature window[4], the viscosity and the relaxation time have increased by 14 orders of magnitude [28].

1.1.2 Correlation functions and relaxation spectra

The evolution of the α-relaxation time (or the viscosity) with the temperature or the density is a shortcut to account for the slowing down of glass-forming liquids. The analysis of correlation functions in the time domain or of relaxation spectra in the frequency domain shows that the increase in the relaxation time is accompanied by a qualitative change of the latter. This suggests a temperature dependence of the relaxation mechanisms. Experiments and simulations usually focus on the correlation function which is associated with the relaxation of density fluctuations, namely, the intermediate scattering function [30]

$$F(\boldsymbol{q}, t) = \frac{1}{N} \langle \rho_{\boldsymbol{q}}(t) \rho_{-\boldsymbol{q}}(0) \rangle \,. \tag{I.1}$$

The brackets represent a thermal average at equilibrium at a temperature T, N stands for the number of particles, while $\rho_{\boldsymbol{q}}(t)$ represents the Fourier component of the density field $\rho(\boldsymbol{x}, t)$ at

[3]However the variation is quite weak, of about 5 K [16].
[4]The difference between T_{m} and T_{g} is often about $T_{\mathrm{m}}/3$.

wave vector $\boldsymbol{q}$ and time t which reads

$$\rho_{\boldsymbol{q}}(t) = \sum_{j=1}^{N} e^{i\boldsymbol{q}\cdot\boldsymbol{r}_j(t)}, \tag{I.2}$$

with $\boldsymbol{r}_j(t)$ the position of particle j at time t. Varying the wave vector $\boldsymbol{q}$ allows one to probe the relaxation at different lengthscales [31]. It is usually taken at the location of the first maximum in the total structure factor which is computed from the Fourier components of the density field at equal times [30], namely,

$$S(\boldsymbol{q}) = \frac{1}{N} \langle \rho_{\boldsymbol{q}} \rho_{-\boldsymbol{q}} \rangle . \tag{I.3}$$

This choice of wave vector amounts to probing the particle motion on lengthscales close to the average inter-particle distance.

Computer simulations have direct access to the positions of the particles and the computation of $F(\boldsymbol{q}, t)$ is rather straightforward. In experiments instead, it requires a coherent neutron scattering apparatus for instance [29]. An example is shown in Fig. I.3. At high temperatures, the relaxation is well approximated by a single exponential. At lower temperatures instead, the intermediate scattering function displays a two-step decay. The first step corresponds to a partial relaxation of the density fluctuations towards a plateau at microscopic timescales (of about 1 ps). From a nanoscopic point of view, this plateau represents the thermal vibrations which are performed by the particles in the cages that are formed by their neighbours. The second step of the relaxation instead represents the complete decorrelation (α-relaxation) on larger timescales (from picosecond to second). It becomes increasingly stretched as the temperature decreases. The time evolution of the correlation function is usually fitted by using a stretched exponential function [32], namely,

$$F(\boldsymbol{q}, t) \propto e^{-(t/\tau)^{\beta}}, \tag{I.4}$$

with τ and β adjustable parameters: τ closely follows τ_α while β slightly decreases when decreasing the temperature [33].

Experiments often deal with relaxation spectra instead of correlation functions. For liquids with dipolar moments, the imaginary part of the dielectric susceptibility $\epsilon''(\nu)$ can be measured [36]. At equilibrium, it is related to the dipole-dipole correlation function by the fluctuation-dissipation theorem [37]. All correlation functions are expected to display the same glassy slowdown as the temperature is decreased [38, 39]. As a result, the dipole-dipole correlation should have the same time and temperature evolution as in Fig. I.3, and the corresponding spectrum should exhibit signatures of the approach to the glass transition. An example is displayed in Fig. I.4. Such as intermediate scattering functions, spectra display richer changes than the simple increase in the relaxation time. At high temperatures, the spectra follow the Debye Lorentzian shape, and they peak at the gigahertz scale. This reflects the near-exponential relaxation on the picosecond timescale in the time domain. As the temperature decreases, the spectra broaden and they acquire a two-peak structure which corresponds to the two-step decay in the time correlation functions. The low-frequency peak accounts for the structural α-relaxation and its position $\omega_\alpha = 1/\tau_\alpha$ shifts towards lower frequencies when the temperature is decreased. This peak is often fitted by several empirical formulas, such as the Cole-Davidson [40] or the Havriliak-Negami [41]

$$\epsilon''(\nu) \propto \mathrm{Im}\left\{ \frac{1}{[1 + i(\omega\tau)^{\alpha}]^{\beta}} \right\} \tag{I.5}$$

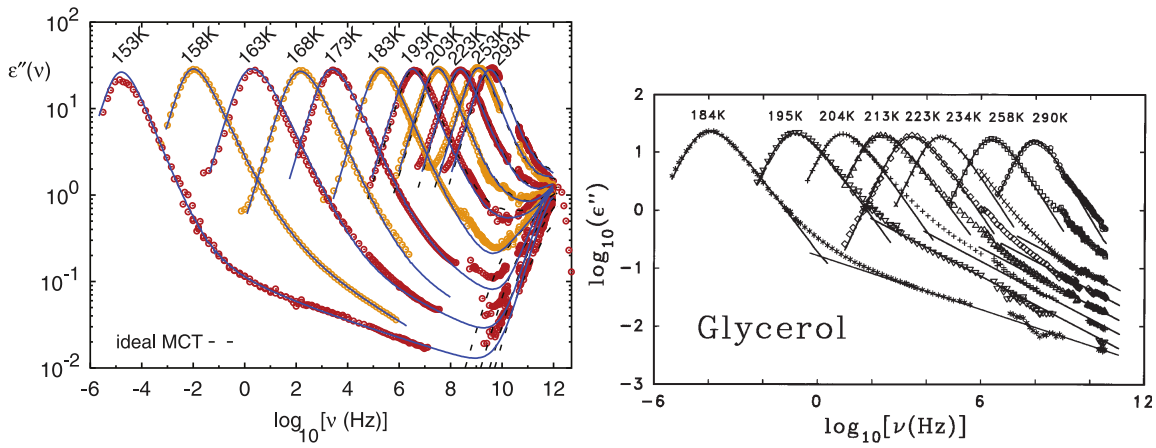

Fig. I.4 | (Left) Dielectric loss $\epsilon''(\nu)$ versus frequency ν of propylene carbonate on a double logarithmic axis for several temperatures which are directly indicated on the graph. The spectra display two peaks at low temperatures which stem for the two-step decay in time correlation functions. As the temperature decreases, the position of the main peak in relaxation spectra shifts towards lower frequencies. This reflects the increase in the relaxation time. The spectra also become increasingly broad, as they cover 10 orders of magnitude close to T_g. Figure from Ref. [34]. (Right) Dielectric spectra for glycerol at several temperatures which are indicated on the graph. Data are represented on a double logarithmic axis and the high-frequency peak is not shown. For low temperatures close to T_g, data are compatible with a sharp α-peak at low frequencies which is fitted by using a Cole-Davidson function, while at intermediate frequencies, data display an "excess wing" which is modelled by a power law. Data from Ref. [35].

laws[5], which are the equivalents of the stretched exponential in the frequency domain [42]. In the above expression, Im{.} denotes the imaginary part of a complex, while α, β and τ are adjustable parameters. As the temperature approaches T_g, the low-frequency part of the spectrum becomes larger and larger, as it almost covers 10 decades. It displays a sharp peak in the millihertz range which is accompanied at intermediate frequencies (in the hertz to megahertz range) by a slowly decaying signal. If one tries to fit the main peak (for instance with the previous Havriliak-Negami process), the signal at intermediate frequencies appears in excess and it is consequently referred to as the "excess wing" in the experimental literature [35]. It is usually fitted by a power law [43] or by using a Cole-Cole law[6] [44]. Even though the signal in dielectric spectra could be more complex due to the chemical details of the material [45], the "excess wing" seems to be a universal feature of the dielectric spectra of glass-forming liquids close to T_g [46–49].

1.1.3 Dynamic heterogeneities

At the level of the average correlation functions or the relaxation spectra, assessing the cause of their broadening as the temperature decreases is difficult. A direct visualisation of the motion of the particles at the microscopic scale is then more insightful. The motion of the particles is found to be spatially heterogeneous and intermittent in time. In other words, the particles

[5]The Cole-Davidson law is obtained from the Havriliak-Negami fitting function by setting $\alpha = 1$. In particular, it behaves as a power law of exponent $-\beta$ at high frequencies and as a power law of exponent 1 at low frequencies.

[6]The Cole-Cole law is obtained from the Havriliak-Negami fitting function by setting $\beta = 1$. In particular, it behaves as a power law of exponent $-\alpha$ at high frequencies.

alternate between sudden jumps and quiescent vibrations around a given position [50]. This suggests that there are strong spatio-temporal dynamic fluctuations and that the supercooled liquid is always populated by mobile and immobile regions which relax on different timescales. However, above the glass transition, the supercooled liquid is ergodic, and slow (resp. fast) regions regularly become fast (resp. slow) [51].

These dynamic heterogeneities consequently represent a natural explanation of the shape of the correlation functions and of the relaxation spectra. Indeed, if one assumes that the dynamics proceeds thanks to the superposition of the relaxation of the different regions of the glass-forming liquid on different timescales, then this should give rise to a large distribution of timescales which should result in broad spectra and correlation functions. The local relaxation can be exponential or already stretched [52] (which corresponds to a "homogeneous" broadening [53]). In the latter case, this intensifies the broadening of the correlation functions and the relaxation spectra. Even though the dynamic heterogeneities account for the broadening of the α-peak, the microscopic origin of the "excess wing" close to T_{g} remains controversial. This stems for the fact that experiments lack a nanoscopic resolution while computer simulations are often limited to temperature and time windows at odds with the experimental studies. So far, "excess wings" have not been reported in computer simulations of the dynamics of glass-forming liquids. In Chap. VI, we tackle this problem by using the recent swap algorithm [54, 55] which allows for the fast thermalisation of size-polydisperse model glass-formers down to the extrapolated experimental glass transition temperature T_{g}.

As the two-point correlation functions, such as the intermediate scattering function, are blind to the local fluctuations of the dynamics, namely, to the dynamic heterogeneities, four-point correlation functions at different points in space and at different times have been introduced to characterise the dynamic heterogeneities, in particular to quantify the typical amplitude of the dynamic fluctuations along with their typical spatial extent and their typical temporal duration [51]. In all the experimental and numerical systems which display glassy behaviour, the variance of the dynamic fluctuations, which is known as the four-point dynamic susceptibility $\chi_4(t)$, grows with time and it reaches a maximum for times $t \simeq \tau_\alpha(T)$, before it decreases at later times [56–58]. Consequently, the α-relaxation time represents the typical duration of the dynamic heterogeneities before the dynamics becomes uncorrelated [50]. The typical size of relaxing domains, which is known as the four-point dynamic length $\xi_4(t)$, also grows with time and it likely saturates at later times [59]. The maximum value $\xi_{\mathrm{d}}(T)$ of the four-point dynamic length, which is called the dynamic correlation length, represents the maximum linear extent of dynamically correlated domains, and it grows upon decreasing the temperature [60, 61].

The origin of the dynamic heterogeneities has been scrutinised in many past studies. In order to disentangle purely dynamic effects from the heterogeneities which are encoded in the structure, the iso-configurational ensemble has been introduced [62, 63]. Several simulations are initiated from the same initial condition with different initial velocities which are drawn from the Maxwell-Boltzmann distribution (in the case of molecular dynamics simulations) or with different sequences of random numbers (in the case of Monte Carlo simulations) [64]. The dynamics of each particle is then averaged over the iso-configurational runs and a propensity field is computed to reveal dynamic heterogeneities which are rooted in the structure of the liquid. In particular, correlations with soft vibrational modes [65–67], local density [67, 68], locally favoured structures [67, 68] or hexatic order [69, 70] have been reported, without being able to reveal direct causal links or to assess the degree of generality of these correlations among systems [71]. However, it is expected that at the single-particle level, the dynamic fluctuations

are essentially of purely dynamic nature. Connections with the statics may only exist at larger lengthscales and timescales [72]. In Chap. V, we define a new structural indicator which relies on the strength of a field to localise a given patch of the liquid close to its initial position. Its correlation with the propensity field would be worth studying in the future.

1.2 Properties of the non-equilibrium glass phase

1.2.1 Tuning glass stability

Below the glass transition temperature T_g, glasses have a relaxation time that exceeds the typical experimental time, and they thus behave as non-equilibrium systems. This situation also happens when the equilibrium supercooled liquid at a temperature T_i is instantaneously quenched at a low temperature $T_\mathrm{f} < T_\mathrm{g} < T_\mathrm{i}$ [73]. Glasses are found to age, which means that they are continuously slowly evolving [74]. One can still define intensive variables, for instance an effective temperature, but they now depend on the waiting or aging time t_w, namely, the elapsed time since the liquid first fell out of equilibrium [75]. The off-equilibrium relaxation time of aging systems can be measured from the two-time intermediate scattering function, namely,

$$F(\boldsymbol{q}, t_\mathrm{w}, t) = \frac{1}{N} \left\langle \sum_{j,k=1}^{N} e^{i\boldsymbol{q}\cdot[\boldsymbol{r}_j(t_\mathrm{w}+t)-\boldsymbol{r}_k(t_\mathrm{w})]} \right\rangle, \tag{I.6}$$

and it also varies significantly with the age of the glass. The larger t_w, the longer it takes for the system to decorrelate. In the case of an instantaneous quench, the relaxation time $\tau(t_\mathrm{w}, T_\mathrm{i}, T_\mathrm{f})$ smoothly evolves from the equilibrium α-relaxation at the initial temperature $\tau_\alpha(T_\mathrm{i})$ to a power law behaviour $\tau(t_\mathrm{w}, T_\mathrm{i}, T_\mathrm{f}) \sim t_\mathrm{w}^\mu$ [76]. The average energy is also a decreasing function of t_w. This suggests that glasses become more stable upon aging [77] (see[7] Fig. I.2). A similar effect appears when the liquid is quenched from a decreasing initial temperature T_i down to T_f. In addition, thanks to temperature cycles, rejuvenation and memory effects can be observed [78].

Overall, the previous facts show that the glass stability (as measured by its lower energy or enthalpy or its higher density or its higher off-equilibrium relaxation time) is related to the age of the latter and to the lowest temperature at which it fell out of equilibrium. Therefore, glass properties can be tuned thanks to aging protocols. However, on experimental timescales, aging does not result in a large change in glass properties. A more efficient way of enhancing glass stability is to use vapor deposition [26, 79]. This new preparation protocol consists in slowly depositing a compound on a substrate at a temperature T_sub. By considering deposition rates of about less than 0.5 nm.s^{-1} and substrate temperatures of about 85 % of the glass transition temperature of the deposited material, more stable glasses with larger density or lower enthalpy can be formed [80, 81]. The glasses which are obtained by vapor deposition are of similar stability as glasses which would be aged for about 3500 years [82] (see Fig. I.2). The high stability of vapor-deposited glasses originates from the very high mobility of the molecules at the free surface (first nanometers) as compared to the bulk (we recall that T_sub is usually a fraction of T_g) [83]. The diffusion coefficient of the molecules at the free surface can be up to 7 orders of magnitude higher than the bulk diffusion constant [84]. Therefore, if the deposition rate is small enough, then the molecules on the surface can find near-equilibrium configurations, and this leads to more stable glasses. In Chap. VII, we present other preparation protocols on

[7] For solid or liquid phases which are poorly compressible, enthalpy and energy are usually roughly equal.

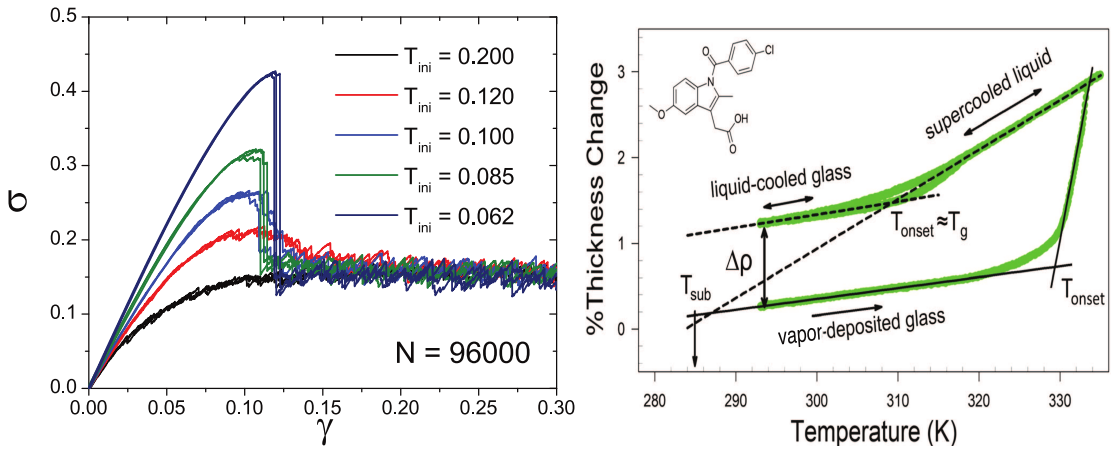

Fig. I.5 | (Left) Stress-strain curves $\sigma(\gamma)$ which are obtained from athermal quasi-static shear simulations of a system of $N = 96000$ size-polydisperse soft spheres. The samples are prepared from equilibrium configurations at different temperatures T_{ini} which are then instantaneously quenched at zero temperature. All the curves display a first elastic regime at small strains and a plastic regime at large strains which are separated by a yielding transition. At large initial temperatures, the yielding transition is a smooth crossover. Instead, at low initial temperatures, the yielding transition becomes a first order non-equilibrium phase transition with a stress discontinuity which takes the form of an overshoot. Figure from Ref. [85]. (Right) Film of vapor-deposited glass of indomethacin (inset) which is first heated at a constant rate of 1 K.min^{-1}. The film thickness shows an abrupt discontinuity in its first derivative with respect to the temperature at a temperature T_{onset} when the sample "melts" to the supercooled liquid state. The liquid is subsequently cooled with a cooling rate of 1 K.min^{-1} and it falls out of equilibrium for a larger thickness and a corresponding lower density. When re-heated at the same rate, the liquid-cooled glass follows the cooling curve which displays a much lower onset temperature $T_{\text{onset}} \simeq T_{\text{g}}$ than the one of the vapor-deposited glass. Figure from Ref. [86].

the computer which are cheap in terms of simulation walltime and which result in more stable glasses than the ones that are obtained by gradual cooling or physical aging.

1.2.2 Influence of glass stability upon shearing or heating

Glass properties are history-dependent and protocol-dependent, and glass stability manifests itself in a variety of phenomena in glasses. First, the behaviour of glasses under shear depends on their stability. When performing athermal quasi-static shear deformations (at zero temperature and in the limit of zero shear rate $\dot{\gamma}$), a glass undergoes a yielding transition from an elastic regime to a plastic-flow regime at a finite yield strain γ_{Y} and a corresponding finite yield stress σ_{Y} in the plastic regime [87, 88]. Nevertheless, the nature of the yielding transition depends on the glass stability and it can turn from ductile to brittle upon increasing the glass stability [85, 89]. In the ductile case, the yielding transition is smooth with a weakening due to small plastic events[8]. In the brittle case instead, the elastic regime extends over a broader range of deformations and there is a sharp stress overshoot which is followed by a discontinuous stress drop. This results in a catastrophic failure of the material and in the formation of a system-spanning shear band[9] [90], see Fig. I.5. Recently, the transition from ductile to brittle yielding upon increasing

[8]This is what happens with toothpaste for example.
[9]This is what happens with the screen of a smartphone for instance.

the glass stability was shown to be controlled by the physics of the zero-temperature random-field Ising model (RFIM) [91] (see Appendix A of Chap. II) when driven by an external magnetic field [92]. The latter displays a hysteresis when the applied magnetic field is first increased and then decreased. There is a non-equilibrium first order phase transition with a discontinuous hysteresis loop at a spinodal [93] and a macroscopic avalanche in the magnetic response [94] for low-enough disorder strength. The line of non-equilibrium first order transition terminates in a second order critical point at a critical disorder. Above this critical point, the RFIM displays a continuous hysteresis loop in its magnetic response [95]. In the mapping of glasses onto the RFIM, the stability of the glass encodes the effective strength of the disorder. In particular, well-annealed (stable) glasses have a low intrinsic disorder and they show a discontinuity in their stress-strain curve. Instead, poorly annealed glasses have a higher disorder and their transition from the elastic regime to the plastic regime upon shearing becomes a mere crossover without any discontinuity in the stress.

A second manifestation of the history- and protocol-dependent behaviour of glasses is found upon heating, see Fig. I.5. When one heats a glass at a finite heating rate, its density or its enthalpy (or its energy) with respect to the temperature usually displays a discontinuity in its slope at an onset temperature T_{onset} which marks its transformation from the glass to the supercooled liquid state [96]. Equivalently, the heat capacity shows a maximum at $T = T_{\text{onset}}$ [97]. This onset temperature is an increasing function of the glass stability[10]: the more stable the glass, the higher the temperature in order to fall back in equilibrium. For instance, the vapor-deposited glasses have a larger onset temperature than the liquid-cooled glasses. This is the manifestation of the enhanced kinetic stability $\mathcal{S}(T) = \tau_{\text{rec}}(T)/\tau_\alpha(T)$ of the vapor-deposited glasses. The latter represents the ratio of the recovery time to transform back to the supercooled liquid when suddenly heated at a temperature T to the bulk relaxation time of the supercooled liquid at the same temperature [99]. The liquid-cooled glasses typically have a kinetic stability ratio of about 10^2 while the ultrastable glasses which are prepared via vapor deposition can reach stability ratios of about 10^5 at a constant pressure [100]. The high kinetic ratio of the ultrastable glasses lies in their recovery mechanism which shares many similarities with the melting of a crystal, even though the liquid and the glass are not a priori two distinct thermodynamic phases. In particular, thin films transform via the propagation of a mobility front which starts from the free surface [101, 102], while larger samples transform thanks to a nucleation-and-growth mechanism with Avrami-like kinetics [99, 103]. In other words, thick glass samples melt because of the appearance of rare nuclei of the supercooled liquid in the glass, which is followed by a rapid growth of these liquid droplets. The influence of the glass stability on the yielding transition or on the heating behaviour is utilised in Chap. VII in order to assess the stability of computer-generated glasses via new annealing schemes.

The glass stability also affects other properties, such as sound propagation [104], heat capacity and conductivity [105–108] (in relation with two-level systems), or vibrational properties [109].

[10] We stress that this temperature is a non-equilibrium and protocol-dependent property, and in particular it is different from the onset temperature of glassy behaviour which is usually defined as the highest temperature at which the equilibrium time correlation functions display a two-step decay [98].

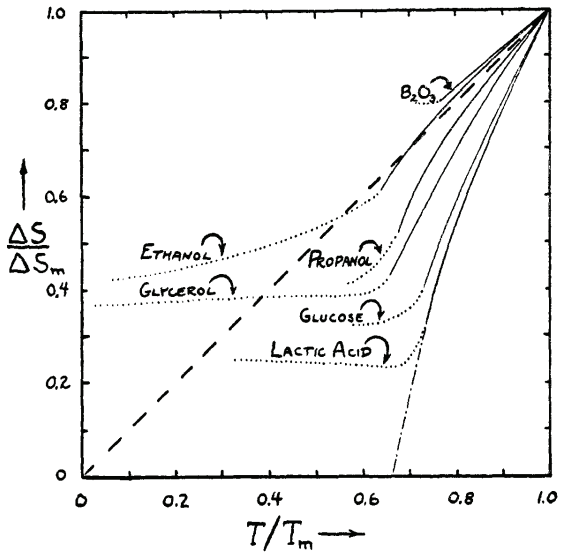

Fig. I.6 | Excess entropy ΔS of several supercooled liquids with respect to the crystal which has been divided by its value ΔS_{m} at the melting point for various glass-formers. Data are plotted as a function of the temperature T which has been rescaled by the melting point temperature T_{m}. The dotted lines represent the value of the excess entropy below the glass transition temperature when the systems are out of equilibrium. Equilibrium data look to extrapolate to zero at a finite temperature T_{K}. Figure from Ref. [110].

1.3 Thermodynamic features

The dynamic glass transition corresponds to a huge increase in the relaxation time with decreasing the temperature. Similarly, the transformation of glasses into supercooled liquids shows similarities with the melting of crystals. By analogy with critical phenomena and first order phase transitions in statistical mechanics, a legitimate question that arises is whether the glass transition is due to the existence of an underlying thermodynamic phase transition at a temperature lower than T_{g} at which the relaxation time truly diverges.

Seventy years ago, Kauzmann measured the temperature evolution of the excess entropy $\Delta S(T) = S_{\mathrm{liq}}(T) - S_{\mathrm{xtal}}(T)$ for several glass-forming liquids, with $S_{\mathrm{liq}}(T)$ and $S_{\mathrm{xtal}}(T)$ the total entropies of the liquid and the crystal at the temperature T respectively [110], see Fig. I.6. The excess entropy is found to decrease sharply as the temperature is decreased, as opposed to other static quantities which vary midly, such as the total pair correlation functions[11] [11]. If one extrapolates Kauzmann's data to lower temperatures by following the supercooled regime, one finds that they are compatible with a vanishing excess entropy at a finite temperature $T_{\mathrm{K}} > 0$. This entropy crisis then naturally accounts for the jump in the heat capacity at the glass transition temperature, see the inset in Fig. I.1. The decrease in the excess entropy and its putative vanishing indicate that the glass transition is not a purely dynamic transition without any thermodynamic change. However, whether this decrease in the excess entropy is related to the glassy slowdown is still today strongly debated [112, 113].

From his analysis, Kauzmann concluded that as $\Delta S(T)$ could not be negative, the liquid should either crystallise or should undergo a thermodynamic phase transition to a glass phase.

[11] Nevertheless, very small variations in the pair correlation function may rationalise large differences in the dynamics, as reported recently [111].

Even though there is no contradiction in the fact that $\Delta S(T)$ becomes negative [114], Kauzmann's intuition of the possibility of a low-temperature thermodynamic singularity has triggered a succession of theoretical breakthroughs which has led to the mean-field theory of the glass transition for infinite-dimensional off-lattice particle systems. In this limit, the Kauzmann entropy crisis is defined in terms of a configurational entropy. It is exactly realised and it corresponds to a genuine thermodynamic phase transition to an ideal glass phase.

2. The mean-field theory of the glass transition

2.1 From fully-connected spin glasses to liquids in infinite dimensions

Mean-field theory is usually the starting point to describe phase transitions or critical phenomena. It amounts to neglecting correlations between fluctuations and to derive an effective field which carries information about the mean interactions between constituents. It is often more tractable than the initial theory and it may be solved exactly [115]. The mean-field theory of the glass transition was first derived in the context of spin glasses, namely, spin systems in the presence of quenched disorder [116–120]. Thanks to the underlying lattice and their mean-field nature, these models can be solved exactly. Based on phenomenological arguments from density functional theory, the results which were obtained for spin glasses were advocated to hold for structural liquids too [121–124].

More recently, the mean-field theory of supercooled liquids and structural glasses was exactly derived in the limit of infinite dimensions of space $d \to +\infty$ (see reviews in Ref. [125, 126]). Qualitatively, the limit of infinite dimensions is of mean-field nature because, for a given particle, the number of its neighbours diverges with d and its interactions with them can be considered as an effective thermal bath [127].

In the next sections, we describe the results which are obtained at the mean-field level. They are next compared with the phenomena which are presented in the previous section.

2.2 The dynamics in infinite dimensions

The equilibrium dynamics of supercooled liquids in infinite dimensions was first derived exactly by using path integrals and the Martin-Siggia-Rose-De-Dominicis-Janssen formalism [128, 129], and by considering a Langevin dynamics at the single-particle level [130]. The result is a generating functional [131] which takes the form of a partition function over trajectories. By analogy with the statistical mechanics of interacting systems at equilibrium, one can then perform a virial expansion of the generating functional in increasing powers of the density [30]. Formally, this amounts to considering a diagrammatic expansion of the generating functional with density vertices and bonds which are formed by Mayer functions. At order n in density, the relevant diagrams are made of n vertices and taking into account diagrams with an increasing number of nodes then corresponds to an expansion in increasing powers of the density. However, we have already mentioned that the number of neighbours of a given particle diverges with d in infinite dimensions. As a result, for a central particle i which interacts with particles j and k, the probability that j and k interact is extremely small. Then, a virial expansion which is truncated at the second order should already give a reasonable estimate. Actually, the truncation of the virial expansion to the second order is exact in the limit $d \to +\infty$ [132, 133]. As a result, a low-density expansion is equivalent to a high-dimension one [134]. Eventually, saddle-

point approximations which become exact in the limit $d \to +\infty$ yield an exact equation for the correlation function (namely, the mean-squared displacement), which involves a memory kernel that is determined self-consistently from the autocorrelation of the interaction force between the particles.

Later on, the mean-field dynamical equations were derived from simpler arguments [126, 127]. By first considering the dynamics at the single-particle level and by assuming that the interaction between a tagged particle and the other ones can be modelled by an effective friction (effective bath), one obtains

$$\zeta \frac{\mathrm{d}\boldsymbol{r}_i}{\mathrm{d}t}(t) = -\beta \int_0^t \mathrm{d}t' M(t-t') \frac{\mathrm{d}\boldsymbol{r}_i}{\mathrm{d}t}(t') + \boldsymbol{\Xi}_i(t), \tag{I.7}$$

where $\beta = 1/T$ (the Boltzmann constant is set to unity) and where the colored noise $\boldsymbol{\Xi}_i(t)$ is of zero mean and of correlation

$$\langle \boldsymbol{\Xi}_i(t) \boldsymbol{\Xi}_j(t') \rangle = \delta_{ij} \left[2T\zeta\delta(t-t') + M(t-t') \right] \mathbb{1}, \tag{I.8}$$

with δ_{ij} the Kronecker delta, which is equal to 1 if $i = j$ and to 0 otherwise. In the above equation, $\mathbb{1}$ represents the identity matrix (the components of the noise in different directions of space are uncorrelated), the first term accounts for the actual thermal bath and the second term represents the effective bath which takes into account the interactions of a tagged particle with all its neighbours and which is added in order for the fluctuation-dissipation theorem to be satisfied. The second term is not delta-correlated in time but it is instead described by a memory kernel which corresponds to the force-force correlation function, namely,

$$M(t-t') = \frac{1}{Nd} \sum_{i \neq j} \langle \boldsymbol{F}_{i \to j}(t) \cdot \boldsymbol{F}_{i \to j}(t') \rangle, \tag{I.9}$$

where the sum runs over all indices $i, j = 1 \dots N$ and where $\boldsymbol{F}_{i \to j}(t)$ is the force which is exerted by particle i on particle j at time t.

The equation for the memory kernel is obtained by considering the dynamic equation for the inter-particle distance $\boldsymbol{r} = \boldsymbol{r}_i - \boldsymbol{r}_j$. By using Eq. (I.7), one finds

$$\frac{\zeta}{2} \frac{\mathrm{d}\boldsymbol{r}}{\mathrm{d}t}(t) = -\frac{\beta}{2} \int_0^t \mathrm{d}t' M(t-t') \frac{\mathrm{d}\boldsymbol{r}}{\mathrm{d}t}(t') + \boldsymbol{\Xi}(t) - \boldsymbol{F}(\boldsymbol{r}(t)), \tag{I.10}$$

where $\boldsymbol{\Xi}(t)$ is a random process of zero mean and of correlation

$$\langle \boldsymbol{\Xi}(t) \boldsymbol{\Xi}(t') \rangle = \left[T\zeta\delta(t-t') + \frac{1}{2} M(t-t') \right] \mathbb{1}, \tag{I.11}$$

and where $\boldsymbol{F}(\boldsymbol{r}(t)) = \boldsymbol{F}_{i \to j}(t)$ is the interaction force between two particles, which depends on their relative distance. Eq. (I.9) and (I.10)-(I.11) represent a closed system from which one can determine the memory kernel self-consistently by iteration. By starting from $M(t) = 0$, one can simulate the process given by Eq. (I.10)-(I.11), then one can compute the corresponding memory kernel thanks to Eq. (I.9) and can insert this new form into Eq. (I.10)-(I.11). Eventually, one can repeat the entire procedure until convergence [135].

Finally, once the memory kernel is known, the differential equation for the mean-squared displacement, *i.e.*,

$$\hat{\Delta}(t) = \left\langle \frac{1}{N} \sum_{i=1}^{N} |\boldsymbol{r}_i(t) - \boldsymbol{r}_i(0)|^2 \right\rangle, \tag{I.12}$$

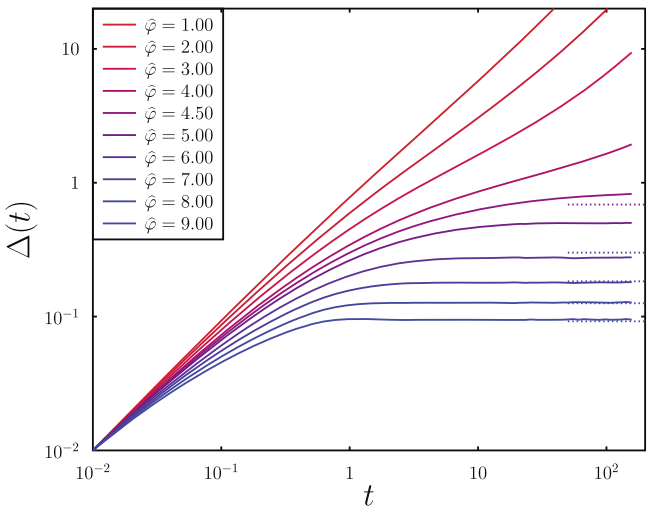

Fig. I.7 | Evolution of the mean-squared displacement $\Delta(t) = \hat{\Delta}(t)d/\ell^2$ for infinite-dimensional hard spheres (with ℓ the diameter of the spheres) for several rescaled packing fractions $\hat{\varphi} = \rho V_d \ell^d/d$, with V_d the volume of the unit sphere in d dimensions and ρ the number density. Time is expressed in units of $\zeta\ell^2/T$. The mean-squared displacement develops a plateau at intermediate times between the diffusive regimes at short times and at long times when increasing the density. At large densities $\hat{\varphi} > \hat{\varphi}_{\mathrm{d}} \simeq 4.8067$, the dynamics is totally arrested with a vanishing long-time diffusion constant. Figure from Ref. [135].

can be derived from Eq. (I.10) and reads

$$\zeta \frac{\mathrm{d}\hat{\Delta}}{\mathrm{d}t}(t) = -\beta \int_0^t \mathrm{d}t' M(t-t') \frac{\mathrm{d}\hat{\Delta}}{\mathrm{d}t}(t') + 2dT. \tag{I.13}$$

The evolution of the mean-squared displacement for hard spheres in the limit $d \to +\infty$ is shown in Fig. I.7. The phenomenology is very similar to what is found experimentally, compare with Fig. I.3. When the density is increased (or the temperature is decreased), the mean-squared displacement is no longer purely diffusive and it develops a two-step increase with a first increase towards a plateau which is followed by a subsequent diffusion at later times. One strong prediction of mean-field theory is that the diffusion constant vanishes at a finite temperature or density. Equivalently, the α-relaxation time diverges at this same state point. This corresponds to the dynamical transition temperature T_{d} or density ρ_{d} which is found by looking for a solution of Eq. (I.13) with a finite limit when $t \to +\infty$. When approaching the dynamical transition from the supercooled liquid side, one finds that the inverse diffusion constant diverges as a power law. Interestingly, a similar result was also found few decades ago within the mode-coupling theory [136]. Even though the two approaches yield equations of similar form for the correlation functions, hence they qualitatively describe the same trends, there are significant quantitative differences which are due to the successive approximations that are involved in the derivation of the mode-coupling equations [137, 138]. In particular, in mode-coupling theory, the memory kernel is expressed as a mere function of the correlation function $\hat{\Delta}(t)$ while here it is computed self-consistently from the dynamic process itself.

2.3 The thermodynamics in infinite dimensions

2.3.1 Definition of metastable states

Below T_d (or above ρ_d), the equilibrium relaxation time is truly infinite. Therefore, the equilibrium dynamics is no longer ergodic and the system only explores a narrow region of the phase space. In real space, this limited exploration corresponds to thermal vibrations of the particles of typical squared amplitude which is given by the plateau value in the mean-squared displacement. As a consequence, the phase space is split into disconnected components in which the system is trapped forever. These components represent the metastable states, hence the name of this thesis. There are two directions of study. On the one hand, one can be interested in the thermodynamics of the system within a metastable state, to account for the properties of the glass when the system falls out of equilibrium. One can aim at computing its free energy, which has two contributions: one comes from the average energy of the configurations that are visited within the metastable state, while the other one comes from the vibrational entropy of the glass within the metastable state. On the other hand, one can also focus on the ergodic supercooled liquid which is obtained when exploring the phase space entirely, *i.e.*, when summing over all the metastable states. For instance, how many metastable states are there? What is their structure? How can they be generated, for instance by looking for the extrema of a given functional?

Here, we describe the second line of thought, and the first one is instead described in the next chapter. Below the dynamical transition temperature, one can formally rewrite the partition function of the supercooled liquid as [139, 140]

$$\mathcal{Z}(T) = \sum_\alpha e^{-N\beta f_\alpha} = \int \mathrm{d}f e^{N[\Sigma(f;T)-\beta f]}, \tag{I.14}$$

where the sum runs over all the metastable states α of free energy per particle $f_\alpha(T)$. The partition function is written in the continuum limit by introducing the complexity

$$\Sigma(f;T) = \frac{1}{N}\ln \mathcal{N}(f;T), \tag{I.15}$$

which represents the logarithm of the number $\mathcal{N}(f;T)$ of metastable states of free energy f at a temperature T per unit particle. The free energy of the liquid can then be computed from the previous partition function by using a saddle-point (Laplace) approximation [141] in the thermodynamic limit ($N \to +\infty$) and it reads

$$F(T) = -\frac{T}{N}\ln \mathcal{Z}(T) = \inf_f\{f - T\Sigma(f;T)\} = f^*(T) - T\Sigma(f^*;T). \tag{I.16}$$

The quantity $f^*(T)$ corresponds to the minimiser of the quantity between brackets and it is thus a solution of

$$\frac{\mathrm{d}\Sigma}{\mathrm{d}f}(f^*;T) = \frac{1}{T}. \tag{I.17}$$

By performing the saddle-point approximation, one implicitly assumes that the complexity remains finite in the thermodynamic limit, or equivalently that the number of metastable states is exponentially large in system size. Equivalently, this means that there is an extensive difference between the free energy of the liquid $F(T)$ and the free energy of a typical glass state $f^*(T)$ at a temperature T, which is precisely the temperature times the complexity. This is confirmed

by direct calculations of the complexity (see the next section). The equilibrium complexity is finally obtained as $\Sigma(T) = \Sigma(f^*; T)$. It is often called the configurational entropy as it quantifies the number of typical metastable states at a given temperature.

The metastable states correspond to distinct regions of the phase space which are made of a set of configurations that are connected by thermal vibrations of the particles. It is then reasonable to associate a different density profile

$$\rho_\alpha(\boldsymbol{x}) = \left\langle \sum_{i=1}^{N} \delta(\boldsymbol{x} - \boldsymbol{r}_i) \right\rangle_\alpha \tag{I.18}$$

to each metastable state α, where the brackets stand for a thermal average over the metastable state α only. By starting from density functional theory, a free energy landscape functional $\mathcal{F}[\rho(\boldsymbol{x})]$ can be conceptually defined [122, 142, 143]. On general grounds, the emergence of the metastable states in the equilibrium dynamics is expected to be associated with the emergence of many metastable minima in the functional $\mathcal{F}[\rho(\boldsymbol{x})]$ (*i.e.*, in the free energy landscape). Therefore, the complexity can in principle be derived by first computing $\mathcal{F}[\rho(\boldsymbol{x})]$ and then by counting the number $\mathcal{N}(f; T)$ of its minima of free energy f [144]. However, deriving the free energy functional from first principles has been impossible so far. The construction is however possible in the context of mean-field spin glasses and it is known as the TAP approach [145–148]. In the following section, we explain how to compute the configurational entropy, even without a detailed description of the free energy landscape.

Before, we stress once again that a metastable state is not a mere configuration but a set of configurations in the phase space. In other words, the free energy landscape should not be confused with the potential energy landscape which corresponds to the total potential energy of the system as a function of the positions of the particles (*i.e.*, the Hamiltonian $\hat{H}[\boldsymbol{r}^N]$). Accordingly, the metastable states should not be confused with the potential energy minima which are called inherent structures [149]. Free energy minima and energy minima only coincide at zero temperature.

2.3.2 Computation of the configurational entropy and the Kauzmann transition

In order to compute the complexity, one can usefully introduce m replicas[12] or copies of the same liquid and assume that the m replicas are constrained to be in the same metastable state [150]. The partition function of this replicated system of m copies then reads

$$\mathcal{Z}_m(T) = \sum_\alpha e^{-N\beta m f_\alpha} = \int \mathrm{d}f e^{N[\Sigma(f;T) - m\beta f]}. \tag{I.19}$$

The latter results in a replicated free energy

$$F_m(T) = \inf_f \{mf - T\Sigma(f; T)\} = mf^*(T) - T\Sigma(f^*; T), \tag{I.20}$$

where $f^*(T)$ is the solution of

$$\frac{\mathrm{d}\Sigma}{\mathrm{d}f}(f^*; T) = \frac{m}{T}. \tag{I.21}$$

[12]The use of replicas to deal with disordered systems is extensively discussed in Chap. II.

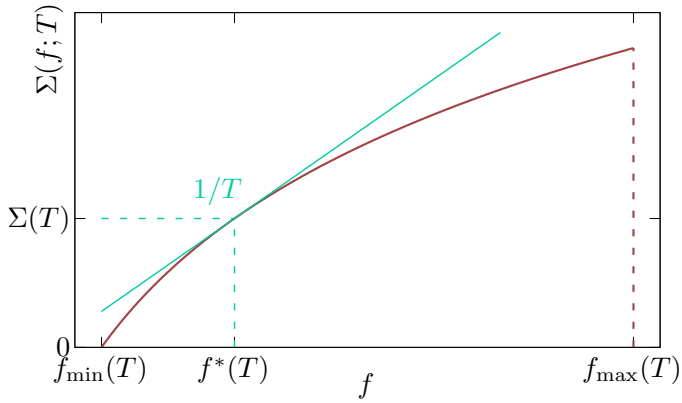

Fig. I.8 | Schematic evolution of the complexity $\Sigma(f;T)$ at a low-enough temperature T (typically for $T < T_{\rm d}$). The configurational entropy vanishes at $f = f_{\min}(T)$, it increases with f and it drops discontinuously to zero at $f = f_{\max}(T)$. The typical free energy $f^*(T)$ of the metastable states at a temperature T is given by the graphical solution of Eq. (I.17).

By computing the replicated free energy for an integer number m of replicas and by then performing an analytical continuation for any real number m, one can derive both the typical free energy of the glassy metastable states [151]

$$f^*(T) = \left.\frac{\partial F_m}{\partial m}\right|_{m\to 1}(T), \tag{I.22}$$

and the configurational entropy

$$\Sigma(T) = \Sigma(f^*;T) = \frac{1}{T}\frac{\partial}{\partial m}\left(\frac{F_m}{m}\right)\Big|_{m\to 1}(T). \tag{I.23}$$

From the parametric plot of $\Sigma(f^*;T)$ with respect to $f^*(T)$, one can eventually reconstruct the curve $\Sigma(f;T)$. The shape of this curve is system-dependent but its schematic evolution is displayed in Fig. I.8. The thermodynamics of the system can now be discussed in the light of the evolution of the complexity. We restrict ourselves to the case $T < T_{\rm d}$[13].

For temperatures $T < T_{\rm d}$, the evolution of the complexity is usually monotonic with f in a range $[f_{\min}(T), f_{\max}(T)]$ and the typical free energy of glassy metastable states $f^*(T)$ is obtained by the graphical solution of Eq. (I.17). The value of the complexity at this free energy gives the configurational entropy $\Sigma(T)$. As the temperature decreases, $1/T$ increases and both $f^*(T)$ and the configurational entropy decrease. Qualitatively, this means that as the temperature is reduced, the typical free energy of the metastable states decreases but the number of metastable states which contribute to the free energy of the supercooled liquid also decreases. At this mean-field level, there is usually[14] a temperature $T_{\rm K} < T_{\rm d}$ at which $f^*(T) = f_{\min}(T)$. At this temperature, the configurational entropy vanishes. This means that the thermodynamics is now dominated by a sub-exponential number of metastable states which correspond to the lowest minima of the free energy landscape. Below $T_{\rm K}$, the configurational entropy remains equal to zero[15] and the metastable states which were dominating at $T_{\rm K}$ continue to control

[13] For $T > T_{\rm d}$, metastable states either do not exist or they may exist below an onset temperature but they do not dominate the thermodynamics.

[14] There are however liquids which do not display an entropy crisis at any finite temperature [126].

[15] The configurational entropy cannot be negative, see Eq. (I.15).

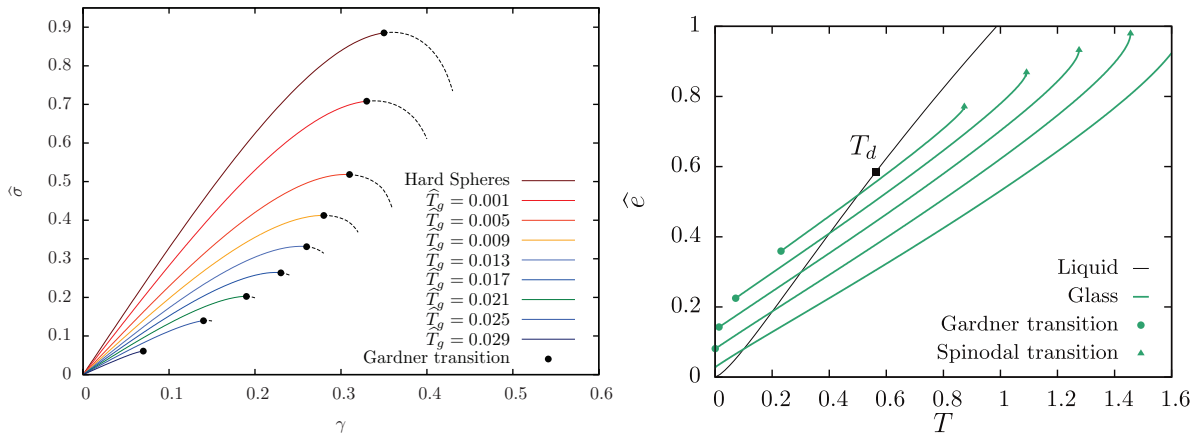

Fig. I.9 | (Left) Mean-field stress-strain curves for harmonic-sphere and hard-sphere glasses which are obtained from equilibrium configurations at a density $\hat{\varphi}_{\rm g} = 6$ (see the caption of Fig. I.7) and different temperatures $\hat{T}_{\rm g}$ below the dynamical transition temperature (where $\hat{T} = Td^2$ and where the temperature is expressed in units of the typical interaction energy ε between harmonic spheres). The rescaled stress is $\hat{\sigma} = \sigma/(Td^3)$ where the usual stress σ is expressed in units of ε/ℓ^3 with ℓ the diameter of the harmonic spheres. Dashed lines represent an approximation of the stress-strain curve above the Gardner transition [157]. Figure from Ref. [158]. (Right) Rescaled energy $\hat{e} = e/d$ (where energies are expressed in units of ε) for harmonic spheres as a function of the temperature. Glasses which are prepared at different initial temperatures leave the supercooled liquid equation of state and follow distinct glass equations of state. When the system is heated infinitely slowly, it follows the non-equilibrium glass equation of state until an onset temperature (triangle) where a spinodal instability occurs and where the glass transforms back to the liquid. Figure from Ref. [159].

the thermodynamic behaviour of the system [152]. At $T = T_{\rm K}$, one can then show that the free energy $F(T)$ and its first derivative with respect to the temperature are continuous but the second derivative is discontinuous. This corresponds to a genuine thermodynamic phase transition[16] which takes place at $T_{\rm K}$ between the liquid phase and the ideal glass phase. Glass formation at the thermodynamic level below $T_{\rm d}$ is therefore controlled by the number of free energy minima rather than the value of the free energy at these minima [$f^*(T)$ weakly varies with the temperature and it does not display any singular behaviour while changing the temperature].

Another way of computing the configurational entropy relies on Eq. (I.16). The configurational entropy represents up to a factor T the difference between the free energy of the liquid and the free energy of the typical metastable states. Therefore, a direct computation of these two terms allows for an estimation of the configurational entropy. The computation of the glass free energy requires to constrain the integration over the phase space to a given metastable state. In practice, this is done by introducing a penalty in the Hamiltonian of the liquid for large excursions from a given reference density profile. This construction, which is known as the theoretical Franz-Parisi construction, is extensively described in Chap. II [153–156].

2.4 Properties of the non-equilibrium glass phase in infinite dimensions

The non-equilibrium behaviour of glasses can also be investigated in mean-field theory by using the constrained thermodynamics formalism, which is described in the next chapter, along

[16]This thermodynamic phase transition is not of second order because the associated order parameter jumps discontinuously, see the next chapter. It is thus often called a random first order transition [122].

with the state-following formalism to follow glasses that are prepared in equilibrium conditions at an initial temperature down to any lower temperature [160]. The behaviour under applied quasi-static shear [158, 161] is summarised in Fig. I.9. An elastic regime with a linear behaviour is first observed which extends on a range that broadens as the initial temperature decreases and the glass stability conversely increases. This behaviour is followed by the plastic regime which corresponds to a spinodal beyond which metastable states no longer exist. For a high glass stability, a stress overshoot is found at the yielding transition.

The behaviour of glasses upon cooling or heating can also be investigated in the mean-field limit, see Fig. I.9. By starting from equilibrium configurations and by following a typical glassy metastable state upon cooling, one finds the glass equation of state which lies above the equilibrium curve. When the glass is further heated infinitely slowly, the metastable state can be followed to higher temperatures than the one at which it first fell out of equilibrium. The glass eventually melts and it transforms back to the liquid at the onset temperature, which increases with increasing the glass stability [159].

The mean-field theory provides a complete framework to describe structural glasses and supercooled liquids with arbitrary interaction potentials between constituents. Other physical properties can also be analysed in this context, for instance the jamming transition and the vibrational properties of glasses [126, 162, 163], or the Gardner transition [157, 162].

3. Towards a theory of the glass transition in finite dimensions

3.1 The fate of the metastable states in finite dimensions

In the previous section, we have reviewed the main results which have derived over the last decade from the mean-field theory of the glass transition for particle systems in the limit of infinite dimensions of space. First, an increase in the relaxation time is found when decreasing the temperature or increasing the density, with a power law divergence at a dynamical transition temperature T_{d} in a similar spirit as in experiments. Below T_{d}, the dynamics is arrested (the relaxation time is truly infinite in the thermodynamic limit) because the liquid remains trapped forever in one of the numerous metastable states which dominate the thermodynamics for $T \leq T_{\mathrm{d}}$. Therefore, in mean-field theory, there is a direct connection between the dynamics and the thermodynamics of supercooled liquids. In addition, the thermodynamics of supercooled liquids reveals the existence of an exponentially-large number of metastable states below T_{d}. The configurational entropy which quantifies the logarithm of this number (per unit particle) vanishes at a lower temperature T_{K}. This corresponds to a genuine thermodynamic phase transition from the supercooled liquid to the ideal glass. This is similar to the extrapolated entropy crisis which was first found by Kauzmann but it is exactly realised at the mean-field level and it does not rely on any extrapolation. Indeed, if one assumes that the vibrational properties and the internal energy of the glass and the crystal at the same temperature are similar, then the mean-field rigorously-defined configurational entropy is comparable (but not rigorously equal [114, 164]) to the excess entropy. Finally, the out-of-equilibrium properties of glasses in mean-field can be investigated. In particular, one can follow the behaviour of the metastable states when shearing or heating a glass and they are in qualitative agreement with finite-dimensional glasses.

Mean-field theory thus reproduces the main features of the phenomenology of glassy systems. A way then to deal with finite-dimensional glasses and supercooled liquids is to consider $1/d$ as

a small parameter to compute expansions from the idealised mean-field limit. This is similar in spirit to what is done in gases and solids (see the beginning of this chapter). However, there is a strong caveat: the dynamical transition is smeared out when d is finite no matter how large, and consequently the metastable states are no longer well-defined because they have a finite lifetime [144]. This is problematic since the dynamics, the Kauzmann transition and the behaviour upon shearing or heating all rely on the very existence of the metastable states and on their properties as a function of the temperature or of a non-equilibrium driving. Ergodicity is thus restored below T_{d} and presumably down to T_{K}. This comes from the mean-field nature of the $d \to +\infty$ limit as, in this case, the liquid is fully-connected (a given particle interacts with a diverging number of neighbours). In other words, the actual liquid below T_{d} does not remain stuck forever in a metastable state but it can escape from the corresponding free energy minimum due to non-perturbative activation processes which do not exist in mean-field [124]. Incorporating activated events and fluctuations in the mean-field theory of the glass transition quantitatively has been impossible to date (see however Ref. [165–168] for first attempts by using instanton calculations [169]). As activation processes are non-perturbative, this would require non-perturbative functional renormalisation group techniques [170] (see Ref. [171] for a tentative perturbative approach via a Migdal-Kadanoff approximation). As a result, the theoretical description of finite-dimensional glass-forming liquids so far relies on scaling laws and qualitative discussions which are usually grouped under the "mosaic state" scenario of the random first order transition (RFOT) theory [122]. This is the object of the next section.

3.2 Spatial definition of the metastable states: the point-to-set length

In this section, we explain why metastable states cannot exist as such in finite dimensions as they are unstable with respect to the escape to another metastable state (activation process). The argument relies on a *gedankenexperiment* [124, 144]. One first assumes that the free energy landscape still displays several metastable minima of density profiles $\rho_\alpha(\boldsymbol{x})$ and free energies per unit volume $f_\alpha(T)$ but with now finite barriers between them. Then, one assumes that all the particles of the liquid are frozen in a metastable state α, except within a cavity of radius R which is free to equilibrate and to explore the phase space at a temperature T in the presence of the amorphous boundary. The state α is assumed to be typical at the temperature T, *i.e.*, $f_\alpha(T) = f^*(T)$. When the cavity is in a metastable state $\gamma \neq \alpha$, there is a mismatch between the density profiles at the boundary of the cavity. Accordingly, one should account for a free energy penalty by introducing a generalised surface tension $\Upsilon_{\alpha\gamma}$ between states α and γ and the corresponding free energy cost $\Upsilon_{\alpha\gamma} R^\theta$ with $\theta \leq d-1$. When $\theta = d-1$, one recovers the usual surface tension term (up to a prefactor which corresponds to the solid angle in d dimensions). This is what was advocated in Ref. [172] by considering a Kac version of a model spin glass which shares similarities with the behaviour of supercooled liquids (see Chap. II). Instead, values of $\theta < d-1$ take into account a renormalised value of the exponent due to wetting phenomena or complex geometries of the interface [173]. For instance, the value $\theta = d/2$ was advocated in Ref. [122, 174].

In order to determine the thermodynamics of the cavity, one computes its partition function, which reads

$$\mathcal{Z}(R,T) = e^{-V_d R^d \beta f_\alpha} + \sum_{\gamma \neq \alpha} e^{-V_d R^d \beta f_\gamma - R^\theta \beta \Upsilon_{\alpha\gamma}}, \tag{I.24}$$

with V_d the volume of the unit sphere in d dimensions. In the continuum limit, by introducing[17]

$$\mathcal{N}_\alpha(f,\Upsilon;T) = p_\alpha(\Upsilon|f;T)\mathcal{N}(f;T) = p_\alpha(\Upsilon|f;T)e^{V_d R^d \Sigma(f;T)}, \tag{I.25}$$

the number of states γ of a given free energy per unit volume f and a given surface tension Υ with the state α, along with the conditional probability $p_\alpha(\Upsilon|f;T)$ to have a surface tension Υ given that the free energy per unit volume is f, one finds

$$\mathcal{Z}(R,T) = e^{-V_d R^d \beta f_\alpha} + \int \mathrm{d}f \int \mathrm{d}\Upsilon p_\alpha(\Upsilon|f;T) e^{-V_d R^d \beta f - R^\theta \beta \Upsilon + V_d R^d \Sigma(f;T)}. \tag{I.26}$$

The above integral can be approximated by the Laplace (saddle-point) method in the limit of large R. The integral over the free energies is dominated by the value $f^*(T)$ of the typical free energy of glass states at the temperature T if $p_\alpha(\Upsilon|f;T)$ is sub-dominant. The integral over the surface tensions is instead dominated by the lowest values and this can lead to a renormalisation of the exponent θ if the conditional probability is not of finite range because of arbitrary-low surface tensions [175]. In any case, after the saddle-point approximation, the partition function reads (with a possible renormalisation of θ)

$$\mathcal{Z}(R,T) = e^{-V_d R^d \beta f^*} \left[1 + \kappa e^{-R^\theta \beta \Upsilon^*(T) + V_d R^d \Sigma(T)}\right], \tag{I.27}$$

where κ is an irrelevant normalisation constant and where $\Upsilon^*(T)$ is a typical surface tension scale (we recall that the metastable state α is typical at the temperature T). Eventually, one finds for the free energy per unit volume in the large R limit

$$\begin{aligned} F(R,T) = -\frac{T}{V_d R^d}\ln \mathcal{Z}(R,T) &= f^*(T) - \frac{T}{V_d R^d}\ln\left[1 + \kappa e^{-R^\theta \beta \Upsilon^*(T) + V_d R^d \Sigma(T)}\right] \\ &= \begin{cases} f^*(T) & \text{for } R \ll \xi_{\mathrm{PTS}}(T), \\ f^*(T) - T\Sigma(T) + O\left(R^{-(d-\theta)}\right) & \text{for } R \gg \xi_{\mathrm{PTS}}(T), \end{cases} \end{aligned} \tag{I.28}$$

where two different extreme cases are distinguished, which depend on the value of the radius R of the cavity with respect to the maximum of the argument of the exponential in Eq. (I.27), namely,

$$\xi_{\mathrm{PTS}}(T) = \left[\frac{\theta \Upsilon^*(T)}{d V_d T \Sigma(T)}\right]^{1/(d-\theta)}. \tag{I.29}$$

If the radius of the cavity is $R \ll \xi_{\mathrm{PTS}}(T)$, then the free energy of the cavity is the one of a single glassy metastable state. The cavity is too constrained by the boundary and the only thermodynamic state which is relevant for the thermodynamics is the same as the one outside the cavity. The system belongs to a well-defined metastable state and behaves as an ideal glass even above T_{K}. On the opposite, if $R \gg \xi_{\mathrm{PTS}}(T)$, the exponential term dominates, and the free energy of the cavity is given by an expression similar to Eq. (I.16), except for the surface free energy term which vanishes if $R \to +\infty$. This means that the cavity is no longer in a single metastable state but it instead resembles a mosaic, and each piece of the mosaic corresponds to a given metastable state.

From the previous argument, one concludes that the metastable states in finite dimensions are only defined up to a certain lengthscale $\xi_{\mathrm{PTS}}(T)$ which is called the point-to-set (PTS) length. For linear sizes larger than the PTS length the liquid cannot belong to a single metastable state:

[17] In this section, the complexity is defined per unit volume.

it forms a pattern of different metastable states of typical size $\xi_{\rm PTS}(T)$ which can of course fluctuate. This is because the system wants to explore the other metastable states despite the surface free energy cost and it prefers gaining entropy. The PTS length also receives another interpretation. This is the typical length over which an amorphous order extends in finite dimensions. Indeed, if the cavity is of radius $R < \xi_{\rm PTS}(T)$, then the only physical state which can be sampled by the cavity is the state that is imposed by the state outside the cavity, namely, on the boundary. In other words, the PTS length quantifies the spatial correlations between a particle inside a cavity and the set of particles on the boundary of the cavity, hence its name. The PTS length grows as the temperature decreases as the configurational entropy also decreases. It diverges as $(T - T_{\rm K})^{-(d-\theta)}$ if there is an entropy crisis, as the configurational entropy can be linearised close to $T_{\rm K}$. In other words, there is a growing amorphous order in the liquid at lower temperatures with a diverging lengthscale at $T_{\rm K}$ as for usual second order phase transitions. To detect amorphous order, one has to introduce two copies or replicas of the same liquid and to consider the overlap or similarity between them [176], which is extensively discussed in Chap. IV.

The construction with a cavity in a frozen environment has been implemented both in experiments [177] and in computer simulations [178–180] in order to measure the PTS length. A modest increase when decreasing the temperature has been reported. In addition, the connection with the configurational entropy has been studied [181, 182]. The computation of the latter requires to consider constrained systems to avoid the escape from the metastable states and to compute the free energy of the individual glass states [114, 164, 181], see Eq. (I.16). The constrained thermodynamics is extensively discussed in Chap. II and its implementation in finite dimensions by using computer simulations is the object of Chap. III.

3.3 Activation and the escape from the metastable states

So far, the focus has been made on the statics and on the formulation of what could be a mean-field-like scenario of the glass transition in finite dimensions. However, the relaxation of the mosaic liquid below $T_{\rm d}$[18] has not been discussed. The dynamics below $T_{\rm d}$ is assumed to be activated, which is a reasonable assumption since the liquid is described as a mosaic of different patches in different free energy minima (metastable states). A droplet of size smaller than the point-to-set (PTS) length $\xi_{\rm PTS}(T)$ cannot relax as it remains trapped forever in a metastable state: it behaves as the mean-field ideal glass. For droplets of size $R > \xi_{\rm PTS}(T)$, the free energy barrier to relax is expected to grow with R and therefore the fastest regions to relax are the smallest, namely, the ones of linear extent $\xi_{\rm PTS}(T)$ [185]. The decorrelation of the droplets of size $\xi_{\rm PTS}(T)$ drives the relaxation of the entire mosaic liquid and their relaxation time should thus be similar to the α-relaxation time $\tau_\alpha(T)$ of the liquid. Rare fluctuations bring the patches of size $\xi_{\rm PTS}(T)$ to another metastable state via a barrier crossing, and a reasonable assumption is that the free energy barrier scales as $[\xi_{\rm PTS}(T)]^\psi$ in analogy with systems that are pinned by random boundaries [186], where $\psi \leq d$ is a new exponent [172, 187]. This leads to

$$\ln\left[\frac{\tau_\alpha(T)}{\tau_0}\right] \sim \frac{[\xi_{\rm PTS}(T)]^\psi}{T} \sim \frac{1}{T[\Sigma(T)]^{\psi/(d-\theta)}}, \tag{I.30}$$

where τ_0 is a microscopic timescale. We note that entropic effects for the selection of the final metastable state have not been taken into account, which are likely to decrease the relaxation

[18] Above $T_{\rm d}$, the mode-coupling theory (or mean-field theory) may correctly describe the dynamics [183]. However, the crossover from non-activated dynamics to activated dynamics at the avoided dynamical transition remains elusive [125, 184].

time [144].

Eq. (I.30) directly relates the relaxation time below the avoided dynamical transition to the configurational entropy. The slowing down of structural liquids is then accounted for by the fact that the number of accessible states for the droplets that compose the mosaic liquid decreases as the temperature decreases, or equivalently by the fact that the dynamics becomes increasingly collective. The above equation predicts that the α-relaxation time significantly increases when approaching the Kauzmann transition and it truly diverges when $T = T_{\rm K}$ along with the PTS length. In addition, if one linearises the configurational entropy close to $T_{\rm K}$, the α-relaxation time is found to follow a generalised Vogel-Fulcher-Tammann (VFT) law [124, 144], namely,

$$\ln\left[\frac{\tau_\alpha(T)}{\tau_0}\right] \sim \frac{1}{(T - T_{\rm VFT})^\alpha}, \tag{I.31}$$

with $\alpha = \psi/(d-\theta)$. Experimental data are usually fitted with a VFT law (with $\alpha = 1$) but of course this does not represent a proof of any kind, as other fitting functions which come from different theories of the glass transition perform equally well [98, 188].

A similar relation as Eq. (I.30) was already derived by Adam and Gibbs in 1965, with $\psi = d$ and $\theta = 0$ ($\alpha = 1$) [189]. By assuming that the liquid is formed by cooperatively rearranging regions which can explore a finite number of states, and that each of these regions relaxes due to activated events, the configurational entropy and the α-relaxation time were related. Eq. (I.30) and its formulation by Adam and Gibbs have been extensively discussed by using computer simulations in Ref. [190]. While the latter is found incompatible with the numerical results, the former instead reproduces the data well and measurements of the exponents θ and ψ have been provided. Yet, there is no theoretical prediction for the exponents which is rooted in first principle calculations.

Overall, measurements of the configurational entropy and of the PTS length establish that the glassy slowdown is indeed accompanied by growing thermodynamic fluctuations which are predicted by the finite-dimensional version of mean-field theory, namely, the random first order transition theory. In addition, a direct comparison between the statics and the dynamics reveals that there might be connections between the two and that the dynamics could be driven by a putative thermodynamic phase transition at $T_{\rm K}$.

3.4 Dynamic heterogeneities and dynamic facilitation

So far, we have discussed the dynamics of the liquid below $T_{\rm d}$ as the independent relaxation of blobs of typical size $\xi_{\rm PTS}(T)$ due to rare fluctuations which lead to the transitions of the patches of the mosaic liquid from one metastable state to another. This picture of the relaxation of the supercooled liquid naturally gives rise to dynamic heterogeneities as all the patches are not going to relax at the same time (see Sec. 1.1.3). In particular, the random first order transition (RFOT) theory predicts a non-monotonic dynamic susceptibility $\chi_4(t)$ with a maximum value for $t \simeq \tau_\alpha(T)$ and a growing dynamic four-point correlation length $\xi_4(t)$ which saturates to $\xi_{\rm d}(T)$ of about few $\xi_{\rm PTS}(T)$ [191].

However, there are two limitations of the description of the dynamics within the RFOT framework we have made so far: (i) it does not account for the stretching of the dynamic time correlation functions and (ii) measurements suggest that the dynamic correlation length $\xi_{\rm d}(T)$ grows more rapidly than the point-to-set (PTS) length $\xi_{\rm PTS}(T)$ for decreasing temperatures [192]. In order to account for these, two modifications of the results of the previous section

should be made. On the one hand, a reasonable assumption is that the mosaic domains are distributed in size [122, 144, 174] and shape [193]. This naturally leads to a distribution of free energy barriers for the transitions between the metastable states, and to a corresponding distribution of the droplet relaxation times [194]. The relaxation should then start with the smallest domains and eventually end with the largest ones, to give rise to larger dynamic heterogeneities and a stretching of the correlation functions. However, there is no indication of what should be the form of the distribution of the free energy barriers and only reasonable guesses can be made [168, 195]. The numerical work of Chap. V is a tentative to measure the actual spatial fluctuations of the PTS length (or equivalently of the configurational entropy), which is usually referred to as the "self-induced" disorder of glass-forming liquids [196, 197] (see Chap. II).

On the other hand, if one droplet relaxes and reaches another metastable state, then the neighbouring droplets experience another amorphous boundary. This is likely to change the barrier for escaping their own metastable state, and to consequently trigger relaxation nearby [195]. Facilitation effects are therefore expected and they may give rise to correlations in the dynamics on larger lengthscales than the PTS length [144]. Facilitation effects are at the core of another theory of the glass transition, namely, the dynamic facilitation theory. In this framework, the relaxation of supercooled liquids is described as the mobility invasion from excitations or defects of purely dynamic origin [112, 198–200]. This theory was built on lattice Kinetically Constrained Models (KCMs) with binary on-site variables, namely, the presence or the absence of an excitation [201]. These models have trivial thermodynamics (typically the one of a non-interacting lattice gas) and non-trivial dynamic rules for the spatio-temporal evolution of the excitations [202]. These rules result in a glassy slowdown which is similar to what is found in supercooled liquids. As a consequence, the dynamic facilitation theory is based on the fact that there is no connection between the thermodynamics and the dynamics, contrary to the RFOT theory [see Eq. (I.30)]. In particular, one of the main differences with the RFOT theory is the nature of the first relaxation events. While they are rooted in the thermodynamics as far as the RFOT theory is concerned, they represent purely dynamic defects in the dynamic facilitation theory. Trying to reconcile the RFOT theory with dynamic facilitation remains a big theoretical challenge, see however Ref. [203–205] for first attempts. In Chap. VI, we assess the respective roles of dynamic facilitation and activation in the dynamics of supercooled liquids close to T_{g} by means of computer simulations.

4. Structure of the manuscript

The present work aims at studying the meaning and the consequences of the description of glass-forming liquids in terms of a "complex free energy landscape" which is characterised by a multitude of "metastable states"[19]. As summarised in this introduction, this description is at the core of the mean-field theory of glass formation and its extension in the form of the random first order transition theory. Yet, what remains of this construction in two- and three-dimensional supercooled liquids and glasses? We delve into this question by using different strategies and mostly by means of state-of-the-art computer simulations.

In Chap. II, we introduce the formalism of constrained thermodynamics in the mean-field theory of the glass transition along with the order parameter of the random first order transition, namely, the overlap or similarity between equilibrium configurations. We show that the changes in the free energy landscape, in particular the emergence of a multitude of metastable states

[19]The quotation marks emphasise that these concepts are a priori ill-defined in finite dimensions.

and their subsequent rarefaction as the temperature is lowered, directly translate into thermodynamic singularities in an extended phase diagram when considering the temperature T and a source ϵ that is linearly coupled to the overlap as control parameters. A line of conventional first order transition for finite ϵ emerges from the random first order transition at T_{K}, and it ends in a critical point at a higher temperature T_{c} and a non-zero field ϵ_{c}. We also discuss the fate of these thermodynamic singularities in finite dimensions in the framework of statistical field theory and of previous numerical works.

In Chap. III, we study the statistics of the overlap order parameter and the constrained thermodynamics of glass-forming liquids in finite dimensions by means of computer simulations. We first show that the glassy slowdown is accompanied by growing thermodynamic fluctuations of the overlap order parameter as the temperature is decreased, which may lead to singularities in the thermodynamics of constrained glass-formers. We then go beyond all past studies by considering constrained glass-formers in $2d$ and $3d$ and we show that they display very different behaviours. For the first time, we are able to perform a *bona fide* finite size scaling analysis in order to characterise the transitions in the phase diagram (ϵ, T) of glass-forming liquids in the thermodynamic limit. In particular, we provide strong evidence that the critical point at the end of the first order transition line at $(\epsilon_{\mathrm{c}}, T_{\mathrm{c}})$ is in the universality class of the random-field Ising model (RFIM) and that its lower critical dimension is $d = 2$. We thus demonstrate the robustness of the mean-field/random first order transition (RFOT) theory in finite dimensions, and for the first time we emphasise a genuine thermodynamic phase transition in the physics of glass-forming liquids, which is not rounded by finite-dimensional fluctuations [206] (as opposed to the dynamical transition for example). The results of this chapter strengthen the analogy between supercooled liquids and the RFIM, and they suggest the measure of a number to quantify the effective "self-induced" disorder in glass-forming liquids. In particular, we expect that performing the analysis of Chap. III in several model glass-formers could lead to a quantitative comparison of the effective disorder in different supercooled liquids, which could later be used to rationalise their equilibrium [207, 208] and non-equilibrium dynamic properties [85].

In Chap. IV, we come back to mean-field theory and we discuss the properties of the order parameter for the ideal glass transition at T_{K}, namely, the overlap between liquid configurations. The latter, which quantifies the similarity between configurations of the liquid, is defined up to a tolerance length whose influence we study systematically. We show that the thermodynamic properties of constrained supercooled liquids in their phase diagram (ϵ, T) are strongly dependent on the coarse-graining (tolerance) length in the definition of the overlap, while the dynamical and static transitions at T_{d} and T_{K} respectively are not. These conclusions also hold in finite dimensions and they are backed by computer simulations. The results of this chapter have practical outcomes and they are likely to ease the computer simulations of constrained glass-forming liquids in the future, which have proved useful in Chap. III to study the complexity of the free energy landscape in finite-dimensional glass-formers. In particular, they open the way for moving the critical point for $\epsilon > 0$ to higher temperatures by a clever choice of the tolerance length, and consequently for considering larger system sizes to approach the thermodynamic limit. Our results also shed light on the structure of the free energy landscape, and they suggest the definition of a new static landscape-inspired "onset temperature" below which "metastable states" manifest themselves.

In Chap. V, we manage to directly assess the "self-induced" disorder in a model glass-former and to measure the fluctuations of the point-to-set length, or equivalently of the configurational entropy, which are introduced in the RFOT theory to account for the static finite-dimensional

fluctuations and the dynamic heterogeneities. By constraining a glass-forming liquid with a field ϵ which is only applied locally in a given region of space, *i.e.*, which is linearly coupled to the local overlap only, we show strong thermodynamic local fluctuations, which account for the local fluctuations of the configurational entropy, and we study for the first time their statistics and their spatial organisation. This opens new directions of research, in particular to study the correlation with other structural indicators or the propensity, and to assess the connection (if any) between the statics and the dynamics at the mesoscopic scale in glass-forming liquids.

In Chap. VI, we study the dynamics of glass-forming liquids at very low temperatures via computer simulations. We are able to surpass all previous numerical studies thanks to the swap algorithm [54] which allows for a fast thermalisation of size-polydisperse glass-formers down to very low temperatures, and to investigate time and temperature ranges which are directly comparable to experiments. In comparison, computer simulations are usually limited to the first microseconds of the dynamics of supercooled liquid (we recall that at the glass transition temperature T_{g}, the experimental relaxation time is about 10^2 s). We demonstrate for the first time the existence of excess wings in the relaxation spectra of a model glass-former in agreement with the experimental relaxation spectra close to T_{g} and we are able to unravel its origin which has been the subject of intense debates for decades. We are also able to rationalise the whole shape of the experimental relaxation spectra by assessing the relative roles of activation and dynamic facilitation in the equilibrium dynamics of supercooled liquids. This paves the way towards a confrontation and/or a conciliation of the RFOT theory and the dynamic facilitation theory.

In Chap. VII, we study the non-equilibrium properties of the glass phase, which depend on its stability. However, physical aging often results in weak changes of the latter on reasonable timescales, and this forbids the systematic investigation of the influence of glass stability in computer simulations, in particular for metallic glasses with a few number of components for which the above swap algorithm cannot be implemented. We present numerical protocols to generate metallic glasses of higher stability than the ones which are obtained by direct aging in an archetypal model glass-former, namely, the Kob-Andersen model. The stability of the generated glasses is analysed by rheology and heating procedures, but also thanks to the inherent structure energies and the fictive temperatures. This allows for a wider exploration of the influence of glass stability in the future. This also opens new research avenues in the study of stable metallic glasses in computer simulations, namely, brittle yielding or melting.

In Chap. VIII, we finally conclude and detail several perspectives.

In Chap. IX, we provide a summary of this work in French.

II An introduction to the theoretical Franz-Parisi construction

In this chapter, we describe the Franz-Parisi theoretical construction which enables one to probe and to characterise the complexity of the free energy landscape of glass-forming liquids. This construction consists in studying the thermodynamics when the system is constrained to stay at a finite overlap with a reference configuration of the same system. The overlap corresponds to the order parameter of the thermodynamic glass transition and it physically represents the degree of similarity between the two replicas (configuration of the constrained liquid and reference configuration). Equivalently, the liquid evolves at a temperature T with a finite attraction of typical strength ϵ with a reference configuration. The latter in effect acts as a source of quenched disorder. The reference configurations correspond to the typical equilibrium configurations at a temperature T_0. We first present the general statistical mechanics framework to describe the behaviour of the constrained liquid. The thermodynamics of the constrained liquid can be related to the properties of the unconstrained liquid (with $\epsilon = 0$) via a change of thermodynamic ensembles. In this connection, the Franz-Parisi potential quantifies the free energy cost to constrain the overlap to a given value in the unconstrained liquid, and it plays a crucial role. We then review mean-field results of a spin glass system, namely, the spherical p-spin, whose behaviour shares similarities with structural glasses. In particular, we summarise the calculations of the Franz-Parisi potential and of the phase diagram (ϵ, T). The latter displays a first order transition line between a delocalised phase of low overlap and a localised phase of higher overlap, which ends in a critical point. We discuss how the thermodynamics in the plane (ϵ, T) is a way of detecting changes in the free energy landscape which do not affect the thermodynamics of the liquid on the $\epsilon = 0$ axis. We extend previous studies of the spherical p-spin, and we present new results about the systematic influence of the temperature of the reference configuration T_0 in the quenched Franz-Parisi setting. In particular, we show that the critical point moves to a higher temperature and a larger source when T_0 decreases. We then present recent statistical field theory arguments beyond mean-field theory which establish that the critical point is in the universality class of the random field Ising model (RFIM), provided it survives despite finite-dimensional fluctuations. Likewise, the first order transition becomes a first order transition in the presence of quenched disorder. We then extend already published works by showing that the mapping onto the RFIM close to the critical point holds for any temperature T_0 of the reference configuration, and we discuss the influence of T_0 on the strength of the effective random fields. We end with a review of existing computer simulation studies of constrained glass-forming liquids in finite dimensions, and we list our directions of study which are pursued in Chap. III. This chapter is therefore a mixture of a review of existing formalisms and results and of a few new contributions.

Outline

1 Presentation 30

2 Statistical mechanics formulation 33

2.1 The canonical free energy $F(\epsilon)$ 33

2.2 Thermal versus disorder fluctuations . . . 33
2.3 The Franz-Parisi potential $V(Q)$ . . . 34
2.4 Connection between the Franz-Parisi potential and the constrained free energy . . . 35
2.5 Ensemble equivalence and phase transitions . . . 36
2.6 Schematic computation of the Franz-Parisi potential . . . 38
3 Exact results from mean-field theory: the spherical p-spin . . . 40
3.1 The model . . . 40
3.2 Calculation of the Franz-Parisi potential . . . 42
3.3 Temperature evolution of the Franz-Parisi potential for equal temperatures . . . 44
3.4 Mean-field phase diagram (ϵ, T) for equal temperatures . . . 47
3.5 Mean-field phase diagrams (ϵ, T) for a fixed temperature of the reference configurations . . . 48
3.6 Variation of the location of the critical point with the temperature of the reference configurations . . . 50
4 Statistical field theory beyond mean-field . . . 52
4.1 The replicated Landau-Ginzburg free energy . . . 52
4.2 Mapping onto the random-field Ising model . . . 56
4.3 The second cumulant of the Franz-Parisi potential and the "self-induced" disorder . . . 57
5 Computer studies of glass-formers in the Franz-Parisi construction . . . 59
5.1 Structural liquids . . . 59
5.2 Plaquette models . . . 60
Appendix
A The random-field Ising model . . . 61
A.1 Presentation . . . 61
A.2 Critical behaviour . . . 62

1. Presentation

The mean-field theory of the glass transition relates the glassy slowdown to the emergence of a large number of free energy minima. Below the dynamical transition temperature T_{d}, the phase space splits into an exponentially-large number of disconnected components which are called metastable states and which dominate the thermodynamics. The configurational entropy $\Sigma(T)$ is the logarithm of this number (per particle) and it decreases when the temperature also decreases until it vanishes at the Kauzmann transition temperature. At this temperature, a phase transition towards the ideal glass phase occurs.

A convenient theoretical way of studying the complexity of the free energy landscape of glass-formers has been put forward by Franz and Parisi [148, 153]. It relies on the constrained thermodynamics which has been briefly discussed in Chap. I. Instead of merely studying the

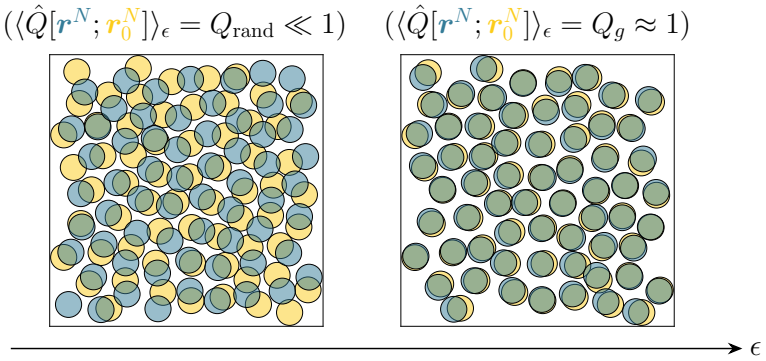

Fig. II.1 | Sketch of the Franz-Parisi setting: a replica of a glass-forming liquid (in blue) evolves at a temperature T, and its overlap with a reference replica of the same liquid (in yellow), which is sampled at equilibrium at a temperature T_0, is linearly coupled to a source ϵ. Equivalently, the constrained liquid evolves in the presence of quenched disorder which is represented by the reference configuration that exerts attractive forces. With a small attraction between the two copies, the average overlap between the replicas is almost zero (delocalised phase) while it grows when ϵ increases (localised phase).

liquid, the Franz-Parisi (FP) method then consists in analysing the thermodynamics of two coupled supercooled liquids in the presence of a finite attraction between them, see Fig. II.1. One thus introduces two replicas of the same liquid, in a similar spirit as in the Monasson construction which has been introduced in Chap. I [150]. The strength of the attraction is denoted by ϵ. In the FP construction, the overlap between the two copies or replicas of the liquid is the order parameter which enables one to distinguish between a delocalised (liquid) phase of typical overlap $Q_{\rm rand} \ll 1$ and a localised (glassy) phase with a significantly larger overlap $Q_{\rm g} \simeq 1$. The overlap can be computed from the positions of the N particles in the first $\boldsymbol{r}_1^N$ and the second $\boldsymbol{r}_2^N$ replicas, and it reads

$$\hat{Q}[\boldsymbol{r}_1^N; \boldsymbol{r}_2^N] = \frac{1}{N}\sum_{i,j} w(|\boldsymbol{r}_{1,i} - \boldsymbol{r}_{2,j}|/a), \tag{II.1}$$

where the sums run over all indices $i, j = 1 \dots N$. In the above equation, $w(x)$ is a window function which decreases from 1 to 0 on a scale $O(1)$, whose precise expression is not important for now. The parameter a stands for the tolerance length modulo which one considers two particles as overlapping. Its role is discussed at length in Chap. IV. Here, we just emphasise that the tolerance length should be taken as a fraction of the average diameter of the particles. If a is taken too large, then a particle can have a significant overlap with several particles in the reference configuration, and the average overlap $\hat{Q}$ can exceed 1, which may seem unphysical. In addition, the mean-field theory of the glass transition pictures the phase space of glass-forming liquids as a set of configurations which forms a single metastable state and which corresponds to a particular average density profile that slightly changes from one configuration to another due to thermal vibrations [121, 126, 174]. The tolerance length is precisely designed to account for these vibrations within a single metastable state in the definition of the overlap.

Two different settings can be imagined. In the annealed setting, both replicas are considered on an equal footing and they feel the attraction when they explore the phase space at a temperature T. In the quenched setting instead, there is an asymmetry between the two replicas. One replica, which we now call the reference configuration and which we denote by $\boldsymbol{r}_0^N$, is

instantaneously frozen after it has been sampled with the unconstrained Hamiltonian

$$\hat{H}[\boldsymbol{r}_0^N] = \frac{1}{2}\sum_{i<j} v(|\boldsymbol{r}_{0,i} - \boldsymbol{r}_{0,j}|), \tag{II.2}$$

where $v(r)$ is the pairwise radial interaction potential between two particles, and where the sums run over all particles $i, j = 1 \dots N$. The reference configurations are sampled at a temperature T_0. The other replica, which we now denote by $\boldsymbol{r}^N$, explores the phase space at a temperature T and it is constrained due to a finite attraction of energy strength ϵ with the reference configuration. The temperature T can be equal or not to T_0. When $T = T_0$, the reference configurations represent configurations which are relevant for the thermodynamics of the liquid at the temperature T. Instead, choosing $T_0 < T$ allows for an exploration of different regions of the free energy landscape, and in particular of metastable states which are typical at lower temperatures [148]. For instance, this could be relevant for the description of the melting of ultrastable glasses [99, 209]. In the remaining of this chapter (and the following ones), we focus on the quenched setting which is the more relevant to describe the properties of the free-energy landscape of glass-forming systems.

The coupling between the two replicas of the same liquid is implemented by linearly biasing the overlap between the two configurations with a source ϵ in order to favour large overlap values when $\epsilon > 0$. A thermodynamic constraint is thus imposed to the overlap in order to forbid the complete decorrelation between the replicas. The Hamiltonian of the constrained liquid when it is coupled to a reference configuration becomes

$$\hat{H}_\epsilon[\boldsymbol{r}^N; \boldsymbol{r}_0^N] = \hat{H}[\boldsymbol{r}^N] - N\epsilon\hat{Q}[\boldsymbol{r}^N; \boldsymbol{r}_0^N] = \frac{1}{2}\sum_{i<j} v(|\boldsymbol{r}_i - \boldsymbol{r}_j|) - \epsilon\sum_{i,j} w(|\boldsymbol{r}_i - \boldsymbol{r}_{0,j}|/a), \tag{II.3}$$

where once again the sums run over all particles $i, j = 1 \dots N$, and where the minus sign in front of the second term in the right-hand side implies that the two replicas are coupled attractively when $\epsilon > 0$. We note that the parameter a can also be seen as the attraction range between the two replicas.

At a fixed temperature T, the state of the constrained liquid is obtained by minimising its free energy. At the mean-field level, and for $T = T_0$ and $T_\mathrm{K} < T < T_\mathrm{d}$, the thermodynamics of the system is ruled by a competition between the configurational entropy and the attraction energy. The contribution of the configurational entropy to the free energy is $-T\Sigma(T)$, while the attraction energy contribution scales like $-\epsilon$. At low fields ϵ, the entropic term dominates the free energy and the system maximises its entropy. Its thermodynamics takes contributions from the exponentially large number of metastable states and the liquid is thus in a delocalised phase. In other words, it has a low overlap with the reference configurations on average. Instead, if ϵ is increased so that $\epsilon \gtrsim T\Sigma(T)$, then the attraction energy term dominates and the system ends up in a localised phase. The liquid only explores a narrow region of the phase space, namely, the metastable state of the reference configuration, and thus it has a large overlap with the quenched replica on average.

From this simple argument, one anticipates that the thermodynamics of a constrained supercooled liquid allows one to unravel the main features of the free energy landscape. In particular, it reveals the existence of the metastable states and it enables one to assess their properties. In addition, the FP construction allows one to explore untypical regions of the free energy landscape by varying the temperature T_0 of the reference configurations. On the other hand, tuning

ϵ enables one to localise the system in one particular metastable state, hence to quantify the number of these metastable states, or equivalently the configurational entropy. Overall, this discussion suggests to systematically study the thermodynamics of constrained supercooled liquids for generic (T, T_0, ϵ). This is the object of the next section.

2. Statistical mechanics formulation

2.1 The canonical free energy $F(\epsilon)$

As mentioned previously, the thermodynamic state of the system is obtained by minimising its free energy at a fixed temperature. For a given reference configuration $\boldsymbol{r}_0^N$, the free energy per particle $F(\epsilon; \boldsymbol{r}_0^N)$ at a fixed temperature T reads

$$F(\epsilon; \boldsymbol{r}_0^N) = -\frac{T}{N} \ln \int \mathrm{d}\boldsymbol{r}^N e^{-\beta \hat{H}_\epsilon[\boldsymbol{r}^N; \boldsymbol{r}_0^N]}, \tag{II.4}$$

with $\beta = 1/T$ (the Boltzmann constant is set to unity). The argument of the logarithm in the previous equation stands for the partition function of the constrained liquid for a fixed reference configuration $\boldsymbol{r}_0^N$. However, contrary to unconstrained liquids, the constrained liquid evolves in the presence of quenched disorder which is represented by the reference configurations. In the thermodynamic limit, the free energy is self-averaging [210], and consequently, it must be equal to its average over the disorder. The free energy of the constrained liquid thus equals

$$F(\epsilon) = \overline{F(\epsilon; \boldsymbol{r}_0^N)} = \frac{\int \mathrm{d}\boldsymbol{r}_0^N e^{-\beta_0 \hat{H}[\boldsymbol{r}_0^N]} F(\epsilon; \boldsymbol{r}_0^N)}{\int \mathrm{d}\boldsymbol{r}_0^N e^{-\beta_0 \hat{H}[\boldsymbol{r}_0^N]}} = -\frac{T}{N} \frac{\int \mathrm{d}\boldsymbol{r}_0^N e^{-\beta_0 \hat{H}[\boldsymbol{r}_0^N]} \ln \int \mathrm{d}\boldsymbol{r}^N e^{-\beta \hat{H}_\epsilon[\boldsymbol{r}^N; \boldsymbol{r}_0^N]}}{\int \mathrm{d}\boldsymbol{r}_0^N e^{-\beta_0 \hat{H}[\boldsymbol{r}_0^N]}}, \tag{II.5}$$

where $\beta_0 = 1/T_0$, where the overline is a short-hand notation for the average over the reference configurations, and where the denominator in the two last equalities corresponds to the partition function of the unconstrained liquid at a temperature T_0. We note that this free energy $F(\epsilon)$ is a function of the triplet (ϵ, T, T_0).

2.2 Thermal versus disorder fluctuations

Once the free energy is computed, thermodynamic properties of the system can be derived from it by differentiating with respect to the control parameters [4]. First, the average overlap is obtained by differentiating the free energy once:

$$\overline{\langle \hat{Q} \rangle_\epsilon} = -F'(\epsilon) = \frac{\int \mathrm{d}\boldsymbol{r}_0^N \int \mathrm{d}\boldsymbol{r}^N e^{-\beta_0 \hat{H}[\boldsymbol{r}_0^N]} e^{-\beta \hat{H}_\epsilon[\boldsymbol{r}^N; \boldsymbol{r}_0^N]} \hat{Q}[\boldsymbol{r}^N; \boldsymbol{r}_0^N]}{\int \mathrm{d}\boldsymbol{r}_0^N \int \mathrm{d}\boldsymbol{r}^N e^{-\beta_0 \hat{H}[\boldsymbol{r}_0^N]} e^{-\beta \hat{H}_\epsilon[\boldsymbol{r}^N; \boldsymbol{r}_0^N]}}, \tag{II.6}$$

where the prime denotes a derivative with respect to the argument and where $\langle . \rangle_\epsilon$ stands for the thermal average in the canonical ensemble at a temperature T, a source ϵ and a fixed reference configuration $\boldsymbol{r}_0^N$.

Likewise, taking the second derivative of the constrained free energy with respect to ϵ yields the connected susceptibility $\chi_\epsilon^{(\mathrm{con})}$, which quantifies the disorder-averaged amplitude of thermal

fluctuations, namely,

$$\chi_\epsilon^{(\mathrm{con})} = N\beta \left[\overline{\langle \hat{Q}^2 \rangle_\epsilon} - \overline{\langle \hat{Q} \rangle_\epsilon^2} \right] = -F''(\epsilon). \tag{II.7}$$

Geometrically, the connected susceptibility is the slope of the tangent line of the isotherms $\overline{\langle \hat{Q} \rangle_\epsilon}$ with respect to ϵ.

In systems with quenched disorder, there are two sources of fluctuations [211, 212], namely, thermal fluctuations and disorder fluctuations. In other words, the connected susceptibility which is defined in the previous equation differs from the total susceptibility which quantifies the total amount of overlap fluctuations,

$$\chi_\epsilon^{(\mathrm{tot})} = N\beta \left[\overline{\langle \hat{Q}^2 \rangle_\epsilon} - \overline{\langle \hat{Q} \rangle_\epsilon}^2 \right]. \tag{II.8}$$

The difference between the total and the connected susceptibilities represents the overlap fluctuations due to the change in the reference configurations. These disorder fluctuations are quantified by the disconnected susceptibility

$$\chi_\epsilon^{(\mathrm{dis})} = \chi_\epsilon^{(\mathrm{tot})} - \chi_\epsilon^{(\mathrm{con})} = N\beta \left[\overline{\langle \hat{Q} \rangle_\epsilon^2} - \overline{\langle \hat{Q} \rangle_\epsilon}^2 \right], \tag{II.9}$$

which cannot be obtained from a derivative of the free energy $F(\epsilon)$ as it does not correspond to the average over the disorder of a random thermodynamic quantity. Geometrically, the disconnected susceptibility represents the typical difference at fixed ϵ between isotherms $\langle \hat{Q} \rangle_\epsilon$ obtained from differents realisations of the reference configuration. Both the connected and the disconnected susceptibilities are positive as they stand for variances of the order parameter.

2.3 The Franz-Parisi potential $V(Q)$

So far the focus has been made on the canonical ensemble in which the temperature T and the field ϵ are control parameters[1]. But several ensembles can be defined by exchanging the control parameter and its conjugate variable. For instance, in usual statistical physics textbooks, the microcanonical ensemble corresponds to the ensemble with the energy as control parameter while in the canonical ensemble the temperature becomes the control parameter [4]. The change from one ensemble to the other stands for a Legendre transform.

One thus considers a "microcanonical"[2] ensemble in which the overlap between the two replicas becomes the control parameter. One introduces the "microcanonical" free energy which is called the Franz-Parisi (FP) potential $V(Q)$ in the context of glass-forming liquids, and which is now a function of (Q, T, T_0) [148, 153–156]. By following the lines of the previous paragraph, the FP free energy in this ensemble reads

$$V(Q) = -\frac{T}{N} \frac{\displaystyle\int \mathrm{d}\boldsymbol{r}_0^N e^{-\beta_0 \hat{H}[\boldsymbol{r}_0^N]} \ln \int \mathrm{d}\boldsymbol{r}^N e^{-\beta \hat{H}[\boldsymbol{r}^N]} \delta(\hat{Q}[\boldsymbol{r}^N; \boldsymbol{r}_0^N] - Q)}{\displaystyle\int \mathrm{d}\boldsymbol{r}_0^N e^{-\beta_0 \hat{H}[\boldsymbol{r}_0^N]}} = \overline{V(Q; \boldsymbol{r}_0^N)}, \tag{II.10}$$

[1]The temperature T_0 of the reference configurations is another parameter but it is not a control parameter in the usual sense for the thermodynamics of the constrained liquid.

[2]We say that this ensemble is "microcanonical" by analogy with the standard formalism of statistical mechanics, even though the temperature is still a control parameter.

where

$$V(Q;\boldsymbol{r}_0^N) = -\frac{T}{N}\ln\int \mathrm{d}\boldsymbol{r}^N e^{-\beta\hat{H}[\boldsymbol{r}^N]}\delta(\hat{Q}[\boldsymbol{r}^N;\boldsymbol{r}_0^N]-Q) \tag{II.11}$$

is the FP potential for a given reference configuration $\boldsymbol{r}_0^N$, which is a self-averaging random variable. We emphasise that the Hamiltonian which is involved in the definition of the FP potential is the unconstrained Hamiltonian.

Before expliciting the relation between the FP potential and the constrained free energy, we note that $V(Q)$ has another physical intepretation, besides being the free energy in the iso-overlap ensemble. Indeed, the argument of the logarithm in Eq. (II.11) corresponds, up to a normalisation constant, to the unconstrained probability distribution (namely, for $\epsilon = 0$) of the overlap $\mathcal{P}(Q;\boldsymbol{r}_0^N)$ for a fixed reference configuration $\boldsymbol{r}_0^N$. More precisely, one has that

$$V(Q;\boldsymbol{r}_0^N) = -\frac{T}{N}\ln\mathcal{P}(Q;\boldsymbol{r}_0^N) - \frac{T}{N}\ln\mathcal{Z}(T), \tag{II.12}$$

where $\mathcal{Z}(T)$ represents the partition function of the unconstrained liquid at a temperature T. As a consequence, the FP potential can be seen as the large deviation rate function of the unconstrained probability distribution of the overlap [213]. This gives a practical way of computing the FP potential when dealing with computer simulations, see Chap. III. But this also tells that the FP potential represents the free energy cost to force the unconstrained liquid to have a given overlap Q with a reference configuration. In other words, it is the Landau free energy which quantifies the free energy penalty for the overlap fluctuations in the unconstrained liquid [214]. It is closely related to the Landau free energy for the overlap fluctuations in the canonical ensemble where the liquid is constrained with a source ϵ. Indeed, in the canonical ensemble, the probability distribution of the overlap for a fixed reference configuration $\boldsymbol{r}_0^N$ reads

$$\mathcal{P}_\epsilon(Q;\boldsymbol{r}_0^N) = \frac{\displaystyle\int \mathrm{d}\boldsymbol{r}^N e^{-\beta\hat{H}_\epsilon[\boldsymbol{r}^N;\boldsymbol{r}_0^N]}\delta(\hat{Q}[\boldsymbol{r}^N;\boldsymbol{r}_0^N]-Q)}{\displaystyle\int \mathrm{d}\boldsymbol{r}^N e^{-\beta\hat{H}_\epsilon[\boldsymbol{r}^N;\boldsymbol{r}_0^N]}} \propto \mathcal{P}(Q;\boldsymbol{r}_0^N)e^{N\beta\epsilon Q}. \tag{II.13}$$

Therefore, the Landau free energy for the overlap fluctuations in the constrained liquid is merely given by

$$V_\epsilon(Q;\boldsymbol{r}_0^N) = -\frac{T}{N}\ln\mathcal{P}_\epsilon(Q;\boldsymbol{r}_0^N) = V(Q;\boldsymbol{r}_0^N) - \epsilon Q, \tag{II.14}$$

up to an irrelevant additive constant.

2.4 Connection between the Franz-Parisi potential and the constrained free energy

Two ensembles have now been introduced in which the control parameter and its conjugate variable have been exchanged. Therefore, in the thermodynamic limit, the canonical free energy $F(\epsilon)$ is the Legendre-Fenchel transform of the "microcanonical" Franz-Parisi (FP) potential [215, 216], which reads

$$F(\epsilon) = \inf_Q\{V(Q) - \epsilon Q\} = V(\tilde{Q}) - \epsilon\tilde{Q}, \tag{II.15}$$

by using a saddle-point (Laplace) approximation. In the above equality, $\tilde{Q}$ (which depends on ϵ) corresponds to the location of the minimum in $V(Q) - \epsilon Q$, namely,

$$V'(\tilde{Q}) = \epsilon, \tag{II.16}$$

by assuming that $V(Q)$ is differentiable.

Geometrically, Eq. (II.15) indicates that $F(\epsilon)$ is the minimum distance between the curve of $V(Q)$ and the straight line of slope ϵ. In addition, it implies that $F(\epsilon)$ is a concave function of ϵ and that the curve $F(\epsilon)$ is always below its tangent lines. This concavity property can also be recovered from Eq. (II.7). In addition, we note that $F(\epsilon)$ is just the minimum of the Landau free energy for the overlap fluctuations in the constrained liquid (II.14), as it should.

2.5 Ensemble equivalence and phase transitions

The constrained free energy has now been related to the Franz-Parisi (FP) potential. But a natural question which arises is whether a reciprocal relation exists to give the FP potential as a function of $F(\epsilon)$. In other words, one wants to know if the FP potential can be expressed as the Legendre-Fenchel transform of the constrained free energy. This is only possible if the two ensembles in which Q and ϵ are the respective control parameters are equivalent. In this case, the FP potential can be written as

$$V(Q) = \sup_{\epsilon}\{F(\epsilon) + \epsilon Q\}. \tag{II.17}$$

Therefore, if the ensembles are equivalent and if Eq. (II.17) correctly gives the FP potential, then the FP potential must be a convex function of Q.

There are three different situations that can be analysed at this stage, and which depend on the convexity properties of the FP potential.

- If the FP potential is strictly convex at a temperature T, then the ensembles in which Q and ϵ are control parameters are equivalent. The free energy in each ensemble is obtained via a Legendre transform of the free energy in the other ensemble.
- If the FP potential is marginally convex at a temperature T with a straight line behaviour of slope ϵ^* in the range $[Q_\mathrm{l}, Q_\mathrm{h}]$ with $Q_\mathrm{l} < Q_\mathrm{h}$, then the ensembles are still equivalent and the FP potential can be computed as the Legendre-Fenchel transform of the free energy. However, the free energy has a discontinuity in its first derivative for $\epsilon = \epsilon^* = [V(Q_\mathrm{h}) - V(Q_\mathrm{l})]/(Q_\mathrm{h} - Q_\mathrm{l})$, because

$$F'(\epsilon) = -\tilde{Q} = -\mathrm{arginf}_Q\{V(Q) - \epsilon Q\}. \tag{II.18}$$

  The situation is depicted in Fig. II.2 (a)-(b) and it thus corresponds to a thermodynamic first order transition in the canonical ensemble (where ϵ is the control parameter) with a discontinuity in the overlap order parameter when ϵ is tuned to ϵ^*. Indeed, from Eq. (II.6), one has that the derivative of the constrained free energy with respect to ϵ corresponds to the opposite of the average order parameter. More precisely, by combining Eq. (II.6) and Eq. (II.18), one notes that for $\epsilon = \epsilon^*$, the average overlap jumps discontinuously from Q_l to Q_h. Finally, if the range over which the FP potential is linear shrinks to a single point at which the second derivative of the FP potential vanishes, the first derivative of the free energy $F(\epsilon)$ becomes continuous but its second derivative diverges, and this corresponds to a second order thermodynamic phase transition and a critical point with diverging susceptibilities. Indeed, by taking the derivative of Eq. (II.16) with respect to ϵ, one finds that

$$F''(\epsilon) = -\frac{\mathrm{d}\tilde{Q}}{\mathrm{d}\epsilon} = -\frac{1}{V''(\tilde{Q})}. \tag{II.19}$$

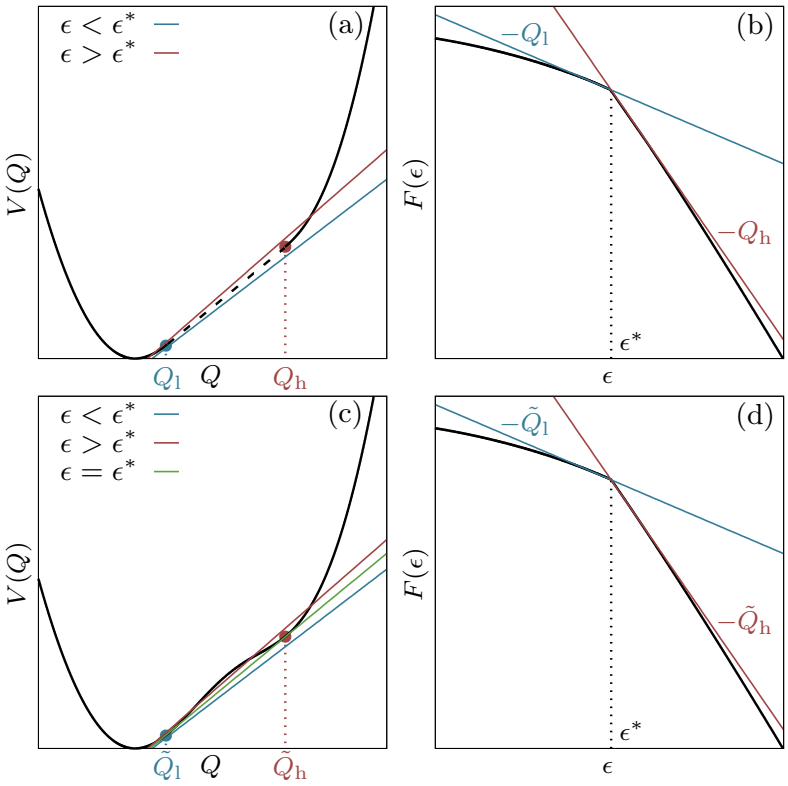

Fig. II.2 | Schematic representation of the Franz-Parisi (FP) potential $V(Q)$ and the canonical free energy $F(\epsilon)$ which is obtained via a Legendre-Fenchel transform of $V(Q)$. Geometrically, $F(\epsilon)$ corresponds to the minimum distance between the curve of $V(Q)$ and the straight lines of slope ϵ, see Eq. (II.15). (a) If the FP potential is marginally convex between Q_l and Q_h with a straight line behaviour of slope ϵ^*, (b) the free energy displays a discontinuity in its first derivative for $\epsilon = \epsilon^*$. (c) If the FP potential is not convex, (d) the free energy has a discontinuous first derivative for $\epsilon = \epsilon^*$ which is obtained thanks to the double-tangent construction to the FP potential. In both cases, this corresponds to a first order phase transition in the canonical ensemble. In panels (a) and (c), the full disks mark the minimiser $\tilde{Q}$ in the Legendre-Fenchel transform of the FP potential for the corresponding value of ϵ, see Eq. (II.15).

- ▶ If the FP potential is not convex at a temperature T, then the two ensembles are no longer equivalent as the FP potential potential cannot be computed from the Legendre-Fenchel transform of the canonical free energy $F(\epsilon)$. The constrained free energy $F(\epsilon)$ is still the Legendre-Fenchel transform of $V(Q)$ but the reciprocal is false. This also corresponds to a thermodynamic first order transition in the canonical ensemble for $\epsilon = \epsilon^*$ with ϵ^* obtained by the double-tangent construction, see Fig. II.2 (c)-(d).

In mean-field models or in systems with long-range interactions, the FP potential can be non-convex, and this corresponds to the first and third previous cases. On the opposite, this is rigorously impossible in finite dimensions with short-range interactions in the thermodynamic limit [217]. As a consequence, the FP potential must be convex, and only the two first cases can occur. Overall, this discussion suggests that the thermodynamics of constrained liquids can be singular with thermodynamic phase transitions and a critical point, which can be detected from the convexity properties of the FP potential. In particular, a critical point in the canonical

ensemble at a temperature T_c and a source ϵ_c exists if there exists an overlap value Q_c such that

$$\begin{cases} V'(Q_\mathrm{c}) & = \epsilon_\mathrm{c}, \\ V''(Q_\mathrm{c}) & = 0, \\ V'''(Q_\mathrm{c}) & = 0. \end{cases} \tag{II.20}$$

In the previous system, the first equation gives the value of ϵ at the critical point, while the last one selects the highest temperature at which the FP potential develops an inflexion point.

2.6 Schematic computation of the Franz-Parisi potential

In this section, we schematically review how the Franz-Parisi (FP) potential can be computed, in order to study its convexity properties and to make some progress in the understanding of the thermodynamics of constrained supercooled liquids. The most convenient way to compute the FP potential is to use the "replica trick[3]" [210], which relies on the following equality:

$$\ln \mathcal{Z} = \lim_{n\to 0} \frac{\mathcal{Z}^n - 1}{n}. \tag{II.21}$$

If one now rewrites Eq. (II.10) by using the partition function $\mathcal{Z}(Q; \boldsymbol{r}_0^N)$ of the liquid at a temperature T for a given fixed overlap Q with the reference configuration $\boldsymbol{r}_0^N$, namely,

$$V(Q; \boldsymbol{r}_0^N) = -\frac{T}{N} \ln \mathcal{Z}(Q; \boldsymbol{r}_0^N), \tag{II.22}$$

then the FP potential reads

$$V(Q) = -\frac{T}{N} \lim_{n\to 0} \left\{ \frac{\overline{\mathcal{Z}^n(Q; \boldsymbol{r}_0^N)} - 1}{n} \right\}. \tag{II.23}$$

The quantity $\mathcal{Z}^n(Q; \boldsymbol{r}_0^N)$ represents the partition function of n non-interacting replicas of the same supercooled liquid $\{\boldsymbol{r}_a^N\}_{a=1\ldots n}$ whose overlaps with the same reference configuration $\boldsymbol{r}_0^N$ are fixed to Q. This "replica trick" thus enables one to replace the logarithm that appears in the definition of the FP potential by a more tractable expression and eventually the limit $n \to 0$ must be taken by assuming an analytical continuation. In consequence, it handles the average over the disorder which is represented by the reference configurations, and it leads to the following expression of the FP potential:

$$V(Q) = -\lim_{n\to 0} \frac{T}{Nn} \left\{ \frac{1}{\mathcal{Z}_0} \int \prod_{\alpha=0}^{n} \mathrm{d}\boldsymbol{r}_\alpha^N e^{-\sum_\alpha \beta_\alpha \hat{H}[\boldsymbol{r}_\alpha^N]} \prod_{a=1}^{n} \delta(\hat{Q}[\boldsymbol{r}_a^N; \boldsymbol{r}_0^N] - Q) - 1 \right\}, \tag{II.24}$$

where $\mathcal{Z}_0$ is the partition function of the unconstrained liquid at a temperature T_0, where $\beta_a = \beta$ for $a = 1 \ldots n$, and where the sum in the exponential runs from $\alpha = 0$ to $\alpha = n$. In the following, we always use greek (resp. roman) indices when they range from 0 (resp. 1) to n.

One can then formally rewrite the previous equation as an integral over all square symmetric overlap matrices of size $n+1$ with diagonal elements equal to 1 and first row and column equal

[3]This is a trick, as opposed to the two replicas which have been introduced previously and which are "real" replicas.

to Q [131, 218], namely,

$$\begin{aligned} V(Q) &= -\lim_{n\to 0}\frac{T}{Nn}\left\{\frac{1}{\mathcal{Z}_0}\int \mathrm{d}Q_{\alpha\gamma}\int\prod_{\alpha=0}^{n}\mathrm{d}\boldsymbol{r}_\alpha^N e^{-\sum_\alpha \beta_\alpha \hat{H}[\boldsymbol{r}_\alpha^N]}\prod_{\alpha,\gamma=0}^{n}\delta(\hat{Q}[\boldsymbol{r}_\alpha^N;\boldsymbol{r}_\gamma^N]-Q_{\alpha\gamma})-1\right\} \\ &= -\lim_{n\to 0}\frac{T}{nN}\left\{\int \mathrm{d}Q_{\alpha\gamma}e^{N\mathcal{S}[Q_{\alpha\gamma}]}-1\right\}. \end{aligned} \tag{II.25}$$

The last equation defines an overlap dependent action $\mathcal{S}[Q_{\alpha\gamma}]$ of order n which is formally obtained by integrating the microscopic degrees of freedom, *i.e.*, the positions of the particles in the replicas. The factor of N in the last row of Eq. (II.25) comes from the fact that the Hamiltonian is extensive and so must be the argument of the exponential. Eventually, the FP potential can be computed from this action by performing a saddle-point (Laplace) approximation in the limit of large N which yields

$$V(Q) = -\lim_{n\to 0}\frac{T}{Nn}\left\{e^{N\mathcal{S}[Q^*_{\alpha\gamma}]}-1\right\} = -T\lim_{n\to 0}\partial_n\mathcal{S}[Q^*_{\alpha\gamma}], \tag{II.26}$$

after doing a Taylor expansion of the exponential whose argument is of order n. The expression of the FP potential involves the derivative of the action $\mathcal{S}[Q_{\alpha\gamma}]$ with respect to the replica index n, which is denoted ∂_n. In addition, the free parameters Q^*_{ab} for $1 \leq a < b \leq n$ of the overlap matrix are solutions of the saddle-point equation

$$\partial_{Q_{ab}}\mathcal{S}[Q^*_{\alpha\gamma}] = 0, \tag{II.27}$$

with $\partial_{Q_{ab}}$ the partial derivative with respect to Q_{ab}, *i.e.*, they maximise the action $\mathcal{S}[Q_{\alpha\gamma}]$.

Even though this recipe can be applied systematically in any glass-forming liquid, in general, deriving the FP potential from the Hamiltonian by integrating over the microscopic degrees of freedom is a formidable task [197, 218]. One could then consider effective actions, like the one of Ref. [167, 168] and from this stage, one could continue the calculations along the lines we detail now.

To derive the FP potential from Eq. (II.26), one needs to solve Eq. (II.27) which actually corresponds to a set of $n(n-1)/2$ non-linear coupled equations. Most of the time, this is done by considering an ansatz for the replica matrix which is motivated by physical considerations. The overlap matrix Q_{ab} corresponds to the matrix of the overlap between equilibrium configurations at a temperature T which are all forced to have an overlap Q with the reference configuration. It is thus sensible to consider a replica symmetric (RS) ansatz [131, 219] where the overlap between two equilibrium configurations is the same for all the replicas and is equal to Q_0, namely,

$$Q^*_{ab} = Q_0 + (1-Q_0)\delta_{ab}, \tag{II.28}$$

where δ_{ab} is the Kronecker delta, which is equal to 1 when $a = b$ and to 0 otherwise. The free parameter Q_0 is the solution of a saddle-point equation. From a mathematical point of view, the action $\mathcal{S}[Q_{\alpha\gamma}]$ is symmetric under replica permutations and considering an ansatz which is consistent with this symmetry is then natural [126]. Even though this ansatz is reasonable because all the replicas are equivalent, it is not always the correct maximiser of the action $\mathcal{S}[Q_{\alpha\gamma}]$. Two things can happen. On the one hand, this RS ansatz can become unstable, which means that it becomes a minimum of the action $\mathcal{S}[Q_{\alpha\gamma}]$. This phenomenon is known as a de Almeida Thouless instability [220–223]. This is something that can be checked by looking at

the eigenvalues of the Hessian matrix of the action $\mathcal{S}[Q_{\alpha\gamma}]$ when it is evaluated for the RS ansatz [221]. On the other hand, the RS solution can be a relative maximum of $\mathcal{S}[Q_{\alpha\gamma}]$ but not the absolute one. This is more difficult to check and this requires physical intuition to guess another ansatz for the overlap matrix.

This new ansatz must explicitely break the symmetry between the replicas whereas the action $\mathcal{S}[Q_{\alpha\gamma}]$ is symmetric under permutations of the replicas. This phenomenon is called spontaneous symmetry breaking and it is at the core of the theory of phase transitions [115]. If one imagines that the phase space is organised into metastable states, it is reasonable to think that the overlap between equilibrium configurations at a temperature T can take two different values, either Q_0 if the two replicas are not in the same metastable state or Q_1 otherwise. This leads to the one-step replica symmetry breaking (RSB) ansatz for the overlap matrix [131, 210, 224–226], namely,

$$Q^*_{ab} = Q_0 + (Q_1 - Q_0)\zeta_{ab} + (1 - Q_1)\delta_{ab}, \tag{II.29}$$

with ζ_{ab} the block diagonal matrix with blocks of size x which are filled with 1. Physically, this RSB ansatz indicates that if one considers two replicas at equilibrium, the overlap can be either Q_0 with probability x, or Q_1 with probability $1 - x$. As a consequence, when $Q_0 = Q_1$, one recovers the RS ansatz of Eq. (II.28). The three free parameters (Q_0, Q_1, x) are the solutions of saddle-point equations. The same problems as for the RS solution can occur, either an instability or the presence of a higher maximum. Nevertheless, one understands from the previous discussion how to generate a full hierarchy of ansatz for the overlap matrix by assuming that each metastable state is actually a metabasin which breaks into smaller metastable states and by introducing more overlap values [210, 225, 226]. One can thus define k-RSB ansatz with $1 \leq k \leq +\infty$. The case $k = +\infty$ corresponds to an ultrametric structure of the overlap matrix which is known as a full replica symmetry breaking [210, 224–228]. The correct ansatz is sensitive to the structure of the free energy landscape and it is thus system-dependent. For simple glasses, a 1-RSB ansatz gives the correct answer at any temperature, see the next section [126].

In this section, we have reviewed the method to compute the FP potential by using replicas. However, one cannot go further on general grounds and one has to consider a specific model in order to analyse the convexity of the FP potential. In the next section, we review the computation of the FP potential and of the phase diagram (ϵ, T) for an archetypal mean-field spin glass model. Even though the precise analytical form of the FP potential is system-dependent, the results of the next section are very general.

3. Exact results from mean-field theory: the spherical p-spin

3.1 The model

We focus on the fully-connected p-spin models (with $p \geq 3$). They correspond to systems of N spins with p-body long-range interactions which are mediated by random coupling constants. This set of models has been introduced as a generalisation of the Sherrington-Kirkpatrick model [219, 229] (which is recovered when $p = 2$), and they behave as the Random Energy Model [230] in the limit $p \to +\infty$. Its thermodynamics has been first studied extensively in the case of Ising spins [117, 231]. We focus here on spherical p-spin models which have been introduced by Crisanti and Sommers [221, 232]. The Hamiltonian of the spherical p-spin is given by

$$\hat{H}\left[\underline{\sigma}\right] = - \sum_{1 \leq i_1 < \cdots < i_p \leq N} J_{i_1 \ldots i_p} \sigma_{i_1} \ldots \sigma_{i_p}, \tag{II.30}$$

where $\boldsymbol{J} = \{J_{i_1 \dots i_p}\}_{1 \leq i_1 < \dots < i_p \leq N}$ are Gaussian random variables of zero mean and of variance

$$\mathbb{E}\{J^2_{i_1 \dots i_p}\} = J^2 p!/(2N^{p-1}). \tag{II.31}$$

In the above equation, J is a constant of unit energy and the scaling with N ensures that the unconstrained free energy is extensive. The spin variables are real numbers on the unit sphere, in other words the spin configurations $\underline{\sigma} = \{\sigma_i\}_{i=1 \dots N}$ fulfill the spherical constraint

$$\frac{1}{N} \sum_{i=1}^{N} \sigma_i^2 = 1. \tag{II.32}$$

In the p-spin model, the overlap between a spin configuration $\underline{\sigma}$ and a reference one $\underline{\sigma}^{(0)}$ is

$$\hat{Q}[\underline{\sigma}; \underline{\sigma}^{(0)}] = \frac{1}{N} \sum_{i=1}^{N} \sigma_i \sigma_i^{(0)}, \tag{II.33}$$

without the need of introducing a cutoff parameter a. With this definition, the spherical constraint is merely written as $\hat{Q}[\underline{\sigma}; \underline{\sigma}] = 1$.

We now comment on this model. Instead of dealing with off-lattice continuous degrees of freedom as for glass-forming liquids, one still treats continuous degrees of freedom but now on a lattice. This first simplification allows one to get rid of the tolerance length a in the definition of the overlap and this makes the overlap an average over the sample of a single site quantity. However, contrary to structural liquids, the p-spin models present a source of external quenched disorder which corresponds to the random coupling constants.Liquids do not display explicit quenched disorder but they generate the disorder by themselves, which is thus said to be "self-induced" [196, 197, 208]. In the p-spin models, the free energy is expected to be self-averaging with respect to the random coupling constants. Also, when dealing with the constrained thermodynamics and the Franz-Parisi construction, the disorder average over the random couplings must be the last to be computed because the constrained p-spin and the reference configuration face the same realisation of the disorder.

Despite these discrepancies, the p-spin models display several similarities with structural glasses. First, for $T = T_{\mathrm{d}}$, the phase space splits into an exponentially-large number of metastable states which dominate the thermodynamics[4]. The dynamical transition temperature has a simple expression in the p-spin models [11], namely,

$$T_{\mathrm{d}} = J \sqrt{\frac{p(p-2)^{p-2}}{2(p-1)^{p-1}}}. \tag{II.34}$$

Contrary to liquids in the limit $d \to +\infty$, the metastable states in the spherical p-spin can be obtained by minimising a free energy in the TAP approach [131, 146, 148, 210], which can be computed by relying on a diagrammatic expansion of the free energy [145, 152], or via the cavity method [210, 233]. The configurational entropy $\Sigma(T)$ is non-zero for $T \leq T_{\mathrm{d}}$ [145–147] and it decreases when the temperature decreases. This illustrates the rarefaction of the metastable states. The p-spin models also display a static transition temperature T_{K} where

[4]In the replica language that we have described in Sec. 2.6, this corresponds to the highest temperature at which a one-step replica symmetry breaking solution appears in the saddle-point equations when the unconstrained free energy is computed.

the number of metastable states becomes sub-exponential in N and where the configurational entropy vanishes[5]. The value of the Kauzmann transition temperature reads

$$T_{\mathrm{K}} = J\sqrt{\frac{py}{2}}(1-y)^{p/2-1}, \tag{II.35}$$

where y is the solution of $1/p = -y(1-y+\ln y)/(1-y)^2$ [152, 233].

The dynamics of the p-spin models is also similar to the one of glass-forming liquids in the limit of infinite dimensions of space. A Langevin equation for the single-spin dynamics is often chosen [234], namely,

$$\frac{\mathrm{d}\sigma_i}{\mathrm{d}t}(t) = -\frac{\partial \hat{H}[\underline{\sigma}]}{\partial \sigma_i(t)} + \Xi_i(t) - \nu\sigma_i(t), \tag{II.36}$$

where $\Xi_i(t)$ is a random Gaussian noise which is delta-correlated in time, and where ν is a Lagrange multiplier in order to ensure the spherical constraint of Eq. (II.32) [232]. From the dynamics of single spins, a closed differential equation can be obtained for the spin-spin correlation function at equilibrium [233, 235–237], which is very similar to the dynamical mean-field equation for the mean-squared displacement in supercooled liquids [130], see Eq. (I.13). In particular, the numerical resolution of these equations shows that, in both cases, the relaxation time diverges from above at $T = T_{\mathrm{d}}$, and the equilibrium correlation function displays a constant plateau at lower temperatures [117, 118, 131, 135].

3.2 Calculation of the Franz-Parisi potential

One can now compute the Franz-Parisi (FP) potential in the p-spin model in order to detect singular behaviours which are sketched in Fig. II.2. In this system, the formal expression of the FP potential is

$$V(Q) = \mathbb{E}\left\{\overline{V(Q;\underline{\sigma}^{(0)},\boldsymbol{J})}\right\} = \mathbb{E}\left\{\int' \mathrm{d}\underline{\sigma}^{(0)} \frac{e^{-\beta_0 \hat{H}[\underline{\sigma}^{(0)}]}}{\mathcal{Z}_0(\boldsymbol{J})} V(Q;\underline{\sigma}^{(0)},\boldsymbol{J})\right\}, \tag{II.37}$$

see Eq. (II.10) for a comparison with structural glasses. The FP potential should be self-averaging with respect to the random coupling constants and the average over them (which is denoted by $\mathbb{E}\{.\}$) must be the last taken. In the last equation, $\mathcal{Z}_0(\boldsymbol{J})$ is the partition function at a temperature T_0 for a given realisation of the random coupling constants and the prime integral denotes the integral over all the spin configurations which respect the spherical constraint. Besides, $V(Q;\underline{\sigma}^{(0)},\boldsymbol{J})$ is the random FP potential for a given reference configuration $\underline{\sigma}^{(0)}$ and a given realisation $\boldsymbol{J}$ of the random coupling constants, namely,

$$V(Q;\underline{\sigma}^{(0)},\boldsymbol{J}) = -\frac{T}{N}\ln\int' \mathrm{d}\underline{\sigma} e^{-\beta\hat{H}[\underline{\sigma}]}\delta(\hat{Q}[\underline{\sigma};\underline{\sigma}^{(0)}] - Q). \tag{II.38}$$

To compute the FP potential, one can use the strategy which is described in Sec. 2.6 and

[5] In the replica language, this corresponds to the lowest temperature at which a one-step replica symmetry breaking solution is found with $x = 1$.

which relies on replicas. By using Eq. (II.23) and Eq. (II.25), one obtains

$$V(Q) = \\ -\lim_{n\to 0}\frac{T}{Nn}\mathbb{E}\left\{\frac{1}{\mathcal{Z}_0(\boldsymbol{J})}\int \mathrm{d}Q_{\alpha\gamma}\int\prod_{\alpha=0}^{n}\mathrm{d}\underline{\sigma}^{(\alpha)}e^{-\sum_\alpha\beta_\alpha\hat{H}[\underline{\sigma}^{(\alpha)}]}\prod_{\alpha,\gamma=0}^{n}\delta(\hat{Q}[\underline{\sigma}^{(\alpha)};\underline{\sigma}^{(\gamma)}]-Q_{\alpha\gamma})-1\right\}. \tag{II.39}$$

We note that the prime integral has been replaced by a full integral as the spherical constraint is taken into account in the product of the delta functions.

Due to the extra source of disorder in the p-spin models, namely, the random coupling constants, another group of replicas should be introduced, in particular to deal with the disorder average of $\mathcal{Z}_0(\boldsymbol{J})$ [148, 156]. However, if $T_0 \geq T_{\mathrm{K}}$, not only the unconstrained free energy at the temperature T_0 is self-averaging, but the partition function also is[6] [208]. We now note $\mathcal{Z}_0 = \mathbb{E}\{\mathcal{Z}_0(\boldsymbol{J})\}$. With this further simplification and because of the mean-field nature of the model [131], the average over the random coupling constants can be computed straightforwardly by using Eq. (II.31), and one ends up with

$$V(Q) = \\ -\lim_{n\to 0}\frac{T}{Nn}\left\{\frac{1}{\mathcal{Z}_0}\int \mathrm{d}Q_{\alpha\gamma}\int\prod_{\alpha=0}^{n}\mathrm{d}\underline{\sigma}^{(\alpha)}e^{(NJ^2/4)\sum_{\alpha,\gamma}\beta_\alpha\beta_\gamma Q_{\alpha\gamma}^p}\prod_{\alpha,\gamma=0}^{n}\delta(\hat{Q}[\underline{\sigma}^{(\alpha)};\underline{\sigma}^{(\gamma)}]-Q_{\alpha\gamma})-1\right\}. \tag{II.40}$$

We note that the average over the random coupling constants now couple all the replicas [115, 131].

So far, the recipe of Sec. 2.6 has been followed. For the p-spin model, one can go further and one can actually integrate over the microscopic degrees of freedom (spin variables). In order to do so, an exponential representation of the δ-functions [131] is introduced, which amounts in softening the overlap constraints. After a saddle-point (Laplace) approximation in the limit of large N, one gets

$$V(Q) = -\lim_{n\to 0}\frac{T}{nN}\left\{\frac{1}{\mathcal{Z}_0}\int \mathrm{d}Q_{\alpha\gamma}e^{(NJ^2/4)\sum_{\alpha,\gamma}\beta_\alpha\beta_\gamma Q_{\alpha\gamma}^p+(N/2)\ln\det Q_{\alpha\gamma}}-1\right\}. \tag{II.41}$$

Therefore, the action $\mathcal{S}[Q_{\alpha\gamma}]$ can be exactly computed for the p-spin model, and it reads

$$\mathcal{S}[Q_{\alpha\gamma}] = \frac{J^2}{4}\sum_{\alpha,\gamma=0}^{n}\beta_\alpha\beta_\gamma Q_{\alpha\gamma}^p + \frac{1}{2}\ln\det Q_{\alpha\gamma} - \frac{J^2\beta_0^2}{4}, \tag{II.42}$$

by using that $\mathcal{Z}_0 = e^{NJ^2\beta_0^2/4}$ in the limit of large N [131, 221].

One can now compute the FP potential from Eq. (II.26) first by solving the saddle-point equation (II.27), which for the p-spin model is

$$\frac{pJ^2\beta^2}{2}[Q_{ab}^*]^{p-1} + (Q^{-1})_{ab}^* = 0, \tag{II.43}$$

[6] A more rigorous method consists in introducing another group of m replicas for the reference configurations and eventually in taking the limit $m \to 0$. For $T_0 \geq T_{\mathrm{K}}$, a replica symmetric ansatz for the overlap matrix of the reference replicas describes the problem correctly and this is strictly equivalent to replacing $\mathcal{Z}_0(\boldsymbol{J})$ by its annealed average over the disorder. For $T_0 \leq T_{\mathrm{K}}$, this simplification does no longer hold. Equivalently, a correct description of the problem when introducing two groups of replicas requires the more general one-step replica symmetry breaking ansatz for the overlap matrix of the reference configurations.

for $1 \leq a < b \leq n$, where $(Q^{-1})_{\alpha\gamma}$ is the inverse matrix of $Q_{\alpha\gamma}$. To solve Eq. (II.43), the most general 1-step RSB ansatz of Eq. (II.29) is inserted. This ansatz is exact at any temperature for the p-spin models with $p \geq 3$ [221, 231], while the resolution of the Sherrington-Kirkpatrick model with $p = 2$ requires a full replica symmetry breaking ansatz [210, 225–227].

The parameters in the definition (II.29) of the overlap matrix are the solutions of saddle-point equations which are obtained by inserting the 1-RSB ansatz into Eq. (II.43), namely,

$$\frac{p\beta^2 J^2}{2} Q_0^{p-1} = \frac{Q_0 - Q^2}{[1-(1-x)Q_1 - xQ_0]^2}, \tag{II.44}$$

$$\frac{p\beta^2 J^2}{2}(Q_1^{p-1} - Q_0^{p-1})(1-x) = \frac{(Q_1 - Q_0)(1-x)}{(1-Q_1)\,[1-(1-x)Q_1 - xQ_0]}, \tag{II.45}$$

and

$$\begin{aligned} &\frac{p\beta^2 J^2 Q_1^{p-1}}{2x}(1-Q_1) - \frac{p\beta^2 J^2 Q_0^{p-1}}{2x}\,[1-(1-x)Q_1 - xQ_0] \\ &+ \frac{\beta^2 J^2}{2}(Q_1^p - Q_0^p) + \frac{1}{x^2}\ln\left[\frac{1-Q_1}{1-(1-x)Q_1 - xQ_0}\right] = 0. \end{aligned} \tag{II.46}$$

Besides, by inserting the 1-RSB ansatz into Eq. (II.42) and by using Eq. (II.26), one obtains the following expression for the FP potential:

$$\begin{aligned} V(Q) = &-\frac{\beta J^2}{4} - \frac{\beta_0 J^2}{2} Q^p + \frac{\beta J^2}{4}\,[(1-x)Q_1^p + xQ_0^p] + \frac{1}{2\beta}\frac{1-x}{x}\ln(1-Q_1) \\ &- \frac{1}{2\beta x}\ln[1-(1-x)Q_1 - xQ_0] - \frac{Q_0 - Q^2}{2\beta\,[1-(1-x)Q_1 - xQ_0]}, \end{aligned} \tag{II.47}$$

where one uses that the diagonal elements of the overlap matrix are equal to 1 and that the elements of the first row and column are equal to Q.

3.3 Temperature evolution of the Franz-Parisi potential for equal temperatures

We numerically solve the saddle-point equations (II.44)-(II.46) in order to compute the Franz-Parisi (FP) potential for the specific case $p = 3$ and to follow its temperature evolution. The resolution of the equations at a fixed temperature T is done numerically by using the Newton-Raphson method [238]. We start by solving the saddle-point equations for $Q = 0$ and we then gradually increase Q. For each value of Q, several initial guesses are considered with different values of (Q_0, Q_1, x) in order to find the one-step replica symmetry breaking (1-RSB) solution if the latter exists. Indeed, a solution with $Q_0 = Q_1$ always exists and it corresponds to the replica symmetric (RS) ansatz of Eq. (II.28). In the case of the p-spin model, the saddle-point equation within the RS ansatz is written as

$$\frac{pJ^2\beta^2}{2} Q_0^{p-1} = \frac{Q_0 - Q^2}{(1-Q_0)^2}, \tag{II.48}$$

while the FP potential reads

$$V_{\mathrm{RS}}(Q) = -\frac{\beta J^2}{4} - \frac{\beta_0 J^2}{2} Q^p + \frac{\beta J^2}{4} Q_0^p - \frac{1}{2\beta}\ln(1-Q_0) - \frac{Q_0 - Q^2}{2\beta(1-Q_0)}. \tag{II.49}$$

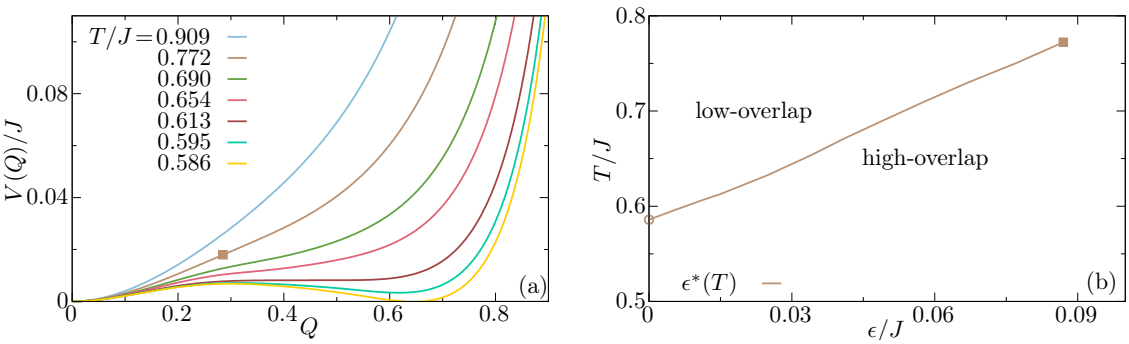

Fig. II.3 | (a) Franz-Parisi (FP) potential for $T = T_0$ and $p = 3$. The curves have been translated so that the value of the FP potential is 0 at its absolute minimum. The FP potential always displays a minimum for $Q = 0$ which corresponds to the most probable value of the overlap between the unconstrained p-spin and the reference configuration, see Eq. (II.12). The FP potential is strictly convex at high temperatures but loses convexity at $T_{\rm cvx}/J = 0.772$ ($\beta_{\rm cvx}J = 1.295$). The square marks the location of the inflexion point ($Q_{\rm c} \simeq 0.285$). Below $T_{\rm cvx}$, the FP potential is no longer convex on an finite overlap range but it remains a monotonic function of Q. At the dynamical transition temperature $T_{\rm d}$ with $T_{\rm d}/J = 0.613$ ($\beta_{\rm d}J = 1.632$), a metastable minimum appears at a high-overlap value. Below this temperature, the FP potential is non-convex with two minima. The high-overlap minimum deepens when the temperature decreases. At the Kauzmann transition temperature $T_{\rm K}/J = 0.586$ ($\beta_{\rm K}J = 1.707$), the two minima are of equal depth. (b) Phase diagram (ϵ, T) for the constrained p-spin in the canonical ensemble (with ϵ as a control parameter) for $T = T_0$. From the thermodynamic glass transition at $(\epsilon, T) = (0, T_{\rm K})$, a line of conventional first order phase transition $\epsilon^*(T)$ emerges and it ends in a critical point at $(\epsilon_{\rm c}, T_{\rm c})$, with $T_{\rm c} = T_{\rm cvx}$ where the FP potential first loses convexity. The line of first order transition separates a delocalised phase of low overlap above from a localised phase of high overlap below.

For $T \geq T_{\rm RSB}$ ($T_{\rm RSB}/J = 0.666$ for $p = 3$), the RS solution provides the correct value of the FP potential. However, when $T \leq T_{\rm RSB}$, the replica symmetry is broken for intermediate values of the overlap $Q \in [Q_{\rm min,RBS}(T), Q_{\rm max,RSB}(T)]$. In this range, the estimate of the FP potential from the 1-RSB solution with $Q_1 \neq Q_0$ and $x < 1$ is larger than its estimate from the RS ansatz. Therefore, the 1-RSB solution should be kept because the overlap matrix must maximise the FP potential. The range over which the replica symmetry is broken increases with decreasing the temperature. For $T \leq T_{\rm K}$, the replica symmetry becomes broken even in the minimum at $Q = 0$. For $T \leq T_{\rm RSB}$, a discontinuous replica symmetry breaking occurs at $Q = Q_{\rm min,RBS}(T)$ (with a jump in Q_1 as a function of Q) when increasing Q from 0, and a continuous one at $Q = Q_{\rm max,RSB}(T)$ (Q_1 remains continuous) when decreasing Q from 1 [222, 239]. The replica symmetry breaking is the manifestation of the fact that the thermodynamics is dominated by a few number of metastable states or equivalently that the configurational entropy has vanished.

The temperature and overlap dependence of the FP potential is first analysed for the case $T = T_0$, see Fig. II.3 (a). At a very high temperature ($T/J = 0.909$), the FP potential is a monotonic function of Q and it displays a unique minimum at $Q = 0$. As the FP potential also corresponds to the large deviation rate function of the unconstrained probability distribution of the overlap [see Eq. (II.12)], this minimum merely reflects the fact that the most probable value of the overlap between equilibrium configurations is 0. The growth of the FP potential indicates that the excursions of the system towards larger overlap cost free energy. When the temperature decreases, the minimum at $Q = 0$ remains but the FP potential decreases for high-overlap values, and this indicates that larger fluctuations of the overlap become possible, as their free energy

cost decreases.

When $T = T_{\rm cvx}$ ($T_{\rm cvx}/J = 0.772$), the FP potential has a vanishing second derivative for an overlap value $Q_{\rm c}$ ($Q_{\rm c} \simeq 0.285$). For $T < T_{\rm cvx}$, the FP potential is non-convex over a finite overlap range but it is still a monotonic function of the overlap. When further decreasing the temperature, one reaches the dynamical transition temperature $T_{\rm d}$ ($T_{\rm d}/J = 0.613$), which is given by Eq. (II.34). For this particular temperature, one observes that the FP potential develops a horizontal inflexion point at a large-overlap value $Q_{\rm g}$ where both its first and its second derivatives vanish. For $T \lesssim T_{\rm d}$, this horizontal inflexion point turns into a secondary minimum. Physically, this means that in the unconstrained liquid, the probability distribution of the overlap now displays two peaks, see Eq. (II.12): a larger peak at $Q = 0$ and a smaller one at $Q = Q_{\rm g}$. The latter is the direct manifestation of the splitting of the phase space into disconnected metastable states. In other words, the absolute minimum in the FP potential at $Q = 0$ corresponds to the overlap between two replicas which belong to different metastable states, while the relative minimum at $Q = Q_{\rm g}$ represents the typical overlap between replicas which are in the same metastable state. In consequence, $Q_{\rm g}$ also corresponds to the value of the free parameter Q_1 when $Q = Q_{\rm g}$.

The depth of the secondary minimum in the FP potential decreases as the temperature is decreased. From a probabilistic point of view, this represents an enhanced probability for two replicas to be in the same metastable state and this thus indicates the rarefaction of the metastable states. This suggests that the height of the secondary minimum may be related to the configurational entropy $\Sigma(T)$. We recall that the FP potential is a Landau free energy and that it corresponds to the free energy cost for the overlap fluctuations in the unconstrained liquid. The value $V(Q_{\rm g})$ of the FP potential at its secondary minimum should then equal the free energy cost to constrain the system in the metastable state of the reference configuration, which is precisely $T\Sigma(T)$. In the p-spin model, both the FP potential and the configurational entropy can be computed and the exact equality between $V(Q_{\rm g})$ and $T\Sigma(T)$ can be verified [153, 156, 222]. Finally, the values of the FP potential at the two minima become identical precisely at the Kauzmann transition temperature $T_{\rm K}$ which is given by Eq. (II.35). This means that the two overlap values $Q = 0$ and $Q = Q_{\rm g}$ are equally probable, or equivalently that the free energy cost to maintain two replicas in the same metastable state has vanished. This is the direct consequence of the Kauzmann entropy crisis.

In the case $T = T_0$, one cannot discuss the shape of the FP potential from the calculations of the previous section when $T \leq T_{\rm K}$ because the latter are restricted to $T_0 \geq T_{\rm K}$. The shape of the FP potential when $T = T_0 \leq T_{\rm K}$ can be found in Ref. [152] and it displays two minima of equal depth for $Q = 0$ and $Q = Q_{\rm g}$. Indeed, in this temperature regime, the configurational entropy is zero and the number of metastable states is sub-exponential in the system size. Consequently, it is equally probable for the system to have a low or a high overlap with another equilibrium configuration whether they belong to the same free energy minimum.

Overall, from this analysis one concludes that the changes in the free energy landscape of the spherical p-spin are directly encoded in the FP potential. As similar changes exist in the free energy landscape of glass-forming liquids at the mean-field level, this temperature evolution of the FP potential is generic for every mean-field glass-former which displays an entropy crisis and a one-step replica symmetry breaking at $T = T_{\rm K}$. Its computation, for instance in computer simulations (see Chap. III), is thus of particular relevance.

3.4 Mean-field phase diagram (ϵ, T) for equal temperatures

One can now perform a change in ensembles to derive the mean-field phase diagram (ϵ, T). The analysis of the temperature evolution of the Franz-Parisi (FP) potential has revealed non-trivial properties, such as its loss of convexity. As explained in Sec. 2.5, this corresponds to a first order transition in the thermodynamics of the constrained p-spin, as shown in Ref. [140, 152, 153, 156, 240]. In this section, the focus is still made on the case $T = T_0$.

The phase diagram is displayed in Fig. II.3 (b) and it was first described in Ref. [153]. It displays a critical point at $T_\mathrm{c} = T_\mathrm{cvx}$ where the FP potential first loses convexity. The value of the source ϵ_c which is needed to be critical is given by the first equation of the system (II.20), hence by the slope of the tangent line to the FP potential at its inflexion point. When the FP potential is not convex, the double-tangent construction locates the field $\epsilon^*(T)$ at which the constrained liquid displays a first order phase transition from a low-overlap (delocalised) phase to a high-overlap (localised) phase. The temperature evolution of the FP potential shows that $\epsilon^*(T)$ decreases when T decreases. More precisely, for $T < T_\mathrm{d}$, the double-tangent construction shows that $\epsilon^*(T)Q_\mathrm{g} \simeq V(Q_\mathrm{g}) = T\Sigma(T)$. This confirms the qualitative discussion of Sec. 1, in particular the fact that the thermodynamics of the constrained system is ruled by a competition between the configurational entropy and the attraction energy. One can also note that $\epsilon^*(T)$ represents a practical way of measuring the configurational entropy, and this has for instance proved useful in computer simulations [181, 241]. When $T = T_\mathrm{K}$, the double-tangent construction gives $\epsilon^* = 0$ and the line of first order transition reaches the random first order transition point at $(\epsilon, T) = (0, T_\mathrm{K})$. Below T_K, the FP potential has a similar shape as what is found at $T = T_\mathrm{K}$. Therefore, as long as $\epsilon > 0$, the system ends up in a high-overlap (localised) phase.

Two other lines can be added to the diagram in Fig. II.3 (b) and can be found in Ref. [153]. They correspond to the spinodal lines, namely, the limits of metastability of the low-overlap phase and of the high-overlap phase. Both lines converge to the critical point at high temperatures. Besides, the analysis of the temperature evolution of the FP potential indicates that the spinodal of the high-overlap phase converges to T_d for $\epsilon = 0$.

In the unconstrained liquid, whose behaviour is found on the $\epsilon = 0$ axis of the phase diagram (ϵ, T), one recovers the thermodynamic phase transition at $T = T_\mathrm{K}$ from the liquid phase to the ideal glass phase. The extension of the phase diagram with an additional control parameter ϵ enables one to emphasise thermodynamic features which are hardly noticeable in the thermodynamics of the unconstrained liquid and which take place at higher temperatures than the Kauzmann transition temperature. Such as the temperature evolution of the FP potential, the shape of the mean-field phase diagram is generic for all the mean-field glass-formers which display a vanishing configurational entropy [154, 155]. Some systems do not have an entropy crisis and instead their configurational entropy remains finite even at zero temperature [126]. For these systems, the phase diagram still resembles the one in Fig. II.3 (b), but the line of first order transition now extends down to zero temperature [242, 243].

The nature of the phase transitions in the diagram (ϵ, T) can finally be discussed. At $T = T_\mathrm{c}$, the transition is of second order with a critical point. At this temperature, the constrained free energy and its first derivative are both continuous but its second derivative diverges. For $T_\mathrm{K} < T < T_\mathrm{c}$, the transition is a conventional first order transition with a discontinuous jump in the order parameter, see Eq. (II.6). The latent heat of this transition from delocalised to localised phases can be computed and it is strictly negative [153]. Finally, for $T = T_\mathrm{K}$, the overlap jumps discontinuously but the latent heat vanishes [153]. This behaviour is intermediate

between the first order and the second order phase transitions and it has been called a random first order transition [122, 144], see Chap. I. The overlap therefore represents an appropriate order parameter to distinguish between the liquid phase and the ideal glass phase on the $\epsilon = 0$ axis above and below $T_{\rm K}$ respectively.

3.5 Mean-field phase diagrams (ϵ, T) for a fixed temperature of the reference configurations

So far, the focus has been made on the case $T = T_0$. However, T_0 is a free parameter, and in particular it is possible to fix T_0 once and for all whatever T, and then to study the constrained thermodynamics of the glass-forming liquid at the temperature T. As already discussed, this corresponds to exploring at a temperature T different metastable states of the glass-forming liquid than the typical ones at this temperature.

In this section, we extend the results of the previous section which have been reported in previous works, and we systematically study the influence of the temperature T_0 of the reference configurations on the mean-field phase diagram in Fig. II.3 (b). By using Eq. (II.47), the Franz-Parisi (FP) potential can be computed for any temperature T_0 of the reference configurations after solving Eq. (II.44)-(II.46) with the method that has already been described before. We first note that Eq. (II.44)-(II.46) do not involve the temperature T_0 of the reference configurations and, as a result, their solution can be computed at once. Once the FP potential is obtained for several temperatures T for a given T_0, its convexity properties can be studied. If it displays non-convexities, the phase diagram (ϵ, T) can be computed as in the previous section via the double-tangent construction.

We show in Fig. II.4 (a) the phase diagram for a fixed T_0 in between $T_{\rm d}$ and $T_{\rm K}$ ($T_0/J = 0.599$ or $\beta_0 J = 1.67$). We observe that the phase diagram still displays a first order transition line $\epsilon^*(T, T_0)$ between a low-overlap phase and a high-overlap phase which ends in a critical point. The diagram nonetheless has several differences with the case $T = T_0$. On the one hand, the location of the first order transition line and of the critical point changes with the temperature T_0. More precisely, we observe that both are shifted to a higher temperature and a larger coupling strength. On the other hand, the first order transition line does not converge to the random first order transition point at $T_{\rm K}$, it becomes instead reentrant at low temperatures and the line $\epsilon^*(T, T_0)$ goes to zero temperature for a finite value of the attraction between the replicas. This is a natural consequence of the fact that the FP potential has a double-well structure with a secondary minimum at a high-overlap value for low-enough temperatures when $T_0 < T_{\rm d}$, as reported in Ref. [222]. When the high-overlap metastable minimum exists, its height has two contributions: one comes from the entropic cost to select a particular metastable state at a temperature T_0, and the other comes from the difference between the free energy of the TAP states which dominate at T_0 and which are followed at T and the equilibrium free energy at the temperature T [148, 222].

The phase diagram in Fig. II.4 (a) also displays a discontinuous replica symmetry breaking (RSB) line $\epsilon_{\rm K}(T, T_0)$ which corresponds to the line where the ansatz that describes the thermodynamics of the constrained system switches from the replica symmetric (RS) one to the 1-RSB one discontinuously (with a jump in Q_1 when varying Q). Equivalently, this is the line where the value of the FP potential for $Q = \tilde{Q} = \overline{\langle \hat{Q} \rangle_\epsilon}$ is higher for the 1-RSB ansatz, where $\tilde{Q}$ is the minimiser in the Legendre-Fenchel transform of Eq. (II.15). On this line, the configurational entropy in the iso-overlap ensemble vanishes [222, 244]. As ensembles are equivalent outside the

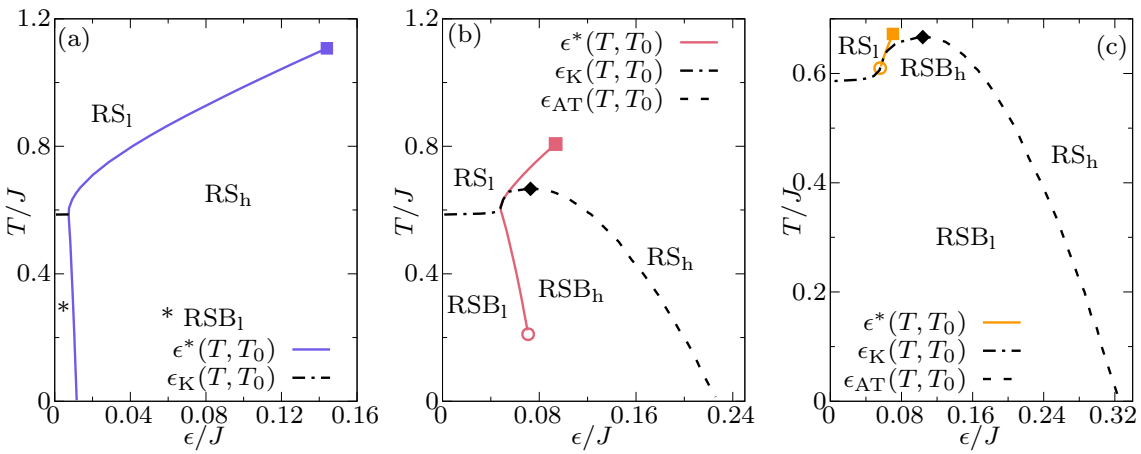

Fig. II.4 | Phase diagram (ϵ, T) of the p-spin model ($p = 3$) for a fixed temperature T_0 of the reference configurations. We show several cases: (a) $T_0 < T_d$ ($T_0/J = 0.599$ or $\beta_0 J = 1.67$), (b) $T_d < T_0 < T_{cvx}$ ($T_0/J = 0.752$ or $\beta_0 J = 1.33$) and (c) $T_0 > T_{cvx}$ ($T_0/J = 0.833$ or $\beta_0 J = 1.2$). We have represented the first order transition line $\epsilon^*(T, T_0)$ from the low-overlap (delocalised) phase to the high-overlap (localised) phase, along with the lines where the ansatz which describes the thermodynamics switches from the replica symmetric (RS) one to the one-step replica symmetry breaking (RSB) one either continuously $\epsilon_{AT}(T, T_0)$ or discontinuously $\epsilon_K(T, T_0)$. The phase diagrams display at most four different phases: a low-overlap RS phase (RS$_l$), a low-overlap 1-RSB phase (RSB$_l$), a high-overlap RS phase (RS$_h$) and a high-overlap 1-RSB phase (RSB$_h$). The full square marks the position of the high-temperature critical point, the empty disk marks the end of the first order transition line at low temperature with a second critical point, and the full diamond stands for the temperature at which RSB effects appear ($T_{RSB}/J = 0.666$). The overlap with the reference configuration is discontinuous on the line $\epsilon^*(T, T_0)$ but it is continuous otherwise.

first order transition region, this means that in the canonical ensemble, the constrained liquid has an entropy crisis on the discontinuous RSB line. On this line, the overlap between the constrained liquid at a temperature T and the reference configuration at a temperature T_0 remains continuous but the overlap between two constrained replicas at the temperature T jumps discontinuously. We note that this discontinuous RSB line is absent in the diagram in Fig. II.3 (b). This is because, in the case $T = T_0$, the thermodynamics of the constrained system is always described by a RS ansatz outside the first order transition region [245, 246].

We can also show the phase diagram for an intermediate case $T_d < T_0 < T_{cvx}$ ($T_0/J = 0.752$ or $\beta_0 J = 1.33$) which appears to be more complex, see Fig. II.4 (b). It still displays a first order transition line $\epsilon^*(T, T_0)$ which ends in a critical point at a high temperature. The position of the line $\epsilon^*(T, T_0)$ and of the critical endpoint are shifted up in temperature and source as compared to the case $T = T_0$, but they appear at lower temperatures and fields than in the case $T_0 < T_d$. Besides, we also observe that for this particular choice of T_0, the first order transition line ends with another critical point at a lower temperature[7]. This behaviour can be understood from the analytical expression of the FP potential, see Eq. (II.47). Indeed, one notes that if $V_T(Q)$ stands for the FP potential for $T = T_0$, then one has for fixed T_0:

$$V(Q) = V_T(Q) + \frac{(\beta - \beta_0)J^2}{2} Q^p. \tag{II.50}$$

[7]The first order transition line seems to go to zero temperature for $T_0 < T_z$ and to end in another critical point for $T_0 > T_z$, with $T_z/J \simeq 0.749$.

The second term in the right-hand side is of the sign of $1/T - 1/T_0$ and it gives a positive contribution to the second derivative of the FP potential if $T < T_0$ and a negative one otherwise. As a result, if T is very small and T_0 is fixed, then $V(Q)$ is less non-convex than $V_T(Q)$: it can eventually become convex again at very low temperatures, and this implies a second low-temperature critical point. Physically, the first order transition line may disappear at a lower critical point because the free energy cost to be in the high-overlap phase may be too prohibitive to be overcome by the field ϵ. Indeed, a plausible assumption is that the system should be similar to the unconstrained liquid at the temperature T_0 (resp. T) when it is forced to have a large (resp. small) overlap with the reference configuration. Consequently, the free energy cost to force the liquid to have a large overlap Q with the reference configuration, as quantified by $V(Q)$, not only takes into account the entropic cost but also the free energy difference between the temperatures T_0 and T which grows as T decreases below T_0.

The phase diagram in Fig. II.4 (b) also displays one more line as compared with that in Fig. II.4 (a). It corresponds to the continuous RSB line $\epsilon_{\rm AT}(T, T_0)$ where the ansatz which describes the thermodynamics switches from the 1-RSB one to the RS one continuously, namely, with $Q_1 - Q_0 \to 0$. On this line, the RS solution becomes unstable and a de Almeida Thouless instability occurs [221–223]. For $T_0 < T_{\rm d}$, the secondary minimum of the FP potential is always described by the RS ansatz and there is not a de Almeida Thouless instability in this case.

We have finally investigated the fate of the phase diagram for a temperature $T_0 > T_{\rm cvx}$, see Fig. II.4 (c) for $T_0/J = 0.833$ ($\beta_0 J = 1.2$). We observe that the critical point and the first order transition line $\epsilon^*(T, T_0)$ survive if T_0 is sufficiently low. In this case, they appear at a lower temperature and a smaller source, as compared to the case $T = T_0$. In addition, the first order transition line still ends with another critical point at a lower temperature. However, the first order transition line has considerably shrunk. As T_0 is increased up to a temperature $T_{\rm max}$ ($T_{\rm max}/J \simeq 0.867$), the ansatz to describe the thermodynamics at the critical point becomes a 1-RSB one and the two critical points which delimitate the first order transition line merge and they eventually annihilate. When $T_0 > T_{\rm max}$, only the discontinuous and continuous RSB lines remain, and any phase transition in the canonical ensemble has disappeared. This is reasonable since the configurational entropy in the constrained liquid vanishes on the discontinuous RSB line and the competition between the entropy and the attraction energy which is central for the existence of the transition in the canonical ensemble no longer exists.

We have found complex phase diagrams when varying the temperature T_0 of the reference configurations. This is reminiscent of what is encountered in the p-spin models with a fraction c of spins which are pinned in an equilibrium configuration that has been sampled at a fixed temperature $T_0 > T$ [247], even though the two settings are different [246]. In particular, we have seen that the location of the first order transition line and the high-temperature critical point varies with T_0: they seem to move upwards (resp. downwards) in temperature and source when T_0 decreases (resp. increases).

3.6 Variation of the location of the critical point with the temperature of the reference configurations

We now systematically study the location of the critical point $(\epsilon_{\rm c}(T_0), T_{\rm c}(T_0))$ when T_0 is varied in the p-spin model. We use the replica symmetric (RS) expression of the Franz-Parisi (FP) potential which is given by Eq. (II.49), as the critical point disappears when it enters the region of replica symmetry breaking. Besides, to simplify notations, we drop the subscript RS.

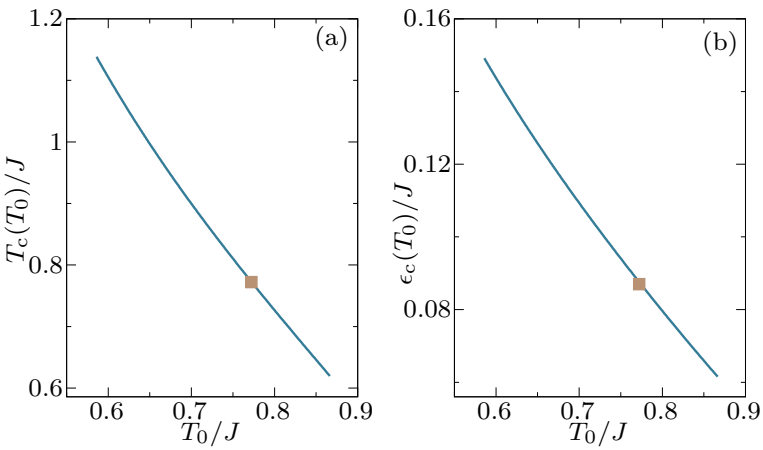

Fig. II.5 | Systematic evolution of the position of the critical point as a function of the temperature T_0 of the reference configurations for the spherical p-spin model with $p = 3$: (a) critical temperature $T_c(T_0)$ and (b) critical field $\epsilon_c(T_0)$. The square marks the location of the critical point for $T = T_0$.

To find the critical point, we need to solve the set of equations (II.20) for the triplet (Q_c, ϵ_c, T_c).

The derivatives in Eq. (II.20) can be computed exactly from Eq. (II.49) while Eq. (II.48) is used to obtain the derivatives of the saddle-point solution Q_0 with respect to Q. The first derivative reads

$$V'(Q) = \partial_Q V(Q) = -\frac{p\beta_0 J^2}{2} Q^{p-1} + \frac{Q}{\beta(1-Q_0)}, \tag{II.51}$$

where ∂_Q stands for the partial derivative with respect to Q, and where the derivative with respect to Q_0 is zero due to the saddle-point condition. The second derivative can be found in the same way and it reads

$$\begin{aligned} V''(Q) &= \partial_Q V'(Q) + \partial_{Q_0} V'(Q) \partial_Q Q_0 \\ &= -\frac{p(p-1)\beta_0 J^2}{2} Q^{p-2} + \frac{1}{\beta(1-Q_0)} + \frac{Q}{\beta(1-Q_0)^2} \partial_Q Q_0, \end{aligned} \tag{II.52}$$

where now we have to take into account the first derivative $\partial_Q Q_0$ of the saddle-point solution with respect to Q. The latter can be computed by differentiating the saddle-point equation (II.49) with respect to Q, and it reads

$$\partial_Q Q_0 = -\frac{2Q}{\frac{p\beta^2 J^2}{2} Q_0^{p-2} (1-Q_0) \left[p - 1 - (p+1)Q_0\right] - 1}. \tag{II.53}$$

The third derivative is obtained similarly and it involves the second derivative of the saddle-point solution with respect to Q, which can be expressed as a function of Q and Q_0 by differentiating Eq. (II.53) with respect to Q.

We solve Eq. (II.20) by means of a Newton-Krylov algorithm. We start from the case $T = T_0$ and we then gradually increase or decrease T_0. We show in Fig. II.5 the evolution of $T_c(T_0)$ and $\epsilon_c(T_0)$ with the temperature T_0 of the reference configurations. We clearly observe that when T_0 is fixed to a value below (resp. above) T_{cvx} (the value of T_c for the case $T = T_0$), the critical point is shifted upwards (resp. downwards) in temperature and source in the phase diagram. The variation of the critical temperature is quite large, of about 25 % between the case $T = T_0$ and

the case of fixed $T_0 = T_{\rm K}$. This feature can be easily understood from the analytical expression of the FP potential, and in particular from Eq. (II.50). Indeed if $T_0 \lesssim T = T_{\rm cvx}$, the second term gives a negative contribution to the second derivative of the FP potential, and this makes the FP potential even more non-convex. Therefore, the critical point appears at a temperature $T_{\rm c}(T_0) > T_{\rm cvx}$. The trend of the critical source $\epsilon_{\rm c}(T_0)$ as a function of the temperature of the reference configurations is more complicated to rationalise. On the one hand, as $T_{\rm c}(T_0)$ increases when T_0 decreases, the thermal fluctuations become more significant and consequently the field to localise the system in the high-overlap phase should increase too. But on the other hand, considering a smaller T_0 leads to a more stable high-overlap phase and it reduces the free energy cost to be localised at a fixed temperature T.

Overall, past studies along with our analysis of the phase diagrams have revealed that the non-trivial modifications of the free energy landscape of glass-forming liquids in the mean-field limit translate into interesting thermodynamic features in the phase diagram (ϵ, T) which are robust with respect to changes in the temperature of the reference configurations (if it is not taken too large). As a consequence, the study of the thermodynamics of constrained supercooled liquids is of great relevance in order to assess the ability of mean-field theory to describe finite-dimensional systems. This is the object of Chap. III which relies on computer simulations in $d = 2, 3$. Calculations of the p-spin model have shown that decreasing T_0 moves the singular thermodynamic behaviours to larger temperatures T well above the glass transition temperature, see Fig. II.5. We expect these trends to be generic in glass-forming liquids and this property is at the heart of our numerical strategy in Chap. III for the study of the phase diagram (ϵ, T) in finite dimensions.

4. Statistical field theory beyond mean-field

Before turning to the computer simulations of finite-dimensional systems, we briefly summarise the first steps towards a thermodynamic description of constrained supercooled liquids in finite dimensions d by using a Landau-Ginzburg functional [214], and by focusing on the high-temperature critical point at $(\epsilon_{\rm c}, T_{\rm c})$ [218]. We first come back to the general case of structural liquids before dealing with the spherical p-spin for explicit calculations.

4.1 The replicated Landau-Ginzburg free energy

In finite dimensions, a good starting point to study the critical point is to build a Landau-Ginzburg free energy. Usually, this is done by starting from a mean-field Landau free energy as a function of the order parameter, and then by considering the possibility of inhomogeneous profiles. By considering the Franz-Parisi (FP) potential $V(Q)$ as the Landau free energy on top of which the spatial fluctuations of the overlap could be added may be tempting. However, in finite dimensions, the only knowledge of the FP potential is not enough to determine the Landau free energy [248]. Indeed, Eq. (II.10) indicates that the FP potential is the average over disorder of a random free energy $V(Q; \boldsymbol{r}_0^N)$. As a result, by computing the FP potential, one has lost most of the properties of the disorder which is represented by the choice of the reference configuration. Nevertheless, one must assess the role of the disorder, which is known to be relevant and to affect the universality class of critical points. For instance random fields destroy any long-range order in $2d$ [249].

As a result, previous works in the literature [196, 197, 218, 250] emphasise that one needs

to compute the different cumulants of the random variable $V(Q;\boldsymbol{r}_0^N)$, and not only its first cumulant which is the FP potential [218, 239]. For instance, the second cumulant quantifies the total variance of the fluctuations of the FP potential among the realisations of the disorder, and it is defined as [208, 239, 248]

$$V^{(2)}(Q_1,Q_2) = N\beta\left[\overline{V(Q_1;\boldsymbol{r}_0^N)V(Q_2;\boldsymbol{r}_0^N)} - \overline{V(Q_1;\boldsymbol{r}_0^N)}\,\overline{V(Q_2;\boldsymbol{r}_0^N)}\right], \tag{II.54}$$

where the factor of N comes from the fact that the FP potential is an intensive quantity and that its typical fluctuations are expected to scale as $N^{-1/2}$, while the factor $\beta = 1/T$ ensures that $V^{(2)}(Q_1,Q_2)$ has the dimension of an energy. The higher order cumulants $V^{(l)}(Q_1,\dots,Q_l)$ ($l \geq 3$) can be defined similarly.

The different cumulants can be generated by introducing n replicas with the same realisation of the disorder (reference configuration), and at the end by taking the limit $n \to 0$, as we have already reviewed for the computation of the FP potential. Nevertheless, in Sec. 2.6, all the replicas are forced to have the same overlap Q with the reference configuration. In order to generate the higher order cumulants, one must consider n replicas but with different overlaps with the reference configuration. For instance, the calculation of the second cumulant requires two different overlap values, see Eq. (II.54). Therefore, one introduces n replicas, each of them having an overlap Q_a with the reference configuration for $a = 1\dots n$, and one is led to define a replicated FP potential $V_{\text{rep}}(\{Q_a\})$ as the large deviation rate function of the joint probability distribution of the overlaps $\{Q_a\}_{a=1\dots n}$ in the n unconstrained replicas [218], namely,

$$e^{-N\beta V_{\text{rep}}(\{Q_a\})} = \overline{e^{-N\beta\sum_a V(Q_a;\boldsymbol{r}_0^N)}} = \frac{\displaystyle\int \prod_{\alpha=0}^{n} \mathrm{d}\boldsymbol{r}_\alpha^N e^{-\sum_\alpha \beta_\alpha \hat{H}[\boldsymbol{r}_\alpha^N]} \prod_{a=1}^{n} \delta(\hat{Q}[\boldsymbol{r}_a^N;\boldsymbol{r}_0^N] - Q_a)}{\displaystyle\int \mathrm{d}\boldsymbol{r}_0^N e^{-\beta_0 \hat{H}[\boldsymbol{r}_0^N]}}. \tag{II.55}$$

The free energy $V_{\text{rep}}(\{Q_a\})$ thus corresponds to the Landau free energy of a mixture of $n+1$ replicas. The above equation is very similar to Eq. (II.24) except that now all the replicas have a different overlap with the reference configuration. One can then once again formally rewrite Eq. (II.55) as an integral over all the square symmetric overlap matrices $Q_{\alpha\gamma}$ of size $n+1$ with diagonal elements equal to 1 and with $Q_{a0} = Q_{0a} = Q_a$:

$$e^{-N\beta V_{\text{rep}}(\{Q_a\})} = \frac{\displaystyle\int \mathrm{d}Q_{\alpha\gamma} \int \prod_{\alpha=0}^{n} \mathrm{d}\boldsymbol{r}_\alpha^N e^{-\sum_\alpha \beta_\alpha \hat{H}[\boldsymbol{r}_\alpha^N]} \prod_{\alpha,\gamma=0}^{n} \delta(\hat{Q}[\boldsymbol{r}_\alpha^N;\boldsymbol{r}_\gamma^N] - Q_{\alpha\gamma})}{\displaystyle\int \mathrm{d}\boldsymbol{r}_0^N e^{-\beta_0 \hat{H}[\boldsymbol{r}_0^N]}} = \int \mathrm{d}Q_{\alpha\gamma} e^{N\mathcal{S}[Q_{\alpha\gamma}]}, \tag{II.56}$$

with the already-introduced overlap dependent action $\mathcal{S}[Q_{\alpha\gamma}]$. In the limit of large N, one can perform a saddle-point (Laplace) approximation which yields

$$V_{\text{rep}}(\{Q_a\}) = -T\mathcal{S}[Q^*_{\alpha\gamma}], \tag{II.57}$$

where the overlap matrix $Q^*_{\alpha\gamma}$ maximises $\mathcal{S}[Q_{\alpha\gamma}]$.

We now review how one can generate the different cumulants of $V(Q;\boldsymbol{r}_0^N)$. The quantity $\sum_a V(Q_a;\boldsymbol{r}_0^N)$ is of order n and one can do a Taylor expansion of the middle-hand side in

Eq. (II.55) in an increasing number of sums over replica indices, which yields

$$\begin{aligned} V_{\rm rep}(\{Q_a\}) = 1 + \sum_{a=1}^{n} V(Q_a) - \frac{1}{2}\sum_{a,b=1}^{n} V^{(2)}(Q_a,Q_b) + \frac{1}{6}\sum_{a,b,c=1}^{n} V^{(3)}(Q_a,Q_b,Q_c) \\ - \frac{1}{24}\sum_{a,b,c,d=1}^{n} V^{(4)}(Q_a,Q_b,Q_c,Q_d) + \dots, \end{aligned} \tag{II.58}$$

where the ellipses represent sums over at least 5 replicas. For instance, if one sets all the replicas to have the same overlap $Q_a = Q$ with the reference configuration, such as in Sec. 2.6, then Eq. (II.58) becomes an expansion in powers of n, namely,

$$V_{\rm rep}(\{Q_a\}) = 1 + nV(Q) - \frac{n^2}{2}V^{(2)}(Q,Q) + \frac{n^3}{6}V^{(3)}(Q,Q,Q) - \frac{n^4}{24}V^{(4)}(Q,Q,Q,Q) + \dots, \tag{II.59}$$

so that in the limit $n \to 0$,

$$V(Q) = \lim_{n\to 0} \partial_n V_{\rm rep}(\{Q_a\}) = -T \lim_{n\to 0} \partial_n \mathcal{S}[Q^*_{\alpha\gamma}]. \tag{II.60}$$

One thus recovers Eq. (II.26). One can do a similar manipulation for the other cumulants. For example, for the second cumulant, one introduces two groups of replicas: one group of n_1 replicas has an overlap Q_1 with the reference configuration and another group of n_2 replicas has an overlap Q_2 with the reference configuration, with $n = n_1 + n_2$. Then Eq. (II.58) becomes

$$\begin{aligned} V_{\rm rep}(\{Q_a\}) = 1 + n_1 V(Q_1) + n_2 V(Q_2) - \frac{n_1^2}{2}V^{(2)}(Q_1,Q_1) - \frac{n_2^2}{2}V^{(2)}(Q_2,Q_2) \\ - n_1 n_2 V^{(2)}(Q_1,Q_2) + O\Big(n_1^3, n_2^3, n_1 n_2^2, n_2 n_1^2\Big), \end{aligned} \tag{II.61}$$

so that in the limit $n_1, n_2 \to 0$,

$$V^{(2)}(Q_1,Q_2) = -\lim_{n_1,n_2\to 0} \partial^2_{n_1 n_2} V_{\rm rep}(\{Q_a\}) = T \lim_{n_1,n_2\to 0} \partial^2_{n_1 n_2} \mathcal{S}[Q^*_{\alpha\gamma}]. \tag{II.62}$$

Now that one has defined a replicated Landau free energy, and that one knows how to generate the different cumulants which are involved in Eq. (II.58), one can focus on the critical point $(\epsilon_{\rm c}(T_0), T_{\rm c}(T_0))$, and on the replicated Landau free energy of the constrained liquid precisely at the critical point which is given by

$$V_{{\rm rep},\epsilon}(\{Q_a\}) = V_{\rm rep}(\{Q_a\}) - \epsilon \sum_{a=1}^{n} Q_a, \tag{II.63}$$

with $\epsilon = \epsilon_{\rm c}$, see Eq. (II.14). One can perform a Taylor expansion of the previous Landau free energy for $Q_a = Q_{\rm c} + \phi_a$ with $\phi_a \ll Q_{\rm c}$ for $a = 1 \dots n$. At the critical point, the second and the third derivatives of the first cumulant $V(Q)$ vanish, see Eq. (II.20). Consequently, one must develop the replicated Landau free energy up to the fourth order in ϕ_a. This result was obtained in Ref. [218] and it reads, up to an irrelevant additive constant,

$$\begin{aligned} &\beta_{\rm c} V_{{\rm rep},\epsilon_{\rm c}}(\{\phi_a\}) = \\ &\sum_{a=1}^{n}\left[\frac{g_2}{2}\phi_a^2 + \frac{g_3}{6}\phi_a^3 + \frac{g_4}{24}\phi_a^4\right] - \frac{1}{2}\sum_{a,b=1}^{n}\phi_a\phi_b\left[\tau_{20} + \frac{\tau_{21}}{2}(\phi_a+\phi_b) + \frac{\tau_{22}}{4}\phi_a\phi_b + \frac{\tau_{23}}{6}\left(\phi_a^2+\phi_b^2\right)\right] \\ &+ \frac{1}{6}\sum_{a,b,c=1}^{n}\phi_a\phi_b\phi_c\left[\tau_{30} + \frac{\tau_{31}}{2}(\phi_a+\phi_b+\phi_c)\right] - \frac{\tau_{40}}{24}\sum_{a,b,c,d=1}^{n}\phi_a\phi_b\phi_c\phi_d + \dots, \end{aligned} \tag{II.64}$$

with $\beta_{\rm c} = 1/T_{\rm c}$, and where the coefficients can be expressed in terms of the derivatives of the cumulants of the FP potential, namely,

$$\begin{cases} g_2 = \beta_{\rm c} V''(Q_{\rm c}) = 0,\ g_3 = \beta_{\rm c} V'''(Q_{\rm c}) = 0,\ g_4 = \beta_{\rm c} V''''(Q_{\rm c}), \\ \tau_{20} = \beta_{\rm c} \partial^2_{Q_1 Q_2} V^{(2)}(Q_{\rm c}, Q_{\rm c}),\ \tau_{21} = \beta_{\rm c} \partial^3_{Q_1^2 Q_2} V^{(2)}(Q_{\rm c}, Q_{\rm c}), \\ \tau_{22} = \beta_{\rm c} \partial^4_{Q_1^2 Q_2^2} V^{(2)}(Q_{\rm c}, Q_{\rm c}),\ \tau_{23} = \partial^4_{Q_1^3 Q_2} V^{(2)}(Q_{\rm c}, Q_{\rm c}), \\ \tau_{30} = \beta_{\rm c} \partial^3_{Q_1 Q_2 Q_3} V^{(3)}(Q_{\rm c}, Q_{\rm c}, Q_{\rm c}),\ \tau_{31} = \beta_{\rm c} \partial^4_{Q_1^2 Q_2 Q_3} V^{(3)}(Q_{\rm c}, Q_{\rm c}, Q_{\rm c}), \\ \tau_{40} = \beta_{\rm c} \partial^4_{Q_1 Q_2 Q_3 Q_4} V^{(4)}(Q_{\rm c}, Q_{\rm c}, Q_{\rm c}, Q_{\rm c}). \end{cases} \tag{II.65}$$

Once the Landau free energy is obtained, one can define the corresponding Landau-Ginzburg free energy functional in d dimensions by considering inhomogeneous overlap profiles $\phi_a(\boldsymbol{x})$ for $a = 1 \dots n$ and $\boldsymbol{x} \in \mathbb{R}^d$, to allow for spatial fluctuations. Then, one introduces a free energy penalty for interfaces, *i.e.*, large spatial variations of the overlap. As usual, one does a Taylor expansion in terms of the gradient of the overlap field $\partial_{\boldsymbol{x}} \phi_a$, and only keeps the least order term which respects the assumptions of locality and invariance with respect to spatial rotations and translations [115]. The Landau-Ginzburg free energy then reads

$$\begin{aligned} &\beta_{\rm c} V_{{\rm rep},\epsilon_{\rm c}}(\{\phi_a(\boldsymbol{x})\}) = \\ &\sum_{a=1}^{n} \int {\rm d}^d \boldsymbol{x} \left[K \left(\partial_{\boldsymbol{x}} \phi_a(\boldsymbol{x})\right)^2 + \frac{g_2}{2} \phi_a(\boldsymbol{x})^2 + \frac{g_3}{6} \phi_a(\boldsymbol{x})^3 + \frac{g_4}{24} \phi_a(\boldsymbol{x})^4 \right] \\ &- \frac{1}{2} \sum_{a,b=1}^{n} \int {\rm d}^d \boldsymbol{x} \phi_a(\boldsymbol{x}) \phi_b(\boldsymbol{x}) \left[\tau_{20} + \frac{\tau_{21}}{2} \left(\phi_a(\boldsymbol{x}) + \phi_b(\boldsymbol{x})\right) \right. \\ &\left. + \frac{\tau_{22}}{4} \phi_a(\boldsymbol{x}) \phi_b(\boldsymbol{x}) + \frac{\tau_{23}}{6} \left(\phi_a(\boldsymbol{x})^2 + \phi_b(\boldsymbol{x})^2 \right) \right] \\ &+ \frac{1}{6} \sum_{a,b,c=1}^{n} \int {\rm d}^d \boldsymbol{x} \phi_a(\boldsymbol{x}) \phi_b(\boldsymbol{x}) \phi_c(\boldsymbol{x}) \left[\tau_{30} + \frac{\tau_{31}}{2} \left(\phi_a(\boldsymbol{x}) + \phi_b(\boldsymbol{x}) + \phi_c(\boldsymbol{x})\right) \right] \\ &- \frac{\tau_{40}}{24} \sum_{a,b,c,d=1}^{n} \int {\rm d}^d \boldsymbol{x} \phi_a(\boldsymbol{x}) \phi_b(\boldsymbol{x}) \phi_c(\boldsymbol{x}) \phi_d(\boldsymbol{x}) + \dots, \end{aligned} \tag{II.66}$$

with K an unknown coefficient.

We now comment on the choice of the inhomogeneous term in the previous equation. In the case of the spherical p-spin, the Landau-Ginzburg functional can be derived exactly by considering its Kac formulation [251–253]. In this construction, the spherical p-spin which is defined on a hypercubic lattice in d dimensions has now finite-range interactions, and the thermodynamic limit ($L \to +\infty$) is taken before taking the limit of infinite interaction range. The obtained inhomogeneous term which accounts for the phase separation is a priori more complicated than the mere squared gradient term one may naively introduce (see the above equation) [166, 172]. The first difference is that the inhomogeneous term involves an overlap dependent "mass" $K(Q_a(\boldsymbol{x}))$ which vanishes when the overlap with the reference configuration goes to zero. However, close to the critical point, the overlap is finite and it is approximately equal to $Q_{\rm c} > 0$. Besides, the prefactor can be regularised by considering a mixed p-spin model. A two-body interaction of typical amplitude J_2 is added to the Hamiltonian of Eq. (II.30) which makes the prefactor of the squared gradient finite and of order J_2. In the limit of small-enough

J_2, the behaviour of the pure p-spin model is recovered. The second difference is that the Landau-Ginzburg functional in the Kac limit displays gradient terms of the saddle-point solutions which have not been included there. As the critical point lies above the Kauzmann transition, one can assume that the saddle-point solutions adiabatically follow the overlaps with the reference configuration [173], and their derivatives can thus be written as a function of the derivatives of the overlaps with the reference configuration. These arguments justify the above approximation of the interfacial free energy cost in terms of a mere squared gradient near the critical point.

4.2 Mapping onto the random-field Ising model

In this section, we extend the result of Ref. [218] where the focus was made on the case $T = T_0$. We show that for any temperature of the reference configurations T_0, if the critical point exists, then it is in the universality class of the random-field Ising model[8] (RFIM). Details about the RFIM can be found in Appendix A. For any temperature T_0 of the reference configurations, one can show that the Landau-Ginzburg free energy of Eq. (II.66) can be mapped onto the replicated Hamiltonian of a system in the presence of a random field $h(\boldsymbol{x})$, a random mass $m(\boldsymbol{x})$ and a random cubic coupling $\lambda(\boldsymbol{x})$. In other words, glass-forming liquids whose overlap with a reference configuration which is sampled at a temperature T_0 is coupled to an external source behaves close to the critical point as a random system which is described by the following disordered Hamiltonian:

$$\begin{aligned}\beta\mathcal{V}[\phi(\boldsymbol{x})] = \int \mathrm{d}^d\boldsymbol{x} \Big[& K' \left(\partial_{\boldsymbol{x}}\phi(\boldsymbol{x})\right)^2 + \frac{g_2}{2}\phi(\boldsymbol{x})^2 + \frac{g_3}{6}\phi(\boldsymbol{x})^3 + \frac{g_4}{24}\phi(\boldsymbol{x})^4 \\ & + \frac{m(\boldsymbol{x})}{2}\phi(\boldsymbol{x})^2 + \frac{\lambda(\boldsymbol{x})}{6}\phi(\boldsymbol{x})^3 - h(\boldsymbol{x})\phi(\boldsymbol{x}) \Big] ,\end{aligned} \tag{II.67}$$

with

$$\begin{cases} \overline{h(\boldsymbol{x})h(\boldsymbol{y})} = \tau_{20}\delta(\boldsymbol{x}-\boldsymbol{y}),\ \overline{h(\boldsymbol{x})m(\boldsymbol{y})} = -\tau_{21}\delta(\boldsymbol{x}-\boldsymbol{y}), \\ \overline{m(\boldsymbol{x})m(\boldsymbol{y})} = \tau_{22}\delta(\boldsymbol{x}-\boldsymbol{y}),\ \overline{h(\boldsymbol{x})\lambda(\boldsymbol{y})} = -\tau_{23}\delta(\boldsymbol{x}-\boldsymbol{y}), \\ \overline{h(\boldsymbol{x})h(\boldsymbol{y})h(\boldsymbol{t})} = -\tau_{30}\delta(\boldsymbol{x}-\boldsymbol{y})\delta(\boldsymbol{x}-\boldsymbol{t}),\ \overline{h(\boldsymbol{x})h(\boldsymbol{y})m(\boldsymbol{t})} = \tau_{31}\delta(\boldsymbol{x}-\boldsymbol{y})\delta(\boldsymbol{x}-\boldsymbol{t}), \\ \overline{h(\boldsymbol{x})h(\boldsymbol{y})h(\boldsymbol{t})h(\boldsymbol{w})} - \overline{h(\boldsymbol{x})h(\boldsymbol{y})}\,\overline{h(\boldsymbol{t})h(\boldsymbol{w})} = \tau_{40}\delta(\boldsymbol{x}-\boldsymbol{y})\delta(\boldsymbol{x}-\boldsymbol{t})\delta(\boldsymbol{x}-\boldsymbol{w}). \end{cases} \tag{II.68}$$

The random field is known to be the most relevant disorder term [248], as in the RFIM, the higher-order random terms are anyway generated along the renormalisation flow. The above derivation shows that, if the critical point at the mean-field level exists for a given value of T_0 and if it survives in finite dimensions [206], then it is in the universality class of the RFIM [250]. Of course, this mapping is only correct if g_4, τ_{20}, τ_{22} and τ_{40} are all positive [218], which must be checked for specific models. In the next section, we come back to the spherical p-spin and we explain how to compute the second cumulant of the FP potential to derive τ_{20}.

The fact that the long-range physical properties of constrained glass-forming liquids fall in the universality class of the RFIM may be confusing. Indeed, in Sec. 1, the physics of constrained liquids has been accounted for by a trade-off between the (configurational) entropy and the attraction energy. On the opposite, the physics of the RFIM is known to be ruled by a

[8] There are multiple analogies between glass-forming liquids and the RFIM. They have been documented in the case of the thermodynamics of constrained liquids, of the non-equilibrium behaviour of glasses when they are sheared (see Chap. I and Ref. [85]), but also of the equilibrium dynamics close to the dynamical transition temperature [208].

zero-temperature fixed point and by a competition between two energies (see Appendix A). In fact, this seeming contradiction can be solved by invoking the mosaic state [144] of the random first order transition theory (see Chap. I). In this framework, the configurational entropy is only defined on a scale below the point-to-set length [196]. It fluctuates from one correlated region to another and therefore it behaves as a random field which is linearly coupled to the overlap [197, 254]. For instance, the regions of larger configurational entropy tend to have a lower overlap with the reference configuration.

Finally, we remark that in this section, we have focused on the system close to its putative critical point in the presence of a finite source ϵ. The mapping onto the RFIM can be extended on the whole first order transition line for the case $T = T_0$ but also for the case of fixed T_0, if the first order transition survives in finite dimensions [218]. When $\epsilon > 0$, the constrained supercooled liquid behaves as the RFIM below its critical temperature in an external magnetic field which experiences an equilibrium first order transition with disorder when the applied magnetic field vanishes [211, 255]. More recently, the mapping was also extended close to $(\epsilon, T) = (0, T_{\mathrm{K}})$ for $T = T_0$, even though the replicated action displays more terms, in particular random bond and power law decaying multi-body interactions [196, 197].

4.3 The second cumulant of the Franz-Parisi potential and the "self-induced" disorder

As already discussed, to compute the second cumulant, one has to introduce two groups of replicas with different overlaps Q_1 and Q_2 with the reference configuration, then to compute the replicated Franz-Parisi (FP) potential from Eq. (II.57), and eventually to use Eq. (II.62). The computation of the replicated FP potential requires to find the overlap matrix which maximises the overlap dependent action $\mathcal{S}[Q_{\alpha\gamma}]$. One can look for a replica symmetric (RS) ansatz. This is justified by the fact that we later compute the second cumulant for the spherical p-spin model for which the critical point is always described by a RS ansatz. One thus considers an overlap matrix at the saddle-point of the form

$$Q^*_{\alpha\gamma} = \begin{pmatrix} 1 & Q_1 & \dots & \dots & Q_1 & Q_2 & \dots & \dots & Q_2 \\ Q_1 & 1 & Q_0^{(1)} & \dots & Q_0^{(1)} & Q_{12} & \dots & \dots & Q_{12} \\ \vdots & Q_0^{(1)} & \ddots & \ddots & \vdots & \vdots & & & \vdots \\ \vdots & \vdots & \ddots & \ddots & Q_0^{(1)} & \vdots & & & \vdots \\ Q_1 & Q_0^{(1)} & \dots & Q_0^{(1)} & 1 & Q_{12} & \dots & \dots & Q_{12} \\ Q_2 & Q_{12} & \dots & \dots & Q_{12} & 1 & Q_0^{(2)} & \dots & Q_0^{(2)} \\ \vdots & \vdots & & & \vdots & Q_0^{(2)} & \ddots & \ddots & \vdots \\ \vdots & \vdots & & & \vdots & \vdots & \ddots & \ddots & Q_0^{(2)} \\ Q_2 & Q_{12} & \dots & \dots & Q_{12} & Q_0^{(2)} & \dots & Q_0^{(2)} & 1 \end{pmatrix}, \tag{II.69}$$

where $Q_0^{(1)}$, $Q_0^{(2)}$ and Q_{12} are free parameters to maximise $\mathcal{S}[Q_{\alpha\gamma}]$.

We now turn to the spherical p-spin for explicit calculations. Inserting the previous ansatz in Eq. (II.42) and in the saddle-point equation (II.43) yields [218, 239]

$$V^{(2)}_{\mathrm{RS}}(Q_1, Q_2) = \frac{\beta J^2}{2} Q_{12}^p - \frac{(Q_{12} - Q_1 Q_2)^2}{2\beta(1 - Q_0^{(1)})(1 - Q_0^{(2)})}, \tag{II.70}$$

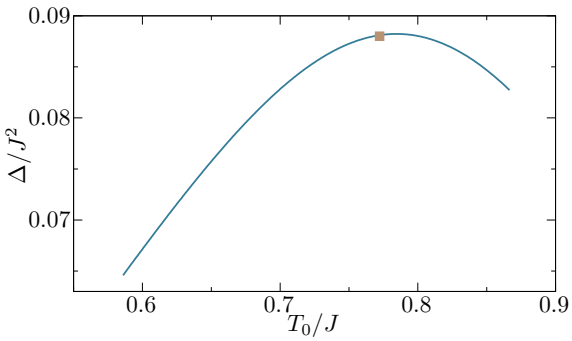

Fig. II.6 | Variance of the effective random fields $\Delta \equiv \tau_{20}$ in the mapping onto the RFIM for the spherical p-spin model (with $p = 3$). The square marks the value of Δ at the critical point when $T = T_0$.

where $Q_0^{(a)}$ $(a = 1, 2)$ is solution of Eq. (II.48) with Q that is replaced by Q_a, while Q_{12} extremises the above expression and is thus solution of

$$\frac{p\beta^2 J^2}{2} Q_{12}^{p-1} = \frac{Q_{12} - Q_1 Q_2}{(1 - Q_0^{(1)})(1 - Q_0^{(2)})}. \tag{II.71}$$

In the case of the spherical p-spin model, neither the expression of the second cumulant (II.70) nor the solution of Eq. (II.71) depend on the temperature T_0 of the reference configurations. In addition, we remark that if $Q_1 = Q_2$ (in particular at the critical point), then $Q_{12} = Q_0^{(1)} = Q_0^{(2)}$.

We can now compute the coefficient $\Delta \equiv \tau_{20}$ from the second derivative of $V^{(2)}(Q_1, Q_2)$ which is evaluated at the critical point, see Eq. (II.65). It represents the variance of the effective random fields in the mapping onto the RFIM and it is thus a measure of the dominant effective and "self-induced" disorder in the constrained p-spin. Its evolution with the temperature of the reference configurations is given in Fig. II.6, where both Δ and T are rescaled by the appropriate measure of the interaction coupling. We first note that it always remains positive, as it should. In addition, it decreases at both large and small values of T_0 while it is maximum for intermediate values of $T_0 \simeq T_{\text{cvx}}$. We recall that T_{cvx} is the critical temperature for the case $T = T_0$. As a result, the case $T = T_0$ corresponds to a relatively high disorder strength. The evolution of $\Delta(T_0)/J^2$ can be understood qualitatively. On the one hand, when T_0 is lowered, the number of metastable states in which the reference configurations can be sampled decreases. On the other hand, when T_0 increases, the free energy landscape becomes more trivial and the disorder is less relevant. If our physical intuition is correct, then the evolution of Δ with the temperature of the reference configurations in realistic glass-forming liquids should be similar when rescaling all quantities by the strength of the effective interactions. As a consequence, decreasing T_0 in constrained glass-forming liquids pushes the critical point at higher temperatures in the liquid region but it reduces the strength of the effective disorder and it potentially makes more difficult to assess the role of the disorder in the physics of glass-forming liquids when they are coupled to a quenched reference.

This section has discussed the first steps towards a statistical field theory of the overlap order parameter in finite dimensions. However, a more realistic description of supercooled liquids requires a knowledge of the overlap dependent action $\mathcal{S}[Q_{\alpha\gamma}]$ from which the cumulants of the FP potential can be computed. In other words, as derived, even though the statistical field theory makes general predictions regarding the nature of the transitions, it does not predict whether

the mean-field phase diagram (ϵ, T) survives the introduction of finite-dimensional fluctuations. Therefore, computer simulations can be helpful to detect phase transitions in constrained supercooled liquids but also to measure $\mathcal{S}[Q_{\alpha\gamma}]$ in model glass-formers. Before presenting our numerical simulations of constrained supercooled liquids in dimensions $d = 2, 3$ in Chap. III, we first review the results which were obtained in previous works and we develop our directions of study.

5. Computer studies of glass-formers in the Franz-Parisi construction

5.1 Structural liquids

Since coupling the overlap with a reference configuration to an external source may induce a first order phase transition between a low-overlap phase and a high-overlap phase and since it may thus reveal the existence of non-trivial thermodynamic fluctuations and of an entropy crisis at a low and inachievable temperature, computer simulations have been performed in several three-dimensional models in order to study the main features of the phase diagram (ϵ, T).

The Franz-Parisi (FP) potential was measured in different model glass-formers for the case $T = T_0$ by using importance sampling techniques which are similar to the ones that are detailed in Chap. III. In particular, in small systems, the FP potential shows a tendency to become non-convex when lowering the temperature, in agreement with the mean-field picture [181, 209, 213, 241]. In larger systems instead, the FP potential turns to become almost linear when lowering the temperature [256]. These results suggest that the mean-field theory of the glass transition remains relevant in finite dimensions.

The thermodynamics in the presence of a finite source ϵ was also measured in computer simulations for the case $T = T_0$. The isotherms $\overline{\langle \hat{Q} \rangle_\epsilon}$ flatten as the temperature is decreased and conversely the susceptibilities grow in small systems. The location of the susceptibility maxima forms a line in the plane (ϵ, T) which is often called the "Widom line". Along the Widom line, the full overlap probability distribution was also computed, see Eq. (II.13), and it becomes bimodal at low temperatures. This is the expected distribution if there is a phase separation between a low-overlap phase and a high-overlap phase [209]. This is also consistent with the direct real-space analysis of overlap profiles which show macroscopic domains of small and large overlap [156, 256]. Finally, the phase diagram (ϵ, T) was explored from a dynamic point of view too. The study of the time variation of the overlap upon heating or cooling for fixed $\epsilon > 0$ has revealed hysteresis as it is expected when crossing a first order transition line [156].

The influence of the disorder which is represented by the reference configurations was also assessed in Ref. [209]. For a fixed ϵ, the overlap probability distribution is shown to be different from one reference configuration to another. Overall, this suggests that the disconnected susceptibility in Eq. (II.9) is non-zero in constrained glass-forming liquids and that the disorder is indeed relevant. In addition, the RFIM-like scaling between the connected and the disconnected susceptibilities [see Eq. (II.79) in Appendix A] was also investigated and it appears to be verified even though the increase in both susceptibilities is mild because of small system sizes.

The role of the temperature T_0 of the reference configuration was studied too [209]. When T_0 is decreased at a fixed temperature T, the overlap probability distribution for the largest total susceptibility is found to become more bimodal. This shows that the overlap fluctuations increase when lowering T_0 and this result is indeed consistent with the fact that the putative

critical point is shifted upwards in temperature, see Fig. II.5.

All the previous results are encouraging. However, their conclusions have been limited to too-large temperatures or too-small system sizes. In particular, most studies have been performed in the case $T = T_0$ for which the critical point may be at or below the avoided dynamical transition (mode coupling crossover) for which equilibration of the unconstrained liquid becomes difficult to ensure for a reasonable simulation walltime, see also Appendix A of Chap. III. In other words, all previous numerical works likely remained above the putative critical point, *i.e.*, along the Widom line. In order to go further in the simulations of constrained supercooled liquids, one needs to be able to go to significantly lower temperatures and to larger system sizes. This is what we achieve in Chap. III by relying on the recently-developed swap algorithm [54]. Finally, we note that numerical works have concentrated on $3d$ systems. However, $2d$ models should also be investigated as the mapping onto the RFIM excludes the existence of a transition at any temperature in the thermodynamic limit (the lower critical dimension is 2, see Appendix A). This is therefore a strong prediction that can be checked. In Chap. III, we also bridge this gap.

5.2 Plaquette models

We also review computer simulations which were performed on plaquette models. The latter correspond to lattice models of Ising spins with p-body interactions in which interacting spins form plaquettes of p spins [201]. These models are related to Ising p-spin models [257] which are at the root of the mean-field theory of the glass transition. However, when the lattices of spins and bonds are isomorph [258], or equivalently when the number of spins per plaquette equals the number of plaquettes to which a given spin belongs, the model is well described by the dynamic facilitation theory as it can be mapped onto a system of localised and non-interacting defects which diffuse with kinetic constraints, namely, onto a kinetically constrained model [257, 259] (see Chap. I).

In Ref. [260], the thermodynamics of the $d = 3$ square pyramid plaquette model which is attractively coupled to a quenched reference configuration was studied numerically. Spin systems are easier to simulate than particle systems and larger system sizes and lower temperatures can thus be achieved. While the dynamics of the unconstrained square pyramid plaquette model is actually described by the dynamic facilitation theory [112], its thermodynamic behaviour was shown to be remarkably consistent with the mean-field theory of the glass transition. A random-field Ising model (RFIM) critical point was found and characterised thanks to a finite-size scaling analysis. The role of the temperature T_0 of the reference configuration on the position of the critical point was also discussed, with a similar trend as in Fig. II.5 (a). For this system, the entropy only vanishes at zero temperature [243, 261] and the results are consistent with a line of first order transition which converges to $(\epsilon, T) = (0, 0)$ in the phase diagram.

The phase diagram (ϵ, T) was also investigated from a dynamic point of view in Ref. [99] for the $2d$ triangular plaquette model. The melting dynamics at a temperature T of equilibrium configurations which were sampled at a temperature T_0 was analysed for the unconstrained liquid ($\epsilon = 0$) and close to Widom line ($\epsilon > 0$). When $0 < T_0 < T$ and when ϵ is small-enough, the dynamics of the constrained system agrees with the Avrami law which describes the rare nucleation of small droplets of the stable (low-overlap) phase into the metastable (high-overlap) one, that is followed by the growth of these nuclei, as it is expected close to a first order transition [103]. However, the Avrami description fails closer to the Widom line as the typical size of the domains over which the overlap field is correlated increases and as the disorder starts

to become relevant (see the Imry-Ma argument in Appendix A). Hence, at short lengthscales and timescales, the system displays mean-field remnants. In addition, the behaviour is consistent with the RFIM criticality and the fact that any phase transition should disappear in the thermodynamic limit in $2d$.

Overall, the fact that plaquette models behave similarly as glass-forming liquids means that the mean-field theory of the glass transition and the dynamic facilitation theory are not completely incompatible. Consequently, the study of constrained glass-formers might be a way of linking these two theories of the glass transition and this gives another motivation to the simulations of the next chapter.

Appendix A - The random-field Ising model

A.1 Presentation

The random-field Ising model (RFIM) is a generalisation of the pure Ising model. It corresponds to a system of Ising spins $S_i = \pm 1$ on a hypercubic lattice in d dimensions which interact with ferromagnetic coupling constants[9] $J_{ij} > 0$. In addition, on each lattice site, the spin S_i interacts with a random field h_i [91]. The random fields are quenched random variables which are usually of zero mean and which are delta-correlated in space. The Hamiltonian of the RFIM is written as

$$\hat{H}[\underline{S}] = -\sum_{\langle i,j \rangle} J_{ij} S_i S_j - \sum_{i=1}^{N} h_i S_i, \tag{II.72}$$

where $\langle i, j \rangle$ denotes the sum over all nearest neighbour pairs.

Alternatively, the RFIM can be described by a Landau-Ginzburg functional which corresponds to a ϕ^4-theory of the form [262, 263]

$$\mathcal{V}(\phi(\boldsymbol{x})) = \int \mathrm{d}^d \boldsymbol{x} \left\{ K(\partial_{\boldsymbol{x}} \phi(\boldsymbol{x}))^2 + \frac{g_2}{2} \phi(\boldsymbol{x})^2 + \frac{g_4}{24} \phi(\boldsymbol{x})^4 - h(\boldsymbol{x}) \phi(\boldsymbol{x}) \right\}, \tag{II.73}$$

where $K > 0$, g_2 and $g_4 > 0$ are multiplicative constants, and where $h(\boldsymbol{x})$ is a random field of zero mean which is delta-correlated in space, namely,

$$\overline{h(\boldsymbol{x})} = 0, \qquad \overline{h(\boldsymbol{x}) h(\boldsymbol{y})} = \Delta \ell^d \delta(\boldsymbol{x} - \boldsymbol{y}), \tag{II.74}$$

with ℓ a microscopic length. The coefficient g_2 vanishes at the mean-field second order phase transition in the pure Ising model (without disorder), it is positive in the paramagnetic phase and it is negative otherwise. The two formulations of Eq. (II.72) and (II.73) describe the same long-range physics and they thus belong to the same universality class. The long-range physics is also independent of the details of the distribution of the random fields, provided there are no long-range correlations among the latter [264]. In practice, a Gaussian distribution is usually considered.

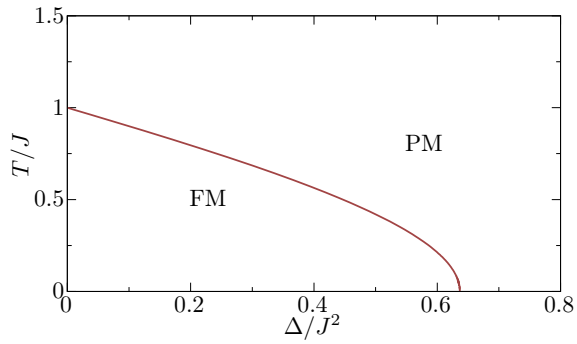

Fig. II.7 | Mean-field phase diagram of the random-field Ising model in the plane $(\Delta/J^2, T/J)$, with J the coupling constant between spins, T the temperature and Δ the variance of the random fields. The phase diagram is obtained for a Gaussian distribution of random fields and it displays a line of second order phase transition between a paramagnetic phase (PM) at high temperatures and disorder and a ferromagnetic phase (FM) at low temperatures and disorder. The transition line converges to zero temperature for a finite critical disorder strength $\Delta_c/J^2 = 2/\pi$. When $\Delta = 0$, one recovers the critical behaviour of the pure Ising model with $T_c(\Delta = 0)/J = 1$.

A.2 Critical behaviour

A.2.1 Mean-field theory

In the mean-field limit, *i.e.*, in the limit of long-range ferromagnetic interactions between spins or of infinite dimensions, the thermodynamics of the random-field Ising model (RFIM) can be computed exactly. This can for instance be done by using replica calculations to deal with the average over the realisations of the random fields [265]. The pure Ising model is described by a single control parameter, namely, the temperature T which is rescaled by the typical ferromagnetic coupling constant J. The RFIM has instead two control parameters, namely, the rescaled temperature T/J and the rescaled variance of the random fields Δ/J^2. A line of second order phase transition $T_c(\Delta)$ in the plane (Δ, T) is then found and separates a paramagnetic phase with a zero magnetisation at high temperatures and high disorder from a ferromagnetic phase with a non-zero magnetisation at low temperatures and low disorder. The phase diagram is shown in Fig. II.7 for the case of a Gaussian distribution of random fields. When $\Delta = 0$, one recovers the critical temperature of the pure Ising model $T_c(0)/J = 1$. When T is fixed below $T_c(0)$, another critical point exists for $\Delta > 0$: the ferromagnetic phase becomes stable for a small amplitude of the disorder when thermal fluctuations are weaker. The line extends down to zero temperature with a critical disorder $\Delta_c/J^2 = 2/\pi$ [266]. This indicates that even at zero temperature, there is a critical point. This also implies that if the disorder strength is such that $\Delta > \Delta_c$, no long-range order is found at any temperature and the system is always in a paramagnetic phase. In consequence, the physics of the RFIM is different from the one of the pure Ising model and it is governed by disorder-induced fluctuations rather than by thermal fluctuations. The existence of a zero-temperature critical point also suggests that the critical behaviour is not ruled by a competition between the entropy and the energy as for usual phase transitions but by a competition between two energies, namely, the Zeeman energy (local alignment with the random field) and the ferromagnetic energy (alignment between spins).

[9] Contrary to spin glasses [*e.g.*, the p-spin model which is defined by the Hamiltonian (II.30)], the ferromagnetic coupling constants J_{ij} are not random in the RFIM.

We have so far discussed the case of a zero external magnetic field. When the latter is added, or equivalently when the random field is no longer of zero mean, the phenomenelogy is similar to the one of the pure Ising model: in the ferromagnetic phase, a thermodynamic first order phase transition is found when the applied magnetic field turns from negative to positive in the thermodynamic limit.

A.2.2 The lower critical dimension

The thermodynamics of the RFIM in finite dimensions d can also be discussed, and the focus is made on the critical behaviour. First of all, the lower critical dimension of the RFIM is $d_{\mathrm{l}} = 2$ [267, 268], unlike the Ising model for which it is equal to 1. This result can be understood qualitatively thanks to the Imry-Ma argument that we review now [91, 249]. As already mentioned, at zero temperature, the transition is ruled by the competition between the Zeeman energy and the ferromagnetic aligment energy. One imagines that the system in d dimensions and in the absence of an external magnetic field is in a ferromagnetic phase of up spins and we want to assess the stability of this state. One now considers a domain of down spins of size L. The interfacial cost to create such a domain is of order JL^{d-1}. Its Zeeman energy is a random quantity of zero mean and of variance ΔL^d. As a result, the domain can gain at most a Zeeman energy which is approximately equal to $\sqrt{\Delta}L^{d/2}$, and its total energy roughly reads $JL^{d-1} - \sqrt{\Delta}L^{d/2}$. For large-enough domains, this energy is negative if $d-1 < d/2$, *i.e.*, if $d < 2$. In this case, the system prefers creating domains in order to gain a Zeeman energy and any long-range order is destroyed.

A.2.3 The zero-temperature fixed point

For dimensions $d > 2$ then, the phase diagram looks like Fig. II.7. The application of renormalisation group techniques [269] proves that the pure critical point at a temperature $T_{\mathrm{c}}(0)$ and at zero random field is unstable, and accordingly the disorder is relevant. Along the line of critical points, the renormalisation flow converges to the zero-temperature fixed point at $\Delta = \Delta_{\mathrm{c}}$ [91, 248]. Therefore, as long as $\Delta > 0$, the critical behaviour is ruled by the zero-temperature fixed point which controls the critical exponents for instance. This confirms the intuition that a competition between two energies controls the physics of the RFIM. However, temperature is a dangerously irrelevant variable and the renormalised temperature converges to the fixed point with a non-trivial critical exponent θ [269]. Because of this new exponent, the system is described by three independent critical exponents [270], for instance by the triplet $(\nu, \eta, \overline{\eta})$. The first one, ν, is the critical exponent which controls the divergence of the correlation length ξ close to the critical point. The two others are the anomalous dimensions which describe the spatial decrease of the connected correlation function,

$$G^{(\mathrm{con})}(\boldsymbol{x}, \boldsymbol{y}) = \overline{\langle \phi(\boldsymbol{x})\phi(\boldsymbol{y})\rangle - \langle \phi(\boldsymbol{x})\rangle\langle \phi(\boldsymbol{y})\rangle} \sim \frac{1}{|\boldsymbol{x}-\boldsymbol{y}|^{d-2+\eta}}, \tag{II.75}$$

and of the disconnected one[10] [270],

$$G^{(\mathrm{dis})}(\boldsymbol{x}, \boldsymbol{y}) = \overline{\langle \phi(\boldsymbol{x})\rangle\langle \phi(\boldsymbol{y})\rangle} - \overline{\langle \phi(\boldsymbol{x})\rangle}\,\overline{\langle \phi(\boldsymbol{y})\rangle} \sim \frac{1}{|\boldsymbol{x}-\boldsymbol{y}|^{d-4+\overline{\eta}}}. \tag{II.76}$$

[10] The integral over space of these correlation functions yields the connected and the disconnected susceptibilities, which are introduced in Sec. 2.2.

In particular, the temperature exponent θ is related to the two anomalous dimensions by the scaling law [270]

$$\overline{\eta} - \eta = 2 - \theta. \tag{II.77}$$

In mean-field theory, $\eta = \overline{\eta} = 0$, and $\theta = 2$.

A.2.4 Dimensional reduction and its breakdown

A main consequence of the existence of a zero-temperature fixed point and of a new temperature exponent is the fact that the hyperscaling relation is no longer satisfied, and instead $2-\alpha = (d-\theta)\nu$ [262, 263, 271], with α the heat capacity exponent. In mean-field theory, $\alpha = 0$, $\nu = 1/2$, and $\theta = 2$. As a consequence, this relation can only be satisfied if $d = d_{\mathrm{u}} = 6$ which is thus the upper critical dimension above which mean-field theory becomes exact to describe the critical behaviour of the RFIM. This upper critical dimension can also be derived from another heuristic argument in the same spirit as the Imry-Ma argument for the lower critical dimension [91, 262].

The critical exponents of the d-dimensional RFIM have been shown to be equal to the ones of the pure Ising model in dimensions $d-2$ by using perturbation theory [272, 273] and also by displaying a hidden supersymmetry [274]. This property is known as dimensional reduction and it is true in particular at the upper critical dimension $d_{\mathrm{u}} = 6$, as the upper critical dimension of the system without disorder is 4. Dimensional reduction then implies that the universality class of the RFIM is merely described by two critical exponents instead of three, and the new scaling law $\eta = \overline{\eta}$ holds [263]. However, dimensional reduction is clearly wrong at the lower critical dimension of the RFIM which is $d_{\mathrm{l}} = 2$ and not $1 + 2 = 3$. In addition, just above the lower critical dimension, the relation $\overline{\eta} = 2\eta$ was proved by using perturbation theory [269], contrary to the dimensional reduction prediction. An exact functional renormalisation group analysis solved this paradox and demonstrated that dimensional reduction breaks down in dimensions $d < d_{\mathrm{DR}} = 5.1$ for the RFIM [275, 276]. Below this dimension, the RFIM and the pure Ising model universality classes are not related, as confirmed by large-scale computer simulations [277].

A.2.5 The number of independent critical exponents

The number of independent critical exponents in the RFIM has been a matter of debate for many years, as several studies have suggested that the relation

$$\overline{\eta} = 2\eta \tag{II.78}$$

should hold in any dimension [278]. Once again, the functional renormalisation group theory brought a clear answer and showed shown that the above relation does not generally hold [263], and that it is actually an inequality which was first derived by Schwartz and Soffer [279], namely, $\overline{\eta} \leq 2\eta$. However, in the range $d_{\mathrm{l}} < d < d_{\mathrm{DR}}$, the deviation from Eq. (II.78) is always quite small, as direct measures of the critical exponents suggest [264, 277, 280]. A consequence of Eq. (II.78) is that when approaching the critical point, the disconnected susceptibility scales as the square of the connected one [270], namely,

$$\chi^{(\mathrm{dis})} = \frac{\Delta}{T_{\mathrm{c}}(\Delta)} {\chi^{(\mathrm{con})}}^2. \tag{II.79}$$

The prefactor in Eq. (II.79) represents the ratio of the variance of the random fields Δ to the critical temperature for the same value of Δ. When $\overline{\eta} \simeq 2\eta$, as it is found in $d = 3$, Eq. (II.79)

represents a very good approximation.

A.2.6 The activated critical dynamics

We finally discuss the dynamics of the RFIM close to its critical point, which is expected to suffer from a critical slowing down. The fluctuations of the order parameter and the associated relaxation mechanisms become collective on the scale of the correlation length ξ which diverges when approaching the critical point. In standard critical phenomena, for instance in the universality class of the pure Ising model, the critical dynamics is described by a dynamic exponent z such that the relaxation time τ scales as $\tau \sim \xi^z$. Therefore, in conventional critical phenomena, τ diverges with a power law at the approach of the critical point [281].

The critical dynamics in the RFIM is different and this is also related to the fact that the critical behaviour of the system is described by a zero-temperature fixed point. The droplet scenario [262, 271] assumes that the system displays a distribution of energy barriers of typical height which grows as ξ^ψ because of the quenched disorder, with ψ another critical exponent. Relaxation then occurs because of thermal activation over these barriers, and this leads to the activated dynamic scaling

$$\ln \tau \sim \xi^\psi. \tag{II.80}$$

Besides, the simplest assumption is that ψ should be equal to θ. In consequence, the critical slowing down in the RFIM is far more dramatic than the conventional dynamic scaling, as the logarithm of the relaxation time instead behaves as a power law of the correlation length. Formally, the RFIM is characterised by a dynamic exponent $z = +\infty$ for $d < d_\mathrm{u}$, while above the upper critical dimension, one should recover the mean-field prediction $z = 2$ [115, 281].

The activated dynamic scaling of Eq. (II.80) and the crossover between non-activated dynamics ($d > d_\mathrm{u}$) and activated dynamics ($d < d_\mathrm{u}$) can be understood by using functional renormalisation group techniques [282]. When dimensional reduction breaks down ($d < d_\mathrm{DR}$), then the relation $\psi = \theta$ is found, in agreement with the droplet scenario. When $d_\mathrm{DR} < d < d_\mathrm{u}$, then the dynamics is still activated contrary to what is expected from dimensional reduction. Therefore, dimensional reduction only applies to static properties. In this regime, ψ decreases with d and it eventually vanishes at $d = d_\mathrm{u}$.

III Phase diagram of finite-dimensional constrained supercooled liquids from computer simulations

We study the thermodynamics of a model supercooled liquid in dimensions $d = 2, 3$ at a temperature T whose overlap with a reference configuration is biased thanks to an external source ϵ. Based on our discussion of Chap. II and in particular building on the analytical calculations of the spherical p-spin model, we consider reference configurations which are sampled at very low temperatures T_0 in order to move all the putative relevant thermodynamic features that are associated with the overlap fluctuations to higher temperatures. These configurations are easily generated by using the swap algorithm. Results for the case $T = T_0$ are instead presented in the Appendix. To explore the phase diagram and to compute the thermodynamic properties of constrained supercooled liquids accurately, we use importance sampling techniques, namely, umbrella sampling and histogram reweighting. We find that the models in both $d = 2$ and $d = 3$ display the mean-field phenomenology in "reasonably small" systems. In particular, the Franz-Parisi potential, which represents the free energy cost for keeping a certain overlap with a reference configuration in the bulk liquid, shows a non-convex behaviour while the isotherms of the overlap with respect to ϵ plateau and the overlap distributions become bimodal at low temperatures, consistently with a first order transition which ends in a critical point. However, in low dimensions, *e.g.*, $d = 2, 3$, strong finite-size effects are expected close to a first order transition or a critical point. In order to assess the fate of the mean-field results in finite dimensions, we perform an extensive finite-size analysis and we study the size evolution of the overlap probability distribution and of the susceptibilities. In agreement with recent field theoretical calculations beyond mean-field theory, we demonstrate the existence of a first order transition line for finite ϵ which ends in a critical point in the universality class of the random-field Ising model (RFIM) in $3d$. Instead, the $2d$ system does not present any sign of singular behaviour in the thermodynamic limit, consistently with the RFIM universality class whose lower critical dimension is equal to 2. The RFIM criticality is confirmed by studying the dynamics of the constrained liquid in $3d$ in the vicinity of its critical point, which is found to be compatible with an activated dynamic scaling. Overall, our results prove that the mean-field results and their extensions to finite dimensions by using statistical field theory are robust in finite dimensions and they emphasise the important role of the disorder in some aspects of the physics of supercooled liquids and glasses, as illustrated by the analogy with the physics of the RFIM.

Outline

1 Introduction . . . 67

2 Model and methods . . . 68

2.1 Numerical strategy . . . 68

2.2 Model . . . 70

2.3 Umbrella sampling . . . 71

2.4 Multi-histogram reweighting . . . 74

2.5 Gaussian ensemble reweighting . . . 76
2.6 Temperature reweighting . . . 79
3 Mean-field-like behaviour in finite systems . . . 80
3.1 Temperature evolution of the Franz-Parisi potential . . . 80
3.2 Thermodynamic properties in the presence of a source ϵ . . . 81
4 Contrasting results in two and three dimensions through a finite-size scaling analysis . . . 83
4.1 System-size dependence of the overlap probability distribution . . . 83
4.2 Finite-size scaling analysis in three dimensions indicates a first order transition in the thermodynamic limit . . . 85
4.3 Finite-size scaling analysis in two dimensions shows no sign of phase transition in the thermodynamic limit . . . 88
5 Characterisation of the critical point in the three-dimensional system . . . 89
5.1 Confirming random-field Ising model criticality via a finite-size scaling analysis . . . 89
5.2 Activated dynamics in the vicinity of the critical point . . . 90
6 Conclusions . . . 93
Appendix
A Simulation results for the case of equal temperatures $T = T_0$ . . . 95

Part of this work has already been published in Ref. [283] and results of this chapter will also be the object of another publication.

1. Introduction

In Chap. II, we have reviewed the Franz-Parisi (FP) setting in the study of glass-forming liquids. It consists in linearly biasing the overlap between a liquid configuration at a temperature T and a quenched reference configuration of the same liquid which has been sampled at a temperature T_0 thanks to an external source ϵ, see Eq. (II.3). Studying the thermodynamics of the constrained liquid reveals the non-trivial changes in the underlying free energy landscape at the mean-field level and it gives access to some properties of the metastable states (free energy minima). In the plane (ϵ, T), a line of first order transition between a low-overlap phase and a high-overlap phase is found, which ends in a critical point at (ϵ_c, T_c) [153–155].

In Chap. II, we have also explained the first steps towards a field theory of the overlap beyond mean-field in finite dimensions d which relies on a replicated Landau-Ginzburg functional of the overlap profiles. We have detailed its main predictions, namely, that the critical point at (ϵ_c, T_c) belongs to the universality class of the random-field Ising model (RFIM) and that the line of first order transition below it corresponds to a transition in the presence of a random field [218, 250]. This is a strong statement as it forbids the existence of any singular behaviour in the thermodynamics of constrained liquids in $d = 2$ [249, 267, 272, 273] or in $d = 3$ if the disorder becomes too large [91, 265].

Even though statistical field theory makes predictions about the properties of the phase diagram of constrained supercooled liquids ($\epsilon > 0$) it does not provide information about the

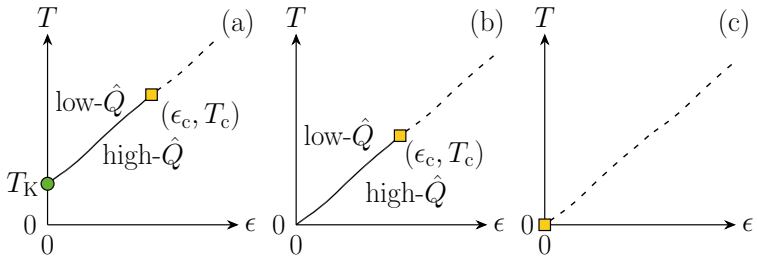

Fig. III.1 | Sketch of the different phase diagrams which can be expected for the thermodynamics of constrained liquids in finite dimensions. The control parameters are the temperature T and the field ϵ which biases the overlap $\hat{Q}$ between the configuration of the liquid and a reference configuration of the same liquid which has been sampled at a temperature T_0. The diagrams are pictured here for the case $T_0 = T$. Panels (a) and (b) represent mean-field-like scenarios for thermal systems, and which depend on the existence [panel (a)] or the absence [panel (b)] of an entropy crisis at a temperature $T_K \geq 0$. Both diagrams display a line of first order transition (full line) between phases of low overlap and high overlap which ends in a critical point (ϵ_c, T_c). Above the critical point, the Widom line (dashed line) represents the loci of the (finite) maximum of the overlap fluctuations. (c) Another phase diagram may also be found with a mere Widom line down to zero temperature, for instance in $d = 2$ or in $d = 3$ if the disorder is too strong.

actual existence of the phase transition or of the critical point in realistic glass-forming liquids. Actually, several different phase diagrams may be envisioned for the thermodynamics of constrained supercooled liquids in finite dimensions, see Fig. III.1. This is because statistical field theory has so far dealt with simplified Landau-Ginzburg functionals. Computer simulations then represent a complementary tool to study the thermodynamics of constrained supercooled liquids. They allow one to measure the actual Landau-Ginzburg functional of the overlap field in realistic glass-formers. The measured functional could later be used as an input of statistical field theory for instance in order to compute the parameters of an effective RFIM description. In this chapter, we use computer simulations to directly assess the existence of the critical point and of the associated first order transition line and to check the theoretical predictions from statistical field theory. We consider the cases $d = 2$ and $d = 3$, and in the next section, we present our numerical strategy.

2. Model and methods

2.1 Numerical strategy

The constrained thermodynamics of supercooled liquids depends on the triplet (ϵ, T, T_0). In the previous chapter, we have computed the mean-field phase diagram (ϵ, T) of the paradigmatic spherical p-spin model for the case $T = T_0$ but also for a fixed temperature of the reference configuration T_0 whatever the temperature T [153, 156]. We have shown that considering the case of a fixed T_0 in between the dynamical transition temperature at which the metastable states first appear and the Kauzmann transition temperature T_K at which the configurational entropy vanishes moves the critical point and the first order transition line to higher temperatures. This also changes the shape of the first order transition line which does no longer converge to the random first order transition point at $(\epsilon, T) = (0, T_K)$ but which instead extends down to zero temperature [222]. We have subsequently rationalised this trend which is thus expected to hold in mean-field glass-forming liquids. We have also reviewed published numerical works which

suggest that it should also hold in finite-dimensional liquids [209] and plaquette models [260].

In addition, past numerical works which have focused on the case $T = T_0$ have been mostly limited to the "Widom line", *i.e.*, the region of the phase diagram above the putative critical point. This is because in the various systems which have been considered, this critical point is likely to be close to or below the mode-coupling crossover[1] $T_{\mathrm{mct}} \simeq T_{\mathrm{d}}$ below which the equilibration of the unconstrained liquid exceeds a reasonable simulation walltime (of about one week) [209, 213, 256], see Appendix A [283]. Pushing the interesting thermodynamic features to higher temperatures would then be beneficial by considering stable equilibrium configurations at a low temperature T_0. This would ease sampling of the phase space of the constrained liquid because of a smaller bulk relaxation time. We have however seen in Chap. III that this might come with a less-pronounced RFIM-like behaviour.

In 2017, the swap algorithm was developed and optimised for a family of models with continous size-polydispersity [54]. The swap algorithm combines standard translational moves with swap Monte Carlo moves which consist in exchanging the positions (or equivalently the sizes) of two randomly-chosen particles while respecting detailed balance. This algorithm corresponds to a non-physical dynamics but it results in an incredibly large equilibration speedup [284] (as quantified by the ratio of the relaxation time of the swap dynamics to the one of the physical dynamics), of about 10^3 at the mode-coupling crossover and up to 10^8 or even 10^{11} at the extrapolated (experimental) glass transition temperature[2] T_{g} in $d = 3$ and $d = 2$ respectively [54, 182]. Consequently, we take advantage of the swap algorithm in order to prepare very stable configurations in equilibrium at a temperature $T_0 \lesssim T_{\mathrm{g}}$, see Tab. III.1. We have also obtained results for the case $T = T_0$ and they are discussed in Appendix A.

To study the thermodynamics of the constrained liquid at a temperature T which is coupled to a reference configuration at a temperature T_0, the easiest thing to do is to directly simulate the system with the Hamiltonian (II.3). However, we need to implement more advanced simulation techniques because of several sampling issues. First, at high temperatures close to the putative critical point, the dynamics (even with the swap algorithm) is expected to slow down significantly [283], see also Sec. 5.2. This critical slowing down is due to diverging thermodynamic fluctuations of the order parameter. In RFIM-like systems, the critical slowing down is far more spectacular than in pure systems as the relaxation time scales exponentially with the correlation length (instead of algebraically) [262, 271], see also Appendix A of Chap. II. In addition, near the anticipated first order transition line, a correct sampling may be hindered due to large nucleation barriers between the metastable phase and the stable one. The system may remain trapped for a long time and it may then only sample one of the two phases.

In the next sections, we give more details about the model that we consider and the way computer simulations are performed. We also explain how the thermodynamics of the constrained liquid is computed without directly simulating the latter but instead via an umbrella sampling and a subsequent reweighting.

[1] See Chap. VI for its measurement.

[2] We define the extrapolated glass transition temperature as the temperature at which the extrapolated relaxation time increases by twelve orders of magnitude from its value at the onset temperature of glassy behaviour. The onset temperature is instead defined as the highest temperature at which the relaxation time departs from its high-temperature Arrhenius behaviour [285–287]. More details can be found in Chap. VI.

	$\mathrm{d}t$	τ_{th}	n_{MD}	n_{swap}	a	κ	T_0	T_{mct}	T_{g}
$2d$	0.005	0.5	50	10	0.22	0.3	0.03	0.115	0.068
$3d$	0.01	0.5	25	1	0.22	20	0.06	0.095	0.056

Tab. III.1 | Parameters which are used to run the simulations: time step $\mathrm{d}t$ for the integration of the equations of motion, damping time of the thermostat τ_{th}, number of molecular dynamics steps n_{MD} between sequences of swap moves, number of swap moves per particle n_{swap}, tolerance length a in the definition of the overlap, curvature κ of the umbrella potential, temperature T_0 of the reference configuration when it is fixed. We also report the mode-coupling crossover temperature T_{mct} and the extrapolated glass transition temperature T_{g} for comparison.

2.2 Model

We study a system of N spherical particles of equal mass m in spatial dimensions $d = 2, 3$ with radial pairwise interactions, as first introduced in Ref. [54]. The diameters $\{\sigma_i\}_{i=1\cdots N}$ of the particles are drawn from the distribution $p(\sigma_i) \propto \sigma_i^{-3}$ for $\sigma_i \in [\sigma_{\min}, \sigma_{\max}]$ with $\sigma_{\max}/\sigma_{\min} \simeq 2.217$. Two particles i and j interact with the repulsive potential

$$v(r_{ij}) = v_0 \left(\frac{\sigma_{ij}}{r_{ij}}\right)^{12} + c_0 + c_2 \left(\frac{r_{ij}}{\sigma_{ij}}\right)^{2} + c_4 \left(\frac{r_{ij}}{\sigma_{ij}}\right)^{4}, \tag{III.1}$$

if their relative distance $r_{ij} = |\boldsymbol{r}_i - \boldsymbol{r}_j|$ satisfies $r_{ij}/\sigma_{ij} < x_{\mathrm{c}} = 1.25$, where their interaction cross-diameter σ_{ij} is given by the non-additive rule ($\mu > 0$)

$$\sigma_{ij} = \frac{\sigma_i + \sigma_j}{2}(1 - \mu|\sigma_i - \sigma_j|). \tag{III.2}$$

The constants c_0, c_2 and c_4 are set in order to make the potential and its two first derivatives continuous at the cutoff distance: $c_0 = -28v_0/x_{\mathrm{c}}^{12}, c_2 = 48v_0/x_{\mathrm{c}}^{14}, c_4 = -21v_0/x_{\mathrm{c}}^{16}$. The distribution of the diameters and the non-additive rule for the cross-diameters reduce the tendency of the system for crystallisation or demixing. The average diameter σ of the particles is used as unit length ($\mu = 0.2$ in this unit), the interaction strength v_0 is used as unit temperature (the Boltzmann constant k_{B} is set to unity), and $\sqrt{m\sigma^2/v_0}$ is used as unit time. The system is simulated in a cubic box of linear size L with periodic boundary conditions [64]. The number density $\rho = N/L^d$ is chosen equal to 1.

The unconstrained system is simulated by using a hybrid scheme which combines molecular dynamics (MD) in the conventional canonical ensemble and the recently developed swap Monte Carlo algorithm in order to speed up equilibration and phase space exploration [55]. The scheme consists in the succession of blocks of MD steps and blocks during which swap moves are performed. The MD is run by implementing the Hoover equations [288] of the Nosé thermostat [289–291] with a time step $\mathrm{d}t$ (see Tab. III.1) and a thermostat damping time τ_{th} (see Tab. III.1). Both have been chosen to maximise the algorithm efficiency along with a proper sampling of the canonical ensemble. The equations of motion are solved by using a reversible integrator which is based on a Liouville formulation of the equations [292, 293]. The MD is run for n_{MD} steps (see Tab. III.1). Then, the positions and the velocities of the particles are frozen and $N_{\mathrm{swap}} = n_{\mathrm{swap}}N$ swap moves are attempted (see Tab. III.1). For an elementary swap move, two particles i and j are randomly selected and their diameters are exchanged. The change in the total potential energy $\Delta\hat{H}_{\mathrm{swap}} = \hat{H}_{\mathrm{swap}} - \hat{H}$ is then computed (the kinetic energy remains

constant), with

$$\hat{H}[\boldsymbol{r}^N] = \frac{1}{2}\sum_{i<j} v(|\boldsymbol{r}_i - \boldsymbol{r}_j|), \tag{III.3}$$

and $\hat{H}_{\text{swap}}$ the total potential energy when particle diameters are swapped. The move is eventually accepted by following the Metropolis rule, namely, with probability equal to $\min(1, e^{-\beta\Delta\hat{H}_{\text{swap}}})$ ($\beta = 1/T$), in order to respect detailed balance [64, 294]. This combination of thermostated MD and Monte Carlo swap moves ensures a proper sampling in the canonical ensemble. The parameters n_{MD} and n_{swap} have been fixed in order to maximise the algorithm efficiency while ensuring a proper sampling in the canonical ensemble.

To compute the overlap between the configuration $\boldsymbol{r}^N$ and a reference configuration $\boldsymbol{r}_0^N$, *i.e.*,

$$\hat{Q}[\boldsymbol{r}^N; \boldsymbol{r}_0^N] = \frac{1}{N}\sum_{i,j=1}^{N} w(|\boldsymbol{r}_i - \boldsymbol{r}_{0,j}|/a), \tag{III.4}$$

we use the continuous window function $w(x) = e^{-x^4 \ln 2}$ and the tolerance length a which is reported in Tab. III.1. The prefactor $\ln 2$ is just conventional and it is chosen so that the window function equals $1/2$ for $x = 1$. Different window functions could be considered, for instance $w(x) = \theta(1 - x)$ with $\theta(x)$ the Heaviside step function [114, 154, 155, 181, 209, 213, 241], a Gaussian [179, 180], or a power law decaying function such as $w(x) = (1 + x^{12})^{-1}$ [156]. As we are performing MD simulations, we require a window function which is differentiable in order to compute forces and this forbids the much used Heaviside function. We have therefore considered a smooth version of the Heaviside function but we have checked that our results are qualitatively similar when considering different window functions. For our choice of $w(x)$, the "random" overlap between two uncorrelated configurations is $Q_{\text{rand}} = \rho S_d a^d \Gamma(d/4)/[4(\ln 2)^{d/4}]$, with S_d the area of the unit sphere in d dimensions, and $\Gamma(x)$ the Euler Gamma function.

The tolerance length a also needs to be fixed. Its influence on the results which are presented here is extensively studied in Chap. IV [295], where we use a mean-field-like model, namely, the liquid-state theory in the hypernetted chain approximation (see Ref. [296–298] and Ref. [154, 155, 299–302] for its application in the Franz-Parisi setting), and computer simulations. We briefly recap our findings here. The qualitative behaviour of the constrained liquid is insensitive to the choice of a, even though the shape of the phase diagram (ϵ, T) is quantitatively changed when varying a. In particular, the critical point is expected to be at a larger temperature when the value of a decreases. Here, we have chosen a relatively small value of a, namely, $a = 0.22$.

In the next sections, we explain how to compute the thermodynamics of the model glass-former we have introduced when the latter is coupled to a reference configuration by means of simulations at $\epsilon = 0$ only. It relies on a two-step "divide and conquer" strategy. The description of the first step, namely, umbrella sampling, is the object of the next section.

2.3 Umbrella sampling

In Eq. (II.13), the probability distribution $\mathcal{P}_\epsilon(Q; \boldsymbol{r}_0^N)$ of the overlap in the constrained liquid has been defined for a fixed reference configuration $\boldsymbol{r}_0^N$ and it is related to the probability distribution of the overlap in the unconstrained liquid for the same reference configuration $\mathcal{P}(Q; \boldsymbol{r}_0^N)$, *i.e.*,

$$\mathcal{P}_\epsilon(Q; \boldsymbol{r}_0^N) \propto \mathcal{P}(Q; \boldsymbol{r}_0^N) e^{N\beta\epsilon Q}. \tag{III.5}$$

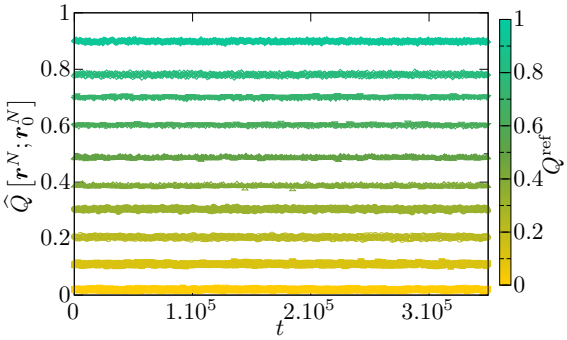

Fig. III.2 | Overlap time series for several biases $Q^{\rm ref}$ for the $3d$ system with $N = 1200$, $T = 0.22$ and the other parameters which are given in Tab. III.1. From bottom to top, $Q^{\rm ref} = 0$, 0.12, 0.22, 0.32, 0.40, 0.50, 0.62, 0.72, 0.80, 0.94.

This comes from the fact that the Hamiltonian of the constrained liquid $\hat{H}_\epsilon[\boldsymbol{r}^N;\boldsymbol{r}_0^N]$ is simply related to the Hamiltonian of the unconstrained liquid $\hat{H}[\boldsymbol{r}^N]$ by

$$H_\epsilon[\boldsymbol{r}^N;\boldsymbol{r}_0^N] = \hat{H}[\boldsymbol{r}^N] - N\epsilon\hat{Q}[\boldsymbol{r}^N;\boldsymbol{r}_0^N]. \tag{III.6}$$

As a result, in principle, the thermodynamics of the constrained liquid for any field ϵ can be obtained from simulations of the unconstrained liquid only, *i.e.*, with $\epsilon = 0$. However, positive values of ϵ make more probable high-overlap values which are very unlikely in the bulk liquid with $\epsilon = 0$, see Fig. II.3 (a). More precisely, Eq. (III.5) indicates that high-overlap values are exponentially more probable in N when ϵ gets larger. Therefore, in order to accurately compute $\mathcal{P}_\epsilon(Q;\boldsymbol{r}_0^N)$ from the unconstrained distribution, fluctuations of the overlap with an exponentially-small weight in N must be measured. In a conventional simulation, the system typically explores a narrow range of overlap values around its random value $Q_{\rm rand}$, which corresponds to the overlap for two uncorrelated configurations and which is the absolute minimum of the Franz-Parisi potential. Consequently, the correct measure of $\mathcal{P}(Q;\boldsymbol{r}_0^N)$ on the entire range $[0,1]$ requires a more sophisticated algorithm in order to sample rare events.

We use umbrella sampling [303–305] to force the liquid towards larger and untypical values of the overlap, and we sample phase space with the biased Hamiltonian

$$\hat{H}_{\rm b}[\boldsymbol{r}^N;\boldsymbol{r}_0^N] = \hat{H}[\boldsymbol{r}^N] + W(\hat{Q}[\boldsymbol{r}^N;\boldsymbol{r}_0^N]) = \hat{H}[\boldsymbol{r}^N] + \frac{1}{2}N\kappa(\hat{Q}[\boldsymbol{r}^N;\boldsymbol{r}_0^N] - Q^{\rm ref})^2, \tag{III.7}$$

which is obtained by adding a harmonic bias $W(Q)$ of center $Q^{\rm ref}$ and curvature κ to the Hamiltonian of the unconstrained liquid. The factor of N ensures that the Hamiltonian remains an extensive quantity. By increasing $Q^{\rm ref}$, we can explore different regions of the phase space, which are characterised by larger overlap values, while the strength of the bias κ mostly controls the amplitude of the fluctuations of $\hat{Q}$. Umbrella sampling controls the amplitude of the overlap fluctuations and it makes them small-enough to be sampled more accurately.

For a given reference configuration $\boldsymbol{r}_0^N$ and a temperature T, we run $n_{\rm s} \in [23, 35]$ simulations in parallel with umbrella potentials $\{W_k\}_{k=1\ldots n_{\rm s}}$ of identical curvature κ and of centers $\{Q_k^{\rm ref}\}_{k=1\ldots n_{\rm s}}$ in order to sample the entire range of overlap values between 0 and 1, see Fig. III.2. In $2d$, we consider systems of moderate size (typically, up to $N = 250$) and simulations are thus very slow when a large bias strength κ is imposed [306]. In consequence, in the $2d$ system, we use a smaller value of the bias strength κ (see Tab. III.1) which results in a significant

overlap between adjacent biased distributions of the order parameter (see Sec. 2.4). In $3d$ instead, we consider unprecedently large system sizes (typically, up to $N = 2400$) for such a type of simulations to investigate the thermodynamic limit because strong finite-size effects are expected close to a critical point or a first order transition [307, 308]. In order for our reweighting scheme to scale adequately with N, we use a large bias strength κ (see Tab. III.1) to narrow the fluctuations (see Sec. 2.5).

For each biased simulation, the system is first equilibrated for $-t_{\text{relax}} < t < 0$. Equilibration is ensured by checking that the simulations which are started from two distinct initial conditions converge towards the same stationary state [180, 309]. Then, the statistical properties of the overlap are measured for $0 < t < t_{\text{eq}}$. In $3d$, we monitor the mean-squared displacement

$$\hat{\Delta}(t) = \frac{1}{N} \sum_{i=1}^{N} |\boldsymbol{r}_i(t) - \boldsymbol{r}_i(0)|^2, \tag{III.8}$$

and we check that at the end of the sampling, it exceeds a target value of 10 [54]. In $2d$, due to the strong Mermin-Wagner fluctuations[3] which induce large collective translational displacements [312, 313], we instead follow the time evolution of the bond-orientational correlation function and we require that it has decreased to 0. The latter is defined as

$$C_{\psi_6}(t) = \frac{1}{N} \sum_{j=1}^{N} \psi_6^{(j)}(t) \left[\psi_6^{(j)}(0)\right]^*, \tag{III.9}$$

where the star denotes the complex conjugate. Its computation requires the definition of the single-particle quantity

$$\psi_6^{(j)}(t) = \frac{1}{n_j(t)} \sum_{l=1}^{n_j(t)} e^{i6\theta_{jl}(t)}, \tag{III.10}$$

where $n_j(t)$ is the number of neighbours of particle j at time t, which are the particles l which fulfill the condition $|\boldsymbol{r}_j(t) - \boldsymbol{r}_l(t)|/\sigma_{jl} < 1.33$, and where $\theta_{jl}(t)$ is the angle between the x-axis and the line joining the centers of the two neighbours j and l [182]. Because this correlation is rotationally-invariant, the choice of the x-axis is made without any loss of generality. These criteria in $2d$ and $3d$ guarantee that the particles have sufficiently moved and that the system explores the phase space ergodically.

We emphasise that thanks to the small temperature T_0 of the reference configurations and the swap algorithm, the thermalisation is achieved for each umbrella simulation without parallel tempering [314]. The latter corresponds to rarely exchanging the configurations of two adjacent umbrella simulations while respecting detailed balance to ease exploration of the phase space. However, its implementation requires that the probability distributions of the order parameter from two adjacent umbrella simulations (adjacent values of Q^{ref}) significantly overlap.

[3] As the overlap $\hat{Q}$ is defined from the positions of the particles, it may also suffer from the large and spurious displacements which are associated with the Mermin-Wagner fluctuations. This would result in the impossibility for the $2d$ system to be localised. All order parameters of mean-field theory (for instance the mean-squared displacement [126]) have the same issue. These large displacements are known to increase with the temperature and (logarithmically) with the system size [310]. For the system sizes and the temperatures which are considered here, these Mermin-Wagner fluctuations are expected to be irrelevant. For instance, the translational (self-intermediate scattering function, see Chap. VI) and orientational (C_{ψ_6}, see later) correlation functions are very similar and the relaxation times which are extracted from the two functions closely follow each other when varying the temperature [311].

Here, instead, we can choose a large curvatuve κ which results in non-overlapping probability distributions of the order parameter, see Fig. III.2.

Thanks to the umbrella sampling, we have turned from one complicated problem to $n_{\rm s}$ simpler tasks as we have shrunk the amplitude of the overlap fluctuations in each umbrella window. We have thus "divided" the problem. We now need to use the statistics from the different simulations to "conquer" and to reconstruct the unconstrained probability distribution $\mathcal{P}(Q;\boldsymbol{r}_0^N)$. This is the object of the next two sections which present histogram reweighting procedures.

2.4 Multi-histogram reweighting

In $2d$, we implement a method which was used in Ref. [181, 209, 213, 241] to compute $\mathcal{P}(Q;\boldsymbol{r}_0^N)$ from the $n_{\rm s}$ different biased simulations and which requires that the biased distributions of the order parameter from consecutive umbrella simulations overlap significantly. It relies on the multiple histogram method, which was first developed with the aim of extrapolating the thermodynamic properties of the Ising model at temperatures at which the system was not directly simulated [294, 315, 316]. This method has since been extended to arbitrary collective variables (such as the overlap) and several potential biases and it is known as the Weighted Histogram Analysis Method (WHAM) [317, 318].

For the $k^{\rm th}$ biased simulation at a temperature T with a reference configuration $\boldsymbol{r}_0^N$, the empirical histogram of the overlap is

$$\frac{\mathcal{N}_k(Q)}{n_k} = \frac{1}{\mathcal{Z}_k}\mathcal{P}(Q;\boldsymbol{r}_0^N)e^{-\beta W_k(Q)}, \tag{III.11}$$

with n_k the total number of times the overlap was stored during the $k^{\rm th}$ biased simulation and $\mathcal{Z}_k$ a normalisation constant. As a consequence, from one biased histogram, it is in principle possible to determine the unconstrained probability distribution $\mathcal{P}(Q;\boldsymbol{r}_0^N)$ of the overlap by inverting the above equation. However, during a simulation of finite duration $t_{\rm eq}$, only a restricted range of overlap values is sampled and in practice, we can only use the above equation to determine $\mathcal{P}(Q;\boldsymbol{r}_0^N)$ in the range in which the histogram has non-zero values. But, as clearly visible from Fig. III.2, this range changes from one simulation to the other, and by combining the different estimates of $\mathcal{P}(Q;\boldsymbol{r}_0^N)$ from each umbrella simulation, we can reconstruct the unconstrained overlap probability distribution on the entire range $[0,1]$.

The reconstruction from Eq. (III.11) requires to know the partition functions $\mathcal{Z}_k$ which are a priori unknown. One possibility would be to first measure the unconstrained probability distribution by a direct simulation of the liquid (without umbrella potential). Then one has to tune by hand the partition functions, by starting from the histograms $\mathcal{N}_k(Q)$ which overlap with $\mathcal{P}(Q;\boldsymbol{r}_0^N)$, in order to obtain a collapse of the different fragments of the distribution [319, 320] (see Chap. VII). This method which is quite simple in spirit is hardly automated. As the reweighting has to be repeated for each reference configuration, we prefer a systematic method to compute $\mathcal{P}(Q;\boldsymbol{r}_0^N)$ and to determine the partition functions self-consistently.

As a reconstruction of the unconstrained overlap probability distribution from all the biased distributions seems possible, we seek $\mathcal{P}(Q;\boldsymbol{r}_0^N)$ as a linear combination of its estimate from each separate biased histogram, namely,

$$\mathcal{P}(Q;\boldsymbol{r}_0^N) = \sum_{k=1}^{n_{\rm s}} y_k n_k^{-1}\mathcal{Z}_k\mathcal{N}_k(Q)e^{\beta W_k(Q)}, \tag{III.12}$$

where $\{y_k\}_{k=1\ldots n_\mathrm{s}}$ are unknown coefficients which verify the condition $\sum_k y_k = 1$. To determine the coefficients y_k, we require that the statistical error on the above estimate is minimum. As the different histograms are measured independently, the squared statistical error on $\mathcal{P}(Q;\boldsymbol{r}_0^N)$ can be expressed as a function of the squared statistical errors on the biased histograms, and it reads

$$\delta\mathcal{P}(Q;\boldsymbol{r}_0^N)^2 = \sum_{k=1}^{n_\mathrm{s}} y_k^2 n_k^{-2} \mathcal{Z}_k^2 \delta\mathcal{N}_k(Q)^2 e^{2\beta W_k(Q)}. \tag{III.13}$$

To estimate the statistical error on the biased histogram $\mathcal{N}_k(Q)$, we make a *gedankenexperiment*. We assume that we have performed n_h times the same simulation with the same bin center Q_k^ref during which we have measured n_k times the value of the overlap. For instance, this would correspond to simulations with different initial conditions or different sequences of random numbers for swap moves. Then, for each bin, the statistical error is given by the variance over the n_h histograms. If we denote by brackets $[\cdot]$ the average over the n_h simulations, the statistical error on the biased histogram is given by [321]

$$\delta\mathcal{N}_k(Q)^2 = g_k\left[\mathcal{N}_k(Q)\right]\left\{1 - \frac{[\mathcal{N}_k(Q)]}{n_k}\right\}, \tag{III.14}$$

with g_k the statistical inefficiency. The latter is given by $g_k = 1 + 2\tau_k/\Delta t_k$ with τ_k the autocorrelation time of the overlap for the kth simulation and Δt_k the constant time interval between two measures of the overlap. If the bin width is small-enough, or if the overlap range which is covered during the kth simulation is sufficiently large, then $[\mathcal{N}_k(Q)] \ll n_k$ and we obtain for the statistical error on the unconstrained probability distribution of the overlap

$$\delta\mathcal{P}(Q;\boldsymbol{r}_0^N)^2 = \mathcal{P}(Q;\boldsymbol{r}_0^N)\sum_{k=1}^{n_\mathrm{s}} y_k^2 n_k^{-1} g_k \mathcal{Z}_k e^{N\beta W_k(Q)}. \tag{III.15}$$

To minimise the above expression with respect to the y_k's with the constraint that their sum equals 1, we minimise the Lagrangian $\mathcal{L} = \delta\mathcal{P}(Q;\boldsymbol{r}_0^N)^2 - \nu\sum_k y_k$, with ν a Lagrange multiplier. By using that $\sum_k y_k = 1$ to determine the Lagrange multiplier, we finally obtain

$$\mathcal{P}(Q;\boldsymbol{r}_0^N) = \frac{\displaystyle\sum_{k=1}^{n_\mathrm{s}} g_k^{-1}\mathcal{N}_k(Q)}{\displaystyle\sum_{k=1}^{n_\mathrm{s}} n_k g_k^{-1}\mathcal{Z}_k^{-1} e^{-\beta W_k(Q)}}. \tag{III.16}$$

We have thus derived an equation to compute the unconstrained probability distribution from the biased histograms and which can be easily automated. Nevertheless, this estimate of $\mathcal{P}(Q;\boldsymbol{r}_0^N)$ still requires the partition functions $\mathcal{Z}_k$. In fact, they can be computed self-consistently by using Eq. (III.11), by summing over all bins and by inserting the above equation, *i.e.*,

$$\mathcal{Z}_k = \int_0^1 \mathrm{d}Q \frac{\displaystyle\sum_{k'=1}^{n_\mathrm{s}} g_{k'}^{-1}\mathcal{N}_{k'}(Q)}{\displaystyle\sum_{k'=1}^{n_\mathrm{s}} n_{k'} g_{k'}^{-1}\mathcal{Z}_{k'}^{-1} e^{-\beta[W_{k'}(Q)-W_k(Q)]}}. \tag{III.17}$$

We have checked that the statistical inefficiencies are not varying much among the different biased simulations (we choose $\Delta t_k = \mathrm{d}t$), and we can simplify the above equations by setting $g_k = 1$ for all k.

Eq. (III.17) are solved self-consistently by starting from $\mathcal{Z}_k = 1$ for all k. The iteration is stopped when the relative change in the partition functions between two iterations is less than 10^{-10}. To avoid overflows or underflows, the partition functions are rescaled at each iteration by the geometric average of the minimum and the maximum partition functions over all simulations. In practice, the convergence of the partition functions is fast and the result of the reweighting procedure weakly depends on the cutoff criterion to stop the iteration [294]. Once the partition functions are converged, the unconstrained probability distribution can be readily obtained from Eq. (III.16) on the entire range $[0, 1]$. We have thus been able to measure exponentially small probabilities in N which correspond to large-overlap values.

The accuracy of the WHAM requires a significant overlap between the adjacent histograms. As the width of the histograms is expected to shrink with N as $1/\sqrt{N}$, increasing the system size requires a larger number of simulations. We could tackle this effect by decreasing the bias curvature κ but this may be problematic as it also decreases the driving force towards configurations with untypically large-overlap values. In $2d$, the system sizes that we have used are moderate (typically, up to $N = 250$), and the multi-histogram method is suitable. In $3d$, we perform a finite-size scaling analysis for large systems (typically, up to $N = 2400$), and the system size is systematically varied. We thus turn to another reweighting procedure in $3d$ that we present in the next section.

2.5 Gaussian ensemble reweighting

In the $3d$ system, we want to implement a method which scales not too fast with system size and in particular which does not require an increasing number of simulations when N increases. The method is similar in spirit to the umbrella integration [322] or the Gaussian ensemble [323, 324], and it does not require a significant overlap between adjacent umbrella probability distributions of the order parameter. Instead of setting κ to a small-enough value to have overlapping adjacent biased histograms, we apply a bias with a large curvature κ in order for the biased histograms to display a sharp peak at their most probable value which we denote by Q_k^* for $k = 1 \dots n_\mathrm{s}$. Taking the logarithm of Eq. (III.11), differentiating with respect to Q, and evaluating at the most probable value yield

$$V'(Q_k^*; \boldsymbol{r}_0^N) = -\frac{W_k'(Q_k^*)}{N} = \kappa \left(Q_k^\mathrm{ref} - Q_k^* \right), \tag{III.18}$$

where the prime denotes the derivative with respect to Q, and where $V(Q; \boldsymbol{r}_0^N)$ is the random Franz-Parisi (FP) potential for a given reference configuration $\boldsymbol{r}_0^N$ which is defined in Eq. (II.11). Equivalently, it stands for the large deviation rate function of $\mathcal{P}(Q; \boldsymbol{r}_0^N)$, *i.e.*,

$$\mathcal{P}(Q; \boldsymbol{r}_0^N) \propto e^{-N\beta V(Q; \boldsymbol{r}_0^N)}, \tag{III.19}$$

see also Eq. (II.12).

We note at this point that the normalisation constants $\mathcal{Z}_k$ have disappeared from the expression of the unconstrained probability distribution, while they represented a difficulty in the reweighting procedure of the previous section. As a result, for each simulation, we just need to measure the most probable value of the overlap. We end up with n_s estimates of the derivative

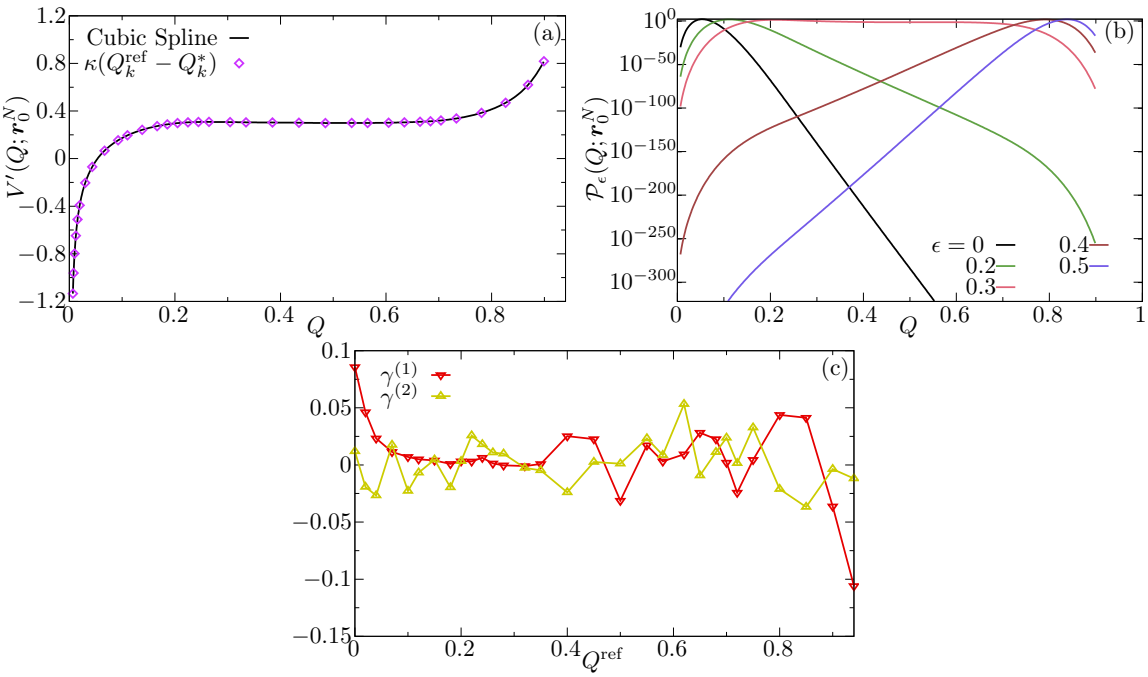

Fig. III.3 | Principle of the Gaussian ensemble reweighting for the $3d$ system with $N = 1200$, $T = 0.22$ and the other parameters which are given in Tab. III.1. (a) Derivative of the large deviation rate function $V(Q;\boldsymbol{r}_0^N)$ at the discrete most probable values $\{Q_k^*\}_{k=1\ldots n_s}$ and its cubic spline interpolation. (b) Unconstrained probability distribution $\mathcal{P}(Q;\boldsymbol{r}_0^N)$ ($\epsilon = 0$) which is obtained by integrating the cubic spline and by using Eq. (III.19). Distributions $\mathcal{P}_\epsilon(Q;\boldsymbol{r}_0^N) \propto \mathcal{P}(Q;\boldsymbol{r}_0^N)e^{N\beta\epsilon Q}$ of the overlap for finite values of $\epsilon = 0.2, 0.3, 0.4, 0.5$ are also represented, see Eq. (III.5). (c) Skewness $\gamma_k^{(1)}$ [see Eq. (III.21)] and kurtosis $\gamma_k^{(2)}$ [see Eq. (III.22)] of the biased histograms $\mathcal{N}_k(Q)$ as a function of the bias center $Q_k^{\rm ref}$.

of $V(Q;\boldsymbol{r}_0^N)$ at different points. As $Q^{\rm ref}(Q^*)$ is a smooth function[4], we interpolate it by using a cubic spline [238, 325]. In other words, $Q^{\rm ref}(Q^*)$ is locally approximated by a third-degree polynomial function. Finally, the cubic spline can be integrated analytically to reach $V(Q;\boldsymbol{r}_0^N)$ up to an additive constant which is chosen so that $V(Q;\boldsymbol{r}_0^N)$ is zero at its global minimum:

$$V(Q;\boldsymbol{r}_0^N) = \kappa \int_{Q_{\rm rand}}^{Q} Q^{\rm ref}(Q^*)\mathrm{d}Q^* - \frac{1}{2}\kappa\left(Q^2 - Q_{\rm rand}^2\right). \tag{III.20}$$

The full procedure is represented in Fig. III.3 (a). The unconstrained probability distribution is eventually obtained from Eq. (III.19), see Fig. III.3 (b). Once again, we stress that, with this procedure, we are able to sample the large deviation rate function of $\mathcal{P}(Q;\boldsymbol{r}_0^N)$ on the full range of overlap values and as a result to measure arbitrary small probabilities.

We now explain how to determine the most probable value of the overlap for a given biased simulation during the course of the simulation, without actually measuring the histogram $\mathcal{N}_k(Q)$. This is because we want to avoid systematic errors which are related to the bin width. Our goal is to derive an expression for the most probable value from quantities which are directly accessible during a simulation, such as the cumulants of the overlap. To obtain more insight about this

[4]We have implicitly assumed that the curvature κ is the same for all the umbrella simulations, but the reweighting formula can be straightforwardly extended if not.

relation, we show in Fig. III.3 (c) the skewness

$$\gamma_k^{(1)} = \frac{\langle (\hat{Q} - \langle \hat{Q} \rangle_k)^3 \rangle_k}{\langle (\hat{Q} - \langle \hat{Q} \rangle_k)^2 \rangle_k^{3/2}}, \tag{III.21}$$

and the kurtosis

$$\gamma_k^{(2)} = \frac{\langle (\hat{Q} - \langle \hat{Q} \rangle_k)^4 \rangle_k}{\langle (\hat{Q} - \langle \hat{Q} \rangle_k)^2 \rangle_k^2} - 3, \tag{III.22}$$

where $\langle . \rangle_k$ denotes the thermal average with the biased Hamiltonian $\hat{H}_\mathrm{b}[\boldsymbol{r}^N; \boldsymbol{r}_0^N]$ with the umbrella potential W_k. They are both close to 0, which is their expected value if the overlap is distributed according to a Gaussian. Besides, the kurtosis remains small for all the biases while the skewness is larger for extreme values of Q^ref.

Therefore, we reasonably assume that the biased histograms are well approximated by [323]

$$\mathcal{N}_k(Q) \propto e^{-\alpha_k (Q-Q_k^*)^2 + \xi_k (Q-Q_k^*)^3} \propto \left[1 + \xi_k (Q - Q_k^*)^3\right] e^{-\alpha_k (Q-Q_k^*)^2}, \tag{III.23}$$

where the third-order term is considered as a perturbation from the Gaussian limit ($\xi_k = 0$) and it is non-zero for extreme values of Q^ref only. We restrict ourselves to expansions at the first order in ξ_k, which are correct if $\xi_k \alpha_k^{-3/2} \ll 1$. We use the proxy in Eq. (III.23) to compute the three first cumulants of the overlap, which read, at the leading order in ξ_k,

$$\begin{aligned} \langle \hat{Q} \rangle_k &= Q_k^* + \frac{3\xi_k}{4\alpha_k^2}, \\ \langle (\hat{Q} - \langle \hat{Q} \rangle_k)^2 \rangle_k &= \frac{1}{2\alpha_k}, \\ \langle (\hat{Q} - \langle \hat{Q} \rangle_k)^3 \rangle_k &= \frac{3\xi_k}{4\alpha_k^3}. \end{aligned} \tag{III.24}$$

Inserting the second and third equations into the first one yields for the most probable value:

$$Q_k^* = \langle \hat{Q} \rangle_k - \frac{\langle (\hat{Q} - \langle \hat{Q} \rangle_k)^3 \rangle_k}{2 \langle (\hat{Q} - \langle \hat{Q} \rangle_k)^2 \rangle_k}. \tag{III.25}$$

In particular, we note that the above equation gives $Q_k^* = \langle \hat{Q} \rangle_k$ when the biased histogram is symmetric and almost Gaussian. In addition, the small parameter in the above expansions $\xi_k \alpha_k^{-3/2} = \sqrt{2} \gamma_k^{(1)}$ is directly related to the skewness of the biased histogram. Fig. III.3 (c) shows that this parameter is indeed smaller than 1, which makes our approach fully self-consistent. Expansions at any order could be done but they require to measure an increasing number of cumulants of the overlap in each biased simulation, which may give rise to larger statistical errors if t_eq is not large-enough and to a larger noise in the calculation of the derivative of the FP potential, see Eq. (III.18).

The Gaussian approximation is even more accurate when κ is large. However, if κ becomes too big, the amplitude of the force which derives from the umbrella bias and which is applied on each particle grows, and the time step for the integration of the equations of motion must be decreased to keep the same numerical accuracy and to continue to sample the phase space correctly. Our choice of κ is the result of this compromise.

Overall, the computer study of the thermodynamics of coupled supercooled liquids is a huge numerical effort as for a given reference configuration $\boldsymbol{r}_0^N$, a given temperature T and a

given system size N, about 30 biased simulations are necessary. This represents a total number of simulations of about twenty thousands, when one multiplies the number of umbrella simulations by the number of temperatures which we sample, the number of reference configurations and the number of system sizes we consider. The temperatures which we sample are $T = 0.40$, 0.35, 0.30, 0.25, 0.22, 0.20, 0.15 in $3d$ and $T = 0.30$, 0.20, 0.12, 0.06 in $2d$. The system sizes which we consider are $N = 300$, 600, 1200, 2400 in $3d$ and $N = 64$, 125, 250 in $2d$. For visualisation, larger sizes are taken, namely, $N = 10000$ in $3d$ and $N = 2000$ in $2d$. Finally, the number of different reference configurations ranges from 10 at large temperatures to 25 at the lowest temperatures.

We have introduced all the methods which are necessary to the study of the thermodynamics of constrained supercooled liquids in $d = 2, 3$. Before presenting our results, we explain how the thermodynamic properties can be extrapolated at temperatures that have not been directly simulated. This is used in Sec. 5.2.

2.6 Temperature reweighting

In order to reduce the number of umbrella sampling simulations, we want to relate the Franz-Parisi (FP) potential for a fixed reference configuration $V_{\mathrm{e}}(Q; \boldsymbol{r}_0^N)$ at a target temperature T_{e} to the FP potential $V(Q; \boldsymbol{r}_0^N)$ at a temperature T [211, 212, 326] with T_{e} close to T. In particular, this strategy allows us to estimate the thermodynamic properties in $3d$ at temperatures $T = 0.23$ and $T = 0.26$ from the umbrella simulations which are done at temperatures $T = 0.22$ and $T = 0.25$. It is only used in Sec. 5.2. We have checked that the temperature reweighting scheme gives similar results to direct simulations at the target temperature.

As we want to do a reweighting in temperature, not only do we have to measure the statistical properties of the overlap in the umbrella sampling simulations but also the statistics of the total energy [294, 315, 316], namely,

$$\hat{H}_{\mathrm{tot}}[\boldsymbol{r}^N; \boldsymbol{v}^N] = \frac{1}{2} m \sum_{i=1}^{N} \boldsymbol{v}_i^2 + \hat{H}[\boldsymbol{r}^N], \tag{III.26}$$

where $\boldsymbol{v}^N = \{\boldsymbol{v}_i\}_{i=1\ldots N}$ are the velocities of the N particles and where $\hat{H}[\boldsymbol{r}^N]$ is given by Eq. (III.3). We advocate that $V_{\mathrm{e}}(Q; \boldsymbol{r}_0^N)$ is derived from $V(Q; \boldsymbol{r}_0^N)$ by using the relation

$$V_{\mathrm{e}}(Q; \boldsymbol{r}_0^N) = \frac{T_{\mathrm{e}}}{T} V(Q; \boldsymbol{r}_0^N) + \frac{1 - T_{\mathrm{e}}/T}{N} E_1(Q; \boldsymbol{r}_0^N) - \frac{(1 - T_{\mathrm{e}}/T)^2}{2NT_{\mathrm{e}}} E_2(Q; \boldsymbol{r}_0^N), \tag{III.27}$$

in the limit of large N, where $E_{1,2}(Q; \boldsymbol{r}_0^N)$ respectively stand for the average and the variance of $\hat{H}_{\mathrm{tot}}$ at a fixed value Q of the overlap and at the temperature T. In the course of the umbrella simulations, the first cumulants of the total energy are directly measured. They represent the evalutation of the quantities $E_{1,2}(Q; \boldsymbol{r}_0^N)$ at the most probable value of the overlap Q_k^* for $k = 1 \ldots n_{\mathrm{s}}$ if the histogram $\mathcal{N}_k(Q)$ is sharp-enough. Eventually, a cubic spline interpolation is performed to obtain $E_{1,2}(Q; \boldsymbol{r}_0^N)$ for arbitrary values of Q, similarly to the procedure which is used for the derivative of the FP potential.

To justify Eq. (III.27), we introduce the joint probability $\mathcal{P}(E, Q; \boldsymbol{r}_0^N)$ of the total energy and the overlap with the reference configuration in the unconstrained liquid at the temperature T. We then make the reasonable assumption that the conditional probability of the total energy

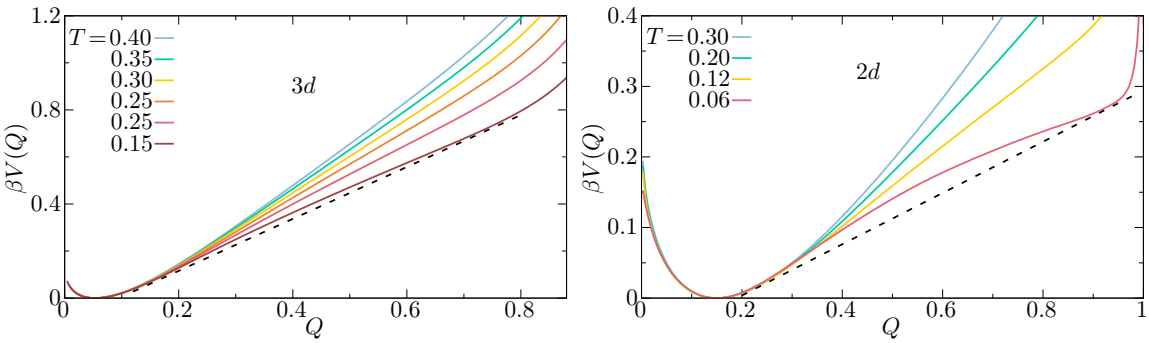

Fig. III.4 | Franz-Parisi (FP) potential for the $3d$ system ($N = 600$, left) and the $2d$ system ($N = 64$, right) at several temperatures T for a fixed temperature T_0 of the reference configurations ($T_0 = 0.06$ in $3d$ and $T_0 = 0.03$ in $2d$). The curves have been shifted so that the absolute minimum of the FP potential is zero. This absolute minimum corresponds to the most probable value of the overlap between equilibrium unconstrained liquid configurations at temperatures T and T_0 respectively. The FP potential becomes more right-tailed as the temperature is decreased, and this reflects a lower free energy cost for the overlap fluctuations. The FP potentiel is convex at high temperatures with a single minimum at $Q = Q_{\rm rand}$ but it becomes non-convex at lower temperatures (the dashed lines are guide for the eye). This non-convexity is a finite-size effect which may indicate a first order transition when the overlap is coupled to an external source ϵ.

given an overlap value Q is a Gaussian, so that the joint probability reads

$$\mathcal{P}(E, Q; \boldsymbol{r}_0^N) = \mathcal{P}(Q; \boldsymbol{r}_0^N) \times \frac{1}{\sqrt{2\pi E_2(Q; \boldsymbol{r}_0^N)}} e^{-[E - E_1(Q;\boldsymbol{r}_0^N)]^2/[2E_2(Q;\boldsymbol{r}_0^N)]}. \tag{III.28}$$

We can eventually derive the unconstrained probability distribution of the overlap at any target temperature $T_{\rm e}$ after reweighting and integration over the energies, namely,

$$\mathcal{P}_{\rm e}(Q; \boldsymbol{r}_0^N) \propto \int {\rm d}E \mathcal{P}(E, Q; \boldsymbol{r}_0^N) e^{-(\beta_{\rm e} - \beta)E}, \tag{III.29}$$

with $\beta_{\rm e} = 1/T_{\rm e}$ and where $\mathcal{P}(E, Q; \boldsymbol{r}_0^N)$ is given by Eq. (III.28). The integration is straightforward to compute and Eq. (III.27) then follows from the definition of the FP potential, see Eq. (III.19).

In the next section, we turn to the presentation of our numerical results. We first focus on small-to-moderate size systems in both $d = 2$ and $d = 3$ and we show that they exhibit mean-field remnants in both cases.

3. Mean-field-like behaviour in finite systems

3.1 Temperature evolution of the Franz-Parisi potential

We first start with the Franz-Parisi (FP) potential $V(Q)$ which has been defined in Chap. II. It represents the Landau free energy which quantifies the free energy cost for keeping liquid configurations at a given overlap Q with a reference configuration. Equivalently, it stands for the large deviation rate function of the unconstrained probability distribution of the overlap, namely,

$$V(Q) = -\frac{T}{N} \overline{\ln \mathcal{P}(Q; \boldsymbol{r}_0^N)} = \overline{V(Q; \boldsymbol{r}_0^N)}, \tag{III.30}$$

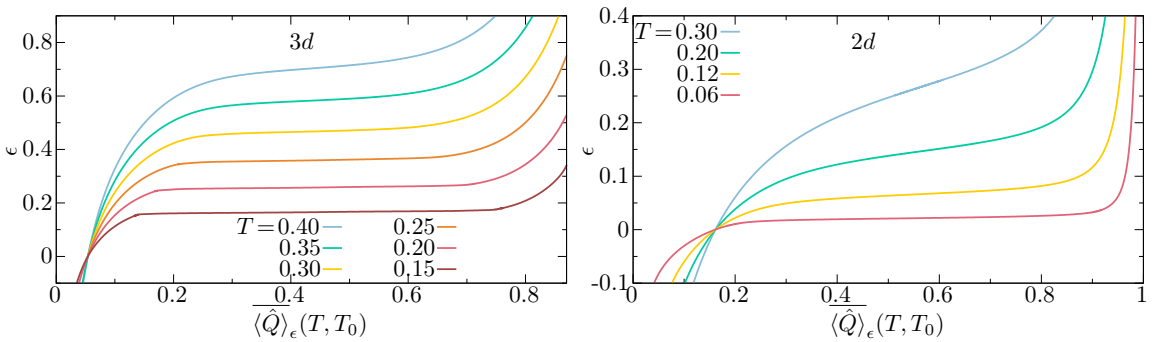

Fig. III.5 | Isotherms $\overline{\langle \hat{Q} \rangle_\epsilon}$ of the overlap order parameter for the $3d$ system ($N = 600$, left) and the $2d$ system ($N = 64$, right) when the external source ϵ is switched on at several temperatures T for a fixed temperature T_0 ($T_0 = 0.06$ in $3d$ and $T_0 = 0.03$ in $2d$) of the reference configurations. Isotherms are strictly increasing at high temperatures but they become almost flat at low temperatures, which may be the evidence for a first order transition which ends in a critical point.

see also Eq. (II.12). We recall that the overline denotes the average over the disorder which is represented by the reference configuration $\boldsymbol{r}_0^N$. The FP potential is defined up to an irrelevant additive constant which is chosen here so that it vanishes at its absolute minimum.

We display the temperature evolution of the FP potential for a fixed temperature T_0 of the reference configurations in Fig. III.4. This picture is very reminiscent of the mean-field results of the spherical p-spin, compare with Fig. II.3. In particular, we observe that the FP potential always displays an absolute minimum for $Q = Q_{\text{rand}}$ which represents the most probable overlap value between two equilibrium configurations at temperatures T and T_0 respectively. The potential at high overlaps steadily decreases when decreasing the temperature. This reflects the lower free energy cost for large excursions of the overlap order parameter. The FP potential is strictly convex at high temperatures. However, it becomes non-convex at the lowest temperatures as in mean-field models (see the dashed lines). This feature is a finite-size effect due to the small system sizes which are considered here, and convexity is necessarily restored in finite-dimensional systems in the thermodynamic limit ($N \to +\infty$) [217].

In mean-field theory, the non-convexities of the FP potential are associated with a first-order transition when a field ϵ is linearly coupled to the overlap. In finite dimensions, one should analyse how the convexity of the FP potential is restored in the thermodynamic limit. A phase transition in the phase diagram (ϵ, T) only exists in the thermodynamic limit if the FP potential displays a linear behaviour for intermediate overlap values, see Fig. II.2. Instead, the transition is totally wiped out if the FP potential becomes strictly convex in the thermodynamic limit. Complementary with the analysis of the convexity properties of the FP potential, one can directly study the thermodynamics of a constrained liquid (with a finite ϵ). This is the object of the next section.

3.2 Thermodynamic properties in the presence of a source ϵ

The isotherms for relatively small systems ($N = 600$ in $3d$ and $N = 64$ in $2d$) are displayed in Fig. III.5. They correspond to the external source ϵ versus the average order parameter $\overline{\langle \hat{Q} \rangle_\epsilon}$ for several temperatures T at a fixed temperature T_0 of the reference configurations, see Eq. (II.6). We recall that $\langle . \rangle_\epsilon$ stands for the thermal average in the constrained liquid for a fixed reference

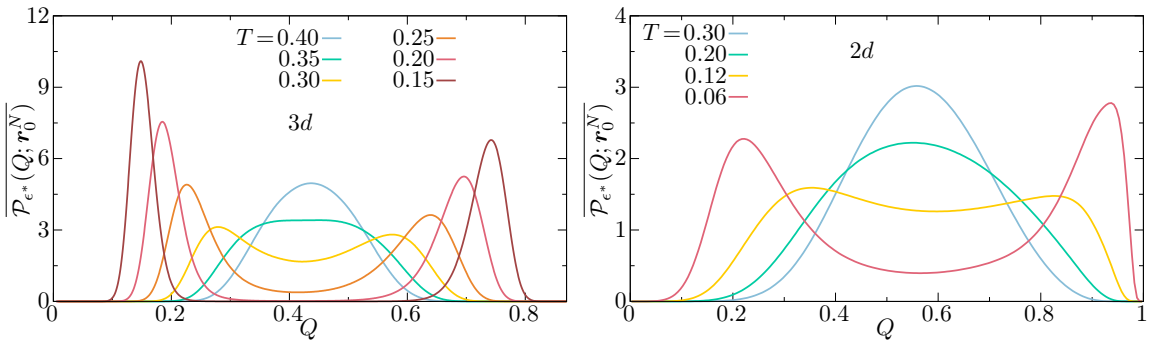

Fig. III.6 | Disorder-averaged probability distribution $\overline{\mathcal{P}_{\epsilon^*}(Q;\boldsymbol{r}_0^N)}$ of the overlap Q for the $3d$ system ($N = 600$, left) and the $2d$ system ($N = 64$, right) for $\epsilon = \epsilon^*(T, T_0)$ which maximises the total variance of the overlap order parameter, several temperatures T and a fixed temperature T_0 ($T_0 = 0.06$ in $3d$ and $T_0 = 0.03$ in $2d$) of the reference configurations. The probability distribution is single-peaked at large temperatures and broadens with decreasing the temperature which indicates larger fluctuations of the order parameter. The probability distribution eventually becomes bimodal at the lowest temperatures which is the expected distribution for a system that displays a phase separation between the low- and the high-overlap phases, hence a first order transition.

configuration $\boldsymbol{r}_0^N$. Equivalently, the isotherms correspond to the first cumulant of the disorder-averaged constrained probability distribution of the overlap. We remark that imposing a finite positive (resp. negative) ϵ biases the overlap to larger (resp. smaller) values than its "random" value Q_{rand}. Isotherms are strictly monotonically increasing at large temperatures with an inflexion point which corresponds to maximised thermal fluctuations at a fixed temperature T. Indeed, we have seen in the previous chapter that for any value of ϵ, the slope of the tangent at the isotherm represents the inverse of the connected susceptibility, see Eq. (II.7). As the temperature decreases, we first note that the field ϵ beyond which the system is localised also decreases, as the attraction between configurations has to counterbalance smaller thermal fluctuations (or equivalently a smaller entropic cost). We also observe that the slope at the inflexion point of the isotherm decreases until the isotherms almost plateau at the lowest temperatures. This directly indicates growing fluctuations of the order parameter when decreasing the temperature.

This phenomenology is fully-consistent with phase coexistence at low temperatures betwen low- and high-overlap phases which ends in a critical point at a larger temperature as predicted from mean-field theory. For instance, the curves in Fig. III.5 are very reminiscent of the Van der Waals isotherms for the liquid-gas transition when they are corrected by the Maxwell construction [9]. The average overlap is here computed in the canonical ensemble in which ϵ is the control parameter and they cannot show any loop even in small systems. The latter can only be observed in the "microcanonical" iso-overlap ensemble which in this case is not equivalent to the canonical ensemble. However, the interpretation of the thermodynamic behaviour from the isotherms may be misleading because the isotherms in the canonical ensemble can become strictly flat in the thermodynamic limit only. For finite-size disordered systems, they display a residual slope of order $1/\sqrt{N}$, see Eq. (III.32). In consequence, a finite-size analysis is necessary to detect a true phase transition in the thermodynamic limit from mean-field remnants and it is done in the next section.

Our numerical strategy not only enables us to carefully measure the average overlap but also its average full probability distribution over the reference configurations $\overline{\mathcal{P}_{\epsilon}(Q;\boldsymbol{r}_0^N)}$ for any source ϵ. Our discussion of the isotherms has revealed that at a fixed temperature, the connected sus-

ceptibility displays a maximum for a given intermediate source, and that this maximum increases with decreasing the temperature. In Chap. II, we have introduced another susceptibility which quantifies the disorder fluctuations and which is known as the disconnected susceptibility. Both susceptibilities are maximum around the same value of the external field, which corresponds to the inflexion point of the isotherms, and we denote by $\epsilon^*(T, T_0)$ the value of ϵ at which the total susceptibility which is the sum of the connected and disconnected ones is maximum. We then show in Fig. III.6 the disorder-averaged probability distribution of the overlap for several temperatures T, a fixed temperature T_0 of the reference configuration and $\epsilon = \epsilon^*(T, T_0)$. At high temperatures, the distribution is almost Gaussian with a single peak at Q which is close to its average value. Then, as the temperature decreases, the width of the distribution increases, and this reflects larger overlap fluctuations as already inferred from the slope of the isotherms. Eventually, the distribution becomes strongly bimodal for the lowest temperatures. This is exactly what is expected if there is a phase separation between a delocalised phase and a localised phase, which is associated with a first order transition line in the phase diagram (ϵ, T).

The fact that the probability distribution becomes increasingly bimodal for a fixed system size as the temperature is decreased represents evidence for the existence of a static (thermodynamic) lengthscale which is associated with the overlap fluctuations and which grows as the temperature is reduced. This is of course consistent with the existence of a critical point at a finite temperature T_c, at which the lengthscale would diverge in the thermodynamic limit. However, several other scenarios cannot be excluded so far, such as a divergence at zero temperature only or a growth without a divergence of the correlation length, recall the schematic phase diagrams in Fig. III.1. A finite-size analysis is required to assess what remains of the mean-field-like behaviour which is found in $2d$ and $3d$ small systems in the thermodynamic limit. This is the object of the next section.

4. Contrasting results in two and three dimensions through a finite-size scaling analysis

4.1 System-size dependence of the overlap probability distribution

To confirm or infirm the existence of a first order transition line that ends in a critical point, we first analyse the system-size dependence of the probability distribution $\overline{\mathcal{P}_{\epsilon^*}(Q; \boldsymbol{r}_0^N)}$ of the overlap for two different temperatures, see Fig. III.7. At the higher temperature in $3d$ ($T = 0.30$), the probability distribution is bimodal in small-enough samples ($N \lesssim 1000$) but this behaviour disappears when considering large-enough systems, see the curve for $N = 2400$. For this temperature, the distribution is therefore expected to become Gaussian in the thermodynamic limit. At the lower temperature in $3d$ ($T = 0.15$), the probability distribution of the overlap is bimodal for all studied system sizes with two maxima at $Q = Q_{\text{low}}$ and $Q = Q_{\text{high}}$. In addition, the distribution gets increasingly bimodal when the system size increases: the width of the two peaks shrinks while the free energy barrier between the two maxima,

$$\beta \Delta \mathcal{F}(T, T_0) = \ln \left[\frac{\sqrt{\overline{\mathcal{P}_{\epsilon^*}(Q_{\text{low}}; \boldsymbol{r}_0^N)}\ \overline{\mathcal{P}_{\epsilon^*}(Q_{\text{high}}, \boldsymbol{r}_0^N)}}}{\overline{\mathcal{P}_{\epsilon^*}(Q_{\text{min}}; \boldsymbol{r}_0^N)}} \right], \tag{III.31}$$

with Q_{min} the location in the relative minimum of the probability distribution in the range $[Q_{\text{low}}, Q_{\text{high}}]$, grows. The probability distribution then appears to tend to a double Dirac distribution in the thermodynamic limit. This gives support to the existence of a critical point at a

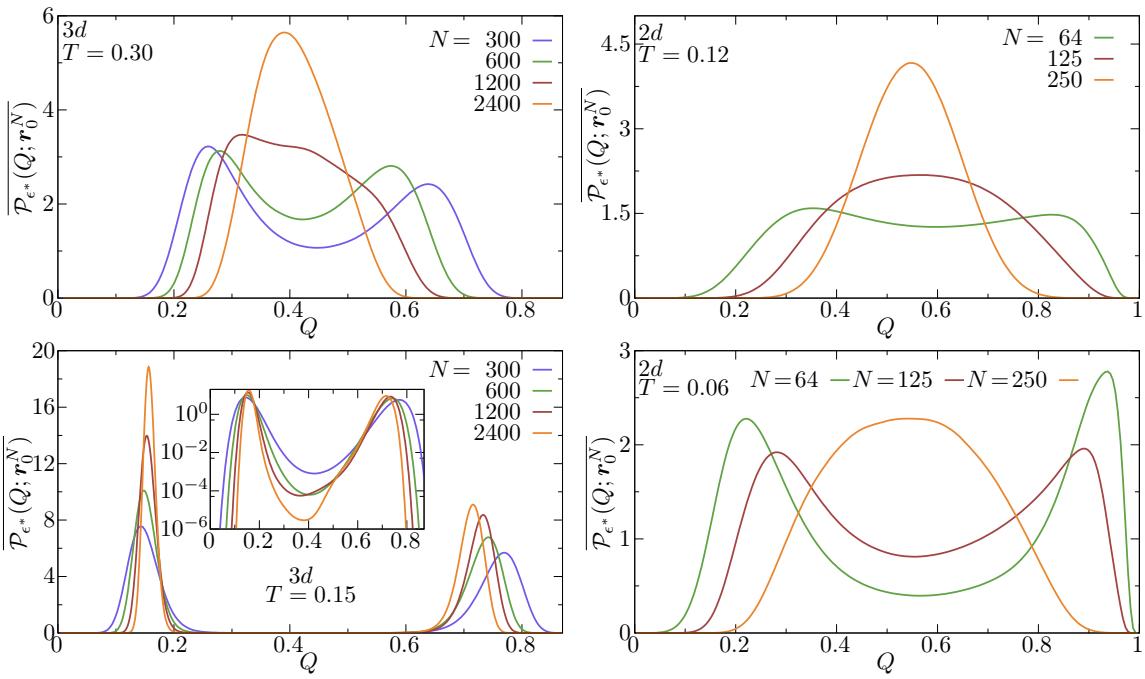

Fig. III.7 | System-size evolution of the probability distribution $\overline{\mathcal{P}_{\epsilon^*}(Q;\boldsymbol{r}_0^N)}$ of the overlap in $3d$ (left) and $2d$ (right) for $\epsilon = \epsilon^*(T, T_0)$ which maximises the total variance of the order parameter. The distributions are shown for two different temperatures T and a fixed temperature T_0 of the reference configurations ($T_0 = 0.06$ in $3d$ and $T_0 = 0.03$ in $2d$). In $3d$, at the higher temperature ($T = 0.30$), the probability distribution is bimodal for small systems but the free energy barrier between the low- and high-overlap phases vanishes for larger systems. For the lower temperature instead ($T = 0.15$), the probability distribution of the overlap becomes increasingly bimodal when N gets larger, consistently with the existence of a first order transition in the thermodynamic limit. The inset in the bottom left panel shows the probability distributions in logarithmic scale to appreciate that the free energy barrier between the low-overlap and the high-overlap phases grows with system size. Instead in $2d$, for any temperature, the probability distribution which is bimodal for small systems always turns to a single-peaked distribution for larger values of N.

finite temperature $T_c \in [0.15, 0.30[$. We want to stress that the system sizes we are dealing with here are unprecedently larger than the ones which were considered in past studies on structural liquids and which were limited to at most a few hundreds of particles [209, 213, 327]. Dealing with too small systems then tends to overestimate the critical temperature T_c or it may even lead to an erroneous conclusion regarding the existence of a critical point or a first order transition (in $d = 2$ for instance, see below).

In $2d$ instead, the overlap probability distribution is bimodal in sufficiently small systems but always narrows and it eventually becomes single-peaked in larger samples. Excluding the unlikely scenario that bimodality reappears at even larger system sizes, this rules out the existence of a critical point in $2d$ for $T \geq 0.06$. We emphasise that thanks to the swap algorithm, we have been able to prepare equilibrium configurations at $T_0 = 0.03$ which is much lower than the estimated experimental glass transition temperature $T_g = 0.068$. They represent equilibrium configurations with an estimated (but unmeasurable) relaxation time of about 10^{37}. Converted into physical units, this corresponds to a relaxation time of about 10^{18} years which is larger than

the age of the universe[5]. In addition, the lowest temperature that we can achieve here ($T = 0.06$) is also below the extrapolated glass transition temperature. As a consequence, if a critical point existed, and considering the small value of T_0, it would likely be observed in the temperature range that we have investigated. We cannot of course exclude the existence of a critical point at still lower temperatures but at least in the temperature range down to the estimated glass transition temperature, there is no signature of a critical point in the thermodynamic limit in the $2d$ system. Despite this negative answer, we note that we need to go to larger system sizes as the temperature is decreased to recover a single-peaked probability distribution of the overlap. This suggests that the previously mentioned static lengthscale which is associated with the overlap fluctuations is indeed growing as the temperature is reduced. Therefore, even though these is no phase transition in the phase diagram (ϵ, T), the thermodynamics is nonetheless non-trivial as the order parameter fluctuations and the associated static lengthscale increase with decreasing the temperature.

We have focused on the case of a fixed T_0. The same analysis of the system-size dependence of the probability distribution can be performed for the case $T = T_0$ and it confirms our findings, see Appendix A. We show the absence of a critical point in $2d$ in the experimentally-relevant temperature regime while in $3d$, data are instead compatible with the existence of a critical point but at a much lower temperature $0.085 \leq T_c < 0.10$ than for $T_0 = 0.06$, close to the mode-coupling crossover ($T_{\rm mct} = 0.095$ in $3d$) in agreement with previous numerical studies [209, 256].

In the next section, we proceed to a more detailed finite-size analysis in the case of a fixed T_0 and we give further evidence for the existence in the thermodynamic limit of a first order transition at the lowest temperature in $3d$ ($T = 0.15$).

4.2 Finite-size scaling analysis in three dimensions indicates a first order transition in the thermodynamic limit

To further confirm that the system is below a critical point and that it undergoes a first order transition as a function of ϵ when $T = 0.15$ in the $3d$ system, and following the results of statistical field theory [218, 250], we assess the validity of the scaling laws of the random-field Ising model (RFIM) at its first order transition in the presence of an applied magnetic field. We consider the constrained liquid in the phase coexistence region, namely, when a field $\epsilon = \epsilon^*(T, T_0)$ is imposed. We first show in Fig. III.8 the system-size dependence of the connected and the disconnected susceptibilities when they are evaluated at $\epsilon^*(T, T_0)$. At a first order transition region in the presence of quenched disorder, the finite-size scaling behaviour is given by [211, 212]

$$\begin{cases} \chi_{\epsilon^*}^{(\rm con)}(T, T_0) \sim & L^{d/2} \sim \sqrt{N}, \\ \chi_{\epsilon^*}^{(\rm dis)}(T, T_0) \sim & L^d \sim N. \end{cases} \tag{III.32}$$

We note in particular that the disconnected susceptibility dominates the connected susceptibility in large systems, consistently with the fact that the large-scale physics of the RFIM is ruled by disorder-induced fluctuations instead of thermal ones and a zero-temperature fixed point [263] (see also Appendix A of Chap. II). Both relations are well satisfied by our data even though errorbars are quite large for the largest system sizes.

We also study the size evolution of the free energy barrier $\Delta\mathcal{F}(T, T_0)$ between the low- and

[5]See Chap. VI for more details on how to translate simulation units into physical times.

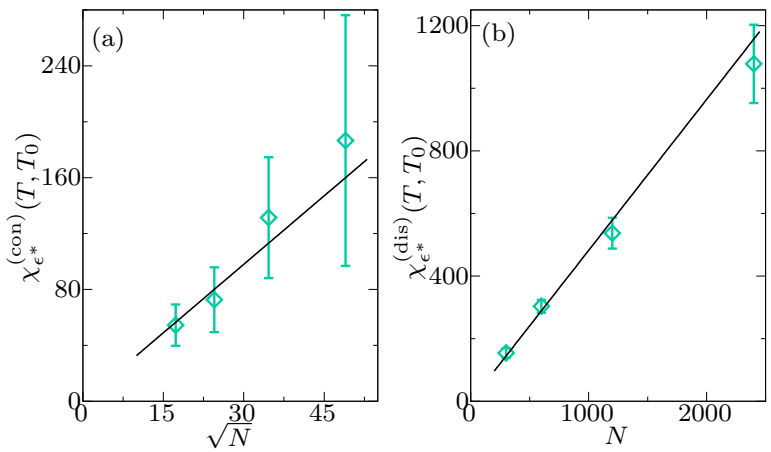

Fig. III.8 | Finite-size scaling analysis of the susceptibilities in $3d$ in the first order transition region. Plot of (a) the connected susceptibility $\chi_{\epsilon^*}^{(\mathrm{con})}(T,T_0)$ and of (b) the disconnected susceptibility $\chi_{\epsilon^*}^{(\mathrm{dis})}(T,T_0)$ at $T=0.15$ for a fixed temperature $T_0=0.06$ of the reference configurations. Full lines are the results of a linear fit of the data. Data follow the peculiar scaling laws of random-field-like systems, see Eq. (III.32). Errorbars are obtained thanks to the jacknife method when the average over the disorder is performed [294].

the high-overlap phases, which is given by Eq. (III.31). This quantity should verify the following scaling law if one assumes a planar interface between the two coexisting phases [328, 329]:

$$\frac{\Delta\mathcal{F}(T,T_0)}{2L^{d-1}} = \Upsilon(T,T_0) + A\frac{\ln L}{L^{d-1}} + \frac{B}{L^{d-1}}. \tag{III.33}$$

In this equation, A and B represent unknown coefficients, while the factor of 2 in the denominator of the left-hand side comes from using periodic boundary conditions. The above relation illustrates that the free energy barrier per unit area should converge to the surface tension $\Upsilon(T,T_0)$ when $L\to+\infty$. When $A=0$, standard scaling is recovered if one assumes that the free energy cost scales as the surface area of the interface, which is planar. Here, we add an extra $\ln L/L^{d-1}$ dependence to account for massless modes due to the invariance of the free energy cost with translations of the planar interface and contributions from non-planar interfaces [330]. For large-enough sizes (as it is the case here), the first factor dominates the other and in Fig. III.9 (a), we show that $\Delta\mathcal{F}(T,T_0)/(2L^{d-1})$ is indeed consistent with a linear behaviour as a function of $\ln L/L^{d-1}$. We extract a finite and positive surface tension $\Upsilon(T,T_0)\simeq 0.0041$ for $T=0.15$. This guarantees the self-consistency of our ansatz and this confirms the phase separation which is associated with the first order transition.

A snapshot of a configuration of the $3d$ system with $N=10000$ at $T=0.15$ for a fixed temperature $T_0=0.06$ of the reference configuration is shown in Fig. III.9 (b). This configuration is obtained during a biased simulation with an umbrella potential that is chosen so that the overlap is intermediate between Q_{low} and Q_{high} ($\hat{Q}\simeq 0.44$) and a phase separation is then expected. This configuration contributes to the minimum in the probability distribution of the overlap at coexistence between the two phases and it is therefore very unlikely in a direct simulation in the canonical ensemble. These configurations become more likely when performing an umbrella sampling. This is equivalent to a sampling in a Gaussian ensemble [323, 324] which interpolates between the canonical ensemble (with fixed ϵ) and the microcanonical ensemble

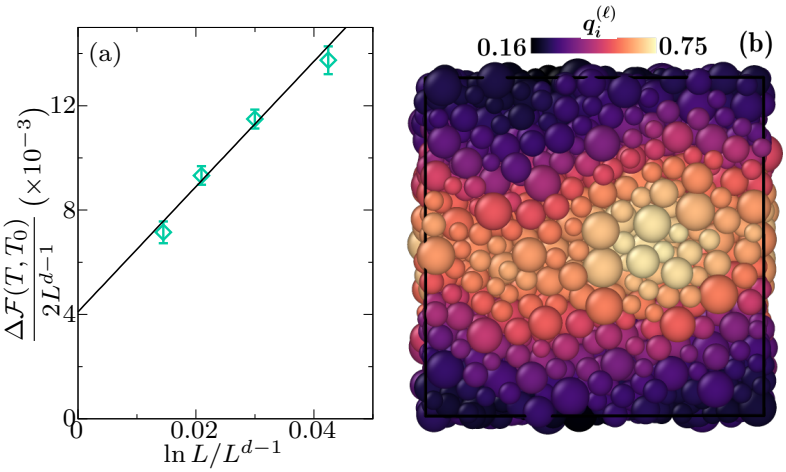

Fig. III.9 | Analysis of the coexistence between the low- and the high-overlap phases in $3d$ in the first order transition region. (a) Size-evolution of the free energy barrier between low- and high-overlap phases $\Delta\mathcal{F}(T,T_0)/(2L^{d-1})$, see Eq. (III.31). Data are consistent with a $\ln L/L^{d-1}$ dependence, see Eq. (III.33). The intercept corresponds to the surface tension between the two coexisting phases $\Upsilon(T,T_0) \simeq 0.0041$ for $T = 0.15$ and $T_0 = 0.06$. Errorbars are obtained thanks to the jacknife method when the average over the disorder is performed [294]. (b) Snapshot of a system of $N = 10000$ in $3d$ for $T = 0.15$, $\hat{Q} \simeq 0.44$ and a fixed temperature $T_0 = 0.06$ of the reference configuration from a configuration which is obtained in the course of an umbrella simulation. The particles are coloured according to their coarse-grained overlap $q_i^{(\ell)}$ with the reference configuration ($\ell = 1$). A macroscopic phase separation is clearly visible.

(with fixed overlap). For each particle, we compute a local overlap

$$q_i = \sum_{j=1}^{N} w(|\boldsymbol{r}_i - \boldsymbol{r}_j^{(0)}|/a), \tag{III.34}$$

and we then coarse-grain this single-particle quantity by using an exponential window of size $\ell = 1$, namely,

$$q_i^{(\ell)} = \frac{\sum_j q_j e^{-r_{ij}/\ell}}{\sum_j e^{-r_{ij}/\ell}}, \tag{III.35}$$

where the sums run over all the particles, and where $r_{ij} = |\boldsymbol{r}_i - \boldsymbol{r}_j|$. This procedure smoothes out the spatial fluctuations of the order parameter [69]. We clearly observe that the system segregates into two phases with distinct values of the overlap. However, the interface is not perfectly planar and there are inhomogeneities of the overlap inside the high-overlap phase. In any case, all the particles with a local overlap larger than the average form a single connected cluster: their relative distance is smaller than 1.5 which corresponds to the first minimum in the radial pair correlation function $g(r)$ [30]. This snapshot illustrates what a phase separation in this system looks like [256] and it strengthens the conclusion of the scaling analysis of the free energy barrier in Eq. (III.33).

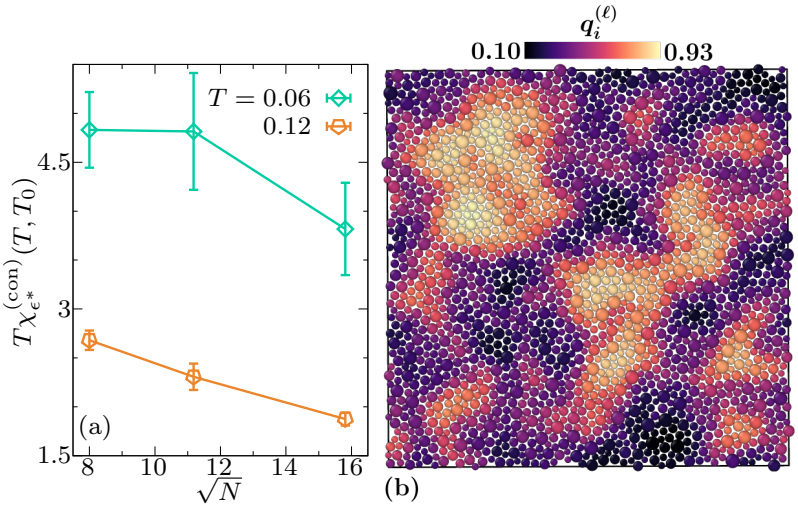

Fig. III.10 | Finite-size scaling analysis in $2d$. (a) Plot of $T\chi_{\epsilon^*}^{(\mathrm{con})}(T, T_0)$ at $T = 0.06$ and $T = 0.12$ for a fixed temperature $T_0 = 0.03$ of the reference configurations. The susceptibility decreases with the system size and it presumably goes to a finite value in the thermodynamic limit for all the temperatures. Errorbars are computed thanks to the jacknife method when the average over the disorder is performed [294]. (b) Snapshot of a system of $N = 2000$ particles in $2d$ for $T = 0.06$, $\hat{Q} \simeq 0.48$ and a fixed temperature $T_0 = 0.03$ of the reference configuration from a configuration which is obtained in the course of an umbrella simulation. The particles are coloured according to their coarse-grained overlap $q_i^{(\ell)}$ with the reference configuration ($\ell = 1$). The system does not show a macroscopic phase separation with a planar interface but small domains instead.

4.3 Finite-size scaling analysis in two dimensions shows no sign of phase transition in the thermodynamic limit

We give further support to the absence of a first order transition in $d = 2$ in the thermodynamic limit for the whole accessible temperature range. We study the system on the Widom line, which we recall is defined as the location of the maxima of the total susceptibility in the (ϵ, T) plane. We plot in Fig. III.10 (a) the maximum of the connected susceptibility for the two temperatures $T = 0.12$ and $T = 0.06$ and a fixed temperature $T_0 = 0.03$ of the reference configurations. We observe that, contrary to what is found for the $3d$ system, the susceptibility decreases with the system size and it presumably converges to a finite value in the thermodynamic limit. In real space, the system does not phase separate, as illustrated in Fig. III.10 (b) where we display a snapshot of a configuration of $N = 2000$ particles which is obtained in the course of an umbrella simulation at $T = 0.06$. Instead of a system-spanning phase separation, the system at intermediate values of the overlap displays small domains which are characterised by a small or a large overlap. The particles with an overlap larger than the average do not form a single connected cluster. This is in contrast with the macroscopic phase separation in $3d$.

Now that we have given strong evidence for the existence of a phase transition in $3d$ at a non-zero temperature, we still need to locate more precisely and to characterise the universality class of the critical point. This is the object of the next section.

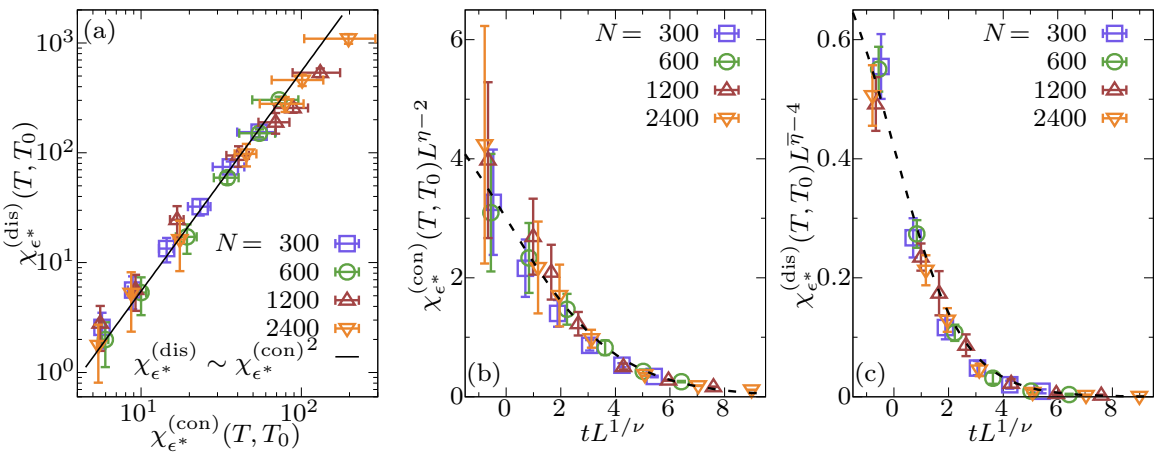

Fig. III.11 | Analysis of the susceptibilities in the $3d$ system close to the critical point. (a) Scatter plot of the maximum value of the connected susceptibility $\chi_{\epsilon^*}^{(\mathrm{con})}(T,T_0)$ versus the maximum value of the disconnected susceptibility $\chi_{\epsilon^*}^{(\mathrm{dis})}(T,T_0)$ for a fixed temperature $T_0 = 0.06$ of the reference configurations. The random-field Ising model quadratic scaling (full line) is well satisfied. (b)-(c) Finite-size scaling analysis close to the critical point in the $3d$ system. Plot of the (b) connected and the (c) disconnected susceptibilities which are rescaled by $L^{2-\eta}$ and $L^{4-\overline{\eta}}$ respectively as a function of the reduced temperature $t = T/T_c - 1$ for a fixed temperature $T_0 = 0.06$ of the reference configurations. The data almost collapse (up to uncertainties) for $T_c \simeq 0.17$. The dashed lines are guide for the eye. For all the panels, errorbars are obtained via the jacknife method when the average over the disorder is performed [294].

5. Characterisation of the critical point in the three-dimensional system

5.1 Confirming random-field Ising model criticality via a finite-size scaling analysis

In order to locate and to characterise the critical point in $3d$, we focus on the analysis of the finite-size behaviour of the connected and the disconnected susceptibilities [283]. When approaching close enough to a critical point in a finite-size system, the correlation length saturates at the linear size L of the system. As a result, on the Widom line, the susceptibilities for $\epsilon = \epsilon^*(T,T_0)$ should verify the finite-size scaling relations [211]

$$\begin{cases} \chi_{\epsilon^*}^{(\mathrm{con})}(T,T_0) = & L^{2-\eta}\tilde{\chi}_{\mathrm{con}}(tL^{1/\nu}), \\ \chi_{\epsilon^*}^{(\mathrm{dis})}(T,T_0) = & L^{4-\overline{\eta}}\tilde{\chi}_{\mathrm{dis}}(tL^{1/\nu}). \end{cases} \tag{III.36}$$

In the above expressions, $\tilde{\chi}_{\mathrm{con}}(x)$ and $\tilde{\chi}_{\mathrm{dis}}(x)$ represent scaling functions, η, $\overline{\eta}$ and ν are the critical exponents of the $3d$ random-field Ising model (RFIM) universality class and $t = T/T_c - 1$ is the reduced temperature. The RFIM in $d > 2$ has a critical point at zero temperature when using the variance of the random field as the control parameter, see Appendix A of Chap. II. In consequence, the critical exponents can be accurately measured by using an efficient algorithm which generates the ground state of the RFIM for a given realisation of the random fields [264, 331, 332]. Thus, we build on these studies and we set the critical exponents in Eq. (III.36) to their reported values that we round to two significant figures: $\eta \simeq 0.52$, $\overline{\eta} \simeq 1.04$ and $\nu \simeq 1.37$. We note that $\overline{\eta} \simeq 2\eta$ [278]. The latter is not an exact equality [263] but the deviation in $3d$ is very small and beyond the precision which is required here.

Combining Eq. (III.32) and (III.36) and the approximate relation between $\overline{\eta}$ and η, we obtain that the disconnected susceptibility scales as the square of the connected one. More precisely, we expect that [270]

$$\chi_{\epsilon^*}^{(\mathrm{dis})}(T,T_0) \simeq \frac{\Delta}{T_\mathrm{c}} \chi_{\epsilon^*}^{(\mathrm{con})}(T,T_0)^2, \tag{III.37}$$

where Δ represents the variance of the effective random fields that emerge in the mapping from the constrained supercooled liquid to the RFIM, and where T_c is the critical temperature, see also Eq. (II.79). In Fig. III.11 (a), we show the scatter plot of the maximum of the connected susceptibility versus that of the disconnected susceptibility in $3d$ for a fixed temperature $T_0 = 0.06$ of the reference configurations. The above equation is well satisfied by our data. The disconnected susceptibility is larger than the connected one at low-enough temperatures or for large-enough system sizes, which means that the quenched disorder is relevant for the system. This is a first evidence of random-field-like physics in the transition from the delocalised phase to the localised phase.

We now turn to the direct finite-size scaling analysis of the two susceptibilities by means of Eq. (III.36). In Fig. III.11 (b)-(c), we show the collapse of the properly rescaled connected and disconnected susceptibilities as a function of the reduced temperature. The critical temperature T_c remains the unique adjustable parameter to ensure the best data collapse on a master curve. Even though mixing-field effects may be present [333, 334], we find that a good collapse is obtained for $T_\mathrm{c} \simeq 0.17$. This estimate of the critical temperature is found by minimising the average quadratic difference between the rescaled data and an unknown master curve [335]. This master curve is taken as a piecewise linear function which is built on a subset of the rescaled data [336].

The good data collapse which is obtained by a rescaling and by using the known critical exponents of the $3d$ RFIM confirms the existence in the $3d$ supercooled liquid of a critical point at a finite temperature T_c and a finite source ϵ_c in the universality class of the RFIM. This is in agreement with field-theoretical treatments [218]. In addition, from the prefactor of the quadratic fit in Fig. III.11 (a) [compare with Eq. (III.37)], and by using our estimate of the critical temperature, we obtain an estimate of the strength of the effective random fields $\sqrt{\Delta} = 0.097$. We remark that in the $3d$ RFIM, one knows from numerical simulations [264, 331] that the disorder destroys the transition whenever $\sqrt{\Delta}/J \gtrsim 2.3$, where J is the coupling constant between Ising spins. Accessing the value of this ratio in the $3d$ liquid would therefore provide an interesting consistency check. Unfortunately, although J may be in principle estimated from the surface tension $\Upsilon(T,T_0)$, the later must be computed at temperatures much below T_c, because $\Upsilon(T,T_0)$ vanishes at the critical point [331]. This is presently out of reach to computer simulations of constrained glass-forming liquids.

5.2 Activated dynamics in the vicinity of the critical point

We now turn to the study of the dynamics of the constrained supercooled liquid in the vicinity of the critical point, a study which has never been attempted before. We perform direct simulations of the constrained liquid in the canonical ensemble (with fixed ϵ). The relaxation of the fluctuations of the order parameter on approaching a critical point is characterised by a slowing down and a divergence of the relaxation time exactly at criticality [281]. In the case of the RFIM, the slowing down is anomalous and it is described by an activated dynamic scaling according to which it is not the relaxation time that grows as a power law of the correlation

length, as usual, but its logarithm, see Eq. (II.80). This is another consequence of the existence of a zero-temperature fixed point.

In order to measure the slowing down of the relaxation of order parameter fluctuations, the dynamics near the critical point at (ϵ_c, T_c) is investigated through the equilibrium overlap autocorrelation function, namely,

$$C_\epsilon(t; \boldsymbol{r}_0^N) = \frac{\langle (\hat{Q}(t) - \langle \hat{Q} \rangle_\epsilon)(\hat{Q}(0) - \langle \hat{Q} \rangle_\epsilon) \rangle_\epsilon}{\langle (\hat{Q}(0) - \langle \hat{Q} \rangle_\epsilon)^2 \rangle_\epsilon}, \tag{III.38}$$

where we recall that $\langle \cdot \rangle_\epsilon$ denotes a thermal average at a temperature T in the presence of the applied source ϵ for a fixed reference configuration $\boldsymbol{r}_0^N$. In addition, $\hat{Q}(t)$ is a short-hand notation for

$$\hat{Q}(t) = \hat{Q}[\boldsymbol{r}^N(t); \boldsymbol{r}_0^N], \tag{III.39}$$

where $\boldsymbol{r}^N(t)$ denotes the configuration of the constrained liquid at time t. The above correlation function is a random function through the dependence on the reference configuration.

To study the dynamics, we run simulations of the $3d$ constrained liquid for a system size $N = 1200$ by considering the swap algorithm with the Hamiltonian (III.6) for 25 different samples $\boldsymbol{r}_0^N$, see Eq. (III.6). We approach the critical point from above, by using several pairs (ϵ, T) close to or at the Widom line $\epsilon^*(T, T_0)$ as determined from the thermodynamic study of the previous sections. The temperatures which we consider are $T = 0.23$, 0.25, 0.26. Lower temperatures could not be investigated because the relaxation time corresponds to too-large simulation walltimes. These disproportionately long relaxation times are a first indication in favour of the existence of a critical slowing down (we recall that the mode-coupling crossover of the unconstrained liquid is $T_{\rm mct} = 0.095$ in $3d$). For a fixed reference configuration $\boldsymbol{r}_0^N$, the liquid is first equilibrated at a temperature T and a field ϵ, and one equilibrium configuration $\boldsymbol{r}_\epsilon^N$ is then stored. Equilibration is checked as in the static study, namely, by running two simulations from distinct initial conditions. Then, we run 60 simulations in the iso-configurational ensemble by starting from the very same configuration $\boldsymbol{r}_\epsilon^N$ and with the initial velocities which are drawn from the Maxwell-Boltzmann distribution at the temperature T [63, 337, 338]. We can then compute $C_\epsilon(t; \boldsymbol{r}_0^N)$ from all runs and we extract the autocorrelation time $\tau_\epsilon(T; \boldsymbol{r}_0^N)$ when the autocorrelation function equals 0.2. We self-consistently check afterwards that the simulations have lasted at least 10 times the autocorrelation time.

We now want to relate $\tau_\epsilon(T; \boldsymbol{r}_0^N)$ to a measurable static quantity which characterises the approach to the critical point. One expects an activated dynamic scaling of the form [339]

$$\tau_\epsilon(T; \boldsymbol{r}_0^N) = \tau_0 [\xi_\epsilon(T; \boldsymbol{r}_0^N)]^z e^{c[\xi_\epsilon(T; \boldsymbol{r}_0^N)]^\psi}, \tag{III.40}$$

where τ_0 and c are some constants, and where z is a dynamic exponent which describes a sub-dominant behaviour, see Eq. (II.80). Instead of the correlation length $\xi_\epsilon(T; \boldsymbol{r}_0^N)$ to which we do not have direct access, we use the thermal susceptibility

$$\chi_\epsilon^{(T)}(T; \boldsymbol{r}_0^N) = N\beta \left[\langle \hat{Q}^2 \rangle_\epsilon - \langle \hat{Q} \rangle_\epsilon^2 \right]. \tag{III.41}$$

This is a random property due to its dependence on $\boldsymbol{r}_0^N$, whose average over the reference configurations gives the connected susceptibility. It is a self-averaging quantity and it should scale as $[\xi_\epsilon(T; \boldsymbol{r}_0^N)]^{2-\eta}$, see Eq. (III.36). For the $3d$ RFIM, as $\overline{\eta} \simeq 2\eta$, we have that $2 - \eta \simeq \theta$, where θ is the temperature exponent, see Eq. (II.77). As the relation $\psi = \theta$ has also been

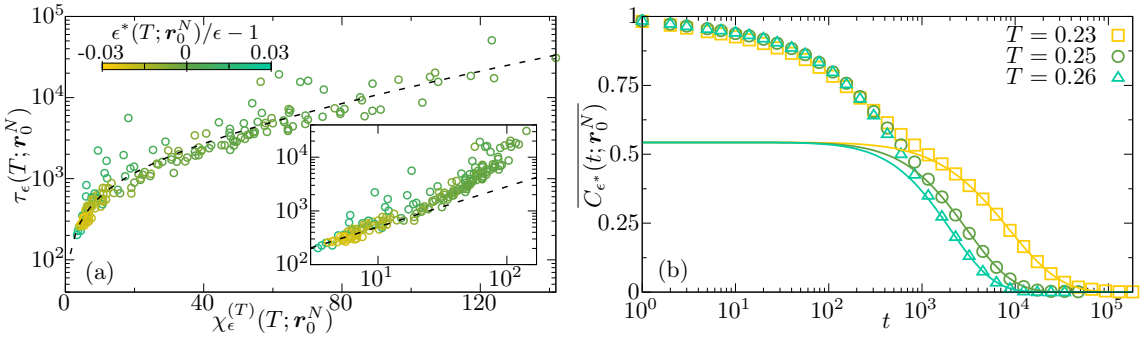

Fig. III.12 | (a) Relaxation time $\tau_\epsilon(T;\boldsymbol{r}_0^N)$ as a function of the thermal susceptibility $\chi_\epsilon^{(T)}(T;\boldsymbol{r}_0^N)$ for several samples $\boldsymbol{r}_0^N$, temperatures T, and sources ϵ close to the Widom line. Relaxation times are obtained when the equilibrium autocorrelation function of the overlap equals 0.2. The latter correlation has been measured by direct simulations of the constrained liquid in the canonical ensemble. The colorbar encodes the relative distance of the couple (ϵ, T) that is used for the simulation from $\epsilon^*(T;\boldsymbol{r}_0^N)$ [field for which $\chi_\epsilon^{(T)}(T;\boldsymbol{r}_0^N)$ is maximum] in the ϵ-direction. All data collapse on a master curve which is well fitted by Eq. (III.42) (dashed line), with $\tilde{c} \simeq 0.015$, $\tilde{\tau}_0 \simeq 88$ and $z \simeq 1.15$. The inset shows a tentative power law fit which obviously fails at high values of the susceptibility. (b) Disorder-averaged overlap autocorrelation function $\overline{C_\epsilon(t;\boldsymbol{r}_0^N)}$ along the average Widom line $\epsilon = \epsilon^*(T, T_0)$ for several temperatures. The full lines represent a fit to the empirical form which is presented in Eq. (III.44), with $C_0 \simeq 0.54$ and $\varphi \simeq 8.2$. The data are consistent with a logarithmic stretching of the correlation functions, see Eq. (III.43).

shown [282], one has that $[\xi_\epsilon(T;\boldsymbol{r}_0^N)]^\psi \sim \chi_\epsilon^{(T)}(T;\boldsymbol{r}_0^N)$. We therefore consider the following form to relate the statics to the dynamics in the vicinity of the critical point:

$$\tau_\epsilon(T;\boldsymbol{r}_0^N) = \tilde{\tau}_0[\chi_\epsilon^{(T)}(T;\boldsymbol{r}_0^N)]^{z/\theta} e^{\tilde{c}\,\chi_\epsilon^{(T)}(T;\boldsymbol{r}_0^N)}, \tag{III.42}$$

where $\tilde{\tau}_0$ and $\tilde{c}$ are new constants. We take $\theta \simeq 1.49$ [331]. Whereas the dominant activated scaling behaviour is independent of the simulated dynamics, the sub-dominant behaviour and the prefactor can be modified by choosing an appropriate algorithm[6]. Here, the swap algorithm is expected to speed up any pre-asymptotic dynamics and it thus enables one to approach the critical point more closely [340]. In fact, we have found that the ordinary molecular dynamics simulations are much too slow near the critical point so that the dynamics cannot be measured for $T \leq 0.30$ (we recall that the critical point is at $T_c \simeq 0.17$).

Fig. III.12 (a) shows the scatter plot of the relaxation time versus the thermal susceptibility. The latter has been directly measured for temperature $T = 0.25$ and otherwise extrapolated by using the direct measurements at $T = 0.22$ and $T = 0.25$ and the procedure of Sec. 2.6. The data are coloured according to the difference between the field ϵ of the simulation and the locus $\epsilon^*(T;\boldsymbol{r}_0^N)$ of the maximum of the thermal susceptibility. The data agree well with the prediction of Eq. (III.42). In particular, even though the increase in the relaxation time is limited to a little more than two orders of magnitude, it is sufficient to distinguish between an activated scaling (main panel) and a conventional power law scaling (inset).

In a second stage, we also look at the average over the disorder of the autocorrelation function along the average Widom line at several temperatures, namely, $\overline{C_\epsilon(t;\boldsymbol{r}_0^N)}$ for $\epsilon = \epsilon^*(T, T_0)$. Another prediction of the activated dynamic scaling in the RFIM is that the correlation function

[6]In other words, z and $\tilde{\tau}_0$ may depend on the algorithm.

should be very stretched, on a logarithmic scale [271], namely,

$$\overline{C_\epsilon(t;\boldsymbol{r}_0^N)} = \widetilde{C}(\ln t/\ln\tau(T)) \tag{III.43}$$

with $\tau(T)$ the autocorrelation time that is obtained when $\overline{C_\epsilon(t;\boldsymbol{r}_0^N)}$ equals 0.2, and $\widetilde{C}(x)$ a scaling function for which no theoretical prediction is available. We find that along the Widom line, we can fit our data with an empirical form which has been previously used in RFIM-like systems [341–343], namely,

$$\widetilde{C}(x) = C_0 \exp(-x^\varphi), \tag{III.44}$$

with C_0 and φ two temperature independent adjustable parameters. As seen in Fig. III.12 (b), the data at large times for all the temperatures agree well with this prediction. A rescaling by using the variable $t/\tau(T)$ as in conventional critical slowing down is instead inconsistent with the data.

To finish, we mention that we have also investigated the dynamics of the system in the first order transition region and we have consistently found the presence of hysteresis loops when ϵ is changed at a finite rate and a fixed temperature T. We have also unsuccessfully looked for avalanches which are typical of RFIM-like systems at zero temperature [344], namely, large and sudden drops of the order parameter when changing the source. In the RFIM, avalanches are well-defined at zero temperature [93] but they are likely blurred by thermal fluctuations at higher temperatures [95]. Despite this limitation, our study of the dynamics of constrained liquids is overall consistent with the existence of a RFIM-like critical point which terminates an associated first order transition line in $3d$.

6. Conclusions

We summarise all our findings in Fig. III.13 where we show the phase diagram of constrained model supercooled liquids in $d = 2, 3$ in the thermodynamic limit. We represent the line $\epsilon^*(T, T_0)$ of the loci of the maxima of the total susceptibility in the phase diagram (ϵ, T). In $3d$, there is a critical point at a finite temperature on this line for $T_\mathrm{c} \simeq 0.17$ and $\epsilon_\mathrm{c} \simeq 0.20$, which separates the first order transition line for $T < T_\mathrm{c}$ from the Widom line above the critical point. In $2d$ instead, there is no sign of criticality and the phase diagram only displays a Widom line down to the lowest achievable temperature (which, again, is below the extrapolated experimental glass transition temperature). We note that the behaviour in $3d$ is consistent with the mean-field prediction, compare with Fig. III.1 (a)-(b). Our results also confirm the recent field-theoretical treatments beyond mean-field [196, 197, 218, 250] which have been reviewed in Chap. II, and which predict that the behaviour of constrained liquids can be mapped onto the random-field Ising model (RFIM). Accordingly, we have found no sign of a critical point in $2d$ as the lower critical dimension of the RFIM is equal to 2, while we have clearly exhibited a critical point and a first order transition with quenched disorder in $3d$.

The results of this chapter are non-trivial for several reasons. On the one hand, our analysis of relatively small systems has revealed that mean-field theory is remarkably robust in finite dimensions. It means that the glassy slowdown of supercooled liquids is actually accompanied by thermodynamic fluctuations of the overlap which represents the degree of similarity between equilibrium configurations and which has been identified as the proper order parameter of the mean-field glass transition. In particular, claims that the glass transition is merely of dynamic nature are difficult to reconcile with what has been presented in this chapter. We also note that

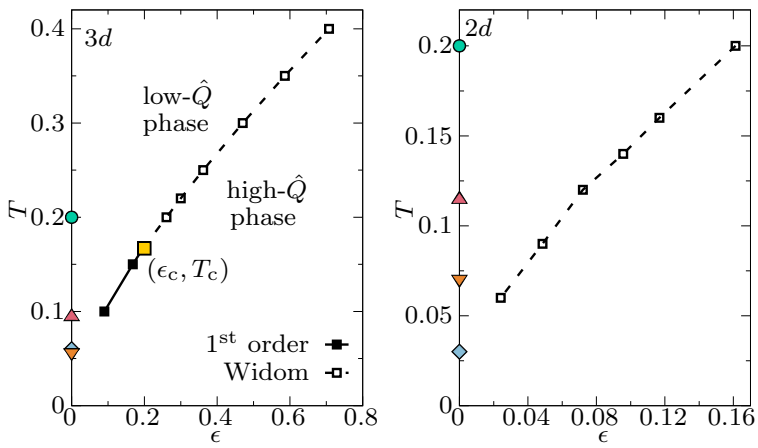

Fig. III.13 | Loci of the maxima of the total susceptibility $\epsilon^*(T, T_0)$ in the phase diagram (ϵ, T) for the $3d$ system (left) and the $2d$ system (right) for a fixed temperature T_0 of the reference configurations ($T_0 = 0.06$ in $3d$ and $T_0 = 0.03$ in $2d$). In $3d$, a critical point (full yellow square) at $T_c \simeq 0.17$ and $\epsilon_c \simeq 0.20$ separates the first order transition line (full line) below the critical point from the Widom line (dashed line) above. In $2d$ instead, there is neither a critical point nor a first order transition line but only a Widom line. In both panels, we give several indicative temperature scales: the onset temperature of glassy behaviour (green disk), the mode-coupling crossover temperature $T_{\rm mct}$ (pink up triangle), the extrapolated experimental glass transition temperature T_g (orange down triangle) and the temperature T_0 of the reference configurations (blue diamond).

studying small systems that display a mean-field-like phenomenology could be used in order to measure the parameters that enter the replicated Landau-Ginzburg functional which has been described in the previous chapter and to build an effective field theory for this system [52]. On the other hand, the existence of a critical point in $3d$ was not guaranteed because it depends on the strength of the effective disorder that is generated by the reference configurations, as compared to the strength of the effective interactions between local overlaps (namely, the ratio $\sqrt{\Delta}/J$). It would be interesting to repeat the analysis of this chapter for other model glass-formers. This would enable one to give a quantitative measure of their relative "self-induced" disorder $\sqrt{\Delta}/J$ (see also Chap. V), and finally to compare these different glass-forming liquids. For the first time, our results give very strong evidence for the existence in the thermodynamic limit of a genuine critical point, with a first order transition line at lower temperatures. This represents, to date, the only piece of the mean-field theory that survives not as a mere crossover when finite-dimensional fluctuations are present.

At the mean-field level and in statistical field theory, the existence of a first order transition and of a critical point in the phase diagram (ϵ, T) is the natural consequence of the existence of an entropy crisis at a Kauzmann transition T_K. From one side, the fact that there is no critical point in $2d$ forbids the existence of a finite Kauzmann temperature. This is consistent with the results of Ref. [182] where it was shown that the configurational entropy for the very same system vanishes at zero temperature only. Similarly, the point-to-set length, which quantifies the spatial extent of amorphous order, can only diverge at zero temperature. This is consistent with our results which show that a static lengthscale is growing along the Widom line but that it remains finite in the accessible temperature range. In particular, studying the temperature evolution of the size of the domains of low and high overlap along the Widom line in the $2d$ system could be interesting [see Fig. III.10 (b)], see Chap. V. From the other side, the existence of a critical

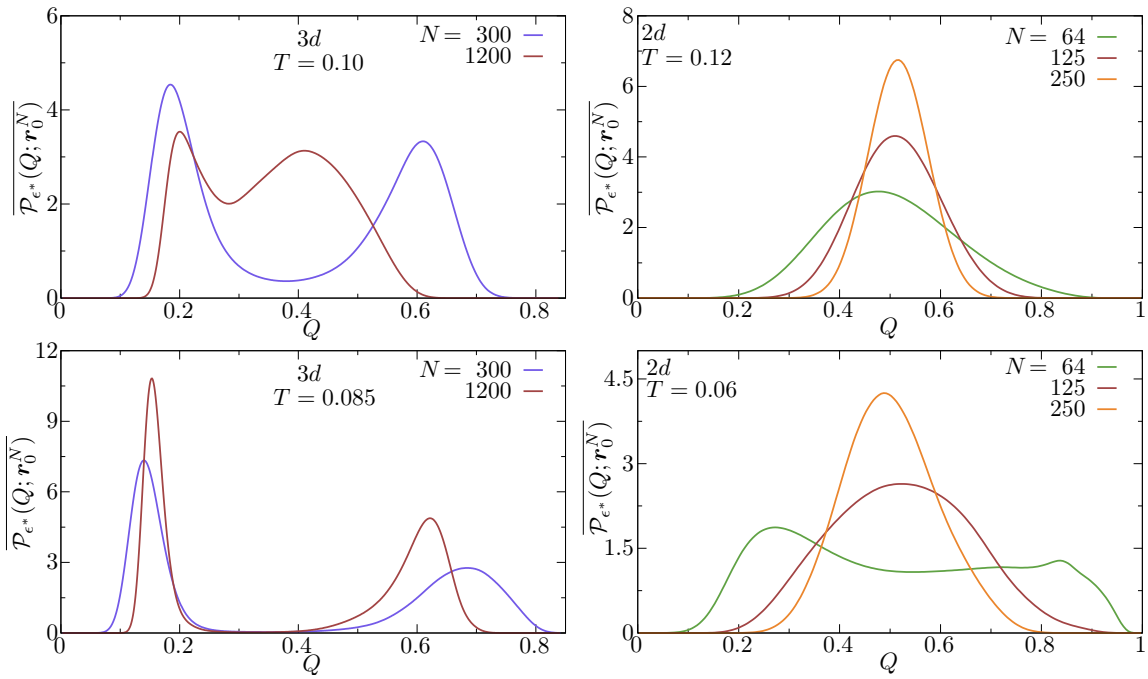

Fig. III.14 | System-size evolution of the probability distribution $\overline{\mathcal{P}_{\epsilon^*}(Q;\boldsymbol{r}_0^N)}$ of the overlap in $3d$ (left) and $2d$ (right) for $\epsilon = \epsilon^*(T)$ which maximises the total variance of the order parameter. The distributions are shown for two different temperatures T in the case $T = T_0$. In $3d$, at the higher temperature ($T = 0.10$), the probability distribution is always bimodal for the system sizes which are considered but the free energy barrier between the two peaks decreases with larger N. At the lower temperature ($T = 0.085$) instead, the free energy barrier grows with system size and the distribution becomes increasingly bimodal. In $2d$, at the larger temperature ($T = 0.12$), the probability distribution is always single-peaked and it narrows when the system size increases. For the lower temperature ($T = 0.06$), the overlap probability distribution goes from a slightly bimodal shape to a single-peaked one when increasing N.

point at a finite temperature T_c in $3d$ is consistent with the existence of a finite Kauzmann transition temperature but, however, does not prove it [243]. Yet, independent measurements of the configurational entropy in the same $3d$ system seem to extrapolate to zero at a finite temperature and, as a result, to corroborate the existence of a finite T_K [114, 164].

Appendix A - Simulation results for the case of equal temperatures $T = T_0$

In this Appendix, we present numerical results for the case where the constrained and the reference configurations are always at the same temperature ($T = T_0$). We analyse the system-size dependence of the disorder-averaged probability distribution of the overlap in both $2d$ and $3d$ for two different temperatures, see Fig. III.14. It is very reminiscent of Fig. III.7 and the same observations and conclusions hold. We remark that in $3d$, the critical point and the associated first order transition below remain but for a lower critical temperature $T_c \in [0.085, 0.10[$ and a lower field $\epsilon_c \in [0.092, 0.125[$, in agreement with the analytical results from mean-field theory (see Fig. II.5) and with past studies [209, 256]. In $2d$ instead, we find that any singular behaviour in the thermodynamics of constrained liquids disappears in the thermodynamic limit

in the experimentally-relevant temperature regime. This result, along with the random-field Ising model criticality which is predicted from statistical field theory, suggests the absence of a transition at any finite temperature in $d = 2$. Interestingly, in $2d$, even though there is not a finite temperature critical point, the static correlation length which is associated with the overlap fluctuations grows with decreasing T_0. Indeed, for $T = 0.12$ for instance, the overlap distribution is bimodal for $N = 64$ when the temperature of the reference configuration is fixed at $T_0 = 0.03$ while it is single-peaked for the case $T = T_0$. As the effect of disorder should be relevant at scales smaller than this static lengthscale this may be related to the high kinetic stability of ultrastable glasses when they melt at high temperatures [99].

IV Detailed analysis of the definition of the overlap between liquid configurations

The overlap, or similarity, between liquid configurations is at the core of the mean-field description of the glass transition, and it represents the order parameter for the random first order transition from the liquid to the ideal glass. It has also proved to be useful when studying three-dimensional glass-forming liquids, as emphasised in Chap. III, and it has revealed non-trivial thermodynamic fluctuations at low temperatures. In liquids, the overlap involves a tolerance, typically of a fraction a/σ of the average particle diameter, which is associated with how precisely similar two configurations must be for belonging to the same physically-relevant "state". We have not heretofore discussed the choice of the numerical value of the tolerance length. Instead, we have rather chosen a "reasonable" value which is similar to what was used in previous studies. Here, we systematically investigate the dependence on the overlap fluctuations of the tolerance length when it is varied over a large range. We mostly focus on the behaviour of the system when the overlap is coupled to an external source ϵ and we study the influence of the coarse-graining length a on the resulting phase diagram (ϵ, T). We show that while the location of the dynamical transition temperature T_{d} and of the static Kauzmann transition temperature T_{K} (if present) is independent of a/σ, that of the critical point at $(\epsilon_{\mathrm{c}}, T_{\mathrm{c}})$ largely depends on the value of a/σ. We rationalise our findings by using liquid-state theory and the hypernetted chain approximation for the correlation functions. We show in particular that a range of a/σ below what is commonly considered maximises the temperature of the critical point T_{c}, by pushing it up in a liquid region where the bulk viscosity is low. We also confirm the theoretical trends thanks to computer simulations by using the same tools as in Chap. III. Finally, we discuss our results and we emphasise what they reveal about the structure of the free energy landscape.

Outline

1 Introduction . . . 98

2 Liquid-state theory in the theoretical Franz-Parisi construction . . . 99

2.1 Computation of the constrained free energy . . . 99

2.2 Computation of the Franz-Parisi potential . . . 102

2.3 Generic properties of the Franz-Parisi potential with respect to the tolerance length . . . 103

3 Hypernetted chain approximation and the Franz-Parisi potential . . . 104

3.1 Presentation of the hypernetted chain closure . . . 104

3.2 Models and methods for the numerical resolution of the integral equations . . . 106

3.3 Temperature evolution of the Franz-Parisi potential and phase diagram (ϵ, T) . . . 107

4 Hypernetted chain results for the critical endpoint . . . 108

4.1 Evolution of the critical point with the tolerance length . . . 108

4.2 Behaviour at small values of the tolerance length 111
4.3 Behaviour at large values of the tolerance length. 113
5 Confronting the hypernetted chain results with computer simulations 115
6 Discussion. 118
6.1 Dependence of the overlap fluctuations on the tolerance length. 118
6.2 Connections with the structure of the free energy landscape 119
Appendix
A Analysis of the hypernetted chain equations in the limit of vanishing tolerance length 121

The results of this chapter have been published in Ref. [295].

1. Introduction

At the mean-field level, glass formation from a liquid is described as a genuine thermodynamic transition whose order parameter is the similarity or overlap between liquid configurations [12, 126]. In Chap. II, we have reviewed analytical calculations of the spherical p-spin model. It is a mean-field model which displays similarities with the behaviour of structural glasses [116, 118, 122], in particular a transition from a replica symmetric liquid phase to a 1-step replica symmetry broken glass phase [144] which is accompanied by a discontinuity in the overlap between equilibrium configurations at the Kauzmann transition temperature $T_{\rm K}$. For this model, the overlap is computed from a single-site quantity. More generally, for lattice models, such as the plaquette models which are discussed in Sec. 5.2 of Chap. II, the overlap between configurations is naturally computed by considering an on-site variable, namely, the product of the spins in two configurations at each lattice site. One can further average this product over the whole sample to obtain a global measure of the similarity between the two configurations. In the case of Ising spins for example, the overlap takes values between -1 for a complete anti-correlation to $+1$ for a complete correlation [210]. A slightly different quantity, the bond overlap which considers nearest neighbour pairs, has also been analysed [345].

For liquids, the definition of the overlap is not as straightforward because it requires to account first for the permutations of identical particles and then for the fact that the particles in two similar configurations never sit exactly at the same place because of thermal vibrations. As a result, the following definition of the overlap between two configurations α and γ of N atoms is chosen:

$$\hat{Q}_a[\boldsymbol{r}_\alpha^N, \boldsymbol{r}_\gamma^N] = \frac{1}{N} \sum_{i,j=1}^{N} w(|\boldsymbol{r}_{\alpha,i} - \boldsymbol{r}_{\gamma,j}|/a), \tag{IV.1}$$

see also Eq. (II.1). We remind that $w(x)$ is a window function which is 1 for $x \lesssim 1$ and 0 for $x \gtrsim 1$, typically a Heaviside step function or a smooth version of it. In a related procedure, the overlap can be defined by discretising space [256, 327]: the sample is divided in small boxes with a linear size a of the order of a fraction of the inter-particle distance and a discrete variable is introduced in each box that takes the value 1 if a particle center is present and 0 otherwise. The overlap then uses the product of these "on-site" variables in two different configurations and the tolerance is now associated with the box size a.

We first note that the double sum in Eq. (IV.1) takes care of particle permutations. Then, a tolerance length a has been introduced to consider that two configurations are similar if the particle centers in the two configurations differ by at most a small but finite distance. To emphasise the importance of this length in this chapter, we write the overlap in the above equation with a subscript a. The tolerance length a has to be fixed, for instance by some physical arguments [209, 213, 241, 346]. It is reasonable to identify this distance with the typical amplitude of the vibrational motion of the particles, a length which is a fraction of the average inter-particle distance. In consequence, in previous studies of model glass-forming liquids (including ours in Chap. III), the cutoff a was taken such that $a/\sigma = 0.2$-0.3, which seems a physically plausible value for a typical vibrational length. However, no one has so far investigated what the effect of changing the ratio a/σ over a significant range is. The goal of the present chapter is to fill this gap.

We now focus on the Franz-Parisi (FP) setting [148] which has been discussed at length in the previous chapters. Namely, we consider the possibility to couple the overlap between the configuration of a liquid and a reference configuration of the same liquid to an external source ϵ to favour large values of the overlap. In mean-field theory, a line of first order transition emerges from the Kauzmann transition $(\epsilon, T) = (0, T_{\rm K})$ in the phase diagram (ϵ, T) and ends in a critical point $(\epsilon_{\rm c}, T_{\rm c})$ at higher temperature (see Chap. II). Strong evidence from computer simulations also support its existence in $3d$ realistic model glass-formers (see Chap. III). In this chapter, we consider another framework for the FP construction, namely, liquid-state theory in the hypernetted chain approximation [151, 154, 155, 300, 301, 347, 348]. In the next section, we present the general statistical mechanics framework.

2. Liquid-state theory in the theoretical Franz-Parisi construction

2.1 Computation of the constrained free energy

In this section, we explain how to compute the constrained free energy in the canonical ensemble (with ϵ as a control parameter) by using results from liquid-state theory. The most convenient way to compute the thermodynamics of constrained liquids for fixed ϵ is to introduce n replicas of the constrained equilibrium configuration $\{\boldsymbol{r}_a^N\}_{a=1\ldots n}$, as already explained in Chap. II. The replica formalism thus amounts to considering an equilibrium liquid mixture of $n+1$ components with Hamiltonian

$$\hat{H}_{{\rm rep},\epsilon}[\{\boldsymbol{r}_\alpha^N\}] = \frac{1}{2}\sum_{\alpha,\gamma=0}^{n}\sum_{i,j=1}^{N} v_{\alpha\gamma}(\boldsymbol{r}_{\alpha,i}, \boldsymbol{r}_{\gamma,j}|\epsilon, a), \tag{IV.2}$$

where the interaction potentials are given by

$$v_{\alpha\gamma}(\boldsymbol{r}, \boldsymbol{r'}|\epsilon, a) = \delta_{\alpha\gamma}\, v(|\boldsymbol{r}-\boldsymbol{r'}|) - [(1-\delta_{\alpha 0})\delta_{\gamma 0} + \delta_{\alpha 0}(1-\delta_{\gamma 0})]\epsilon\, w(|\boldsymbol{r}-\boldsymbol{r'}|/a), \tag{IV.3}$$

with $v(r)$ the pair potential between two particles and $\delta_{\alpha\gamma}$ the Kronecker delta, which is equal to 1 if $\alpha = \gamma$ and to 0 otherwise. The first term represents the interaction between two particles in a single replica, while the second term describes the attraction with the reference configuration.

In liquid-state theory, the free energy can be derived from the Morita-Hiroike functional $\Gamma_{\rm MH}$ [296, 298]. The computation of the latter relies on a diagrammatic expansion of the one-particle densities $\rho_\alpha^{(1)}(\boldsymbol{r})$ and the two-particle densities $\rho_{\alpha\gamma}^{(2)}(\boldsymbol{r}, \boldsymbol{r'})$ of the replicated $(n+1)$-component liquid mixture [349]. Here, we consider the case where the reference configurations

are taken at the same temperature and the same density as the constrained liquid for simplicity. All the replicas thus have the same one-particle density $\rho_\alpha^{(1)}(\boldsymbol{r}) = \rho^{(1)}(\boldsymbol{r})$. The two-particle densities are related to the pair correlation functions via [30]

$$\rho_{\alpha\gamma}^{(2)}(\boldsymbol{r},\boldsymbol{r'}) = \rho^{(1)}(\boldsymbol{r})\rho^{(1)}(\boldsymbol{r'})[1 + h_{\alpha\gamma}(|\boldsymbol{r}-\boldsymbol{r'}|)], \tag{IV.4}$$

where $g_{\alpha\gamma}(r) = 1 + h_{\alpha\gamma}(r)$ is the conventional pair correlation function [30, 64], namely,

$$g_{\alpha\gamma}(r) = \frac{1}{N\rho^{(1)}(\boldsymbol{r})}\langle\sum_{i,j}\delta(\boldsymbol{r}-\boldsymbol{r}_{\alpha,i}+\boldsymbol{r}_{\gamma,j})\rangle_\epsilon, \tag{IV.5}$$

with $r = |\boldsymbol{r}|$ and the sums which run over $i, j = 1 \dots N$ (with $i \neq j$ if the two replicas α and γ are the same).

Since we are interested in homogeneous phases, considering uniform one-densities $\rho^{(1)}(r) = \rho$ is sufficient. The Morita-Hiroike functional (per unit volume) then reads [196, 197, 296, 350]

$$\begin{aligned}\Gamma_{\mathrm{MH}}[\{h_{\alpha\gamma}\}] &= (n+1)\rho(\ln\rho - 1) + \frac{1}{2}\rho^2\sum_{\alpha,\gamma=0}^{n}\int \mathrm{d}\boldsymbol{r}[1+h_{\alpha\gamma}(r)]\beta v_{\alpha\gamma}(r|\epsilon,a)\\ &+ \frac{1}{2}\rho^2\sum_{\alpha,\gamma=0}^{n}\int \mathrm{d}\boldsymbol{r}[1+h_{\alpha\gamma}(r)]\left\{\ln[1+h_{\alpha\gamma}(r)]-1\right\}\\ &+ \frac{1}{2}\sum_{p\geq 3}\frac{(-1)^p\rho^p}{p}\sum_{\alpha_1,\dots,\alpha_p=0}^{n}\int \mathrm{d}\boldsymbol{r}_2\int \mathrm{d}\boldsymbol{r}_3\cdots\int \mathrm{d}\boldsymbol{r}_p h_{\alpha_1\alpha_2}(r_2)h_{\alpha_2\alpha_3}(|\boldsymbol{r}_3-\boldsymbol{r}_2|)\cdots h_{\alpha_p\alpha_1}(r_p)\\ &+ 2\mathrm{PI},\end{aligned} \tag{IV.6}$$

with $v_{\alpha\gamma}(|\boldsymbol{r}-\boldsymbol{r'}|\,|\epsilon,a) = v_{\alpha\gamma}(\boldsymbol{r},\boldsymbol{r'}|\epsilon,a)$, $\beta = 1/T$ (the Boltzmann constant is set to unity), and where 2PI denotes the sum of the two-particle irreducible diagrams which are formed with density vertices that are linked by total correlation functions [296, 298]. Without these terms, the above expression reduces to the well known hypernetted chain (HNC) approximation of liquid-state theory [30]. We also note that the interaction potential with a dependence on ϵ and a only appears in the second term of the right-hand side of Eq. (IV.6). As the purpose of this chapter is to study the influence of the parameter a, we usefully isolate the terms which depend on the potential to formally rewrite the Morita-Hiroike functional as

$$\Gamma_{\mathrm{MH}}[\{h_{\alpha\gamma}\}] = \frac{1}{2}\rho^2\sum_{\alpha,\gamma=0}^{n}\int \mathrm{d}\boldsymbol{r}[1+h_{\alpha\gamma}(r)]\beta v_{\alpha\gamma}(r|\epsilon,a) + \mathcal{F}[\{h_{\alpha\gamma}\}], \tag{IV.7}$$

where $\mathcal{F}$ is independent of the pair potentials.

The equilibrium total correlation functions are obtained by looking for the stationary points of the Morita-Hiroike functional,

$$\frac{\delta\Gamma_{\mathrm{MH}}}{\delta h_{\alpha\gamma}(r)} = 0, \text{ or } \frac{\delta\mathcal{F}}{\delta h_{\alpha\gamma}(r)} = -\frac{1}{2}\rho^2\beta v_{\alpha\gamma}(r|\epsilon,a), \tag{IV.8}$$

for $0 \leq \alpha,\gamma \leq n$, where $\delta(.)/\delta h_{\alpha\gamma}(r)$ denotes the functional derivative with respect to the correlation function $h_{\alpha\gamma}(r)$ which is evaluated at the position r. As we are interested in the liquid phase above the ideal glass transition and as we focus on homogeneous phases, we assume replica symmetry between the n constrained replicas (replica 0 is different due to the attractive

coupling) in the solution of the above equations and then take the limit $n \to 0$. One thus needs to consider 4 distinct functions, $h^*_{11}(r)$, $h^*_{12}(r)$, $h^*_{00}(r)$ and $h^*_{01}(r)$, where the superscript * means that the functions correspond to the solutions of Eq. (IV.8). This is the equivalent of the replica symmetric ansatz of Eq. (II.28). The latter involves two overlap parameters which represent the overlap with the reference configuration and the overlap between two constrained replicas. The correlation functions $h^*_{01}(r)$ and $h^*_{12}(r)$ play similar roles. The first one represents the correlation function between the positions of the particles in the constrained liquid and in the reference configuration, the second one the correlation function between the positions of the particles in two different constrained replicas. Here we need to add two other correlation functions which correspond to the self correlation functions in the reference configuration $h^*_{00}(r)$ or in a constrained replica $h^*_{11}(r)$.

We want to focus on the correlation between the constrained replicas and the reference one, *i.e.*, on $h_{01}(r)$. This is because it is directly related to the overlap order parameter, see Eq. (IV.13). To do this, one can solve the minimisation equations for $h_{00}(r)$, $h_{11}(r)$ and $h_{12}(r)$. The solutions are then functionals of $h_{01}(r)$ and of the potential $v(r)$, except $h_{00}(r)$ which only depends on $v(r)$ and is decoupled from the other total correlation functions in the limit $n \to 0$. The solutions also depend on ρ and T but they do not explicitely depend on ϵ and a. We call $\mathcal{F}[h_{01}]$ the functional which results from replacing $h_{00}(r)$, $h_{11}(r)$ and $h_{12}(r)$ in $\mathcal{F}[\{h_{\alpha\gamma}\}]$ by their solution. The Morita-Hiroike functional in the limit $n \to 0$ then reads

$$\lim_{n\to 0}\left\{\frac{\Gamma_{\rm MH}[\{h_{\alpha\gamma}\}]-\Gamma_{\rm MH,0}}{n}\right\}\Bigg|_{\rm RS} = -\rho^2\int {\rm d}\boldsymbol{r}[1+h_{01}(r)]\beta\epsilon w(r/a)+\mathcal{F}[h_{01}], \tag{IV.9}$$

where RS denotes replica symmetry and where $\Gamma_{\rm MH,0}$ is the Morita-Hiroike functional for the reference replica, which is evaluated for $h^*_{00}(r)$, and which is obtained by setting $n = 0$ in Eq. (IV.6). The functional $\mathcal{F}[h_{01}]$ is defined by the above equation and it is equal to

$$\mathcal{F}[h_{01}] = \lim_{n\to 0}\left\{\frac{\mathcal{F}\{h_{\alpha\gamma}\}]-\Gamma_{\rm MH,0}}{n}\right\}\Bigg|_{\rm RS} + \frac{1}{2}\rho^2\int {\rm d}\boldsymbol{r}[1+h^*_{11}(r)]\beta v(r). \tag{IV.10}$$

The key point is that the functional $\mathcal{F}[h_{01}]$ is independent of ϵ and a. On the other hand, the function $h^*_{01}(r)$, which is now obtained as the solution of

$$\frac{\delta\mathcal{F}[h_{01}]}{\delta h_{01}(r)} = \rho^2\beta\epsilon w(r/a), \tag{IV.11}$$

depends on ϵ and on a, see Eq. (IV.8). However, when $\epsilon = 0$, the dependence on a drops out because the right-hand side of the above equation is simply zero. We note that there is no factor 1/2 in the above equation because the correlation functions are symmetric, *e.g.*, $h_{10}(r) = h_{01}(r)$. This equation could also be obtained by a direct differentiation of Eq. (IV.9) with respect to $h_{01}(r)$.

Eventually, the replica symmetric free energy $F_a(\epsilon)$ which is introduced in Eq. (II.5) and which corresponds to the free energy of the constrained liquid with fixed ϵ can be derived from the functional $\mathcal{F}[h_{01}]$ as

$$\beta F_a(\epsilon) = \lim_{n\to 0}\left\{\frac{\Gamma_{\rm MH}[\{h_{\alpha\gamma}\}]-\Gamma_{\rm MH,0}}{n\rho}\right\}\Bigg|_{\rm RS} = -\rho\int {\rm d}\boldsymbol{r}[1+h^*_{01}(r)]\beta\epsilon w(r/a)+\frac{1}{\rho}\mathcal{F}[h^*_{01}], \tag{IV.12}$$

by using Eq. (IV.9). The division by ρ in the limit of the above equation comes from the fact that the Morita-Hiroike functional is defined per unit volume. We have also emphasised the dependence on the tolerance length of the free energy with the subscript a.

At this stage, we can come to the Franz-Parisi potential $V_a(Q)$ that we also write with a subscript a to emphasise its dependence on the tolerance length. This is the object of the next section.

2.2 Computation of the Franz-Parisi potential

From Eq. (IV.1) and the definition of $h_{01}(r)$, the average overlap between the constrained and the reference configurations can be expressed as

$$\overline{\langle \hat{Q}_a \rangle_\epsilon} = \rho \int \mathrm{d}\boldsymbol{r}[1 + h_{01}(r)]w(r/a). \tag{IV.13}$$

We recall that the brackets represent the thermal average for a given field ϵ and a fixed reference configuration, while the overline stands for the average over the reference configurations. When the constrained and the reference configurations are uncorrelated, $h_{01}(r) \equiv 0$, and the overlap takes its "random" value

$$Q_{a,\mathrm{rand}} = \rho \int \mathrm{d}\boldsymbol{r} w(r/a). \tag{IV.14}$$

If the canonical ensemble (with fixed ϵ) and the microcanonical ensemble (with fixed overlap) are equivalent, which is the case outside the first order transition region, the Franz-Parisi (FP) potential is obtained by a Legendre-Fenchel transform which yields

$$\beta V_a(Q) = \sup_\epsilon \{\beta F_a(\epsilon) + \beta \epsilon Q\} = \beta F(\tilde{\epsilon}_a) + \beta \tilde{\epsilon}_a Q, \tag{IV.15}$$

see Eq. (II.17). The field $\tilde{\epsilon}_a$, which depends on a, is such that the expression between brackets is maximum, and thus corresponds to the field such that the canonical average of $\hat{Q}$ is precisely Q, see Eq. (II.6). Therefore, the FP potential reads, by using Eq. (IV.12),

$$\beta V_a(Q) = -\rho \int \mathrm{d}\boldsymbol{r}[1 + h^*_{01}(r)]\beta \tilde{\epsilon}_a w(r/a) + \frac{1}{\rho}\mathcal{F}[h^*_{01}] + \beta \tilde{\epsilon}_a Q. \tag{IV.16}$$

As the "random" overlap varies significantly with a, the FP potential is more conveniently expressed in terms of $\Delta Q = Q - Q_{a,\mathrm{rand}}$ rather than Q, and we obtain

$$\beta V_a(\Delta Q) = -\rho \int_{\mathbf{r}} h^*_{01}(r)\beta \tilde{\epsilon}_a w(r/a) + \frac{1}{\rho}\mathcal{F}[h^*_{01}] + \beta \tilde{\epsilon}_a \Delta Q. \tag{IV.17}$$

By definition of $\tilde{\epsilon}_a$, the two terms which explicitely depend on it cancel out, and we eventually obtain

$$\beta V_a(\Delta Q) = \frac{1}{\rho}\mathcal{F}[h^*_{01}], \tag{IV.18}$$

where $h^*_{01}(r)$ is now considered as a function of ΔQ and a.

From the above discussion, we can give a practical way of computing the FP potential. For a given value of ϵ, one can solve Eq. (IV.11) to obtain the correlation function $h^*_{01}(r)$. This amounts to minimising the total Morita-Hiroike functional Γ_{HM}. Then, the FP potential is computed thanks to Eq. (IV.18) and the corresponding value of $\Delta Q = \overline{\langle \Delta \hat{Q}_a \rangle_\epsilon}$ from Eq. (IV.13), namely,

$$\overline{\langle \Delta \hat{Q}_a \rangle_\epsilon} = \overline{\langle \hat{Q}_a \rangle_\epsilon} - Q_{a,\mathrm{rand}} = \rho \int \mathrm{d}\boldsymbol{r} h^*_{01}(r) w(r/a). \tag{IV.19}$$

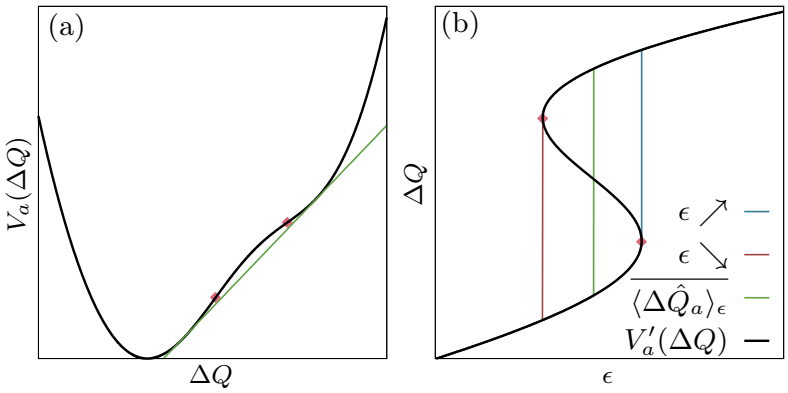

Fig. IV.1 | (a) Schematic representation of the Franz-Parisi (FP) potential $V_a(\Delta Q)$ when it is non-convex. The region between the diamonds corresponds to the range over which the FP potential is concave $[V_a''(\Delta Q) < 0]$. The straight line represents the double-tangent construction to locate the first order transition in the canonical ensemble (fixed ϵ). (b) Derivative of the FP potential and the corresponding isotherm in the canonical ensemble which is obtained by the Maxwell construction of equal areas, see Eq. (II.16). The diamonds correspond to the limit of metastability of the high- and low-overlap branches in the canonical ensemble. The blue and red curves correspond to the average order parameter when ϵ is increased or decreased from a high or low value and they may transiently follow the metastable branches.

By scanning the range of ϵ, we can reconstruct the FP potential. At a high-enough temperature T or a low-enough density ρ, Eq. (IV.11) has a unique solution for each value of ϵ and the full curve of $V_a(\Delta Q)$ can be deduced by systematically varying ϵ. This is the situation above the critical point in the phase diagram (ϵ, T), or equivalently when the FP potential is convex, as the ensembles are equivalent. At lower temperatures or higher densities, Eq. (IV.11) may have two solutions[1] which correspond to two distinct minima of the Morita-Hiroike functional and to two different correlation functions $h_{01}^*(r)$. These two solutions give the stable and the metastable branches of the isotherm $\overline{\langle \Delta \hat{Q}_a \rangle_\epsilon}$ in the canonical ensemble. This is the situation in the first order transition region, or equivalently when the FP potential is no longer convex. In this case, by finding both the stable and the metastable minima, not only are we able to reconstruct the FP potential from Eq. (IV.18) when the two ensembles are equivalent, but also on the entire range of overlap values over which the FP potential is convex, even though the two ensembles are not equivalent, see Fig. IV.1. This range in particular includes the secondary minimum if present.

2.3 Generic properties of the Franz-Parisi potential with respect to the tolerance length

We are now in a position to discuss two generic properties of the Franz-Parisi (FP) potential as a function of the cutoff parameter a.

On the one hand, if the FP potential has several extrema, as it does in mean-field treatments, the value of ϵ at which these extrema are obtained is zero, see Eq. (IV.11) and Eq. (IV.18). As stressed above, the functions $h_{01}^*(r)$ are then independent of a and they correspond to the

[1] More precisely, Eq. (IV.11) can have three solutions but one of them is a maximum of the Morita-Hiroike functional and is thus unstable.

various extrema of the functional $\mathcal{F}[h_{01}]$. The temperature and the density at which these extrema appear and disappear as well as the value of the associated free energy are intrinsic properties of $\mathcal{F}[h_{01}]$ and therefore they do not depend on a. As a result, neither $T_{\rm d}$ at which an horizontal inflexion point appears in the FP potential nor $T_{\rm K}$ at which the two minima of the FP potential become of equal depth depend on the choice of a. However, the value of the overlap at these extrema depends on a through Eq. (IV.13). Requiring for physical consistency that the value of ΔQ at the secondary minimum (that is denoted by $\Delta Q_{\rm g} = Q_{a,{\rm g}} - Q_{a,{\rm rand}}$ in Chap. II) which corresponds to the emerging glass phase is positive may put an upper bound on the value of a, but this does not correspond to a real physical singularity: this point is illustrated and discussed in more detail below. In addition, the complexity, which represents the free energy cost to constrain the liquid within a single metastable state and which corresponds to the height of the secondary minimum in the FP potential, must also be independent of a.

On the other hand, the critical point at $T_{\rm c}$ in the plane (ϵ, T) that we have mentioned in the introduction and studied at length in the simulations of Chap. III corresponds to the temperature at which the FP potential recovers strict convexity in mean-field approximations or in large-enough finite-dimensional systems (see Chap. II). In other words, there is a critical value $\Delta Q_{\rm c}$ of the overlap and a critical field $\epsilon_{\rm c}$ such that

$$\begin{cases} \beta_{\rm c} V_a'(\Delta Q_{\rm c}) = & \beta_{\rm c}\epsilon_{\rm c}, \\ \beta_{\rm c} V_a''(\Delta Q_{\rm c}) = & 0, \\ \beta_{\rm c} V_a'''(\Delta Q_{\rm c}) = & 0, \end{cases} \tag{IV.20}$$

with $\beta_{\rm c} = 1/T_{\rm c}$, see Eq. (II.20). Generically, not only $\Delta Q_{\rm c}$, but also $\epsilon_{\rm c}$ and $T_{\rm c}$ should now depend on a. The location of the critical point, and as a consequence of the whole first order transition line in the phase diagram (ϵ, T), therefore varies with the choice of a. Actually, in the theory of critical phenomena, the non-universal quantities, such as the location of the critical point, are well known to depend on the short-range fluctuations due to the microscopic details of a system, and hence on a [242]. Instead, the universality class of the critical point is controlled by long-range, potentially scale-free, fluctuations and should instead be independent of a. However here, the situation is more subtle because the properties ($T_{\rm d}$ or $T_{\rm K}$) on the $\epsilon = 0$ axis of the phase diagram are also independent of a, and this applies whether or not the system is at criticality.

In the next section we illustrate the above described generic features in the case of an approximate mean-field treatment which is based on the hypernetted chain closure of liquid-state theory.

3. Hypernetted chain approximation and the Franz-Parisi potential

3.1 Presentation of the hypernetted chain closure

The hypernetted chain (HNC) approximation is one of the standard tools of liquid-state theory to describe the structure and the thermodynamics of liquids. It amounts to neglecting the two-particle irreducible diagrams in the Morita-Hiroike functional in Eq. (IV.6) [296, 298]. With this simplification, the functional $\mathcal{F}[h_{01}]$ can be written by using the Fourier transforms

of the correlation functions and reads

$$\begin{aligned}\mathcal{F}[h_{01}] = \rho(\ln\rho - 1) + \frac{1}{2}\rho^2 \int \mathrm{d}\boldsymbol{r}[1 + h^*_{11}(r)]\{\ln[1 + h^*_{11}(r)] - 1 + \beta v(r)\} \\ + \rho^2 \int \mathrm{d}\boldsymbol{r}[1 + h_{01}(r)]\{\ln[1 + h_{01}(r)] - 1\} - \frac{1}{2}\rho^2 \int \mathrm{d}\boldsymbol{r}[1 + h^*_{12}(r)]\{\ln[1 + h^*_{12}(r)] - 1\} \\ + \rho \int \frac{\mathrm{d}\boldsymbol{q}}{(2\pi)^3} \Big\{ h^*_{11}(q) - \frac{\rho}{2} h^*_{11}(q)^2 - \rho h_{01}(q)^2 + \frac{\rho}{2} h^*_{12}(q)^2 - \frac{1}{\rho}\ln\{1 + \rho[h^*_{11}(q) - h^*_{12}(q)]\} \\ + \frac{\rho h_{01}(q)^2}{[1 + \rho h^*_{00}(q)]\{1 + \rho[h^*_{11}(q) - h^*_{12}(q)]\}} - \frac{h^*_{12}(q)}{1 + \rho[h^*_{11}(q) - h^*_{12}(q)]} \Big\},\end{aligned} \tag{IV.21}$$

where $\boldsymbol{q}$ denotes the wave vector (with $q = |\boldsymbol{q}|$), and where we keep the same notation for the functions in Fourier and in real spaces. The minimisation equations in Eq. (IV.8) can be cast in a more familiar form by introducing the direct correlation functions $c_{\alpha\gamma}(r)$ that are related to the total correlation functions by the Ornstein-Zernicke equations [30]. By assuming again replica symmetry in the limit $n \to 0$, one finds in Fourier space [351, 352]:

$$\begin{cases} 1 + \rho h_{00}(q) = \dfrac{1}{1 - \rho c_{00}(q)}, \\ 1 + \rho h_{\mathrm{con}}(q) = \dfrac{1}{1 - \rho c_{\mathrm{con}}(q)}, \\ h_{12}(q) = [1 + \rho h_{\mathrm{con}}(q)]^2 \left\{ c_{12}(q) + \rho[1 + \rho h_{00}(q)] c_{01}(q)^2 \right\}, \\ h_{01}(q) = [1 + \rho h_{00}(q)][1 + \rho h_{\mathrm{con}}(q)] c_{01}(q), \end{cases} \tag{IV.22}$$

where the "connected" correlation functions can be introduced, namely, $h_{\mathrm{con}} = h_{11} - h_{12}$ and $c_{\mathrm{con}} = c_{11} - c_{12}$[2]. The HNC closure which is derived from the minimisation equations can then be written as

$$\begin{cases} c_{00}(r) = & -\beta v(r) + h_{00}(r) - \ln[1 + h_{00}(r)], \\ c_{11}(r) = & -\beta v(r) + h_{11}(r) - \ln[1 + h_{11}(r)], \\ c_{12}(r) = & h_{12}(r) - \ln[1 + h_{12}(r)], \\ c_{01}(r) = & \beta\epsilon w(r/a) + h_{01}(r) - \ln[1 + h_{01}(r)]. \end{cases} \tag{IV.23}$$

From the solution of these equations, one obtains the free energy $\beta F_a(\epsilon)$ [see Eq. (IV.12)] and the Franz-Parisi (FP) potential [see Eq. (IV.18)], whereas the overlap difference with the random limit ΔQ is given by Eq. (IV.19).

The HNC approximation is of mean-field character as it leads to a non-convex potential at low-enough temperatures for glass-forming liquids and then sustains infinitely long-lived metastable states [354]. It has already been well studied in the context of the glass transition [151, 154, 155, 300, 301, 347, 348], including a calculation of the FP potential [154, 155]. Our purpose is not to repeat all of these calculations but to investigate the role of the cutoff parameter a in the definition of the overlap.

[2] In the context of disordered systems, h_{12} and c_{12} are also called the "disconnected" correlation functions [353].

3.2 Models and methods for the numerical resolution of the integral equations

We consider different single-component liquid models in three dimensions in which the particles all have the same diameter σ. We deal with two different interaction potentials: a hard sphere model with the interaction potential

$$v(r) = \begin{cases} +\infty & \text{for } r < \sigma, \\ 0 & \text{otherwise,} \end{cases} \tag{IV.24}$$

and a soft sphere model with the pair potential

$$v(r) = \begin{cases} v_0 \left(\frac{\sigma}{r}\right)^{12} + \kappa_0 + \kappa_2 \left(\frac{r}{\sigma}\right)^2 + \kappa_4 \left(\frac{r}{\sigma}\right)^4 & \text{for } r \leq 1.25\sigma, \\ 0 & \text{otherwise.} \end{cases} \tag{IV.25}$$

The latter has already been introduced[3] in Chap. III, see Eq. (III.1). The control parameter is the density ρ in the hard sphere case and the temperature T in the soft sphere case (in this case, the density is set to $\rho\sigma^3 = 1$). For the threshold function in the definition of the overlap [see Eq. (IV.1) or Eq. (IV.13)], we have chosen the continuous window function $w(x) = e^{-x^4 \ln 2}$ as in Chap. III. In the hypernetted chain approximation where we consider homogeneous configurations, the liquid never crystallises and it always forms an ideal glass through a thermodynamic phase transition at a low-enough temperature T_{K} or a high-enough density ρ_{K}.

Correlation functions in real space are defined on a linear mesh of size $\mathrm{d}r = \sigma/128$ for $a/\sigma \geq 0.1$ and $\mathrm{d}r = \sigma/512$ otherwise (to ensure that $a/\mathrm{d}r > 10$), with a large distance cutoff of $L = 8\sigma$. We have checked that taking a larger cutoff distance and/or a smaller mesh size only leads to very small quantitative changes of our results. The functions in Fourier space are defined on the reciprocal mesh of step $2\pi/L$. Eq. (IV.22) and (IV.23) are solved iteratively. This requires to compute the Fourier transform and its inverse. In $3d$ and for spherically-symmetric functions, this procedure is easily implemented by using the fast sine transform algorithm [238] which relies on the following formulas for a correlation function $h(r)$ and its Fourier transform $h(q)$ [347]:

$$\begin{cases} \dfrac{qh(q)}{2\pi} = 2\displaystyle\int_0^{+\infty} \mathrm{d}r \sin(qr) rh(r), \\ rh(r) = \dfrac{1}{\pi}\displaystyle\int_0^{+\infty} \mathrm{d}q \sin(qr) \dfrac{qh(q)}{2\pi}. \end{cases} \tag{IV.26}$$

In particular, one can directly work with the functions $rh(r)$ and $qh(q)/(2\pi)$ and the sine transform of one function is the other one up to a prefactor.

The iterative resolution of Eq. (IV.22) and (IV.23) is done by using the Picard's method and works in the following way [151]. From the correlation functions $\{c_{\alpha\gamma}^{(k)}(r), h_{\alpha\gamma}^{(k)}(r)\}$ in real space at iteration k, we compute the Fourier transforms of the direct correlation functions $\{c_{\alpha\gamma}^{(k)}(q)\}$. Then, thanks to Eq. (IV.22), we compute the total correlation functions $\{h_{\alpha\gamma}^{(k+1)}(q)\}$ in Fourier space at the next iteration step. After that, the inverse Fourier transforms of the new total correlation functions $\{h_{\alpha\gamma}^{(k+1)}(r)\}$ are computed and the new direct correlation functions $\{c_{\alpha\gamma}^{(\mathrm{new})}(r)\}$ are obtained from Eq. (IV.23). Eventually, to smooth changes in the correlation

[3] We remind that the constants κ_0, κ_2 and κ_4 ensure that $v(r)$ and its two first derivatives are continuous at $r = 1.25\sigma$.

functions between two iterations, we take as direct correlation functions $\{c_{\alpha\gamma}^{(k+1)}(r)\}$ for the next iteration $c_{\alpha\gamma}^{(k+1)}(r) = \eta c_{\alpha\gamma}^{(\mathrm{new})}(r) + (1-\eta)c_{\alpha\gamma}^{(\mathrm{k})}(r)$ with $\eta = 0.1$. The iteration is stopped when the total relative change in all the direct correlation functions between two consecutive iterations, namely,

$$\sum_{\alpha\gamma} \frac{\int \mathrm{d}\boldsymbol{r}[c_{\alpha\gamma}^{(k+1)}(r) - c_{\alpha\gamma}^{(k)}(r)]^2}{\int \mathrm{d}\boldsymbol{r} c_{\alpha\gamma}^{(k)}(r)^2}, \tag{IV.27}$$

is below a threshold of 10^{-10}. As the equations for the reference replica are uncoupled from the others, we can compute $h_{00}(r)$ independently for each temperature T and density ρ and then deal with the three other ones by using $h_{00}(r)$ and $c_{00}(r)$ as inputs.

For a given value of a and a given density ρ (in the hard sphere case) or a given temperature T (in the soft sphere case), we follow the recipe which is pictured in Fig. IV.1 to compute the Franz-Parisi (FP) potential and the phase diagram (ϵ, T). We compute the curves $\overline{\langle \Delta\hat{Q}_a \rangle_\epsilon}^{(\pm)}$ from Eq. (IV.19) by increasing the source ϵ from 0 (+) or decreasing it from a high-enough value (-). The first order transition region is detected when there is a range of ϵ values for which the two curves for increasing and decreasing ϵ differ. With this procedure, we are able to locate the critical point with an arbitrary degree of precision. In the following, we restrict ourselves to a precision of 10^{-3} for $\rho_\mathrm{c}\sigma^3$ and 10^{-5} for $\beta_\mathrm{c}\epsilon_\mathrm{c}$ in the hard sphere case and of 10^{-3} for T_c/v_0 and 10^{-5} for ϵ_c/v_0 in the soft sphere case.

Before presenting our results, we comment on the replica symmetric ansatz we consider here. Such as the spherical p-spin, replica symmetry breaking effects are expected for intermediate values of the overlap [222] and even close to the absolute low-overlap minimum when approaching the Kauzmann transition from above. We have not tried to solve the hypernetted chain equations with a more general one-step replica symmetry breaking ansatz which would require another correlation function $h_{13}(r)$ for replicas that belong to the same metastable state along with a real parameter x for the size of the blocks with off-diagonal elements $h_{13}(r)$ in the matrix of the correlation functions between the replicas. The replica symmetry breaking effects are nonetheless expected to be more limited than for the spherical p-spin [148] because the FP potential cannot be computed anyway in a given range of intermediate values of the overlap because of ensemble inequivalence. We may under-estimate the FP potential at high densities or low temperatures, but its shape is expected to remain qualitatively similar when replica symmetry breaking effects are taken into account.

3.3 Temperature evolution of the Franz-Parisi potential and phase diagram (ϵ, T)

We now illustrate in Fig. IV.2 the behaviour of the Franz-Parisi (FP) potential $V_a(\Delta Q)$ for the hard sphere system as the density increases for two different values of the cutoff parameter, namely, $a/\sigma = 0.2$ and $a/\sigma = 0.5$. The potential has a similar shape and evolution as first found in Ref. [154, 155]. We observe that the FP potential at high densities is not obtained on the entire range $[0, 1]$ because of ensemble inequivalence which is discussed in Sec. 2.2. We nonetheless note that we are able to construct a curve which is not equal to its convex envelop by following the metastable solutions of the hypernetted chain (HNC) equations. In particular, we can detect the secondary minimum in $V_a(\Delta Q)$ when it exists.

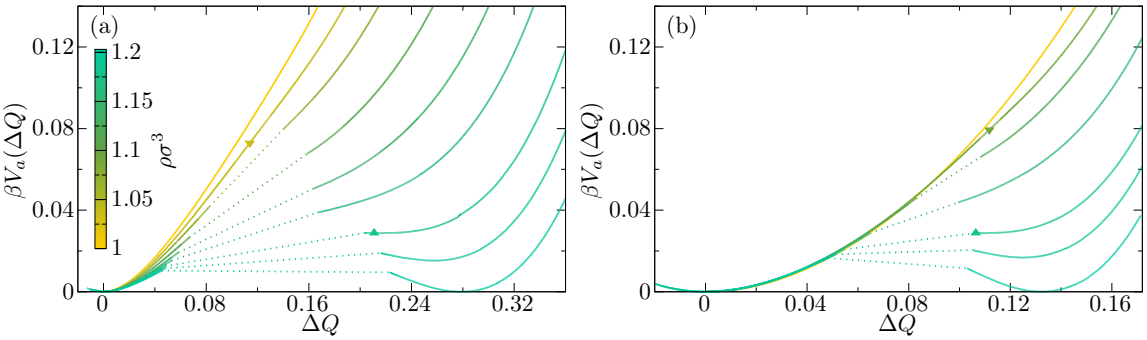

Fig. IV.2 | Evolution with the density of the Franz-Parisi potential $V_a(\Delta Q)$ in the hypernetted chain (HNC) approximation for a three-dimensional hard sphere system, the two replicas of same density $\rho = \rho_0$, and two different values of the cutoff parameter a, namely, (a) $a/\sigma = 0.2$ and (b) $a/\sigma = 0.5$. In both panels, the up and the down triangles mark the values of ΔQ at the dynamical transition (spinodal of the metastable glass minimum) and the critical point in the plane (ϵ, T), respectively. For both figures, the color code is the same and it is given by the colorbar in panel (a). The dotted lines represent the region where there is no replica symmetric solution to the HNC equations in the canonical ensemble.

At $\rho_{\rm K}\sigma^3 = 1.203$ the potential has two minima of equal height and the high-overlap minimum becomes metastable as ρ decreases until it disappears in a saddle point at $\rho_{\rm d}\sigma^3 = 1.183$ (above the value of 1.17 which is given in Ref. [154, 155] but in agreement with the value which is provided in Ref. [151]). At still lower densities, the potential retains a non-convex shape down to some critical density $\rho_{\rm cvx} = \rho_{\rm c}$ at which convexity is eventually recovered. This temperature evolution of the FP potential is what is expected for glassy systems in mean-field which display a random first order transition, see Fig. II.3 (a) for comparison. By comparing the two panels of Fig. IV.2, we stress that the values of $\rho_{\rm K}$ and $\rho_{\rm d}$ do not depend on the choice of a as we have already emphasised. However, those of the overlap at the metastable minimum do depend on a. We also find, as we further describe below, that the value of the critical density $\rho_{\rm c}$ depends on a significantly.

In Fig. IV.3 we show the phase diagram of the hard sphere model in the $(\beta\epsilon, (\rho\sigma^3)^{-1})$ plane for the same two values of a as in Fig. IV.2. As we have already explained in Chap. II, the non-convexities of the FP potential give rise to a line of first order transition which emerges from the thermodynamic glass transition at $\epsilon = 0$ and $\rho = \rho_{\rm K}$. The line ends in a critical point at $(\beta_{\rm c}\epsilon_{\rm c}, (\rho_{\rm c}\sigma^3)^{-1})$. As clearly seen, the location of the line is different for the two values of a, and that of the critical endpoint as well.

4. Hypernetted chain results for the critical endpoint

4.1 Evolution of the critical point with the tolerance length

Overall, the results of the previous section are consistent with previous studies on structural liquids within the hypernetted chain (HNC) approximation and also with mean-field theory [151, 154, 155, 347]. In particular, constrained liquids in the HNC approximation display a line of first order transition from the Kauzmann point which ends in a critical point that is associated with the return to convexity of the Franz-Parisi potential. In this section, we systematically investigate the dependence on a of the critical point in the HNC framework. The critical

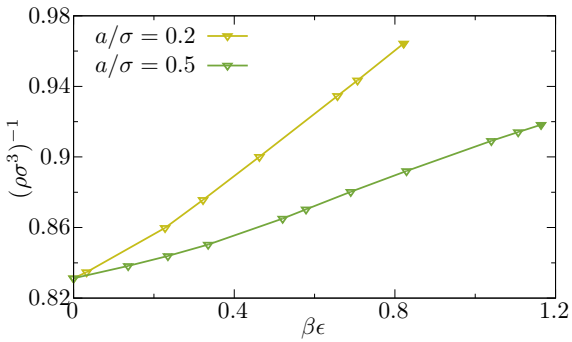

Fig. IV.3 | Phase diagram in the $(\beta\epsilon, (\rho\sigma^3)^{-1})$ plane for the three-dimensional hard sphere model in the hypernetted chain approximation, the two replicas of same density $\rho = \rho_0$, and the two same values of a/σ as in Fig. IV.2. A line of first order transition (empty symbols) emerges from the random first order transition at $\epsilon = 0$ and it ends in the critical point (full symbol) at $(\beta_c\epsilon_c, (\rho_c\sigma^3)^{-1})$. The line of first order transition has been obtained thanks to the Maxwell construction of equal areas on the isotherms $\overline{\langle \Delta\hat{Q}_a \rangle_\epsilon}^{(\pm)}$.

density $\rho_c(a)$ for hard spheres or the critical temperature $T_c(a)$ for soft spheres along with the critical overlap $\Delta Q_c(a)$ are determined by the two last conditions in Eq. (IV.20), while $(\beta_c\epsilon_c)(a)$ is obtained from the first equality in Eq. (IV.20). Their variation with a is shown in Fig. IV.4, panels (a)-(c) for the hard sphere system and panels (d)-(f) for the soft sphere case.

We first analyse the variation with a of the critical density $\rho_c(a)$ for hard spheres and the critical temperature $T_c(a)$ for soft spheres. Both quantities vary by a large amount: more than 15 % for ρ_c and a factor of 2 for T_c over the covered range of a. For comparison, we recall that within HNC the relative change between ρ_d and ρ_K for hard spheres is 1.7 %. Similarly, we have found that the relative change between T_d and T_K for soft spheres is about 14 %[4]. Furthermore, the evolution of either ρ_c or T_c with a is non-monotonic with a minimum in ρ_c for $a \simeq 0.08\sigma$ and a maximum in T_c for $a \simeq 0.09\sigma$. By choosing a/σ around 0.08-0.09, one can then move the critical point in the liquid phase quite significantly away from the dynamic and the thermodynamic glass transitions, as compared to the conventional choice of $a = 0.3\sigma$.

We now look at the values of the source or coupling $\epsilon_c(a)$ [or rather of $(\beta_c\epsilon_c)(a)$] and of the overlap $Q_c(a)$ [or rather of the difference $\Delta Q_c(a)$ with the random value] at the critical point. Their variations with a are non-monotonic, with a minimum in $\beta_c\epsilon_c$ and a maximum in ΔQ_c around $a \simeq 0.35\sigma$, both for the hard sphere and the soft sphere systems. In particular, we observe that their behaviour is of different trend as the one of ρ_c or T_c. We also note that the variation with a of the location of the critical point is not given by a simple physical argument. Indeed, one could naively expect the source at the critical point ϵ_c to be a decreasing function of the coarse-graining parameter a. Smaller lengthscales a lead to a localisation of the atoms in the constrained liquid in a smaller volume and may require larger fields. This is indeed what is observed at small values of a but the behaviour at larger values of a clearly contradicts this naive expectation. The observed non-monotonic trend and the detailed evolution at small a and large a are much more involved, and this stems from the non-trivial structure and variation with a of the pair correlation functions.

Before discussing these two limits, we show in Fig. IV.5 the HNC total correlation functions

[4]For our model, $T_d/v_0 = 0.0535$ and $T_K/v_0 = 0.0464$ are obtained via the temperature evolution of the Franz-Parisi potential, similar to Fig. IV.2.

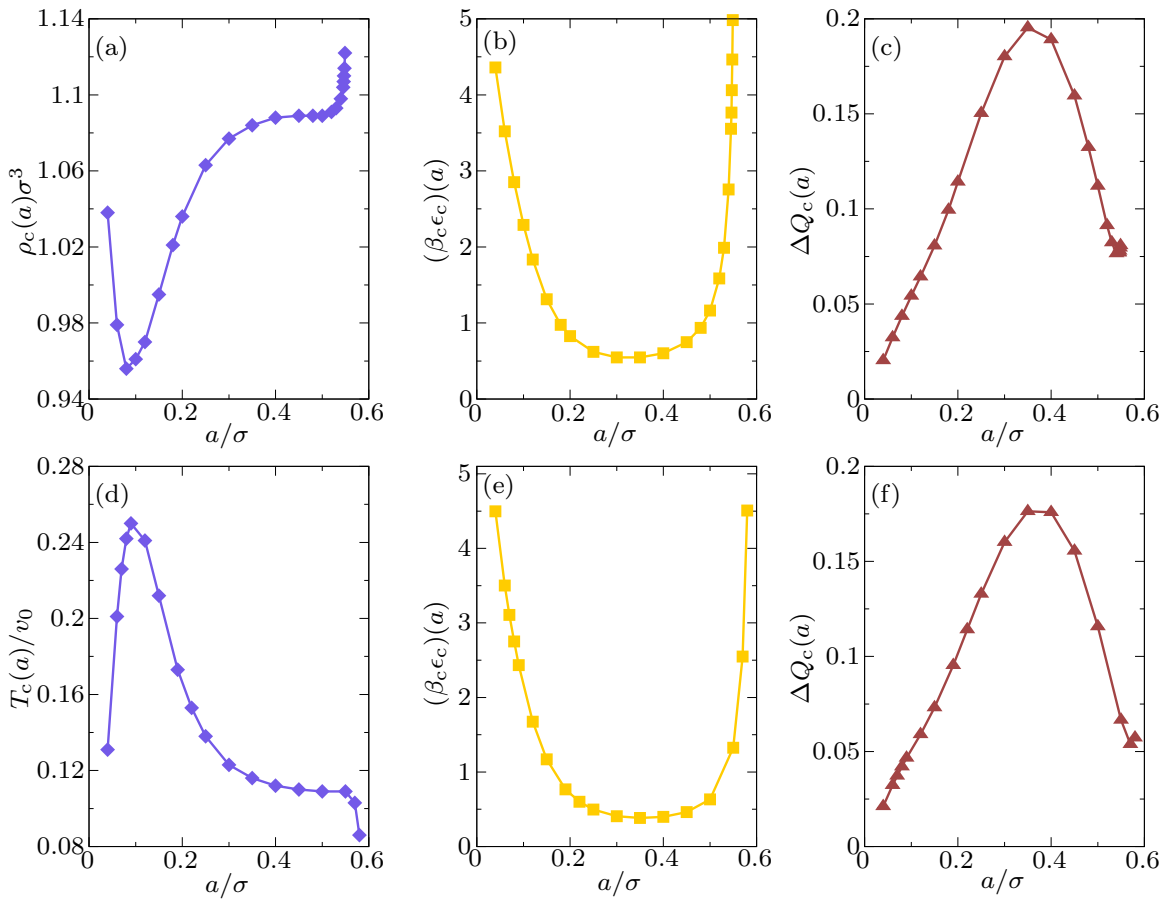

Fig. IV.4 | Variation with the cutoff parameter a in the hypernetted chain approximation of (a) the critical density $\rho_c(a)$, of (b) the critical value of the source $(\beta_c\epsilon_c)(a)$, of (c) the overlap difference $\Delta Q_c(a)$ at the critical point for the three-dimensional hard sphere system for the the two replicas of equal density and of (d) the critical temperature $T_c(a)$, of (e) the critical value of the source $(\beta_c\epsilon_c)(a)$ and of (f) the overlap difference $\Delta Q_c(a)$ at criticality for soft spheres and the two replicas of equal temperature.

$h_{01,c}(r)$, $h_{12,c}(r)$, and $h_{11,c}(r)$ at criticality for a wide range of values of a in the case of the hard sphere system (we now drop the superscript *). We first note that due to the hard-core exclusion, $h_{11,c}(r) = -1$ for $r < \sigma$. We see that $h_{11,c}(r)$ does not vary much with a and that it reflects the liquid structure with periodic peaks of spacing σ which correspond to the consecutive shells around a given particle at $r = 0$. We also remark that the maximum in $h_{11,c}(r)$ (which is marked with a full disk) is non-monotonic with a, and that the highest maxima are obtained for low or high values of a. This is a direct consequence of the fact that $\rho_c(a)$ is a non-monotonic function of a and that it is also maximum for high or low values of a. In fact, we have found that $h_{11,c}(r)$ is always very similar to $h_{00,c}(r)$ which we recall do not depend on a but only on $\rho_c(a)$, see Appendix A. On the other hand, $h_{01,c}(r)$ and $h_{12,c}(r)$ have a non-trivial r dependence on a scale $r \sim a < \sigma$. This amounts to the fact that if there is a particle at $r = 0$ in a constrained replica, *e.g.*, replica 1, then there is a non-zero probability to find a particle at a distance smaller than a in another constrained replica, *e.g.*, replica 2, or in the reference replica 0. At larger distances, we observe periodic peaks of spacing σ due to the underlying structure of the liquid. Interestingly, we observe that the value of the two correlation functions at small $r \ll a$ varies significantly

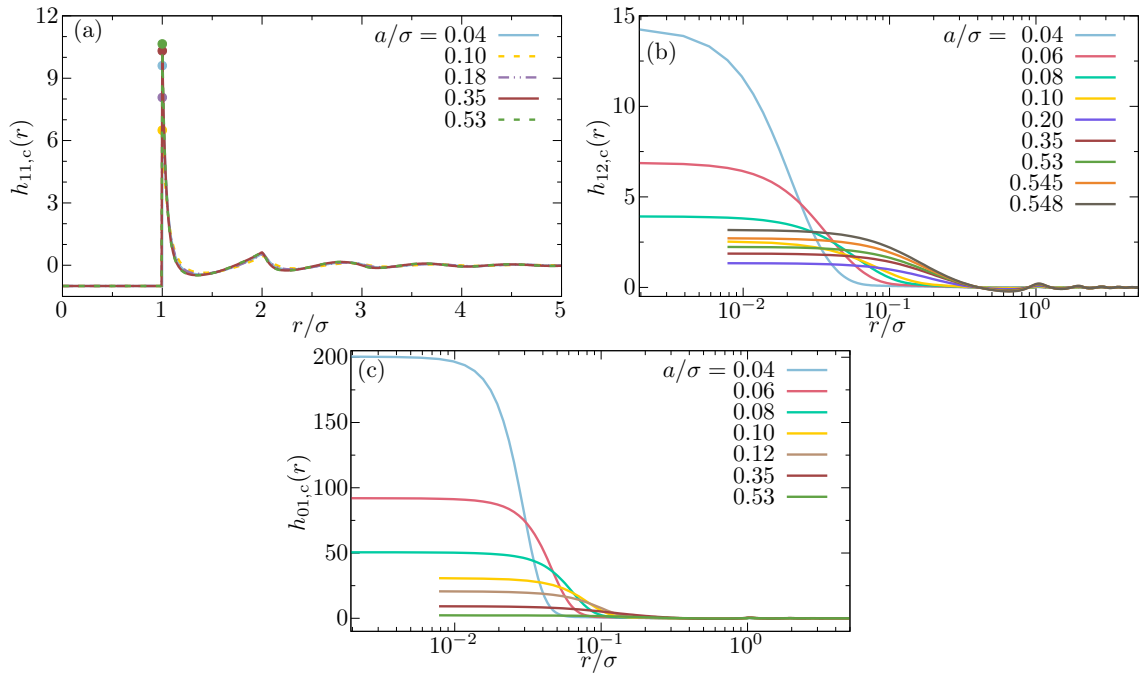

Fig. IV.5 | Total correlation functions (a) $h_{11,c}(r)$, (b) $h_{12,c}(r)$, and (c) $h_{01,c}(r)$ versus r/σ (on a linear scale for the first panel and on a logarithmic scale for the two last ones) at criticality for a wide range of values of a for hard spheres in the hypernetted chain approximation and for the two replicas of equal density. In panel (a) the full disk marks the maximum value in $h_{11,c}(r)$.

with a as it strongly increases as a decreases when $a \leq 0.2\sigma$. In particular, this means that if two constrained replicas have a given finite overlap with the reference configuration, then their mutual overlap is also finite and non-zero.

4.2 Behaviour at small values of the tolerance length

We now focus on the limit in which $a \to 0^+$, where as seen from Fig. IV.4 and Fig. IV.5, $\Delta Q_c(a)$ seems to go to 0 whereas $(\beta_c \epsilon_c)(a)$ and the values of $h_{01,c}(r)$ and $h_{12,c}(r)$ for $r \ll a$ seem to diverge. To make some progress in trying to rationalise this limiting behaviour, we assume that $\rho_c(a)$ and $T_c(a)$ remain strictly positive and finite when $a \to 0^+$, which is compatible with the data in Fig. IV.4 (a) and Fig. IV.4 (d). We also assume that the total correlation functions $h_{01,c}(r)$ and $h_{12,c}(r)$ can be decomposed into a part that varies on the scale of a, whose amplitude grows as $a \to 0^+$, and a part that varies on the scale of σ, whose amplitude goes to zero as $a \to 0^+$ (we remind that when $a = 0$, the replicas are decoupled, *i.e.*, $h_{12} = h_{01} \equiv 0$ and $h_{11} = h_{00}$). The function $h_{11,c}(r)$ on the other hand only varies on the scale of σ with a $O(1)$ amplitude, and so does $h_{00,c}(r)$ (which is independent of a).

Through heuristic arguments in the limit $a \to 0^+$ (see Appendix A), we derive that a consistent solution of the equations is obtained for the total correlation functions at criticality

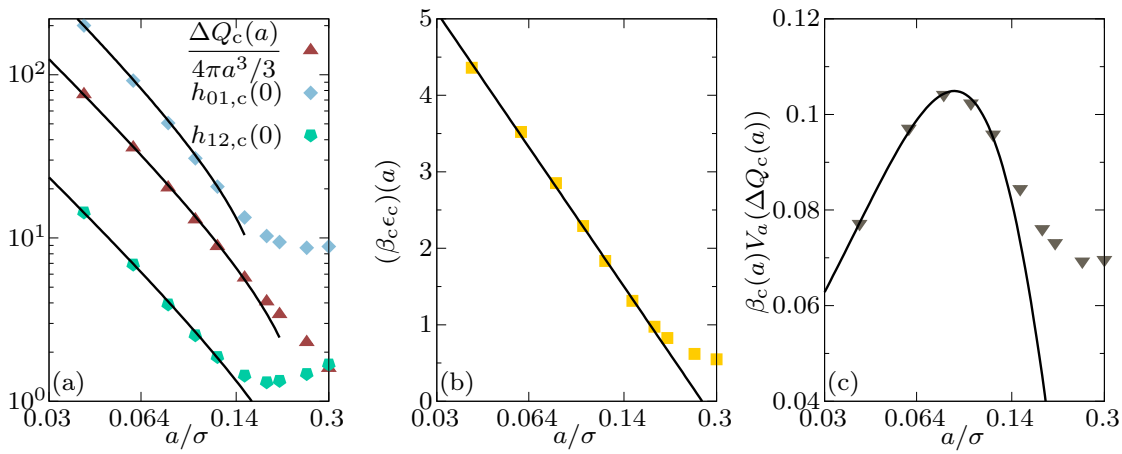

Fig. IV.6 | Limit $a \to 0^+$ of the hypernetted chain calculation in the case of hard spheres for the two replicas of equal density. (a) Plot of $\Delta Q_c(a)/(4\pi a^3/3)$, $h_{01,c}(r \to 0)$ and $h_{12,c}(r \to 0)$ versus a/σ on a double logarithmic scale. The continuous lines show the expected $a^{-3/2}|\ln a|^{1/2}$ dependence. (b) $(\beta_c\epsilon_c)(a)$ on a linear scale versus a/σ on a logarithmic scale along with the expected $|\ln a|$ behaviour (continuous line). (c) $\beta_c(a)V_a(\Delta Q_c(a))$ on a linear scale versus a/σ on a logarithmic scale along with the expected $a^{3/2}|\ln a|^{3/2}$ trend (continuous line).

in the form

$$\begin{cases} h_{01,c}(r) = & a^{-3/2}|\ln a|^{1/2}\hat{h}_{01}(r/a) + a^{3/2}|\ln a|^{1/2}\tilde{h}_{01}(r/\sigma), \\ h_{12,c}(r) = & a^{-3/2}|\ln a|^{1/2}\hat{h}_{12}(r/a) + a^{3/2}|\ln a|^{1/2}\tilde{h}_{12}(r/\sigma), \\ h_{11,c}(r) = & \tilde{h}_{00}(r/\sigma) + O(a^3|\ln a|)\,, \\ h_{00,c}(r) = & \tilde{h}_{00}(r/\sigma), \end{cases} \tag{IV.28}$$

where all the functions $\hat{h}_{\alpha\gamma}(x)$ and $\tilde{h}_{\alpha\gamma}(x)$ have an amplitude and a range of $O(1)$. With the above ansatz, one finds for the critical overlap

$$\Delta Q_c(a \to 0^+) \sim a^{3/2}|\ln a|^{1/2} 4\pi\rho_c(0^+)\int_0^\infty \mathrm{d}x x^2 w(x)\hat{h}_{01}(x), \tag{IV.29}$$

and for the critical source, by using the HNC closure equations (IV.23),

$$(\beta_c\epsilon_c)\,(a \to 0^+) \sim \widehat{\beta\epsilon}|\ln a|, \tag{IV.30}$$

with $\widehat{\beta\epsilon}$ a constant. In particular, one finds that

$$\beta_c(a)V_a(\Delta Q_c(a)) \simeq (\beta_c\epsilon_c\Delta Q_c)\,(a) \sim (a|\ln a|)^{3/2} \times 4\pi\rho_c(0^+)\widehat{\beta\epsilon}\int_0^\infty \mathrm{d}x x^2 w(x)\hat{h}_{01}(x) \tag{IV.31}$$

when $a \to 0^+$.

We compare the above predictions with the numerical solution of the HNC equations for small a in Fig. IV.6 for the hard sphere system. Similar trends are observed for the soft sphere case. The limit when $r \to 0$ of the correlations functions are assimilated at their value for $r = \mathrm{d}r$. We observe that $\Delta Q_c(a)/(4\pi a^3/3)$, $h_{01,c}(r \to 0)$, and $h_{12,c}(r \to 0)$ all diverge as $a^{-3/2}|\ln a|^{1/2}$ [panel (a)], that $(\beta_c\epsilon_c)(a)$ diverges as $|\ln a|$ [panel (b)] and that $\beta_c(a)V_a(\Delta Q_c(a))$ vanishes as $a^{3/2}|\ln a|^{3/2}$ [panel (c)], as expected from the above equations. Even though the results agree with the predictions correctly, data at lower values of a could be beneficial to have further

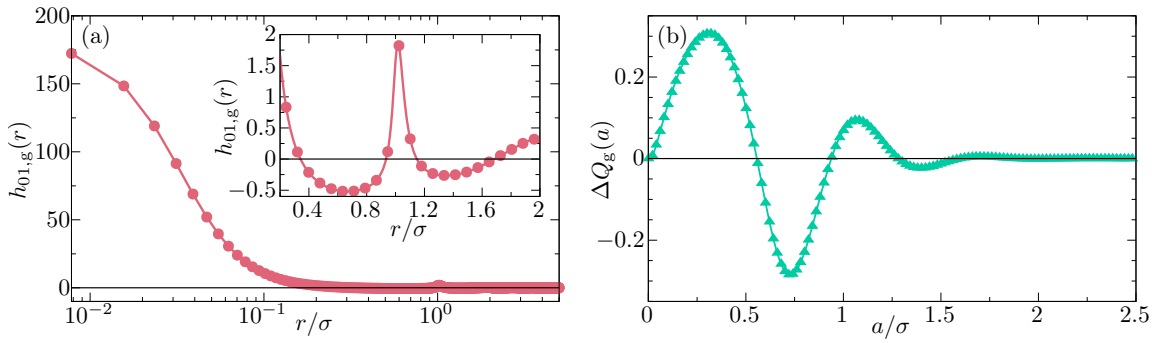

Fig. IV.7 | Result for the metastable glass minimum of the Franz-Parisi potential in the hypernetted chain approximation for hard spheres at a density $\rho\sigma^3 = 1.193$ which is intermediate between ρ_{d} and ρ_{K} and the two replicas of equal density $\rho = \rho_0$: (a) total correlation function $h_{01,\mathrm{g}}(r)$ and (b) difference in overlap ΔQ_{g} with the global minimum as a function of a, see Eq. (IV.32).

confirmation. However, we have not succeeded in obtaining the position of the critical point for $a < 0.04$. Several reasons can be found. On the one hand, when $a \to 0$, all the singular features of the Franz-Parisi potential become concentrated on a very narrow region as $\Delta Q_{\mathrm{c}} \to 0$ and finding the critical point accurately becomes more difficult. On the other hand, for smaller values of a the critical point may be described by a one-step replica symmetry breaking ansatz and thus cannot be obtained with our more simple replica symmetric solution.

4.3 Behaviour at large values of the tolerance length

Finally, we discuss the case of large values of a. As can be seen from Fig. IV.4 (c) and Fig. IV.4 (f), the overlap difference $\Delta Q_{\mathrm{c}}(a)$ with its random value [which gives the location of the stable liquid minimum of the Franz-Parisi (FP) potential] decreases as a increases for $a/\sigma \gtrsim 0.35$ and seems to stick to a finite value for $a/\sigma \simeq 0.55$. For $a \gtrsim 0.55$, the numerical solutions of Eq. (IV.22) and (IV.23) become more difficult to follow even for $\rho \geq \rho_{\mathrm{d}}$ (or $T \leq T_{\mathrm{d}}$). At the same time, the hypernetted integral equations do not seem to be driven to any singularity.

To try to understand this behaviour, we first analyse the behaviour of the metastable minimum when it exists, *i.e.*, beyond the dynamical transition. As we have already noted, the total correlation functions at the minima of the FP potential are independent of a. We introduce $\Delta Q_{\mathrm{g}}(a)$ the difference between the overlap at the metastable glass minimum and that at the global minimum for $\rho \geq \rho_{\mathrm{d}}$. By using Eq. (IV.19), it equals

$$\Delta Q_{\mathrm{g}}(a) = 4\pi\rho \int_0^{+\infty} \mathrm{d}r r^2 w(r/a) h_{01,\mathrm{g}}(r), \tag{IV.32}$$

with $h_{01,\mathrm{g}}(r)$ the total correlation function between a constrained replica and the reference one at the secondary minimum of the FP potential, which again is independent of a. In Fig. IV.7 (a), we show $h_{01,\mathrm{g}}(r)$ for the hard sphere model at a density $\rho_{\mathrm{d}} < \rho < \rho_{\mathrm{K}}$. We clearly observe that it becomes negative for $r \gtrsim 0.35\sigma$. Hence, if a becomes too large, the integral in Eq. (IV.32) can become negative for some values of a. This is directly shown in Fig. IV.7 (b) where we plot ΔQ_{g} as a function of a: it is positive for small values, then it turns negative for $a/\sigma \geq 0.556$, it becomes positive again for $a/\sigma \geq 0.938$ and it eventually weakly oscillates around a slightly positive value. This is found for all the densities above ρ_{d}. The value a_*/σ for which $\Delta Q_{\mathrm{g}}(a)$ first turns negative does not vary much with density: it is equal to 0.5576 at ρ_{d} and to 0.555 at ρ_{K}.

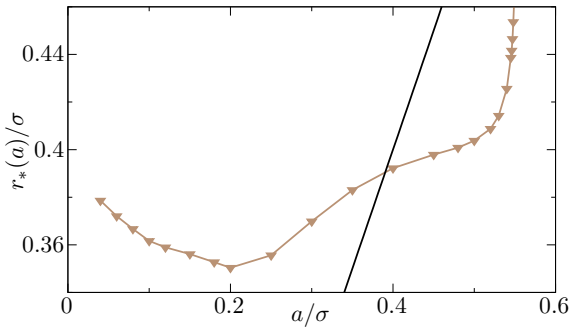

Fig. IV.8 | Lowest value of r for which $h_{01,\mathrm{c}}(r)$ vanishes. The straight line which corresponds to the equation $r_*(a) = a$ crosses the data for $a \simeq 0.39$.

In consequence, while the underlying physics is unchanged, by changing the cutoff parameter in the definition of the overlap, one can switch from correlated replicas at the metastable glass minimum ($\Delta Q_\mathrm{g} > 0$) to anti-correlated replicas ($\Delta Q_\mathrm{g} < 0$). For physical reasons, working with $\Delta Q_\mathrm{g} > 0$ and restricting the range of a to $a < a_*$ seem more pleasant, but this restriction is not motivated by the presence of a physical singularity.

From the above considerations, we can rationalise the evolution of the critical point as a/σ approaches values close to 0.55. By replacing for simplicity the smooth $w(r/a)$ by a discontinuous step function, we can rewrite the critical value of the overlap as

$$\Delta Q_\mathrm{c}(a) \simeq 4\pi\rho_\mathrm{c}(a) \int_0^a \mathrm{d}r r^2 h_{01,\mathrm{c}}(r). \tag{IV.33}$$

The maximum in $\Delta Q_\mathrm{c}(a)$ [see Fig. IV.4 (c) and Fig. IV.4 (f)] should then appear in the close vicinity of the value of a for which $a = r_*(a)$, where $r_*(a)$ is the lowest value of r for which $h_{01,\mathrm{c}}(r) = 0$. This quantity is plotted in Fig. IV.8. We observe that the equality $a = r_*(a)$ is obtained for $a \simeq 0.39\sigma$, consistently with the position of the maximum in $\Delta Q_\mathrm{c}(a)$ at $a_\mathrm{max}/\sigma \simeq 0.35$. For $a > a_\mathrm{max}$, $\Delta Q_\mathrm{c}(a)$ decreases because the integral involves negative values of $h_{01,\mathrm{c}}(r)$. As a result, when ΔQ_c becomes too small, all the non-trivial features of the FP potential become concentrated essentially in a point and one can no longer numerically solve Eq. (IV.20), such as in the case of small values of a. However, this is not associated with any physical phenomenon.

We now discuss what happens when a is further increased above 0.55. For a small range of values of a, namely, for $0.555 \leq a \leq 0.5576$ (see above), an unrealistic behaviour of the phase transition line between low-overlap and high-overlap phases is expected, which includes a divergence and a change of sign of ϵ along the first order transition line between ρ_d and ρ_K. Then, for larger values of a (but still lower than the next value of a for which ΔQ_g vanishes), a well behaved first order transition line should be found, yet with a critical endpoint which is characterised by $\Delta Q_\mathrm{c}(a) < 0$ and $\beta_\mathrm{c}(a)\epsilon_\mathrm{c}(a) < 0$. This is confirmed by the results in Fig. IV.9 which are obtained in the three-dimensional hard sphere model and for a value of the cutoff parameter $a = 0.73\sigma$. In Fig. IV.9 (a), we plot the FP potential, which has the same behaviour as in Fig. IV.2 except that all its noticeable characteristics are located in the range $\Delta Q < 0$. In particular, we still find that the FP potential develops an inflexion point at $\Delta Q_\mathrm{g} < 0$ with a horizontal tangent line at the dynamical transition and a symmetric double-well structure at the Kauzmann transition. In addition, as the FP potential displays non-convexities, a critical point is indeed found but with $\beta_\mathrm{c}\epsilon_\mathrm{c} < 0$ and a negative critical overlap difference, as illustrated

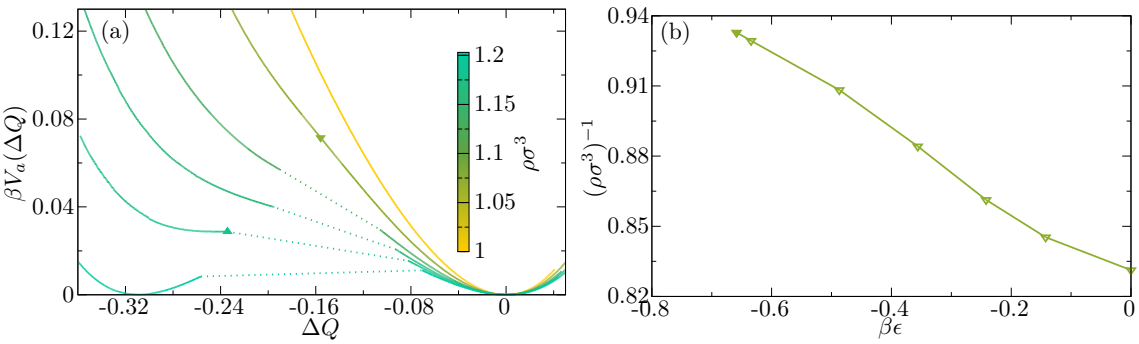

Fig. IV.9 | Results for three-dimensional hard spheres in the hypernetted chain (HNC) approximation, $a/\sigma = 0.73$, and the two replicas of equal density. (a) Franz-Parisi potential for various densities which are indicated by the colorbar. The dotted lines represent the regions where there is no replica symmetric solution to the HNC equations in the canonical ensemble. The up and down triangles mark the inflexion point at the dynamical transition and at the critical density respectively. (b) Phase diagram in the $((\rho\sigma^3)^{-1}, \beta\epsilon)$ plane with the critical point which is emphasised with a closed symbol. The line of first order transition has been obtained thanks to the Maxwell construction of equal areas on the isotherms $\overline{\langle \Delta\hat{Q}_a \rangle_\epsilon}^{(\pm)}$.

in Fig. IV.9 (b). A corresponding line of first order transition is found in the region of negative source and it converges to the Kauzmann transition at zero source.

We have so far developed a complete description of the evolution of the critical point with the coarse-graining parameter a in the limit of liquid-state theory in the hypernetted chain approximation. In the next section, we confront these results with computer simulations by using the methods of Chap. III to assess their degree of generality.

5. Confronting the hypernetted chain results with computer simulations

To complement the detailed but approximate analysis that we have obtained through the hypernetted chain (HNC) treatment, we turn to the three-dimensional glass-forming liquid model of soft spheres which is studied in Chap. III, and we perform computer simulations with the swap algorithm to accelerate the thermalisation. The computer model is very similar to the soft sphere case of our above analytical calculations, but two differences must be noted. On the one hand, the simulations deal with a continuous polydisperse mixture and non-additive cross-diameters to avoid crystallisation and fractionation [54]. On the other hand, the computer simulations of Chap. III are mostly performed for the case of a fixed temperature of the reference configurations $T_0/v_0 = 0.06$ close to the extrapolated glass transition temperature in order to push to higher temperatures the critical point. Instead, the above analytical calculations in the HNC approximation are obtained for the case $T = T_0$. To allow for a comparison with HNC predictions, we repeat the HNC calculations for the case where $T_0 \neq T$ is held fixed and for the single-component soft sphere liquid. To be quantitatively similar with the choice of the temperature of the reference configurations in the simulations, we consider an intermediate T_0 between T_d and T_K, namely, $T_0/v_0 = 0.0499$ and we then solve the equations of the HNC approximation. In this situation, the correlation functions for the reference replica are computed once and for all independently and they are then used as an input for the subsequent calculations with a source ϵ.

In the simulations, the statistical properties of the overlap are computed by using an umbrella sampling and a subsequent reweighting [283], see Chap. III for details about the methods. This strategy enables us to compute the Franz-Parisi potential but also all the thermodynamic properties of the liquid when it is coupled to the quenched reference configuration with an arbitrary applied source ϵ. In particular, for each temperature in the simulations, we can determine the disorder-averaged probability distribution $\overline{\mathcal{P}_\epsilon(Q;\boldsymbol{r}_0^N)}$ of the overlap for the value of the source $\epsilon = \epsilon^*(T,T_0)$ that maximises the total susceptibility (*i.e.*, the total variance of the order parameter). These distributions are shown in Fig. III.6 for a system of size $N = 600$ particles with $a = 0.22\sigma$. We notice that the probability distribution of the overlap becomes bimodal for temperatures significantly above the critical temperature T_c. We recall that for the same value of a, $T_\mathrm{c} \simeq 0.17$ while the distributions are already bimodal for $T \leq 0.30$. As a result, above the critical point (along the "Widom line") and as long as the overlap distribution is bimodal, we can study the overlap fluctuations by restricting the integration over the overlap values to one of the two peaks [211]. In the following, we focus on the low-overlap connected susceptibility $\chi_\epsilon^{(\mathrm{con,\,low})}$ at $\epsilon = \epsilon^*(T,T_0)$ for each temperature T of the constrained liquid, which represents the disorder-averaged amplitude of the thermal fluctuations of the order parameter in the low-overlap "phase".

Rigorously, as already emphasised in the previous chapter, the location of the critical point in a simulation study can only be found through a finite-size scaling analysis. For instance, by taking into account the dependence on a, the low-overlap connected susceptibility on the Widom line should scale as

$$\chi_{\epsilon^*}^{(\mathrm{con,\,low})}(T,T_0) = B_a L^{2-\eta}\tilde{\chi}_{\mathrm{con,\,low}}(y_a t L^{1/\nu}), \tag{IV.34}$$

with $t = T/T_\mathrm{c}(a) - 1$ the reduced temperature, $L \propto N^{1/3}$ the linear size of the system, η and ν some critical exponents, $\tilde{\chi}_{\mathrm{con,low}}(x)$ a universal scaling function, and B_a and y_a a-dependent constants, see Eq. (III.36). We recall that statistical field theory arguments predict that the critical point is in the universality class of the random-field Ising model (RFIM) [218, 250], and this is confirmed by our results in Chap. III. Therefore, η and ν should be taken as the critical exponents of the $3d$ RFIM. The scaling function $\tilde{\chi}_{\mathrm{con,low}}(x)$ has a maximum for $x = x^*$ which can be understood by studying the two limits of low and high temperatures. On the one hand, at a temperature T which is smaller than T_c, the probability distribution of the overlap at $\epsilon^*(T,T_0)$ is composed of two well-separated and narrow peaks. The width of the peaks decreases with decreasing the temperature, which makes $\chi_{\epsilon^*}^{(\mathrm{con,\,low})}$ smaller and smaller as T is reduced. For T larger than T_c but not too large, the overlap probability distribution at $\epsilon^*(T,T_0)$ is bimodal. When T is raised, the peaks merge and the free energy barrier between the low- and the high-overlap peaks vanishes, which leads to a decrease in $\chi_{\epsilon^*}^{(\mathrm{con,\,low})}$ with increasing T. The position of the maximum in the connected susceptibility corresponds to a temperature $T^*(a,L) = T_\mathrm{c}(a)(1 + x^* L^{-1/\nu}/y_a)$. If one assumes that y_a depends only slightly on a, the measure of $T^*(a,L)$ at a fixed system size ($N = 600$ in the remaining of this section) gives a reasonable proxy for the evolution of the critical temperature with a, but the absolute value of the temperature is too high.

A comparison between the results of the simulations and the HNC calculations is shown in Fig. IV.10. The trends as a decreases are very similar, in particular a sharp increase in the temperature is found. The HNC prediction for the critical temperature $T_\mathrm{c}(a)$ passes through a maximum around $a/\sigma \simeq 0.09$ whereas the simulation data appear to plateau at the lowest studied values. It is unclear if this difference would persist at even lower values of a in the simulations or with a better determination of the critical temperature. However, studying such

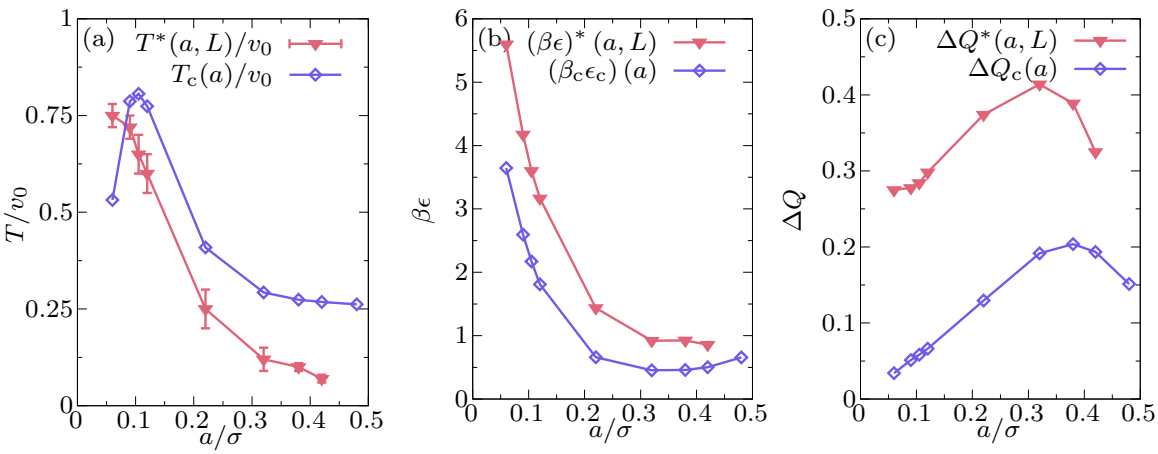

Fig. IV.10 | Comparison between the results of computer simulations of a size-polydisperse mixture of $N = \rho L^3 = 600$ ($\rho\sigma^3 = 1$ with σ the average diameter of the particles) soft spheres with a reference configuration at a low temperature $T_0 = 0.06v_0$ and the results of the hypernetted chain (HNC) calculations for a single-component soft sphere liquid ($\rho\sigma^3 = 1$ with σ the diameter of the particles) with a reference configuration at a temperature $T_0 = 0.0499v_0$. (a) Location of the maximum of the low-overlap connected susceptibility $T^*(a,L)$ for the simulations and of the critical temperature $T_c(a)$ for the HNC calculations. The temperature $T^*(a,L)$ in simulations has been bounded by running simulations at different temperatures T and this provides our errorbar for the estimate of $T^*(a,L)$. (b) Estimates of the source on the Widom line $(\beta\epsilon)^*(a,L) = \epsilon^*(T^*(a,L),T_0)/T^*(a,L)$ in the simulations and of the critical source $(\beta_c\epsilon_c)(a)$ in the HNC calculations. (c) Plot of the average overlap difference with the random limit $\Delta Q^*(a,L)$ at the temperature $T^*(a,L)$ and the source $\epsilon^*(T^*(a,L),T_0)$ in the simulations and of the overlap difference at criticality $\Delta Q_c(a)$ in the HNC approximation. Errorbars on $T^*(a,L)$ propagate to $(\beta\epsilon)^*$ and $\Delta Q^*(a,L)$ but they are not reported.

small values of a becomes computationally prohibitively costly as one has to reduce the time step in the integration of the equations of motion due to the increasing forces which derive from the umbrella potential when a decreases. The agreement is also good when comparing the evolution of the critical value of the source $\beta\epsilon$. For both simulation and HNC results, this quantity first decreases with increasing a. The HNC prediction for $(\beta_c\epsilon_c)(a)$ reaches a minimum for $a/\sigma \simeq 0.35$ and it subsequently increases with a slowly while it seems to plateau in the simulations. However, for the latter, the critical point falls in a temperature range for which the equilibration becomes difficult to ensure, even with the swap algorithm. Consequently, we cannot state whether the quantity $(\beta\epsilon)^*$ in the simulations would eventually increase when a gets even larger, or whether this tendency would remain with a better determination of the critical point. Finally, the evolution of $\Delta Q_c(a)$ strengthens the agreement between the simulations and the HNC calculations. In both cases, we observe an increase with a at small values of a, which is followed by a maximum for $a/\sigma \simeq 0.35$, and a subsequent decrease. This indicates that our above discussion about the a-dependence of $h_{01,c}(r)$ also seems to hold in the numerical simulations.

The evolutions with a in the simulations and in the HNC treatment of a three-dimensional glass-forming liquid are thus in qualitative agreement. This is in spite of expected discrepancies that we list now. First, although the interaction potential has the same analytical form in both cases, the numerical study is performed with continuous size-polydisperse systems to avoid crystallisation and demixing, while the HNC calculations are done in a monodisperse system. Besides, the HNC equations are mean-field-like and they lack non-trivial long-range fluctua-

tions. Finally, finite-size effects close to the critical point may depend on a, which may lead to varying systematic errors in the determination of $T_c(a)$ in computer simulations from $T^*(a, L)$. Nevertheless, the results of this section overall suggest that the fate of the critical point and of the first order transition line with finite ϵ when varying a goes beyond the HNC approximation.

6. Discussion

6.1 Dependence of the overlap fluctuations on the tolerance length

In this chapter, we have studied the influence of the coarse-graining length a on the definition of the overlap or similarity which describes the complex free energy landscape of glassy systems and which also provides the order parameter for the glass transition at the mean-field level. We have more precisely focused on the dependence of the overlap fluctuations on the parameter a/σ in three-dimensional models of glass-forming liquids by relying on the hypernetted chain (HNC) approximation of liquid-state theory. We have shown that while the dynamical and thermodynamic glass transitions in this mean-field-like approximation are independent of a/σ, the whole phase diagram which involves a transition between a low-overlap phase and a high-overlap one in the presence of an applied source ϵ strongly depends on the value of a/σ. We have rationalised through analytical and numerical arguments the evolution of the location of the critical point ending the transition line between low-overlap and high-overlap phases for small and large values of a/σ and we have also confirmed the theoretical predictions by computer simulations of a three-dimensional size-polydisperse glass-forming liquid.

At the level of the HNC approximation, but also in computer simulations, we have clearly shown that the critical temperature T_c is pushed up by a factor of 2 or more for values of a/σ that are significantly lower than the values $a/\sigma \simeq 0.2$-0.3 which were systematically taken in previous studies of the overlap in glass-forming liquids. The critical point then appears in the liquid region where the viscosity is low and the equilibration may be significantly faster. A similar effect is found when the density is the control parameter but the relative change is of course smaller although still of the order of 10 %. This represents an important practical asset for computer simulations. Indeed, it offers the possibility to fasten the simulations in the context of the study of the phase diagram (ϵ, T), and therefore to consider larger system sizes than the ones that have been considered so far, for instance in the purpose of a finite-size scaling analysis as we do in Chap. III.

However, there are practical limitations to taking too small values of a/σ. In molecular dynamics simulations, the magnitude of the forces which are exerted by the reference configuration when $\epsilon > 0$ (or when considering umbrella sampling techniques) increases with decreasing a, which implies to reduce the time step in the integration of the equations of motion. On the other hand, in Monte Carlo simulations, significant variations of the overlap are triggered by smaller amplitudes of the particle displacements as a/σ is reduced, which require trial moves of smaller size. The trade-off between shifting up the critical temperature and maximising the algorithmic efficiency (simulated physical time versus computer walltime) therefore leads to an operational optimum value of a, which is around 0.1σ.

Choosing a around 0.1σ would then significantly accelerate the computer simulations of constrained supercooled liquids. In addition, this choice could prove useful for glass-forming liquid models for which the swap algorithm is inefficient and cannot provide reference equilibrium configurations at a low temperature T_0 to shift up the critical temperature. Indeed, almost all

previous simulation attempts [156, 209, 213, 256] to study the critical point in $3d$ model glass-formers, with the typical choice $a/\sigma \simeq$ 0.2-0.3 and both the reference and the constrained replicas at the same temperature, were limited in practice to temperatures above the putative critical temperature T_c and to rather small system sizes. Indeed, T_c seems to fall close to the mode-coupling crossover which represents the lowest temperature for which the equilibration can be ensured in a reasonable computer walltime without using the swap algorithm. By choosing an optimised value of a in the definition of the overlap, one could more convincingly study the existence and the properties of the critical point in a variety of models of glass-forming liquids. This may be useful to quantify the "self-induced" disorder in different liquids (see Chap. III).

6.2 Connections with the structure of the free energy landscape

In this section, we address the physical meaning, if any, of the dependence that we have found on the tolerance parameter a in the definition of the similarity between liquid configurations, beyond its practical outcomes. The physical idea behind the definition of the overlap order parameter is to define some sort of metric between configurations that allows one to sort them in "metastable states", when the liquid is in equilibrium at a temperature T. At the mean-field level, where metastable states are well defined, the distinguishing property of such states is not their free energy density and their number (as quantified by the configurational entropy) is an important factor [139]. But, how exactly similar should two liquid configurations be to be considered as belonging to the same state in the complex landscape? Varying the tolerance a is a way to check how the properties of the coarse-grained landscape depend on the more or less strict definition of the similarity, hence on the coarse-graining length.

We have found that the shape of the phase diagram in the (ϵ, T) plane for the case $T = T_0$ is very robust with the choice of the tolerance a. However, the non-monotonic dependence of the location of the first order transition line (except T_K) and of its critical endpoint implies for instance that at a given temperature between T_K and $T_c^{(\max)} = \max_a\{T_c(a)\}$, there is a range of tolerance a for which one always finds a value of the applied source ϵ at which coexistence between low-overlap and high-overlap phases exists, whereas for the complementary domain of a one is above the critical point and a unique phase is found whatever the applied source. Above $T_c^{(\max)}$ there are no more singularities in the thermodynamics of constrained liquids and hence no more signatures of a complex free energy landscape, whatever the choice of a. This temperature[5] is therefore a candidate for a purely static definition of the "onset temperature" below which glassy features starts to set in. Then, the value of a for which this maximum is achieved should represent the typical displacement magnitude of the particles in order for the system to fall in another "metastable state". In lattice models or mean-field spin glasses, the above onset temperature would be the unique value of T_c in the case $T = T_0$.

This new definition of the onset temperature could then be confronted with other landscape-inspired ones. To do so, we come back to the case of the spherical p-spin model which is discussed in Chap. II. The latter behaves similarly as mean-field structural glasses, in particular it undergoes a one-step replica symmetry breaking transition at a temperature T_K, and metastable states rule its thermodynamics below a higher temperature T_d [116–120]. Meanwhile, some metastable states survive above the dynamical transition at T_d and the ones which dominate

[5] Of course here, we have only considered one window function, namely, $w(x) = e^{-x^4 \ln 2}$. A more complete definition of the onset temperature would be to take the maximum in the critical temperature over the window functions and over the tolerance lengths.

the thermodynamics at $T_{\rm K}$ cease to exist for $T_{\rm TAP}/J = \sqrt{2/(py)}(1-2/p)^{p/2-1} = 0.792$ for $p=3$ [with y solution of $1/p = -y(1-y+\ln y)/(1-y)^2$ and J the strength of the coupling between spins] [131, 145, 146, 148, 152, 210, 233]. This temperature scale then represents another measure of a static onset temperature below which the glassy behaviour settles. By comparing with the critical temperature for the p-spin model (with $p=3$) in the case $T=T_0$ which is $T_{\rm c}/J = T_{\rm cvx}/J = 0.772$, we note that $T_{\rm TAP} > T_{\rm c}$ which is sensible as the transition from the delocalised phase to the localised one is controlled by a competition between the configurational entropy and the attraction energy between the replicas. As a consequence, the two estimates are somehow close but not equal. At least, they both indicate that the structure of the landscape is changing at much higher temperatures than the other temperature scales, namely, $T_{\rm d}$ and $T_{\rm K}$. We should also note that contrary to $T_{\rm TAP}$ which is only well defined in the mean-field limit and which requires to be able to compute a TAP free energy (a task which has been impossible so far for structural liquids [126]), our definition of the onset temperature is also valid in finite dimensions. Finally, we can also compare our definition of the onset temperature to another landscape-inspired one but which relies on the potential energy landscape rather than the free energy landscape. One can look at the out-of-equilibrium gradient descent dynamics, *i.e.*, the zero-temperature dynamics, from equilibrium configurations at a finite temperature T. It is usually found that the long-time limit energy of the system (in the so-called inherent state) converges to a value that depends on T only if T is below a threshold temperature that can also be considered as an onset temperature [355, 356]. In the case of the pure p-spin model, the onset temperature which is obtained from the gradient descent dynamics is actually equal to the dynamical transition temperature. This is a peculiarity of pure p-spin models which do not display temperature chaos. However, mixed p-spin models indeed have a high-temperature onset temperature [357] which is well above the dynamical transition temperature. This could be compared to $T_{\rm TAP}$ or $T_{\rm c}$ for mixed p-spin models.

The above discussion naturally leads to come back to the question of the configurational entropy which corresponds to the logarithm of the number of "metastable states" per unit particle. In a mean-field setting, the configurational entropy is obtained as the difference in the Franz-Parisi (FP) potential between the metastable and the stable minima for temperatures between $T_{\rm d}$ and $T_{\rm K}$, and is independent of the choice of a/σ. In a $3d$ glass-former, there are no $T_{\rm d}$ and no metastable minimum in the FP potential. Instead, at low temperatures, the FP potential is non-convex (see Fig. III.4) in small systems or marginally convex in the thermodynamic limit with a linear behaviour (see Fig. II.2). However, there is still a special point, namely, the high-overlap limit of the straight segment (or of the double-tangent construction in small systems), that can serve as a proxy for the value of the overlap in the "metastable minimum". One can thus tentatively define a configurational entropy as the difference in the FP potential between this point and the stable minimum [114, 181, 241]. What the results of this chapter show is that this estimate of the configurational entropy depends on the choice of a/σ, because the nature or the size of the states that are counted may change with it. In other words, the FP potential is no longer singular in finite dimensions and the choice of the overlap value to compute the difference in the FP potential with respect to the stable minimum is now a-dependent. One may invoke at this point a physical constraint to fix the value of a and provide the "most reasonable" counting by setting a to some typical vibrational length[6]. However, and as the practical measurements of the configurational entropy in the computer simulations of glass-forming liquid models are

[6]For instance, one could consider the height of the plateau in the equilibrium mean-squared displacement, at least at temperatures for which the plateau is indeed observed.

currently an important research topic [114, 164, 181, 182, 190, 241, 358], the question should certainly be investigated more thoroughly.

We finally stress that we have considered here the static overlap between equilibrium configurations, with no reference to the dynamics. One can also investigate the similarity between a configuration at a given time t', and the same configuration which has evolved under the dynamics of its constituents, after an elapsed time t [359]. In Eq. (IV.1), $\boldsymbol{r}_{\alpha,i}$ and $\boldsymbol{r}_{\gamma,j}$ are then replaced by $\boldsymbol{r}_i(t')$ and $\boldsymbol{r}_j(t+t')$. This time-dependent overlap is similar to the intermediate scattering function in Chap. I. Consequently, the fluctuations of this time-dependent overlap correspond to the four-point dynamic susceptibility $\chi_4(t)$ and they are useful to describe the spatially heterogeneous nature of the dynamics and the growing extent of dynamic correlations as one cools a glass-forming liquid [51]. In this case too, the definition of the overlap involves a tolerance a, but the physical significance and the effect of the latter are more readily understandable than what has been presented in this chapter [360]. If a/σ is too small, the involved dynamics is controlled by only weakly-coupled vibrations and the dynamic correlations remain small. On the opposite, if a/σ is large, one encounters the rather unphysical feature that a particle from the configuration at time t' can overlap with several other particles at time $t+t'$. In between there is an optimal value of the ratio (around 0.3) for which the spatial correlations in the dynamics grow bigger. The study of the dynamics of supercooled liquids at very low temperatures and the associated dynamic heterogeneities are studied in more details in Chap. VI.

Appendix A - Analysis of the hypernetted chain equations in the limit of vanishing tolerance length

In this Appendix, we study the equations of liquid-state theory in the hypernetted chain (HNC) approximation in the limit $a \to 0$ in order to derive the scaling laws of Sec. 4.2. When $a/\sigma \to 0^+$, the correlation functions should vary on two very different scales. On the scale r/σ one expects a perturbation from the case $a=0$ whereas a singular behaviour should appear on the scale r/a. We then consider the following ansatz at the critical point:

$$\begin{cases} h_{01,\mathrm{c}}(r) = & \hat{f}_1(a)\hat{h}_{01}(r/a) + \tilde{f}_1(a)\tilde{h}_{01}(r/\sigma), \\ h_{12,\mathrm{c}}(r) = & \hat{f}_2(a)\hat{h}_{12}(r/a) + \tilde{f}_2(a)\tilde{h}_{12}(r/\sigma), \\ h_{11,\mathrm{c}}(r) = & \tilde{h}_{11}^{(0)}(r/\sigma) + \tilde{f}_3(a)\tilde{h}_{11}^{(1)}(r/\sigma), \\ h_{00,\mathrm{c}}(r) = & \tilde{h}_{00}(r/\sigma), \end{cases} \tag{IV.35}$$

where the hat and tilde correlation functions have an amplitude and a range of $O(1)$ and where the prefactors are functions of the tolerance a. Except for $\tilde{h}_{00}$ which is independent of a, they could still have sub-dominant terms in a as we have shown explicitly for $\tilde{h}_{11}$. In Fourier space, the above expressions translate into

$$\begin{cases} h_{01,\mathrm{c}}(q) = & a^3\hat{f}_1(a)\hat{h}_{01}(qa) + \tilde{f}_1(a)\sigma^3\tilde{h}_{01}(q\sigma), \\ h_{12,\mathrm{c}}(q) = & a^3\hat{f}_2(a)\hat{h}_{12}(qa) + \tilde{f}_2(a)\sigma^3\tilde{h}_{12}(q\sigma), \\ h_{11,\mathrm{c}}(q) = & \sigma^3\tilde{h}_{11}^{(0)}(q\sigma) + \tilde{f}_3(a)\sigma^3\tilde{h}_{11}^{(1)}(q\sigma), \\ h_{00,\mathrm{c}}(q) = & \sigma^3\tilde{h}_{00}(q\sigma), \end{cases} \tag{IV.36}$$

where for simplicity we keep the same notation for the functions in real and Fourier spaces.

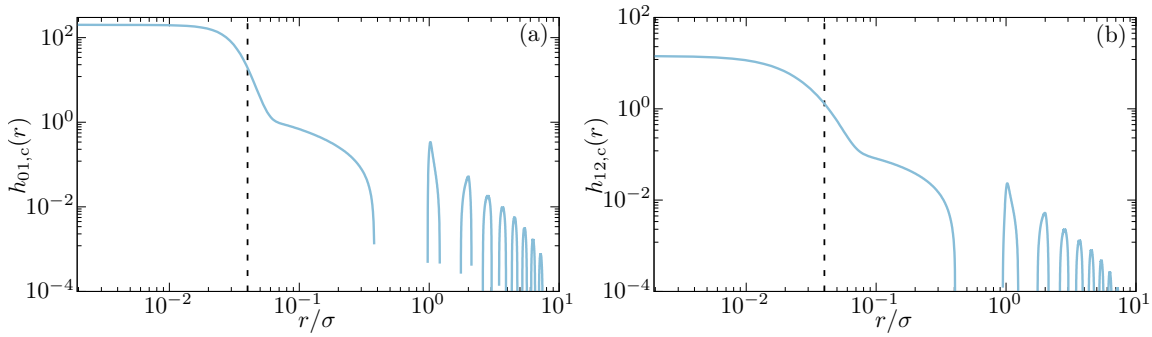

Fig. IV.11 | Plot on a double logarithmic scale of the total correlation functions (a) $h_{01,c}(r)$ and (b) $h_{12,c}(r)$ versus r/σ at criticality for $a/\sigma = 0.04$ in the case of hard spheres in the hypernetted chain approximation for the two replicas of equal density. A decoupling of scales is clearly visible between the range $r \sim a$ where a monotonic decrease is observed and the range $r \sim \sigma$ where oscillations due to the underlying liquid structure occur (the dashed line marks $r = a$).

We expect that the prefactors which express the dependence on $a \to 0^+$ satisfy

$$\begin{cases} \hat{f}_1(a),\ \hat{f}_2(a) & \to +\infty, \\ a^3\hat{f}_1(a),\ a^3\hat{f}_2(a) & \to 0, \\ \tilde{f}_1(a),\ \tilde{f}_2(a),\ \tilde{f}_3(a) & \to 0. \end{cases} \tag{IV.37}$$

The first equation indicates that the amplitude of the correlation functions $h_{01,c}(r)$ and $h_{12,c}(r)$ should diverge as $a \to 0$ as seen from Fig. IV.5. The last one instead indicates that the corresponding terms are perturbations of the case $a = 0$ if $\rho_c(a)$ or $T_c(a)$ are not singular when $a \to 0$. Finally, the second equation indicates that the critical overlap difference with the random value vanishes when $a \to 0$ in agreement with Fig. IV.4 (c) and Fig. IV.4 (f).

The tilde functions which vary on the scale σ should keep track of the liquid structure and peak in Fourier space around $2\pi/\sigma$. On the other hand, the hat functions are expected to behave roughly as the function w and decay in Fourier space on a scale $q \sim 1/a$, see Fig. IV.11. As a result, a complete separation of scales between the hat and tilde functions requires $2\pi/\sigma \ll 1/a$. This is of course verified in the limit $a \to 0^+$ but this is more difficult to achieve in the numerical solution of the HNC equations. For instance, when $a/\sigma = 0.06$, $2\pi a/\sigma$ is still about 0.38, which is smaller but not much smaller than 1, and corrections to the asymptotic analysis of the functions should then be expected. By using the separation of the scales a and σ, the HNC closure in Eq. (IV.23) then leads to direct correlation functions that have a similar structure as their counterparts in Eq. (IV.35). They are given at the first dominant orders by

$$\begin{cases} c_{01,c}(r) = & \left\{\hat{f}_1(a)\hat{h}_{01}(r/a) - \ln[1 + \hat{f}_1(a)\hat{h}_{01}(r/a)] + \hat{f}_3(a)\widehat{\beta\epsilon w}(r/a)\right\} + \tilde{f}_1(a)^2\tilde{c}_{01}(r/\sigma), \\ c_{12,c}(r) = & \left\{\hat{f}_2(a)\hat{h}_{12}(r/a) - \ln[1 + \hat{f}_2(a)\hat{h}_{12}(r/a)]\right\} + \tilde{f}_2(a)^2\tilde{c}_{12}(r/\sigma), \\ c_{11,c}(r) = & \tilde{c}_{11}^{(0)}(r/\sigma) + \tilde{f}_3(a)\tilde{c}_{11}^{(1)}(r/\sigma), \\ c_{00,c}(r) = & \tilde{c}_{00}(r/\sigma), \end{cases} \tag{IV.38}$$

where

$$\begin{cases} \tilde{c}_{01}(r/\sigma) = & \tilde{h}_{01}(r/\sigma)^2/2, \\ \tilde{c}_{12}(r/\sigma) = & \tilde{h}_{12}(r/\sigma)^2/2, \\ \tilde{c}_{11}^{(0)}(r/\sigma) = & -\beta v(r) + \tilde{h}_{11}^{(0)}(r/\sigma) - \ln[1 + \tilde{h}_{11}^{(0)}(r/\sigma)], \\ \tilde{c}_{11}^{(1)}(r/\sigma) = & \tilde{h}_{11}^{(1)}(r/\sigma)\tilde{h}_{11}^{(0)}(r/\sigma)/[1 + \tilde{h}_{11}^{(0)}(r/\sigma)], \\ \tilde{c}_{00}(r/\sigma) = & -\beta v(r) + \tilde{h}_{00}(r/\sigma) - \ln[1 + \tilde{h}_{00}(r/\sigma)], \end{cases} \tag{IV.39}$$

and where we have assumed that, at criticality, when $a \to 0^+$,

$$(\beta_{\rm c}\epsilon_{\rm c})(a) = \hat{f}_3(a)\widehat{\beta\epsilon} \quad \text{with} \quad \hat{f}_3(a) \to +\infty. \tag{IV.40}$$

As mentioned above, the functions $\hat{h}_{01}(r/a)$ and $\hat{h}_{12}(r/a)$ are expected to behave roughly as $w(r/a)$, *i.e.*, to decay essentially monotonically on a scale of $O(1)$. As a result, we rewrite

$$\begin{cases} \ln[1 + \hat{f}_1(a)\hat{h}_{01}(r/a)] \simeq & \ln[\hat{f}_1(a)]\hat{F}_1(r/a), \\ \ln[1 + \hat{f}_2(a)\hat{h}_{12}(r/a)] \simeq & \ln[\hat{f}_2(a)]\hat{F}_2(r/a), \end{cases} \tag{IV.41}$$

where the functions $\hat{F}_{1,2}$ have an amplitude and a range of $O(1)$. For instance, if $\hat{h}_{01}(r/a)$ is approximated by a step function, the function $\hat{F}_1(r/a)$ verifies $\hat{F}_1(r/a) \simeq \hat{h}_{01}(r/a)/\hat{h}_{01}(0)$.

In Fourier space, the expressions in Eq. (IV.38) become

$$\begin{cases} c_{01,\rm c}(q) = & \Big\{a^3\hat{f}_1(a)\hat{h}_{01}(qa) - a^3\ln[\hat{f}_1(a)]\hat{F}_1(qa) + a^3\hat{f}_3(a)\widehat{\beta\epsilon}\, w(qa)\Big\} + \tilde{f}_1(a)^2\sigma^3\tilde{c}_{01}(q\sigma), \\ c_{12,\rm c}(q) = & \Big\{a^3\hat{f}_2(a)\hat{h}_{12}(qa) - a^3\ln[\hat{f}_2(a)]\hat{F}_2(qa)\Big\} + \tilde{f}_2(a)^2\sigma^3\tilde{c}_{12}(q\sigma), \\ c_{11,\rm c}(q) = & \sigma^3\tilde{c}_{11}^{(0)}(q\sigma) + \tilde{f}_3(a)\sigma^3\tilde{c}_{11}^{(1)}(q\sigma), \\ c_{00,\rm c}(q) = & \sigma^3\tilde{c}_{00}(q\sigma)\,. \end{cases} \tag{IV.42}$$

We now consider the Ornstein-Zernike equations [Eq. (IV.22)] that can be studied for $q \sim 1/a \gg 2\pi/\sigma$ and for $q \sim 2\pi/\sigma \ll 1/a$ separately. First, the relation between $h_{01,\rm c}(q)$ and $c_{01,\rm c}(q)$ reads

$$\begin{aligned} & a^3\hat{f}_1(a)\hat{h}_{01}(qa) + \tilde{f}_1(a)\sigma^3\tilde{h}_{01}(q\sigma) = \\ & [1 + \sigma^3\rho\tilde{h}_{00}(q\sigma)][1 + \sigma^3\rho\tilde{h}_{11}^{(0)}(q\sigma) + \tilde{f}_3(a)\sigma^3\rho\tilde{h}_{11}^{(1)}(q\sigma) - a^3\hat{f}_2(a)\rho\hat{h}_{12}(qa) - \tilde{f}_2(a)\sigma^3\rho\tilde{h}_{12}(q\sigma)] \\ & \times \{a^3\hat{f}_1(a)\hat{h}_{01}(qa) - a^3\ln[\hat{f}_1(a)]\hat{F}_1(qa) + a^3\hat{f}_3(a)\widehat{\beta\epsilon}\, w(qa) + O\Big(\tilde{f}_1(a)^2\Big)\}. \end{aligned} \tag{IV.43}$$

The decoupling between the two scales in Fourier space is achieved when $a \to 0^+$ if all the $\tilde{h}_{\alpha\gamma}(q\sigma)$'s go to zero fast enough when $q\sigma \to \infty$. It is expected that they indeed do so at least as fast as $1/(q\sigma)^2$, as in the Ornstein-Zernike approximation [30]. In this case, one can totally neglect the contributions of the tilde terms when expanding for $q \sim 1/a \to +\infty$ as $a \to 0$. In this framework, the above equation implies that

$$a^3\hat{f}_1(a)\hat{f}_2(a)\rho\hat{h}_{12}(qa)\hat{h}_{01}(qa) + \ln[\hat{f}_1(a)]\hat{F}_1(qa) = \hat{f}_3(a)\widehat{\beta\epsilon}\, w(qa). \tag{IV.44}$$

From the above equation, we can directly deduce that $\hat{f}_3(a)$ is sub-leading with respect to $\hat{f}_1(a)$. By using this result, we now obtain another equation from Eq. (IV.43) when $q \sim 2\pi/\sigma$, namely,

$$a^3\hat{f}_1(a)\hat{h}_{01}(q=0)\{1 - [1 + \sigma^3\rho\tilde{h}_{00}(q\sigma)][1 + \sigma^3\rho\tilde{h}_{11}^{(0)}(q\sigma)]\} + \tilde{f}_1(a)\sigma^3\tilde{h}_{01}(q\sigma) = 0, \tag{IV.45}$$

where the right-hand side only contains terms that are sub-dominant with respect to $a^3\hat{f}_1(a)$ and/or $\tilde{f}_1(a)$ and is thus set to 0. The above equation therefore implies that $\hat{f}_1(a)$ and $\tilde{f}_1(a)$ are both non-zero and verify

$$\tilde{f}_1(a) = a^3\hat{f}_1(a). \tag{IV.46}$$

It also implies that

$$\sigma^3\tilde{h}_{01}(q\sigma) = \hat{h}_{01}(q=0)\{[1+\sigma^3\rho\tilde{h}_{00}(q\sigma)][1+\sigma^3\rho\tilde{h}_{11}^{(0)}(q\sigma)]-1\}, \tag{IV.47}$$

with an unimportant choice of normalisation of the functions.

We now proceed in a similar way for the Ornstein-Zernike equation that relates $h_{12,\mathrm{c}}(q)$ and $c_{12,\mathrm{c}}(q)$. It reads

$$\begin{aligned}
&a^3\hat{f}_2(a)\hat{h}_{12}(qa) + \tilde{f}_2(a)\sigma^3\tilde{h}_{12}(q\sigma) = \\
&[1+\sigma^3\rho\tilde{h}_{11}^{(0)}(q\sigma) + \tilde{f}_3(a)\sigma^3\rho\tilde{h}_{11}^{(1)}(q\sigma) - a^3\hat{f}_2(a)\rho\hat{h}_{12}(qa) - \tilde{f}_2(a)\sigma^3\rho\tilde{h}_{12}(q\sigma)]^2 \\
&\times\Big\{a^3\hat{f}_2(a)\hat{h}_{12}(qa) - a^3\ln[\hat{f}_2(a)]\hat{F}_2(qa) + O\Big(\tilde{f}_2(a)^2\Big) \\
&+\rho[1+\sigma^3\rho\tilde{h}_{00}(q\sigma)][a^3\hat{f}_1(a)\hat{h}_{01}(qa) + o\Big(a^3\hat{f}_1(a)\Big)]^2\Big\},
\end{aligned} \tag{IV.48}$$

where we have again used that $\hat{f}_3(a)$ is negligible with respect to $\hat{f}_1(a)$. When $q \sim 1/a$, we can neglect the contributions of the tilde functions again to obtain

$$a^3\hat{f}_1(a)^2\rho\hat{h}_{01}(qa)^2 = 2a^3\hat{f}_2(a)^2\rho\hat{h}_{12}(qa)^2 + \ln[\hat{f}_2(a)]\hat{F}_2(qa). \tag{IV.49}$$

The above equation implies that $a^3\hat{f}_1(a)^2$ is at best of the same order as $a^3\hat{f}_2(a)^2$ when $a \to 0$. In particular, it implies that $a^3\hat{f}_1(a)^2$ is negligible with respect to $\hat{f}_2(a)$. Therefore, by using this statement and by considering the Ornstein-Zernike equation for $h_{12,\mathrm{c}}$ and $c_{12,\mathrm{c}}$ in the case $q \sim 2\pi/\sigma$, we obtain

$$a^3\hat{f}_2(a)\hat{h}_{12}(q=0)\{1-[1+\sigma^3\rho\tilde{h}_{11}^{(0)}(q\sigma)]^2\} + \tilde{f}_2(a)\sigma^3\tilde{h}_{12}(q\sigma) = 0, \tag{IV.50}$$

where the right-hand side is sub-dominant with respect to $a^3\hat{f}_2(a)$ and $\tilde{f}_2(a)$ and is thus set to 0. This implies that

$$\tilde{f}_2(a) = a^3\hat{f}_2(a), \tag{IV.51}$$

and that

$$\sigma^3\tilde{h}_{12}(q\sigma) = \hat{h}_{12}(q=0)\{[1+\sigma^3\rho\tilde{h}_{11}^{(0)}(q\sigma)]^2-1\}, \tag{IV.52}$$

with an unimportant choice of normalisation of the functions.

Although Eq. (IV.44) and Eq. (IV.49) could have several possible solutions, a non-trivial solution is obtained by assuming that in each of these equations all the terms are of the same order. This gives

$$\begin{cases} a^3\hat{f}_1(a)\hat{f}_2(a) \sim & \hat{f}_3(a) \sim & \ln[\hat{f}_1(a)], \\ a^3\hat{f}_1(a)^2 \sim & a^3\hat{f}_2(a)^2 \sim & \ln[\hat{f}_2(a)], \end{cases} \tag{IV.53}$$

whose solution is then, at the leading order when $a \to 0^+$,

$$\begin{cases} \hat{f}_1(a) \sim & \hat{f}_2(a) \sim & a^{-3/2}\sqrt{|\ln a|}, \\ & \hat{f}_3(a) \sim & |\ln a|. \end{cases} \tag{IV.54}$$

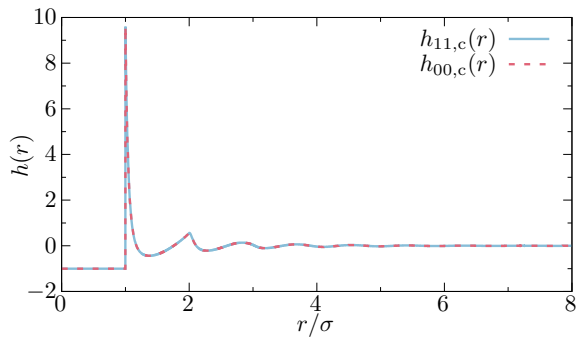

Fig. IV.12 | Total correlation functions $h_{11,\mathrm{c}}(r)$ and $h_{00,\mathrm{c}}(r)$ versus r/σ at criticality for $a/\sigma = 0.04$ in the case of hard spheres in the hypernetted chain approximation and for the two replicas of equal density. The two functions nearly coincide.

Finally, we consider the Ornstein-Zernike equation relating $h_{\mathrm{con,c}}(q)$ and $c_{\mathrm{con,c}}(q)$[7], namely,

$$1 + \sigma^3\rho\tilde{h}_{11}^{(0)}(q\sigma) + \tilde{f}_3(a)\sigma^3\rho\tilde{h}_{11}^{(1)}(q\sigma) - a^3\hat{f}_2(a)\rho\hat{h}_{12}(qa) - \tilde{f}_2(a)\sigma^3\rho\tilde{h}_{12}(q\sigma) = \\ \Big\{1 - \sigma^3\rho\tilde{c}_{11}^{(0)}(q\sigma) - \tilde{f}_3(a)\sigma^3\rho\tilde{c}_{11}^{(1)}(q\sigma) + \tilde{f}_2(a)\rho\hat{h}_{12}(qa) - a^3\ln[\hat{f}_2(a)]\rho\hat{F}_2(qa) + O\Big(\tilde{f}_2(a)^2\Big)\Big\}^{-1}. \tag{IV.55}$$

At the leading order this immediately leads to

$$1 + \sigma^3\rho\tilde{h}_{11}^{(0)}(q\sigma) = \frac{1}{1 - \sigma^3\rho\tilde{c}_{11}^{(0)}(q\sigma)}, \tag{IV.56}$$

and since the HNC closures for $\tilde{c}_{11}^{(0)}$ and $\tilde{c}_{00}$ have the same form, to

$$\tilde{h}_{11}^{(0)}(q\sigma) = \tilde{h}_{00}(q\sigma), \tag{IV.57}$$

which is well verified by our numerical solution of the HNC equations (see Fig. IV.12).

In addition, by using Eq. (IV.57) as well as Eq. (IV.52), we find at the next-to-leading order and when $q \sim 2\pi/\sigma$ that

$$\tilde{f}_3(a)\sigma^3\{\tilde{h}_{11}^{(1)}(q\sigma) - [1+\sigma^3\rho\tilde{h}_{00}(q\sigma)]^2\tilde{c}_{11}^{(1)}(q\sigma)\} = a^3\ln[\hat{f}_2(a)]\hat{F}_2(q=0)[1+\sigma^3\rho\tilde{h}_{00}(q\sigma)]^2. \tag{IV.58}$$

By assuming that the terms on both sides of the equation are of the same order, Eq. (IV.58) leads to

$$\tilde{f}_3(a) = a^3\ln[\hat{f}_2(a)] \sim a^3|\ln a|, \tag{IV.59}$$

at the leading order when $a \to 0^+$, and to

$$\sigma^3\tilde{h}_{11}^{(1)}(q\sigma) = [1 + \sigma^3\rho\tilde{h}_{00}(q\sigma)]^2[\sigma^3\tilde{c}_{11}^{(1)}(q\sigma) + \hat{F}_2(q=0)]. \tag{IV.60}$$

The above derivation provides the expressions which are given in Sec. 4.2.

[7]We recall that the connected correlations are $h_{\mathrm{con,c}} = h_{11,\mathrm{c}} - h_{12,\mathrm{c}}$ and $c_{\mathrm{con,c}} = c_{11,\mathrm{c}} - c_{12,\mathrm{c}}$.

V Local fluctuations of the "self-induced" disorder in glass-forming liquids

Glass-forming liquids are intrinsically disordered and their disorder-induced fluctuations are believed to be important to understand their equilibrium properties, their dynamic behaviour and their non-equilibrium driving, as suggested by the multiple analogies between glass-forming liquids and the random-field Ising model. However, contrary to the latter, the disorder in supercooled liquids is not a priori quenched as it is rather "self-induced". Few studies have addressed the characterisation and the quantification of the effective disorder at the mesoscopic scale between the single-particle level and the macroscopic scale. The objective of this chapter is to present a numerical method to measure the local fluctuations of the "self-induced" effective disorder in glass-forming liquids. It consists in linearly biasing the overlap or similarity between a liquid configuration and a reference configuration of the same liquid in a randomly-centered small cavity with an external field. The field which is required for the liquid to have a locally high overlap with the reference configuration represents a proxy for the local entropic cost (configurational entropy) to remain close to the reference configuration, and we show that it displays large spatial fluctuations. We analyse the spatial and the statistical properties of these fluctuations and we show that they are well described by a generalised Gumbel distribution with an exponential tail at large localising fields. We rationalise this tail by invoking an additional free energy surface cost due to the mismatch in the density profiles between the cavity when it is confined close to the reference configuration and the exterior. Finally, we describe several future directions of study. In a first line of thought, we would like to assess the correlation between these thermodynamic local fluctuations and local structural properties of the reference configurations. In a second line of thought, we aim at trying to connect the measured thermodynamic fluctuations with the dynamic heterogeneities which are universally encountered in the equilibrium dynamics of supercooled liquids when approaching their glass transition temperature.

Outline

1 Introduction . . . 127
2 General formalism . . . 130
3 Model and methods . . . 132
4 Thermodynamic spatial fluctuations . . . 135
  4.1 Fluctuations of the Franz-Parisi potential . . . 135
  4.2 Influence of the boundaries . . . 138
5 Conclusions and perspectives . . . 139
  5.1 Statistics of the local Franz-Parisi potential . . . 139
  5.2 Correlation with structural indicators and the dynamic heterogeneities . . . 141

This chapter describes a still ongoing work.

1. Introduction

Mean-field theory accounts for the dynamic and the thermodynamic properties of supercooled liquids by the existence of a rugged free energy landscape with an exponentially large number of metastable minima (see Chap. I) [122]. The logarithm of this number (per unit particle) is the configurational entropy $\Sigma(T)$ and it vanishes at the Kauzmann transition temperature $T_{\rm K}$, where a genuine thermodynamic phase transition to the ideal glass phase occurs with a jump in the average overlap order parameter, namely, the similarity between equilibrium configurations [126]. This behaviour is elegantly encompassed in the temperature evolution of the Franz-Parisi (FP) potential (see Chap. II) which represents the free energy cost to constrain the global overlap between the configuration of a liquid and a quenched reference configuration of the same liquid to have a given value [148]. Equivalently, it stands for the large deviation rate function of the unconstrained probability distribution of the overlap [213].

The FP potential $V(Q;\boldsymbol{r}_0^N)$ is a random quantity through the choice of the reference configuration $\boldsymbol{r}_0^N$. At the mean-field level, its first cumulant $V(Q)=\overline{V(Q;\boldsymbol{r}_0^N)}$ shows a double-well structure at $T_{\rm K}$ with two minima of equal depth. The low-overlap (resp. high-overlap) minimum at $Q=Q_{\rm rand}$ (resp. $Q=Q_{\rm g}$) corresponds to the average overlap for two uncorrelated (resp. correlated) copies or replicas, *i.e.*, to replicas that belong to different metastable minima (or states) in the free energy landscape (resp. the same metastable state). Above $T_{\rm K}$, the high-overlap minimum becomes metastable and disappears at the dynamical (mode-coupling) transition $T_{\rm d}$. In the temperature range $T_{\rm K}<T<T_{\rm d}$, the difference in height between the two minima of the FP potential corresponds to the free energy cost to constrain the liquid in the metastable state of the reference configuration and it thus equals $T\Sigma(T)$. Above $T_{\rm d}$, the FP potential has a single minimum for $Q=Q_{\rm rand}$ but it keeps a non-convex shape up to an "onset temperature" $T_{\rm c}$. For $T>T_{\rm c}$, the FP potential is convex with a single minimum [156]. As already explained in Chap. II, non-convexities of the FP potential directly translate into thermodynamic transitions when the overlap order parameter with a reference configuration is linearly coupled to a source ϵ. A line of first order transition emerges from the thermodynamic glass transition at $(0,T_{\rm K})$ and ends in a critical point at $(\epsilon_{\rm c},T_{\rm c})$ [153]. In finite dimensions, the FP potential must be convex but it may develop a linear behaviour for intermediate overlap values which still corresponds to a first order phase transition in the plane (ϵ,T).

The average FP potential captures the average thermodynamics of the liquid but not the sample-to-sample fluctuations which are induced by the change in the reference configuration [208]. These fluctuations are nonetheless interesting. For instance, in an archetypal mean-field spin glass model which displays similarities with glass-forming liquids, namely, the p-spin model [117, 221], the random FP potential $V(Q;\boldsymbol{r}_0^N)$ can still display a secondary minimum above the dynamical transition temperature when the reference configuration is very stable, *e.g.*, when the latter is sampled in the metastable states which survive above $T_{\rm d}$ [239] (see also Chap. IV). These sample-to-sample fluctuations are expected to be crucial in finite dimensions. The argument was already given in Chap. II and relies on the mosaic state of the random first order transition (RFOT) theory, *i.e.*, the finite-dimensional formulation of mean-field theory [124, 144]. We reformulate it here by using the FP potential, see Fig. V.1 [196]. In finite dimensions, one can formally divide the liquid into small blobs of linear size equal to the average point-to-set (PTS) length, which corresponds to the linear extent of amorphous order and the lengthscale

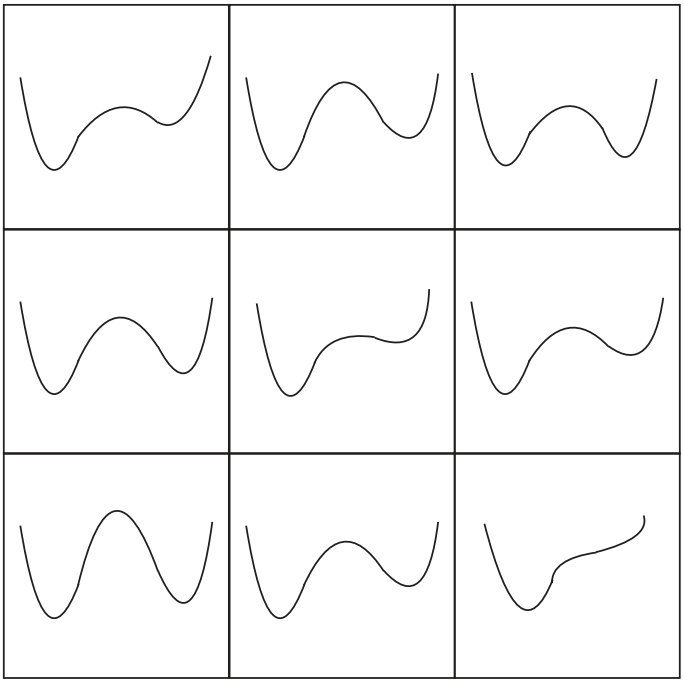

Fig. V.1 | Schematic representation of a system which is divided in several blobs of linear size smaller than the average point-to-set length. The local Franz-Parisi potential fluctuates from one domain to another, and these large fluctuations stand for the "self-induced" disorder in glass-forming liquids. Figure from Ref. [196].

below which metastable states remain well defined in finite-dimensional glass-forming liquids. The blobs can be in one of the many metastable states and the FP potential in each blob can be non-convex. However, fluctuations of the PTS length (or equivalently of the configurational entropy) are expected and the FP potential should thus fluctuate from one blob to another. In blobs of smaller configurational entropy, or equivalently of FP potential with a deeper secondary minimum, large overlap values are more likely. Therefore, the fluctuations of the FP potential are equivalent to a random field which is linearly coupled to the overlap with the reference configuration in each blob [254].

This analogy was put on firmer grounds recently, as already mentioned in Chap. II. By considering a model Landau-Ginzburg functional to describe the overlap fluctuations in glass-forming liquids close to T_{K} and $\epsilon = 0$, the latter was mapped onto a replicated action which derives from a random Hamiltonian in the universality class of the random-field Ising model (RFIM) [196, 197]. The mapping was also shown to hold on the whole first order transition line for $\epsilon > 0$ in the phase diagram (ϵ, T) and at the critical point at $(\epsilon_{\mathrm{c}}, T_{\mathrm{c}})$ [218, 250], if they survive finite-dimensional fluctuations [206]. However, there is a difference between glass-forming liquids and the RFIM as the disorder in glass-forming liquids is generated by the system itself and the nature of the quenched random field is more elusive. This makes the definition and the quantification of disorder in glass-formers more delicate. There are strong consequences of this analogy between glass-forming liquids and the RFIM which have already been reported in the previous chapters. In particular, random fields destroy long-range order in $2d$ [249]: the existence of a finite temperature Kauzmann entropy crisis is therefore forbidden and the FP potential must be strictly convex in the thermodynamic limit at any finite temperature. On the

opposite, the Kauzmann transition can survive in $3d$ if the strength of the effective disorder is not too large [331]. Consequently, the FP potential can be marginally non-convex at low-enough temperatures and the mean-field phase diagram (ϵ, T) can survive as such. These predictions have been confirmed in Chap. III by means of computer simulations.

Therefore, quantifying the strength of the effective disorder in glass-forming liquids is important. For instance, it could allow for a determination of the fate of the unreachable Kauzmann transition in finite dimensions. We have already proposed a way to give a quantitative measure of the effective disorder in supercooled liquids by studying constrained liquids near the critical point at $(\epsilon_{\rm c}, T_{\rm c})$ in Chap. III. The method relies on measuring the ratio of the standard deviation of the random fields to the strength of the coupling constant between spins in the effective RFIM which describes the physics of the overlap close to the critical point [218]. This protocol provides a single number whose value might constrain the existence of the Kauzmann transition [196, 197]. However, we have been unable to apply the method completely as the computation of the effective coupling constant between spins requires simulations at very low temperatures. In addition, this protocol does not allow for the study of the temperature evolution of the "self-induced" disorder nor of its spatial organisation (see Fig. V.1).

A more complete and intuitive determination of the "self-induced" disorder in glass-forming liquids requires to study the spatial fluctuations of a static and coarse-grained RFOT-like quantity, *e.g.*, the local configurational entropy or the local PTS length. However, local static properties are usually computed at the single-particle level and they may eventually be averaged over larger lengthscales to yield a coarse-grained quantity, see however Ref. [361, 362] for a coarse-grained and collective quantity in the context of the rheology of glasses. Instead, in this chapter, we want to propose a coarse-grained and static quantity which can be measured in equilibrium conditions and which is not built from a single-particle quantity. In addition, in the framework of the RFOT theory, the local static fluctuations, for instance of the configurational entropy, are directly related to the dynamic heterogeneities with the regions of larger configurational entropy able to relax faster [174, 195]. The correlation between the statics and the dynamics has been mostly investigated in the extreme cases of the single-particle and of the macroscopic scales by running simulations in the so-called isoconfigurational ensemble [62, 63]. This corresponds to different trajectories which start from the same initial condition and which are generated by running the dynamics with different initial particle velocities in molecular dynamics or different sequences of random numbers in Monte Carlo simulations [64]. The correlation between dynamic properties and structural quantities which are computed from the initial configuration of the particles is eventually assessed. At the single-particle level, a single-particle propensity is defined as the average of a single-particle dynamic quantity (*e.g.*, the displacement magnitude or the self-overlap of a given particle) over the trajectories and the correlation with the static single-particle quantities is subsequently assessed [65–71]. At the macroscopic scale, a structural quantity is defined for the bulk initial condition and is then correlated to the bulk relaxation time which is extracted from the average over the trajectories of a global dynamic property (*e.g.*, the self-intermediate scattering function or the global self-overlap) [190, 363]. However, the correlation between the dynamics and the statics at the mesoscopic scale would be worth studying. In particular, according to the RFOT theory, the generalised Adam-Gibbs relation [see Eq. (I.30)] between the local relaxation time and the local configurational entropy (or the local PTS length) should hold [124, 144], and studying such a connection could be a more severe test of the ability of the RFOT theory to describe glass formation in finite dimensions.

In this chapter, we propose a new way of measuring the intrinsic disorder in supercooled

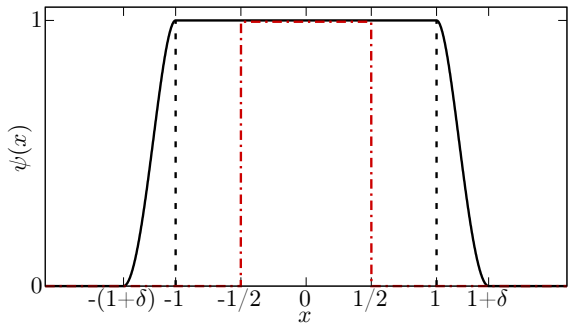

Fig. V.2 | Window function $\psi(x)$ to define the local overlap, see Eq. (V.1). The parameter δ is introduced to smooth out the variations of the window function at the boundaries of the cavity ($x = 1$). Equivalently, $1 + \delta$ stands for the linear extent (in units of the cavity radius R) over which the source ϵ is imposed. The dashed-dotted curve is the window function to define the core overlap, see Eq. (V.6).

liquids by directly probing the spatial fluctuations of the random FP potential. This requires to deal with small systems (ideally of linear extent similar to the PTS length) in order to remove the long-range finite-dimensional fluctuations [206]. In consequence, two different numerical strategies can be implemented to measure these fluctuations. On the one hand, bulk systems with periodic boundary conditions can be considered. This choice of boundary conditions limits the extent of the spatial fluctuations to the linear size of the system and also avoids surface effects [64]. This is what was done in Ref. [52] and in the previous chapter. However, small samples of supercooled liquids tend to crystallise more easily, even when dealing with size-polydisperse systems. This imposes a lower bound on the sizes which can be achieved in simulations. In addition, when dealing with periodic boundary conditions, neither the spatial organisation of the fluctuations of the FP potential nor the role of the boundaries can be assessed. Indeed, in the qualitative picture of Fig. V.1, the FP potential in the different blobs are assumed to be independent. Accordingly, for a given blob, this suggests that the FP potential should be taken as the average over all the realisations of the boundaries.

We thus turn to another method which consists in introducing a local probe in a bulk system with periodic boundary conditions (significantly larger than the PTS length) to measure the FP potential in a small spherical cavity of radius R roughly similar to the PTS length while performing an annealed average over its boundary. This method is directly inspired from the sketch in Fig. V.1. We describe the general formalism in the next section, and we compare it with the conventional cavity construction to define the PTS length [124, 144].

2. General formalism

We first define in the spherical cavity which is centered at a position $\boldsymbol{x}$ a local overlap between a liquid configuration $\boldsymbol{r}^N$ and a reference configuration $\boldsymbol{r}_0^N$ of the same liquid, namely,

$$\hat{Q}_{\boldsymbol{x}}^{(R)}[\boldsymbol{r}^N; \boldsymbol{r}_0^N] = \frac{\sum_{i,j} w(|\boldsymbol{r}_i - \boldsymbol{r}_{0,j}|/a)\psi(|\boldsymbol{r}_i - \boldsymbol{x}|/R)}{\sum_i \psi(|\boldsymbol{r}_i - \boldsymbol{x}|/R)}, \tag{V.1}$$

where the sums run over all the particles $i, j = 1 \ldots N$. The window function $w(x)$ and the tolerance length a are discussed extensively in Chap. IV. We have defined another window function $\psi(x)$ which is typically 1 for $x \lesssim 1$ and 0 otherwise to select the particles in the cavity,

i.e., the particles with $|\boldsymbol{r}_i - \boldsymbol{x}| \lesssim R$, see Fig. V.2. We then define the Franz-Parisi (FP) potential in the cavity at a temperature T for a fixed reference configuration $\boldsymbol{r}_0^N$,

$$V_{\boldsymbol{x}}^{(R)}(Q; \boldsymbol{r}_0^N) = -\frac{T}{\rho V_d R^d} \ln \mathcal{P}_{\boldsymbol{x}}^{(R)}(Q; \boldsymbol{r}_0^N), \tag{V.2}$$

where ρ is the number density, V_d the volume of the unit sphere in d dimensions, and where $\rho V_d R^d$ represents the average number of particles in the cavity, see Eq. (II.12). We have also introduced the probability distribution $\mathcal{P}_{\boldsymbol{x}}^{(R)}(Q; \boldsymbol{r}_0^N)$ of the local overlap with the reference configuration $\boldsymbol{r}_0^N$ [which is given by Eq. (V.1)] in the cavity of radius R at a position $\boldsymbol{x}$, namely,

$$\mathcal{P}_{\boldsymbol{x}}^{(R)}(Q; \boldsymbol{r}_0^N) = \langle \delta(\hat{Q}_{\boldsymbol{x}}^{(R)}[\boldsymbol{r}^N; \boldsymbol{r}_0^N] - Q) \rangle = \frac{\displaystyle\int \mathrm{d}\boldsymbol{r}^N e^{-\beta \hat{H}[\boldsymbol{r}^N]} \delta(\hat{Q}_{\boldsymbol{x}}^{(R)}[\boldsymbol{r}^N; \boldsymbol{r}_0^N] - Q)}{\displaystyle\int \mathrm{d}\boldsymbol{r}^N e^{-\beta \hat{H}[\boldsymbol{r}^N]}}, \tag{V.3}$$

with $\beta = 1/T$ (the Boltzmann constant is set to 1) and $\hat{H}[\boldsymbol{r}^N]$ the Hamiltonian of the bulk liquid. In the above formula, $\langle . \rangle$ stands for the thermal average at the temperature T. We note that this definition amounts to an annealed average over the boundaries, *i.e.*, over the positions of the particles outside the cavity.

In order to reveal the thermodynamic fluctuations of the local overlap, we introduce a field ϵ which is linearly coupled to the overlap with the reference configuration $\boldsymbol{r}_0^N$ in the cavity of radius R, as already done for the global overlap in bulk glass-forming liquids. In this case, the system evolves with the biased Hamiltonian[1]

$$\hat{H}_{\epsilon,\boldsymbol{x}}^{(R)}[\boldsymbol{r}^N; \boldsymbol{r}_0^N] = \hat{H}[\boldsymbol{r}^N] - (\rho V_d R^d) \times \epsilon \hat{Q}_{\boldsymbol{x}}^{(R)}[\boldsymbol{r}^N; \boldsymbol{r}_0^N]. \tag{V.4}$$

Equivalently, the particles inside the cavity feel an attraction with the particles in the reference configuration. The particles outside the cavity of radius R do not instead feel any attraction and the exterior of the cavity thus behaves as a reservoir of particles. In other words, our construction amounts to imposing a local field ϵ which is linearly coupled to the space dependent overlap field with the reference configuration. This indeed corresponds to an annealed average over the boundaries.

We comment on the qualitative behaviour of the system when it is coupled to a local field. For temperatures $T > T_{\mathrm{K}}$ (if the latter exists), the average overlap between equilibrium configurations is $Q_{\mathrm{rand}} \ll 1$. As a result, our setting is in spirit equivalent to a cavity which is free to evolve with the constraint that the overlap on the boundary is close to 0[2]. Whatever the size of the cavity with respect to the point-to-set (PTS) length, the local overlap between the cavity and the reference configuration is always close to $Q_{\mathrm{rand}} \ll 1$ for small-enough fields ϵ. One has to increase ϵ in order to create an inhomogeneous overlap profile and to force the cavity to have a larger overlap with the reference configuration, *i.e.*, to be localised close to the reference configuration. As a result, the value of the localising field $\epsilon^{*(R)}(\boldsymbol{x}; \boldsymbol{r}_0^N)$ corresponds to an estimate of the local configurational entropy $\Sigma(\boldsymbol{x}; \boldsymbol{r}_0^N)$, namely, $\epsilon^{*(R)}(\boldsymbol{x}; \boldsymbol{r}_0^N) \simeq T\Sigma(\boldsymbol{x}; \boldsymbol{r}_0^N)$. We stress that the localising field (and the local configurational entropy) is a local property of the

[1] We note that the factor of N in front of the biasing term has been consistently replaced by the average number of particles in the cavity of radius R, namely, $\rho V_d R^d$ with ρ the number density and V_d the volume of the unit sphere in d dimensions.

[2] This is not rigorously true, see Fig. V.3.

reference configuration only, as we average over the positions of the particles in the constrained liquid (both in the cavity and outside).

We finally mention that our method is different from the usual cavity method to measure the PTS length (see the *gedankenexperiment* in Chap. I) [124, 144, 179, 180]. In the latter, a configuration $\boldsymbol{r}_0^N$ is prepared at a temperature T. Then, all the particles are frozen except the ones in a cavity of radius R which are free to explore the phase space at the temperature T. There is not an imposed field ϵ and the overlap on the boundaries of the cavity is thus fixed to 1 (if one considers the initial configuration $\boldsymbol{r}_0^N$ as the reference configuration). The control parameter is instead the radius R of the cavity. For small cavities, *i.e.*, for cavities of smaller radius than the local PTS length, the overlap field is slightly inhomogeneous and it converges to a high value close to 1 at the center (which corresponds to the overlap for the "metastable glassy minimum" Q_{g} of the FP potential). Instead, for larger cavities than the local PTS length, the overlap field strongly decreases when approaching the center of the cavity to reach the "random" overlap value $Q_{\mathrm{rand}} \ll 1$. Nevertheless, our method and the usual cavity setting are both expected to reveal the local fluctuations of the PTS length, or equivalently of the configurational entropy, by systematically changing the position of the center $\boldsymbol{x}$ of the cavity. One advantage of our method is that confined cavities are usually much slower to relax and to explore the phase space than the bulk liquid [178]. On the opposite, we expect that in our method the exterior of the cavity which is free to evolve represents a reservoir of particles and does not hinder the relaxation of the particles in the cavity.

3. Model and methods

We simulate the size-polydisperse model glass-forming liquid [54] which is introduced in Chap. III with the Hamiltonian (V.4) by using the hybrid scheme which combines molecular dynamics with a thermostat and swap Monte Carlo moves [55]. The overlap is defined with the window function $w(x) = e^{-x^4 \ln 2}$ and the tolerance length $a = 0.22$ as in Chap. III. The other window function $\psi(x)$ in the definition (V.1) of the local overlap should be smooth on the boundary of the cavity. Indeed, in the course of a simulation, the particles can enter or leave the cavity and discontinuities in the forces that are exerted on the particles should be avoided. We choose

$$\psi(x) = \begin{cases} 1 & \text{if } x \leq 1, \\ \dfrac{e^{-(x-1)^4} - e^{-\delta^4}}{1 - e^{-\delta^4}} + c_2'(x-1)^2 + c_3'(x-1)^3 & \text{if } 1 < x \leq 1+\delta, \\ 0 & \text{otherwise,} \end{cases} \tag{V.5}$$

with $\delta = 0.07$ (see Fig. V.2), and where the constants c_2' and c_3' enforce that $\psi(x)$ and its first derivative are continuous at $x = 1$ and $x = 1 + \delta$, *i.e.*, $c_2' = -\delta c_3'$ and $c_3' = 4\delta e^{-\delta^4}/(1 - e^{-\delta^4})$. The choice of δ results from the compromise between a smooth evolution of the forces that are exerted on a particle when it leaves or enters the cavity and the sharp definition of the region of space where the field ϵ is imposed.

For a given position $\boldsymbol{x}$ of the cavity center, a given reference configuration $\boldsymbol{r}_0^N$ which is prepared at a temperature T_0 thanks to the swap algorithm, a given temperature T and a given field ϵ, the radial overlap field $\langle q(r; \boldsymbol{r}_0^N)\rangle_\epsilon$ is inhomogeneous, see Fig. V.3 for an example in $2d$, where $\langle . \rangle_\epsilon$ stands for the thermal average with the Hamiltonian $\hat{H}_{\epsilon,\boldsymbol{x}}^{(R)}[\boldsymbol{r}^N; \boldsymbol{r}_0^N]$. We observe that the overlap profile is maximum for $r \leq R$ and that it decays at large distances to its random

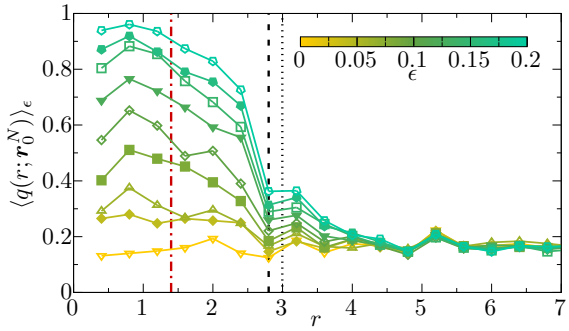

Fig. V.3 | Overlap profile in a $2d$ system in and near one cavity of radius $R = 2.8$ when the local overlap in the cavity with a reference configuration $\boldsymbol{r}_0^N$, which has been sampled at a temperature $T_0 = 0.03$, is biased with a field ϵ. The exterior of the cavity instead evolves without any thermodynamic constraint. The brackets stand for the thermal average at a temperature $T = 0.1$ and for a spherical spatial average. The system size is $N = 2000$, which corresponds to a linear size $L \simeq 45$ (the number density is $\rho = 1$). The black dashed line marks the radius R of the cavity, the black dotted line corresponds to the vanishing of the window function $\psi(r/R)$ at $r = (1+\delta)R$, hence the linear extent over which the field ϵ is imposed, and the red dashed-dotted line stands for the half-radius of the cavity. The overlap profiles are found to decay to the random overlap value $Q_{\rm rand} \simeq 0.16$ at large distances on a typical lengthscale which is larger than the lengthscale over which the field ϵ is imposed. The overlap at the center of the cavity ($r = 0$), or equivalenty the core overlap which is averaged over space for $r \leq R/2$, increases with larger ϵ.

value $Q_{\rm rand} = \rho S_d a^d \Gamma(d/4)/[4(\ln 2)^{d/4}] (\simeq 0.16$ in $2d)$, with S_d the surface of the unit sphere in d dimensions and $\Gamma(x)$ the Euler Gamma function. The overlap profile at the center of the cavity also clearly increases with increasing ϵ. However, we note that the overlap is not constant in the cavity, *i.e.*, we already observe a significant decrease in the overlap for $r \leq R$ when ϵ increases. As a result, and similarly to studies on the point-to-set length, we define a core overlap for a given cavity of radius R at a position $\boldsymbol{x}$ [175], namely,

$$\hat{Q}^{(R)}_{{\rm c},\boldsymbol{x}}[\boldsymbol{r}^N;\boldsymbol{r}_0^N] = \frac{\sum_{i,j} w(|\boldsymbol{r}_i - \boldsymbol{r}_{0,j}|/a)\,\theta(R/2 - |\boldsymbol{r}_i - \boldsymbol{x}|)}{\sum_i \theta(R/2 - |\boldsymbol{r}_i - \boldsymbol{x}|)}, \tag{V.6}$$

where $\theta(x)$ represents the Heaviside step function (see Fig. V.2). The variations of the core overlap are expected to be sharper with ϵ and likely yield to a more precise definition of the localising field for which the fluctuations of the core overlap are maximum. In other words, we define the localising field $\epsilon^{*(R)}(\boldsymbol{x};\boldsymbol{r}_0^N)$ as

$$\epsilon^{*(R)}(\boldsymbol{x};\boldsymbol{r}_0^N) = {\rm argmax}_\epsilon\{\langle \hat{Q}^{(R)\,2}_{{\rm c},\boldsymbol{x}}\rangle_\epsilon - \langle \hat{Q}^{(R)}_{{\rm c},\boldsymbol{x}}\rangle_\epsilon^2\}. \tag{V.7}$$

However, we stress that ϵ is coupled to the average overlap in the cavity, not to the core overlap.

We now explain how to measure the localising field for a given position $\boldsymbol{x}$ of the cavity of radius R, for a given temperature T, and a given reference configuration $\boldsymbol{r}_0^N$. This requires to measure the thermal fluctuations of the core overlap for any ϵ and eventually to locate their maximum. We thus turn to histogram reweighting techniques [315–318, 364]. We perform $n_{\rm s}$ simulations with fields $\{\epsilon_k\}_{k=1\ldots n_{\rm s}}$, we measure n_k times the local overlap (V.1) and the core overlap (V.6) and we compute their normalised joint histograms $\mathcal{N}_k(Q, Q_{\rm c})$ for $k = 1\ldots n_{\rm s}$. Then, the joint probability distribution of the local and the core overlaps in the cavity of radius

R at a position $\boldsymbol{x}$ for a field ϵ and a reference configuration $\boldsymbol{r}_0^N$ reads

$$\mathcal{P}_{\epsilon,\boldsymbol{x}}^{(R)}(Q,Q_{\rm c};\boldsymbol{r}_0^N) = \langle \delta(\hat{Q}_{\boldsymbol{x}}^{(R)} - Q)\delta(\hat{Q}_{{\rm c},\boldsymbol{x}}^{(R)} - Q_{\rm c})\rangle_\epsilon = \frac{\sum_{k=1}^{n_{\rm s}} n_k \mathcal{N}_k(Q,Q_{\rm c})}{\sum_{k=1}^{n_{\rm s}} n_k \mathcal{Z}_k^{-1} e^{\beta\rho V_d R^d(\epsilon_k-\epsilon)Q}}, \tag{V.8}$$

where the partition functions $\mathcal{Z}_k$ are computed self-consistently by iterating the following formula:

$$\mathcal{Z}_k = \int_0^1 {\rm d}Q \int_0^1 {\rm d}Q_{\rm c} \frac{\sum_{k'=1}^{n_{\rm s}} n_{k'} \mathcal{N}_{k'}(Q,Q_{\rm c})}{\sum_{k'=1}^{n_{\rm s}} n_{k'} \mathcal{Z}_{k'}^{-1} e^{\beta\rho V_d R^d(\epsilon_{k'}-\epsilon_k)Q}}. \tag{V.9}$$

More details about the reweighting procedure can be found in Chap. III. The probability distribution of the core overlap is then derived from the joint distribution:

$$\mathcal{P}_{\epsilon,\boldsymbol{x}}^{(R)}(Q_{\rm c};\boldsymbol{r}_0^N) = \int_0^1 {\rm d}Q \mathcal{P}_{\epsilon,\boldsymbol{x}}^{(R)}(Q,Q_{\rm c};\boldsymbol{r}_0^N) = \int_0^1 {\rm d}Q \frac{\sum_{k=1}^{n_{\rm s}} n_k \mathcal{N}_k(Q,Q_{\rm c})}{\sum_{k=1}^{n_{\rm s}} n_k \mathcal{Z}_k^{-1} e^{\beta\rho V_d R^d(\epsilon_k-\epsilon)Q}}. \tag{V.10}$$

Finally, its second cumulant, namely, the variance of the core overlap, can be computed to yield the localising field $\epsilon^{*(R)}(\boldsymbol{x};\boldsymbol{r}_0^N)$, see Eq. (V.7).

By biasing the local overlap with different fields ϵ, we are able to sample efficiently the overlap fluctuations and to scan the entire range of overlap values in the range $[0,1]$. In other words, the histogram reweighting procedure also allows for a sampling of the tails of the distribution of the local overlap in the unconstrained cavity and for a computation of the Franz-Parisi (FP) potential via

$$\mathcal{P}_{\boldsymbol{x}}^{(R)}(Q;\boldsymbol{r}_0^N) = \int_0^1 {\rm d}Q_{\rm c} \mathcal{P}_{\epsilon=0,\boldsymbol{x}}^{(R)}(Q,Q_{\rm c};\boldsymbol{r}_0^N) = \int_0^1 {\rm d}Q_{\rm c} \frac{\sum_{k=1}^{n_{\rm s}} n_k \mathcal{N}_k(Q,Q_{\rm c})}{\sum_{k=1}^{n_{\rm s}} n_k \mathcal{Z}_k^{-1} e^{\beta\rho V_d R^d \epsilon_k Q}}, \tag{V.11}$$

see Eq. (V.2).

For each position $\boldsymbol{x}$ of the cavity and each field ϵ, the equilibration is ensured as in Chap. III by checking that the simulations from two different initial conditions converge to the same stationary state. Once the stationary state is obtained, we verify that the cavity explores the phase space ergodically. We monitor the identity of the particles in the cavity (*i.e.*, the particles i with $|\boldsymbol{r}_i - \boldsymbol{x}| < R$). We define the ratio of the number of particles in the cavity at time t which already were in the cavity at time 0 to the number of particles in the cavity at time 0 and we check that it has decreased to 0.

In the following, we focus on two-dimensional systems ($d = 2$). Indeed, we note in Fig. V.3 that the decorrelation length of the overlap profile is larger than the length over which the field ϵ is imposed. In other words, the overlap profile extends outside the cavity on a typical

lengthscale equal to the average inter-particle distance. In consequence, even though the overlap with the reference configuration is biased in the cavity of radius R only, this affects an effective number of particles which is larger than the average number of particles in the cavity. The ratio of the effective number of particles which are affected to the number of particles in the cavity scales as $(1 + 1/R)^d$ and therefore it increases with d and decreases with R. In consequence, we choose $d = 2$ to minimise this effect and to actually perform a local measure of the FP potential. This also eases the visualisation of the local fluctuations of $\epsilon^{*(R)}(\boldsymbol{x}; \boldsymbol{r}_0^N)$ and allows for the construction of $2d$ maps.

The size of the system must be taken sufficiently larger than the radius of the cavity in order for the cavity not to feel the periodic boundary conditions. The cavity radius also should exceed several particle average diameters in order to measure coarse-grained quantities. We thus consider cavities of radius $R = 4$ (we recall that the distances are expressed in units of the average particle diameter) in a system of linear size $L = 24$. This choice corresponds to an average number of 50 particles in the cavity while the total number of particles in the system is $N = 576$. For each reference configuration which is equilibrated at a temperature T_0, we run simulations at a temperature T for different positions $\boldsymbol{x}$ of the center of the cavities on a grid of linear spacing $u = R/2 = 2$ in both directions of space. This represents a total of $(L/u)^2 = 144$ positions of the cavities for a given reference configuration $\boldsymbol{r}_0^N$. For each cavity, we simulate about 10-15 different values of ϵ to reconstruct the FP potential and the cumulants of the local and the core overlaps adequately. This represents a parallelisable task of more than a thousand simulations for a given reference configuration. Eventually, more statistics are obtained by repeating the above procedure for several reference configurations.

Most of the results are shown for the case $T = T_0$ with temperatures which range from the onset of glassy behaviour $T_{\rm on} \simeq 0.20$ to the extrapolated laboratory glass transition temperature $T_{\rm g} \simeq 0.07$ (see Chap. III for the temperature scales of the $2d$ system and Chap. VI for their definition). Previous measurements of the point-to-set length in the same system show that it midly increases from $\xi_{\rm PTS} \simeq 1.97$ at $T = 0.2$ to $\xi_{\rm PTS} \simeq 3.34$ at $T = 0.07$ [182]. We thus note that $\xi_{\rm PTS}$ is always much smaller than the linear size L of the system but close to the radius R of the cavities with the choices of L and R that we have made.

4. Thermodynamic spatial fluctuations

4.1 Fluctuations of the Franz-Parisi potential

We start by showing the results for a given reference configuration $\boldsymbol{r}_0^N$ in Fig. V.4 for the case $T = T_0 = 0.1$ which is between the mode-coupling crossover [136] and the extrapolated glass transition temperature. In Fig. V.4 (a), we display the variation of the average core overlap with ϵ for four different locations of the center of the cavity. For all the cavities, we observe a monotonic increase in the average core overlap with ϵ. The isotherms display an inflexion point which corresponds to the location of the maximum in the core overlap fluctuations for $\epsilon = \epsilon^{*(R)}(\boldsymbol{x}; \boldsymbol{r}_0^N)$ (see Chap. II). We note significant spatial fluctuations of the isotherms and accordingly of the localising field $\epsilon^{*(R)}(\boldsymbol{x}; \boldsymbol{r}_0^N)$ which are shown in Fig. V.4 (b). The map has been computed from the estimates of $\epsilon^{*(R)}(\boldsymbol{x}; \boldsymbol{r}_0^N)$ in the 144 cavities via an extrapolation on a lattice of thinner spacing $\mathrm{d}r = 0.05$ by using an exponential weight of characteristic lengthscale

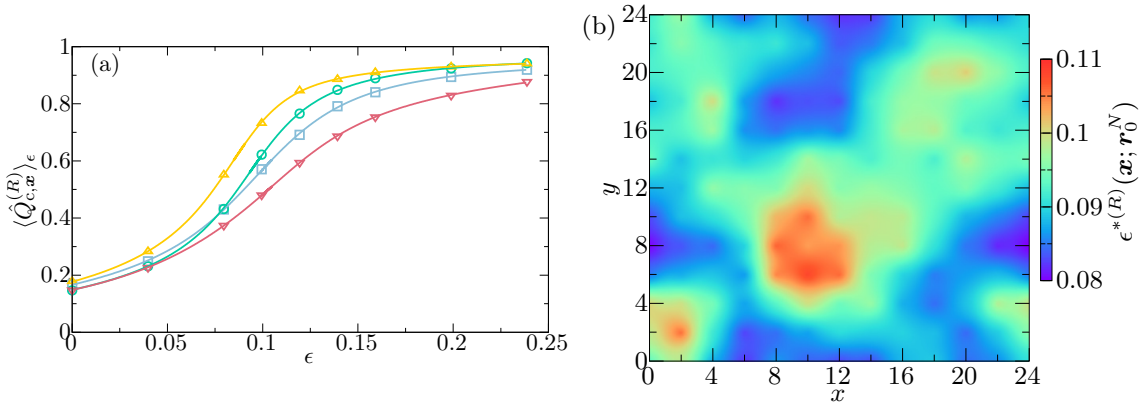

Fig. V.4 | (a) Isotherms of the core overlap $\langle \hat{Q}^{(R)}_{c,\boldsymbol{x}} \rangle_\epsilon$ for four different cavities. The symbols represent the simulation results while the full curves are obtained via a histogram reweighting. We observe spatial fluctuations of the isotherms, and consequently of the localising field $\epsilon^{*(R)}(\boldsymbol{x}, \boldsymbol{r}_0^N)$ (location of the inflexion point) which are summarised in the map of panel (b). This result is obtained for a single reference configuration in $2d$, with $N = 576$ ($L = 24$), $R = 4$ and $T = T_0 = 0.1$.

$\ell = u/2 = 1$, *i.e.*, for any $\boldsymbol{y} \in [0, L]^d$:

$$\epsilon^{*(R)}(\boldsymbol{y}; \boldsymbol{r}_0^N) = \frac{\sum_{\boldsymbol{x}} \epsilon^{*(R)}(\boldsymbol{x}; \boldsymbol{r}_0^N) e^{-|\boldsymbol{x}-\boldsymbol{y}|/\ell}}{\sum_{\boldsymbol{x}} e^{-|\boldsymbol{x}-\boldsymbol{y}|/\ell}}, \tag{V.12}$$

where the sums run over all the positions $\boldsymbol{x}$ of the cavities. In Fig. V.4 (b), we observe non-trivial fluctuations which form domains of spatially-correlated values of the localising field with a typical linear extent equal to 2-3 particle diameters.

We now turn to the statistical properties of the localising field which are obtained for many reference configurations $\boldsymbol{r}_0^N$ in the case $T = T_0$. In Fig. V.5 (a), we plot its average $\epsilon^{(R)}_{c,1}(T) = \overline{\langle\langle \epsilon^{*(R)}(\boldsymbol{x}; \boldsymbol{r}_0^N) \rangle\rangle}$ and its standard deviation $\epsilon^{(R)}_{c,2}(T) = [\overline{\langle\langle \epsilon^{*(R)}(\boldsymbol{x}; \boldsymbol{r}_0^N)^2 \rangle\rangle} - \overline{\langle\langle \epsilon^{*(R)}(\boldsymbol{x}; \boldsymbol{r}_0^N) \rangle\rangle}^2]^{1/2}$ as a function of the temperature T, where the symbol $\langle\langle . \rangle\rangle$ stands for an average over the location of the cavities for a fixed reference configuration $\boldsymbol{r}_0^N$ while the overline denotes an average over the reference configurations. Both cumulants of the localising field have been divided by the temperature because the relevant control parameter in the Boltzmann weight is $\beta\epsilon$ (the Boltzmann constant is set to unity). We observe that the first cumulant decreases with decreasing the temperature, by about 30 % between the onset temperature of glassy behaviour and the glass transition temperature. The variation of the standard deviation with the temperature is more difficult to determine from the data because of the high statistical errors but the latter also looks to decrease when decreasing the temperature, by about 13 %. Accordingly, the ratio of the standard deviation $\epsilon^{(R)}_{c,2}(T)$ to the average localising field $\epsilon^{(R)}_{c,1}(T)$ seems to increase while decreasing the temperature, which indicates larger relative static fluctuations at lower temperatures. However, better statistics would be valuable to clarify the dependence of the cumulants of the localising field on the temperature.

In order to gain more insight on the fluctuations of the local field, we consider the probability distribution $p^{(R)}(\epsilon)$ of the localising field which is computed over several reference configurations for different temperatures $T = T_0$, see Fig. V.5 (b). We observe that the histograms for all the temperatures from the onset temperature of glassy behaviour down to T_g follow a master curve

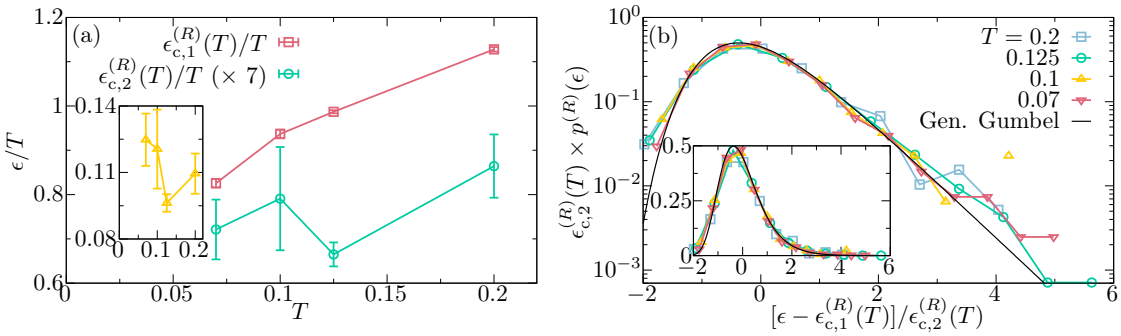

Fig. V.5 | (a) Average $\epsilon_{c,1}^{(R)}(T)$ and standard deviation $\epsilon_{c,2}^{(R)}(T)$ of the localising field for several temperatures which range from the experimental glass transition temperature to the onset temperature of glassy behaviour and for the case $T = T_0$. Both quantities have been divided by the temperature (the Boltzmann constant is set to unity). The standard deviation has been multiplied by 7 in order to cover a similar range as the first moment. Errorbars are computed thanks to the jacknife method when the average over the reference configurations is performed [294], they are too small to be seen for the first cumulant. The inset represents the ratio of the standard deviation to the average localising field, namely, $\epsilon_{c,2}^{(R)}(T)/\epsilon_{c,1}^{(R)}(T)$, with respect to the temperature T. (b) Histograms $p^{(R)}(\epsilon)$ of the localising field for the case $T = T_0$. The data have been rescaled by $\epsilon_{c,2}^{(R)}(T)$ and plotted as a function of $[\epsilon - \epsilon_{c,1}^{(R)}(T)]/\epsilon_{c,2}^{(R)}(T)$, see Eq. (V.13). They follow a master curve which is well fitted by a generalised Gumbel distribution with a single adjustable parameter $\alpha \simeq 1.3$, see Eq. (V.14).

when they are plotted as a function of $[\epsilon - \epsilon_{c,1}^{(R)}(T)]/\epsilon_{c,2}^{(R)}(T)$ and rescaled by $\epsilon_{c,2}^{(R)}(T)$, *i.e.*,

$$p^{(R)}(\epsilon) = \left[\epsilon_{c,2}^{(R)}(T)\right]^{-1} \mathcal{F}\left(\frac{\epsilon - \epsilon_{c,1}^{(R)}(T)}{\epsilon_{c,2}^{(R)}(T)}\right), \tag{V.13}$$

where the prefactor comes from the normalisation of the distribution and where $\mathcal{F}(x)$ is a temperature independent function. The histograms display a temperature independent large tail at high values of ϵ which decays exponentially while the low-ϵ part of the histogram decreases sharply and faster than an exponential. The fluctuations of the localising field are therefore right-tailed and non-Gaussian, and they are well approximated by a generalised Gumbel distribution with a single free parameter α [365], *i.e.*,

$$\mathcal{F}(x) = \frac{\mu_\alpha \alpha^\alpha}{\Gamma(\alpha)} e^{-\alpha(z+e^{-z})}, \quad z = \mu_\alpha(x + \lambda_\alpha), \tag{V.14}$$

with

$$\begin{cases} \mu_\alpha = & \sqrt{\dfrac{1}{\Gamma(\alpha)}\dfrac{\mathrm{d}^2\Gamma}{\mathrm{d}\alpha^2}(\alpha) - \left[\dfrac{1}{\Gamma(\alpha)}\dfrac{\mathrm{d}\Gamma}{\mathrm{d}\alpha}(\alpha)\right]^2}, \\ \lambda_\alpha = & \dfrac{1}{\mu_\alpha}\left[\ln\alpha - \dfrac{1}{\Gamma(\alpha)}\dfrac{\mathrm{d}\Gamma}{\mathrm{d}\alpha}(\alpha)\right]. \end{cases} \tag{V.15}$$

The parameters of the generalised Gumbel distribution involve the Euler Gamma function $\Gamma(\alpha)$ and its two first derivatives which read for $n \geq 1$:

$$\begin{cases} \Gamma(\alpha) = & \displaystyle\int_0^{+\infty} \mathrm{d}t\, t^{\alpha-1} e^{-t}, \\ \dfrac{\mathrm{d}^n\Gamma}{\mathrm{d}\alpha^n}(\alpha) = & \displaystyle\int_0^{+\infty} \mathrm{d}t\, t^{\alpha-1} e^{-t} (\ln t)^n. \end{cases} \tag{V.16}$$

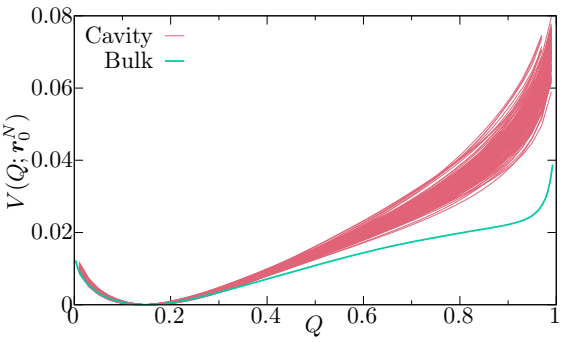

Fig. V.6 | Franz-Parisi (FP) potentials $V_{\boldsymbol{x}}^{(R)}(Q;\boldsymbol{r}_0^N)$ in cavities of radius $R = 4$ at a temperature $T = 0.07$ for a fixed reference configuration $\boldsymbol{r}_0^N$ which has been sampled at $T_0 = 0.04$. The FP potential $V(Q;\boldsymbol{r}_0^N)$ for a single reference configuration in a bulk system with periodic boundary conditions of linear size $L = 2R = 8$ at the same temperatures is also represented for comparison: it is smaller at large overlap values and it displays more pronounced non-convexities.

The best estimate of $\alpha \simeq 1.3$ for fitting our data has been found by minimising the sum $\chi^2(\alpha)$ of the residuals, namely, the quadratic difference between the rescaled histograms at all the temperatures and the master curve. However, our estimate of α suffers from large uncertainties, and for instance the values $\alpha = 1$ or $\alpha = \pi/2$ (see later) perform almost equally well, even though the corresponding values of $\chi^2(\alpha)$ are slightly higher.

When α is an integer, this distribution is usually encountered in extreme-value statistics and describes the fluctuations of the αth largest value in an ensemble of independent and identically distributed random variables [366]. The generalised Gumbel distribution was also interpreted as the distribution of the infinite sum of independent and exponentially distributed random variables [367]. It was first found in the XY model [368] for the distribution of the average magnetisation at the critical point [369] and has now been displayed in several other strongly correlated systems, for instance turbulence [370] and interface growth [371], with an apparent universal reported value $\alpha = \pi/2 \simeq 1.57$. However, the connection between our system and these phenomena is not clear. Indeed, in the latter, the Gumbel distribution describes the fluctuations of a global spatially averaged variable [372]. On the opposite, here, we have found that the field which is linearly coupled to the overlap with a reference configuration is distributed according to a generalised Gumbel distribution, while the distribution of the overlap is almost symmetric at any temperature.

4.2 Influence of the boundaries

To understand the origin of this non-Gaussian distribution of the localising field, we compare our protocol with the simulations of small systems with periodic boundary conditions. In Ref. [52], an almost Gaussian distribution of the localising field was found. As the only difference between the protocols is the existence of boundaries, the latter should be responsible for the emergence of a tail at large values of ϵ. By using the change in ensembles in Chap. II, the boundary should also impact the Franz-Parisi (FP) potential $V_{\boldsymbol{x}}^{(R)}(Q;\boldsymbol{r}_0^N)$ in the cavities for a fixed reference configuration $\boldsymbol{r}_0^N$. In Fig. V.6, we display the FP potentials for several cavities of radius $R = 4$ at a temperature $T = 0.07$ for a given reference configuration $\boldsymbol{r}_0^N$ which has been sampled at a temperature $T_0 = 0.04$. We choose a lower temperature of the reference configuration as this may lead to more pronounced non-convexities of the FP potential at a

fixed temperature T (for the influence of the temperature T_0, see Chap. II and Chap. III). The FP potential in the different cavities is directly compared to the FP potential for a system with periodic boundary conditions which has been computed via the methods that are presented in Chap. III. The temperatures T and T_0 are the same in both cases and the size of the bulk liquid is chosen to be similar to the size of the cavities: the bulk liquid is taken of linear size $L = 2R = 8$ which corresponds to a total number $N = 64$ of particles. We observe that the FP potential in the cavities is not as non-convex as its counterpart in small systems with periodic boundary conditions. This suggests that the annealed average over the boundaries is likely to destabilise the metastable glassy phase in the cavity. Qualitatively, this comes from the fact that when ϵ increases, the overlap profile penetrates more and more outside the cavity (see Fig. V.3) and in consequence a larger field is required in order to localise the cavity close to the reference configuration. In other words, not only $\epsilon^{*(R)}(\boldsymbol{x}; \boldsymbol{r}_0^N)$ reflects the configurational entropy cost to enforce a large overlap within the cavity but it also takes a contribution from the free energy cost to smooth out the mismatch in the density fields just outside the cavity. This is similar to the contribution of the surface tension in the nucleation argument of the random first order transition theory [124, 144]. This rationalises the emergence of a tail in $p^{(R)}(\epsilon)$ at large values of ϵ in Fig. V.5 (b) (as the localising field is the slope of the tangent line at the FP potential) and this suggests that the generalised Gumbel distribution should merely be considered as a convenient fitting function. If our intuition is correct, then the shape of the distribution $p^{(R)}(\epsilon)$ is likely to change upon increasing the radius R of the cavity to tend to its counterpart in systems with periodic boundary conditions, because the relative weight of the surface free energy cost is expected to scale as $R^{-(d-\theta)}$, with $\theta \leq d - 1$ [122, 124, 144, 175].

5. Conclusions and perspectives

5.1 Statistics of the local Franz-Parisi potential

In this chapter, we have presented a new method to measure the local fluctuations of the Franz-Parisi (FP) potential which represents the free energy cost to maintain the local overlap or similarity between a liquid configuration and a reference configuration of the same liquid at a given value. In the framework of the random first order transition (RFOT) theory, namely, the finite-dimensional version of the mean-field theory of glass formation, the local configurational entropy, which corresponds to height of the secondary minimum of the FP potential, behaves as a random field which is linearly coupled to the local overlap between equilibrium configurations, as the mapping of glass-forming liquids onto the random-field Ising model (RFIM) suggests [196, 197]. The static and spatial fluctuations of the local overlap in a cavity of radius R can be magnified by coupling the latter to an external field ϵ, while the exterior is free to evolve without any thermodynamic constraint. We have revealed non-trivial fluctuations of the field $\epsilon^{*(R)}(\boldsymbol{x}; \boldsymbol{r}_0^N)$ which is needed to localise a patch of radius R close to a reference configuration, namely, to induce a large local overlap. We have shown that these fluctuations are spatially correlated, *i.e.*, they form domains of about 2-3 particle average diameters. A more accurate computation of the correlation length of the localising field remains to be done to assess its temperature evolution. In particular, the latter should be comparable to the one of the point-to-set (PTS) length which quantifies the typical linear extent of amorphous order in glass-forming liquids and the lengthscale below which mean-field metastable states are well defined in finite dimensions. The correlation length of the localising field and the PTS length seem roughly similar but we need to accumulate more data to confirm this point [182]. In addition, we have shown that the average

and the standard deviation of the localising field $\epsilon^{*(R)}(\boldsymbol{x};\boldsymbol{r}_0^N)$ both decrease when decreasing the temperature, while their ratio seems to increase. We have argued that the fluctuations of this field represent a reasonable proxy for the spatial variations of the configurational entropy. Our results are therefore compatible with a decrease in the local configurational entropy and an increase in its relative fluctuations. This is overall consistent with the RFOT theory which predicts that the average configurational entropy decreases with the temperature and vanishes at the Kauzmann transition (if it exists) while its standard deviation remains finite at the Kauzmann transition: the relative fluctuations of the configurational entropy are thus expected to diverge at the putative Kauzmann transition [168].

We have also studied the distribution $p^{(R)}(\epsilon)$ of the fluctuations of $\epsilon^{*(R)}(\boldsymbol{x};\boldsymbol{r}_0^N)$ which is well approximated by a temperature independent generalised Gumbel distribution when the data are properly rescaled and for all the temperatures that range from the onset temperature of glassy behaviour down to the extrapolated experimental glass transition temperature. Interestingly, the distribution displays an exponential right tail which corresponds to regions of very large localising field. However, the form of the distribution is likely to be caused by the presence of the boundary and the fact that $\epsilon^{*(R)}(\boldsymbol{x};\boldsymbol{r}_0^N)$ not only must overcome the free energy penalty to localise a given region of the liquid close to the reference configuration but also the free energy cost to smooth out the density mismatch between the cavity and the exterior. This point deserves a more thorough investigation to properly account for the precise shape of the distribution $p^{(R)}(\epsilon)$ along with the scaling form in Eq. (V.13). In particular, the latter predicts that the skewness or the excess kurtosis (see Chap. III) of the localising field should be independent[3] of the temperature T. In addition, we have advocated that the shape of the distribution, especially its exponential tail, should depend on the radius R of the cavity: a systematic investigation of the R dependence of $p^{(R)}(\epsilon)$ is left for future work.

Even though these preliminary results are encouraging, our setting is worth comparing to a similar one in which the exterior of the cavity is frozen in a configuration which has a random overlap with the reference configuration. This corresponds to a quenched average over the boundaries. In particular, this strategy might be able to confirm or infirm our interpretation of the results and to disentangle the two sources of fluctuations which are captured by $\epsilon^{*(R)}(\boldsymbol{x};\boldsymbol{r}_0^N)$, namely, fluctuations of the local configurational entropy and of the surface free energy cost. However, this protocol is far more demanding. On the one hand, cavities with frozen boundaries are much slower than their bulk counterpart [178], and an accurate sampling would require longer simulations and/or more clever algorithms, for instance parallel tempering [180, 314]. On the other hand, an average over the realisations of the boundaries must be taken for a fixed reference configuration and for each cavity, which multiplies the total number of simulations.

Finally, we come back to the usual cavity setting, as discussed before, which is inspired from the RFOT theory and which consists in freezing all the particles outside a cavity of radius R while the particles inside the cavity are free to relax in the presence of the amorphous boundary [124, 144, 175, 178–180, 182, 185]. This amounts to forcing a large overlap close to 1 with the reference configuration on the boundary of the cavity (in this case $\epsilon = 0$). By decreasing the radius R of the cavity, a crossover from a low to a high overlap at the center of the cavity is found for R equal to the PTS length. When varying the location of the cavity, the crossover radius fluctuates and these fluctuations of the local PTS length also reflect local static fluctuations. The local fluctuations of the PTS length may be related to the fluctuations that we have put forward in this

[3]For instance, the generalised Gumbel distribution with $\alpha \simeq 1.3$ implies that the skewness should be approximately equal to 0.99 at any temperature.

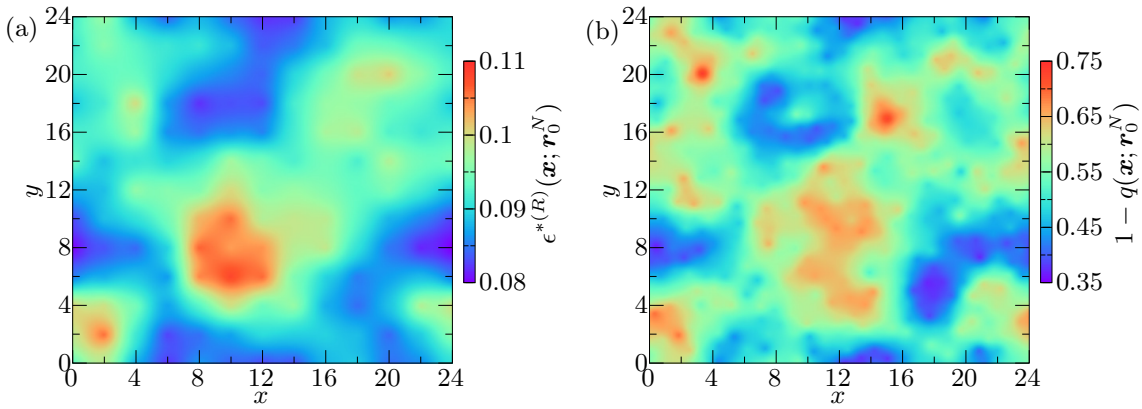

Fig. V.7 | (a) Same as Fig. V.4 (b). (b) Map of the local overlap in a bulk liquid of $N = 576$ particles at a temperature $T = 0.1$ with the same reference configuration as in panel (a) ($T_0 = 0.1$). Be careful that the map shows $1 - q(\boldsymbol{x}; \boldsymbol{r}_0^N)$. The two maps are highly correlated (the Pearson correlation $r_{q\epsilon}$ is about -0.64), which means that the regions of high localising field correspond to the regions of small overlap when the average global overlap is fixed.

chapter, namely, the fluctuations of the localising field $\epsilon^{*(R)}(\boldsymbol{x}; \boldsymbol{r}_0^N)$. In particular, the regions of larger PTS length shoud be correlated with the regions of lower localising field. An analysis of the similarities and the differences between our method and the usual cavity construction is also left for future work.

5.2 Correlation with structural indicators and the dynamic heterogeneities

Our protocol reveals static fluctuations of the localising field $\epsilon^{*(R)}(\boldsymbol{x}; \boldsymbol{r}_0^N)$. The cavities of larger (resp. smaller) $\epsilon^{*(R)}(\boldsymbol{x}; \boldsymbol{r}_0^N)$ correspond to regions where the overlap is likely to be lower (resp. higher) and somehow to hotter (resp. colder) zones. A structural characterisation of these regions could be interesting, for instance by measuring the correlation between the localising field and several structural indicators [373], such as the local orientational order [69], the machine learning based softness [374], the vibrational modes, the local energy, the local density [67] or the local yield stress [361, 362]. Except for the latter, all of the previously mentioned quantities are defined at the single-particle level and assessing their connection with $\epsilon^{*(R)}(\boldsymbol{x}; \boldsymbol{r}_0^N)$ requires a coarse-graining, see later.

As a first step to assess the physical relevance of the fluctuations of the localising field, we have used umbrella sampling simulations in order to force the bulk liquid to have a global finite overlap with the reference configuration

$$\hat{Q}[\boldsymbol{r}^N; \boldsymbol{r}_0^N] = \frac{1}{N} \sum_{i=1}^{N} q_i[\boldsymbol{r}^N; \boldsymbol{r}_0^N] = \frac{1}{N} \sum_{i,j=1}^{N} w(|\boldsymbol{r}_i - \boldsymbol{r}_{0,j}|/a), \tag{V.17}$$

where q_i is the overlap of particle i, see Chap. III. More precisely, we have run simulations of the liquid with the Hamiltonian

$$\hat{H}_{\mathrm{b}}[\boldsymbol{r}^N; \boldsymbol{r}_0^N] = \hat{H}[\boldsymbol{r}^N] + \frac{1}{2} N\kappa(\hat{Q}[\boldsymbol{r}^N; \boldsymbol{r}_0^N] - Q^{\mathrm{ref}})^2, \tag{V.18}$$

with $\kappa = 0.3$ and where Q^{ref} controls the average value of the global overlap. In $2d$ and for large-enough samples, the system displays small domains of low and high overlap with the reference

configuration, see Fig. V.7 (b). The map has been obtained from the measure of the average local overlap of each particle $\langle q_i \rangle_{\rm b}$ (where $\langle . \rangle_{\rm b}$ denotes an average with the Hamiltonian $\hat{H}_{\rm b}[\boldsymbol{r}^N; \boldsymbol{r}_0^N]$ for a fixed reference configuration $\boldsymbol{r}_0^N$ and a fixed temperature T) via an extrapolation on a lattice of spacing $\mathrm{d}r = 0.05$ by using an exponential weight of characteristic lengthscale $\ell = 0.5$, *i.e.*, for any $\boldsymbol{y} \in [0, L]^d$:

$$q(\boldsymbol{y}; \boldsymbol{r}_0^N) = \frac{\sum_i \langle q_i \rangle_{\rm b} e^{-|\boldsymbol{r}_i - \boldsymbol{y}|/\ell}}{\sum_i e^{-|\boldsymbol{r}_i - \boldsymbol{y}|/\ell}}, \tag{V.19}$$

where the sums run over $i = 1 \dots N$. The reference configuration is the same as in Fig. V.4 (b) [see also Fig. V.7 (a)] and the center of the umbrella potential has been chosen to maximise the correlation (see later). The domains of large overlap seem to coincide with the regions of small $\epsilon^{*(R)}(\boldsymbol{x}; \boldsymbol{r}_0^N)$: when the overlap is fixed, the domains of low (resp. high) overlap are preferably pinned on the regions of high (resp. low) field. In $2d$, there is no phase transition in the phase diagram (ϵ, T) when the global overlap $\hat{Q}[\boldsymbol{r}^N; \boldsymbol{r}_0^N]$ is coupled to a field ϵ, see Chap. III. According to our discussion in Chap. II, fixing the global overlap to Q is thus equivalent to imposing a uniform field ϵ in the sample such that the average overlap is Q. Therefore, when the global overlap is biased via an external field, the system displays micro-domains. The domains of high overlap are located in the regions where $\epsilon^{*(R)}(\boldsymbol{x}; \boldsymbol{r}_0^N) < \epsilon$ as the global field is high enough to switch to a locally high-overlap state. The regions of localising field $\epsilon^{*(R)}(\boldsymbol{x}; \boldsymbol{r}_0^N) > \epsilon$ remain instead in a locally delocalised state. These results are encouraging but their robustness needs to be systematically checked by changing the reference configuration, the temperature or the dimension. In particular, in $3d$ and at low-enough temperatures, the system displays a macroscopic phase separation when its global overlap is fixed (see Fig. III.9), and the correlation with the localising field is worth assessing in this case. In particular, the domains of low or high overlap are rough and their shape could maybe be rationalised because their interfaces are pinned by large or small values of the localising field, as for random-fields systems [375].

Moreover, the regions of higher localising field somehow represent hotter regions, hence regions which should relax faster than the bulk. This suggests to study the potential connection between the thermodynamic fluctuations which are presented in this chapter and the dynamic heterogeneities which are universally found in supercooled liquids at low temperatures, as already discussed in the introduction. This requires to define a dynamic quantity for each cavity whose correlation with $\epsilon^{*(R)}(\boldsymbol{x}; \boldsymbol{r}_0^N)$ may then be assessed. A first and simple way of characterising the dynamics of the cavities consists in coarse-graining the single-particle propensity which is obtained from the iso-configurational runs of the physical dynamics (without swap) that start from the reference configuration and with randomised initial velocities [62, 63]. One can be interested in the equilibrium dynamics (with $T = T_0$) but also in the out-of-equilibrium melting dynamics of very stable reference configurations which are instantaneouly heated at a higher temperature T ($T > T_0$). In particular, rare regions from which the transformation to the supercooled liquid initiates may be correlated with the regions of relatively high localising field [205, 376].

We are currently measuring the correlation between the fluctuations of the Franz-Parisi potential and coarse-grained mesoscopic static or dynamic properties. As correlations can suffer from large uncertainties when data are interpolated [377], we do not propose an interpolation scheme to define $\epsilon^{*(R)}(\boldsymbol{x}; \boldsymbol{r}_0^N)$ at the single-particle level but we instead coarse-grain single-particle quantities at the cavity lengthscale, as explained above. For a single-particle quantity $\omega_i[\boldsymbol{r}_0^N]$ which is defined in the reference configuration (for instance the propensity, the orienta-

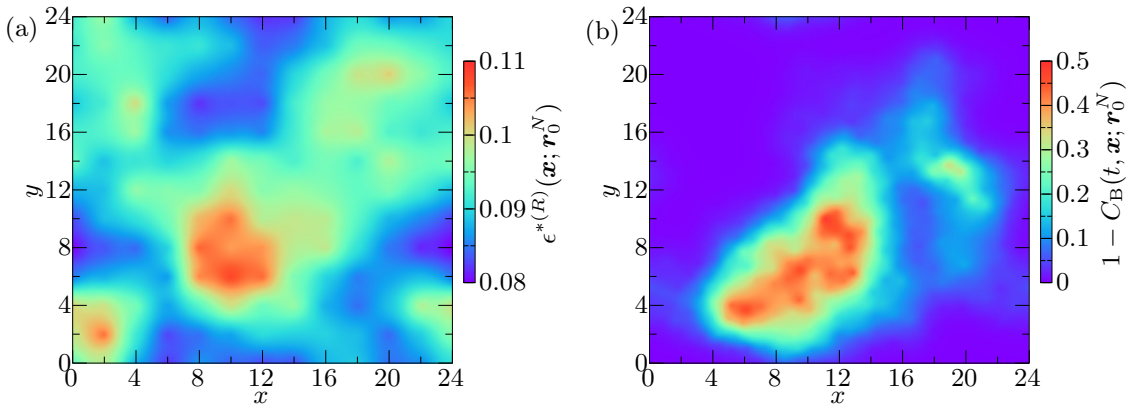

Fig. V.8 | (a) Same as Fig. V.4 (b). (b) Map of the local bond-breaking correlation in a bulk liquid of $N = 576$ particles at a temperature $T = 0.1$ for the relaxation dynamics from the same reference configuration as in panel (a) ($T_0 = 0.1$). Be careful that the map displays $1 - C_{\mathrm{B}}(t, \boldsymbol{x}; \boldsymbol{r}_0^N)$. The two maps seem to be correlated (the Pearson correlation $r_{C_{\mathrm{B}}\epsilon}$ is about -0.42). The time t has been chosen to maximise the correlation, and corresponds to $t/\tau_\alpha \simeq 1.5 \times 10^{-2}$, where the α-relaxation time τ_α is extracted from the isoconfigurational average of the bulk orientational correlation function, see Eq. (III.9).

tional order, the energy, etc.), we first define an associated cavity quantity

$$\omega^{(R)}(\boldsymbol{x};\boldsymbol{r}_0^N) = \frac{\sum_i \omega_i[\boldsymbol{r}_0^N]\,\theta(R - |\boldsymbol{r}_{0,i} - \boldsymbol{x}|)}{\sum_i \theta(R - |\boldsymbol{r}_{0,i} - \boldsymbol{x}|)}, \tag{V.20}$$

where the sums run over all particles $i = 1 \dots N$, by averaging $\omega_i[\boldsymbol{r}_0^N]$ over all the particles which are in the cavity [we recall that $\theta(x)$ denotes the Heaviside step function]. For the propensity, $\omega_i[\boldsymbol{r}_0^N]$ also depends on time and the positions of the particles in the previous formula are the ones at the initial time. Eventually, the temperature dependent Pearson correlation $r_{\omega\epsilon}(T)$ with the localising field can be computed by averaging over the position $\boldsymbol{x}$ of the cavities and the reference configurations $\boldsymbol{r}_0^N$, *i.e.*,

$$r_{\omega\epsilon}(T) = \frac{\overline{\langle\langle \omega^{(R)}(\boldsymbol{x};\boldsymbol{r}_0^N)\epsilon^{*(R)}(\boldsymbol{x};\boldsymbol{r}_0^N)\rangle\rangle} - \overline{\langle\langle \omega^{(R)}(\boldsymbol{x};\boldsymbol{r}_0^N)\rangle\rangle}\;\overline{\langle\langle \epsilon^{*(R)}(\boldsymbol{x};\boldsymbol{r}_0^N)\rangle\rangle}}{\left[\overline{\langle\langle \omega^{(R)}(\boldsymbol{x};\boldsymbol{r}_0^N)^2\rangle\rangle} - \overline{\langle\langle \omega^{(R)}(\boldsymbol{x};\boldsymbol{r}_0^N)\rangle\rangle}^2\right]^{1/2}\left[\overline{\langle\langle \epsilon^{*(R)}(\boldsymbol{x};\boldsymbol{r}_0^N)^2\rangle\rangle} - \overline{\langle\langle \epsilon^{*(R)}(\boldsymbol{x};\boldsymbol{r}_0^N)\rangle\rangle}^2\right]^{1/2}}. \tag{V.21}$$

We have obtained preliminary results but we hope to collect new data in the following weeks to present for the PhD defense. In Fig. V.8, we show a map of the local bond-breaking correlation $\omega_i = C_{\mathrm{B}}^i(t)$ for the isoconfigurational physical (without swap) and unconstrained (with $\epsilon = 0$) dynamics which is initiated from the same reference configuration as in Fig. V.4. The definition of $C_{\mathrm{B}}^i(t)$ is given in Chap. VI, see Eq. (VI.9). Briefly, this number monitors the change in the environment of a given particle i: the particles which have relaxed and escaped their initial position are characterised by a bond-breaking correlation which is close to 0, the others have a bond-breaking correlation which is close to 1. The time t has been chosen to maximise the correlation with the localising field, and is about two decades before the α-relaxation time. Accordingly, the average over the sample of the bond-breaking correlation is about 0.9, which means that only 10 % of the particles have relaxed. We observe a non-zero anti-correlation between the map of the localising field and the map of the bond-breaking

correlation: the particles which relax the first are preferably located in the cavities with the larger localising fields. The correlation is found to decay to 0 both at early and late times, which suggests that the localising field is predictive of the first dynamic events, namely, the relaxation of some regions of the sample few decades before the bulk. This is compatible with the results which are presented in Chap. VI, especially with the interplay between activation and dynamic facilitation in this system.

VI Escaping "metastable states": watching 1 millisecond of the equilibrium relaxation in supercooled liquids

In this chapter, we combine the swap Monte Carlo algorithm to long multi-CPU molecular dynamics simulations to analyse the equilibrium dynamics of model bulk supercooled liquids over a time window of 10 decades and for temperatures down to the experimental glass transition temperature T_g. We start with ensemble-averaged time correlation functions which slow down and which display a plateau that extends over several decades when decreasing the temperature. We then show that more interesting features can be found either by computing the relaxation spectrum in the Fourier domain, or by quenching into the inherent structures and by obtaining the corresponding inherent structure mean-squared displacement. Both procedures reveal non-trivial motions at much shorter timescales than the bulk relaxation time for temperatures close to T_g. These short-time processes manifest themselves into a power law signal in the relaxation spectrum which is known as the "excess wing". The latter has been documented in many experimental studies but its observation in simulations of glass-forming liquids in equilibrium conditions is a major novelty. Equivalently, in the inherent structure mean-squared displacement, the short-time processes which populate the excess wing contribute to a systematic sub-diffusive behaviour. We then use the possibility which is offered by computer simulations to study the dynamics at the single-particle level and we reveal strong dynamic heterogeneities at times much smaller than the α-relaxation time. These heterogeneities enable us to distinguish between mobile and immobile particles at short times. A detailed spatio-temporal analysis reveals that the structural relaxation starts in rare, localised regions of mobile particles which form clusters. They are characterised by a power law waiting time distribution which directly accounts for the emergence of a power law in the relaxation spectra or a sub-diffusive signal in the inherent structure mean-squared displacements. We further analyse the dynamics at longer times and we show that the structural relaxation proceeds via dynamic facilitation from these initially relaxed regions. In particular, we find that the motion of the particles is persistent and correlated among neighbours, and that the effect of dynamic facilitation becomes stronger as T_g is approached. Overall, our results show that the structural relaxation in glass-forming liquids near T_g can now be analysed in computer simulations over experimentally relevant time and temperature windows. They mainly reveal that the dynamics in deeply supercooled liquids is controlled by two minimal ingredients, namely, (i) rare and time-distributed events which likely occur via thermal activation, and (ii) mobility coarsening thanks to dynamic facilitation.

Outline

1 Introduction 146

2 Model and methods 148

2.1 Model and numerical strategy 148

2.2 Dynamic observables 149

2.3 Mobility at the single-particle level . . . 150
2.4 Dictionary to confront experiment and simulation timescales . . . 151
3 Equilibrium correlation functions towards the glass transition . . . 152
3.1 Time correlation functions . . . 152
3.2 Emergence of "excess wings" in the relaxation spectra near the glass transition . . . 154
3.3 Sub-diffusive motion in the inherent structure mean-squared displacements . . . 155
4 Short-time relaxation much before the bulk . . . 156
4.1 Dynamic heterogeneities and mobility classification . . . 156
4.2 Birth and growth of independent clusters . . . 158
5 Dynamic facilitation towards the α-relaxation . . . 160
5.1 Mobility percolation . . . 160
5.2 Multiple relaxations and mobility propagation . . . 161
6 Conclusions . . . 164
6.1 Summary of the results . . . 164
6.2 Microscopic origin of the shape of the relaxation spectra . . . 165
Appendix
A Suppression of the "excess wing" in stable glasses . . . 166

The work of this chapter is done in collaboration with C. Scalliet. Some of these results have already been the object of an article which is currently under review, see Ref. [378].

1. Introduction

In the previous chapters, we have studied the free energy landscape of glass-forming liquids from a thermodynamic point of view. Our analysis has been based on mean-field concepts like metastable states, configurational entropy or constrained thermodynamics. We have shown in Chap. III by using computer simulations that mean-field theory is remarkably robust in finite dimensions as the thermodynamics of constrained glass-forming liquids is similar to the mean-field behaviour. This is consistent with other works which focused on the measure of the configurational entropy [114, 164, 181, 241] or of the point-to-set length [178–180]. Therefore, in finite dimensions, the dynamic slowdown at the origin of the glass transition is accompanied by increasing thermodynamic fluctuations of a well chosen order parameter, namely, the overlap or similarity between equilibrium configurations, which becomes correlated on an increasing lengthscale as the temperature decreases.

At the mean-field level, there is also a clear connection between the statics of a glass-forming liquid at low temperatures and its equilibrium dynamics (see Chap. I). Indeed, as the liquid is cooled down to the dynamical transition temperature, the equilibrium relaxation time $\tau_\alpha(T)$ diverges because the system remains stuck in one of the many metastable states whose number becomes exponential in system size precisely at this temperature [126]. In physical dimensions instead, both statements cannot be correct as such. On the one hand, metastable states become ill-defined because free energy barriers are not extensive and they do not diverge in the

thermodynamic limit [144]. On the other hand, the dynamical (or mode-coupling) transition at $T_{\rm mct} \simeq T_{\rm d}$ is avoided and it becomes a mere crossover. This avoided transition is advocated to be due to the activated events and the fact that below $T_{\rm mct}$ the system can escape the free energy minima, see Chap. I. However, the nature and the properties of these non-perturbative activated events remain elusive [125, 184]. In addition, even though the glass transition in finite dimensions is accompanied by growing static fluctuations, their connection with the dynamics is still an open question. In a complementary line of thought, the dynamic facilitation theory, which is inspired from the study of kinetically constrained models, accounts for the structural relaxation by the diffusion of rare defects without resorting to static properties [112].

To address these questions and to test the various theories of the glass transition, computer simulations are a powerful asset. On the one hand, they allow one to study the dynamics at the single-particle level and in consequence to reveal the microscopic processes responsible for the relaxation. On the other hand, they can measure mean-field-inspired thermodynamic observables. For instance, dynamic facilitation has been well documented in computer simulations at moderately low temperatures [379–381]. The connection between the α-relaxation time and the configurational entropy or the point-to-set length has also been investigated [190]. However, in simulations, dynamic studies are typically limited to short timescales, about 5 decades of increase in the relaxation time, and therefore the equilibrium dynamics can be only analysed down to the mode-coupling (avoided) transition or just below. This is problematic since for instance the previously mentioned activated events are expected to control the dynamics below the mode-coupling crossover, even though they may still exist above $T_{\rm mct}$ [382]. In addition, the influence of facilitation has not been assessed at lower temperatures, nor its relative role with respect to thermal activation.

On the opposite, experiments have access to the dynamics of supercooled liquids over 12 decades of increase in the relaxation time. However they usually lack microscopic resolution and thermodynamic measurements are often harder to relate to mean-field-like quantities. A huge number of works has been dedicated to the measure of the dielectric spectra $\chi''(\omega)$ of glass-forming liquids in the frequency domain [383], see Chap. I. They have revealed that the dynamic slowdown as monitored by the increase in the α-relaxation time is accompanied by richer relaxation spectra [384, 385]. At high temperatures, the spectra usually display a single peak at high frequencies which corresponds to a Debye (exponential) relaxation on the GHz or the picosecond ranges. As the temperature is lowered, the spectra broaden and they form two peaks which reflect the two-step decay of the equilibrium correlation functions in the time domain. The first peak lies in the GHz range and it is attributed to the microscopic relaxation, namely, the first decay on the picosecond range of the correlation functions to a well defined plateau in the time domain. The second peak in the dielectric spectra is at much lower frequency and it stands for the stretched exponential relaxation of the correlation functions in real time. The position of the peak $\omega_\alpha = 1/\tau_\alpha$ shifts towards lower frequencies when the temperature is decreased, and this stands for the dynamic slowing down and the increase in the α-relaxation time. When decreasing the temperature, the low-frequency peak becomes increasingly large and much wider than what would be expected from a stretched exponential relaxation. The signal takes the form of a power law $\chi''(\omega) \sim \omega^{-\sigma}$ for $\omega\tau_\alpha \gg 1$ with an exponent $0.2 \leq \sigma \leq 0.4$ which decreases when decreasing the temperature [43]. On logarithmic scales, this signal resembles an "excess wing" of the α-peak. At $T_{\rm g}$, the wing extends over the Hz-MHz range with an "amplitude" of about 1 % of the α-peak.

Even though the signal in dielectric spectra could be very complex due to extra microscopic

processes which originate from the chemical details of the materials [45], the "excess wing" seems to be a universal feature of the dielectric spectra of glass-forming liquids close to $T_{\rm g}$ [46–49] and it can help testing the predictions which come from different theories of the glass transition. Indeed, a complete theory of the glass transition must account for the shape of the relaxation spectra (and not only for the shift of the low-frequency peak or the increase in the α-relaxation time), and this requires insights from computer simulations to elucidate the dynamics at the microscopic scale. However, the excess wing has never been observed in computer simulations because of the impossibility to deal with experimentally-relevant time and temperature ranges. This has led to a collection of phenomenological models to rationalise the shape of the relaxation spectra which rely on more or less reasonable physical motivations rather than on undisputable facts. One class of models accounts for the excess wing by coupling the structural relaxation to another degree of freedom [386–388]. A second class of models relies on heterogeneous dynamics of static [389–395] or of purely dynamic origin [396].

Recently, the swap Monte Carlo algorithm was developed [54]. It allows for the fast equilibration of computer models down to arbitrarily low temperatures. It has already been used to extend the range of temperatures over which thermodynamic quantities can be computed in equilibrium conditions. However, the equilibrium physical (without swap) dynamics has not so far been investigated. The objective of this chapter is to fill this gap. In this chapter, we show that we are now able to access time and temperature ranges which are similar to what is achieved in experiments. We compute relaxation spectra close to $T_{\rm g}$ from simulations and we show that they also display excess wings. We then use the single-particle resolution of computer simulations to unravel the two main features of the equilibrium dynamics in model deeply supercooled liquids down to the extrapolated experimental glass transition temperature, namely, dynamic heterogeneities and dynamic facilitation.

2. Model and methods

2.1 Model and numerical strategy

We study the equilibrium dynamics of the system which is described in Sec. 2.2 of Chap. III. By using the hybrid scheme that combines molecular dynamics simulations with swap Monte Carlo moves [55], one can equilibrate the system down to very low temperatures. Then, via the swap algorithm, we generate $n_{\rm s} \in [200, 450]$ independent equilibrium configurations at temperatures T which range from the onset temperature of glassy behaviour down to T_g. In this chapter, we define the onset temperature as the highest temperature where the evolution of the α-relaxation time with the temperature departs from its high-temperature Arrhenius behaviour $\tau_\alpha(T) \propto e^{E_{\rm on}/T}$ (where $E_{\rm on}$ is an adjustable parameter and where the Boltzmann constant is set to unity) [285–287].

Each equilibrium configuration is then taken as the initial condition of a conventional multi-CPU molecular dynamics (MD) simulation (without swap). The $n_{\rm s}$ independent simulations run for up to 2×10^9 MD steps, which corresponds to a walltime of about one week when using 2 CPUs. We present quantitative results in $3d$ for a system size $N = 1200$. We have verified that our results were not a finite-size artefact by running simulations in $3d$ for systems of size $N = 10000$. These larger systems are also used for visualisation purposes. Our results also seem to hold in $2d$ when the right observables are considered (*cf.* Mermin-Wagner fluctuations).

From an average over the n_s runs[1] at a given temperature, we can determine different dynamic observables that are discussed in the next section. We stress that this procedure allows for accessing the equilibrium dynamics because simulations are run from initial equilibrium conditions which are generated through the swap algorithm. This strategy saves simulation walltime, namely, the time to generate equilibrium configurations. Indeed, with modern computers, the number of MD steps which can be done for a few number of CPUs and a simulation walltime of one week is about 10^9 MD steps with an optimised choice of the time step $\mathrm{d}t$. At the onset temperature, the relaxation time usually represents 10^2 MD steps. This means that by starting from equilibrium configurations which are generated by the swap algorithm, one can directly observe the 7 first decades of the increase in the relaxation time. In conventional simulations instead, one first has to prepare equilibrium configurations by running the physical dynamics. A usual criterion consists in letting the system equilibrate at a temperature T for at least $10\tau_\alpha$ and up to $10^2\tau_\alpha$, with τ_α the α-relaxation time at this temperature. As a consequence, one cannot measure the one to two last decades of glassy slowdown anymore and instead one only observe the usual 5 decades of the increase in the relaxation time.

2.2 Dynamic observables

To quantify the glassy dynamics in the system, we first focus on time correlation functions and we analyse the temperature behaviour of the self-intermediate scattering function

$$F_\mathrm{s}(t) = \frac{1}{N}\left\langle \sum_{i=1}^{N} \cos\left[\boldsymbol{q}\cdot\Big(\boldsymbol{r}_i(t)-\boldsymbol{r}_i(0)\Big)\right]\right\rangle. \tag{VI.1}$$

The brackets stand for the ensemble average over the n_s trajectories which initiate from equilibrium configurations at a temperature T, along with a spherical average over all wave vectors $\boldsymbol{q}$ such that $|\boldsymbol{q}| = 6.9$, which corresponds to the first peak in the total structure factor. The sum runs over all particles, and $\boldsymbol{r}_i(t)$ denotes the position of particle i at time t. The structural relaxation time τ_α is defined by $F_\mathrm{s}(\tau_\alpha) = e^{-1}$. Errorbars are computed thanks to the jacknife method when the average of the n_s runs is computed [294].

In order to compare with experiments directly, we define a relaxation spectrum from the simulations in the frequency domain by assuming that the dynamics can be described by a superposition of exponential/Lorentzian processes with a distribution of timescales $\Pi(\ln\tau)$. The relaxation spectrum then reads [398, 399]

$$\chi''(\omega) = \int_{-\infty}^{+\infty} \Pi(\ln\tau)\frac{\omega\tau}{1+(\omega\tau)^2}\mathrm{d}\ln\tau, \tag{VI.2}$$

with ω the angular frequency. We can approximate the above distribution of timescales by

$$\Pi(\ln\tau) \simeq -\frac{\mathrm{d}F_\mathrm{s}}{\mathrm{d}\ln t}(\ln\tau), \tag{VI.3}$$

which amounts to assimilating the self-intermediate scattering function to a persistence function [396].

The computation of the relaxation spectra $\chi''(\omega)$ first requires to differentiate the correlation function with respect to the natural logarithm of time. This is done by using a first-order finite

[1] This procedure was called the "swarm" relaxation in Ref. [397].

difference approximation. During the n_s simulations, configurations are stored at logarithmically spaced times $\{t_k\}_{k=1\ldots n}$, and we thus have that

$$\frac{\mathrm{d}F_\mathrm{s}}{\mathrm{d}\ln t}(t_k) = \frac{F_\mathrm{s}(t_k) - F_\mathrm{s}(t_{k-1})}{\ln t_k - \ln t_{k-1}} \text{ if } k > 1. \tag{VI.4}$$

The integral in Eq. (VI.2) can then be evaluated by using the right-hand (rectangle) rule at any angular frequency ω, *i.e.*,

$$\chi''(\omega) = -\sum_{k=2}^{n} \frac{\mathrm{d}F_\mathrm{s}}{\mathrm{d}\ln t}(t_k) \frac{\omega t_k}{1+(\omega t_k)^2} \ln(t_k/t_{k-1}). \tag{VI.5}$$

However, the error on the numerical integration gets larger at small frequencies when the complete decorrelation of the self-intermediate scattering function is not observed (at temperatures close to T_g), as the integral becomes dominated by the long-time behaviour of $F_\mathrm{s}(t)$. The error also increases at large frequencies due to the time discretisation. Computing $\chi''(\omega)$ only at discrete angular frequencies $\omega_k = 2\pi/t_k$ for $k = 1\ldots n$ is enough to guarantee a small-enough error and a fine-enough spacing in the frequency range. Errorbars on the relaxation spectrum are estimated by computing the typical amplitude of the spectrum which is obtained from a random Gaussian signal of zero mean and of standard deviation equal to the maximum over time of the uncertainty on $F_\mathrm{s}(t)$.

Complementary with the time correlation functions and the relaxation spectra, we also monitor the mean-squared displacement (MSD)

$$\hat{\Delta}(t) = \frac{1}{N}\left\langle \sum_{i=1}^{N} |\boldsymbol{r}_i(t) - \boldsymbol{r}_i(0)|^2 \right\rangle. \tag{VI.6}$$

If the particles all vibrate around their initial position, then $\hat{\Delta}(t)$ is a non-zero constant. This is what is usually observed at intermediate times for glassy systems (after the ballistic regime) because all the particles are trapped in the cages which are formed by their neighbours. In order to filter these vibrations, we use a strategy which was already devised in Ref. [400, 401]. We quench at different times (including $t = 0$) the configuration $\boldsymbol{r}^N(t)$ of the system to its corresponding inherent state (IS) $\boldsymbol{r}^N_\mathrm{IS}(t)$. This is achieved by minimising the total potential energy $\hat{H}[\boldsymbol{r}^N]$ thanks to a conjugate-gradient algorithm. From the time series of the positions in the IS, an inherent structure mean-squared displacement (IS-MSD) $\hat{\Delta}_\mathrm{IS}(t)$ is defined similarly to Eq. (VI.6). If all the particles vibrate around a given position, then the structure of the system is expected to be unchanged and $\hat{\Delta}_\mathrm{IS}(t)$ to remain very small. In addition, if few particles perform non-trivial displacements and escape their cage, the mean-squared displacement $\hat{\Delta}(t)$ is likely to be blind to these as it is dominated by the overwhelming majority of particles which vibrate in their cages. Thus, the variations of $\hat{\Delta}_\mathrm{IS}(t)$ may reveal non-trivial displacements of particles which lead to changes in the structure above thermal vibrations. Such as correlation functions, errorbars on the mean-squared displacements are computed thanks to the jacknife method when the average over the n_s independent runs is performed.

2.3 Mobility at the single-particle level

The above dynamic observables determine the average dynamics. In order to study the dynamic heterogeneities, we look at the distribution of the displacements of the particles, namely,

the self-part of the van Hove distribution

$$G_{\mathrm{s}}(r,t) = \frac{1}{N}\left\langle \sum_{i=1}^{N} \delta(\boldsymbol{r} - |\boldsymbol{r}_i(t) - \boldsymbol{r}_i(0)|) \right\rangle, \tag{VI.7}$$

with $\delta(x)$ the Dirac delta function. Its second moment with respect to space at fixed time t represents the mean-squared displacement $\hat{\Delta}(t)$. This distribution can be defined either for the normal dynamics or for the inherent structure (IS) dynamics, and in the latter case, the distribution is denoted by $G_{\mathrm{s,IS}}(r,t)$. Dynamic heterogeneities correspond to the coexistence of regions of space in which particles move freely with frozen areas, and consequently of mobile and immobile particles whose definition must be specified (see Chap. I).

We consider several mobility definitions. The first one is based on the displacements: a particle is said to be mobile at time t if its displacement in the inherent structure is larger than a given threshold that we extract from the properties of the above van Hove distribution. It is introduced in Sec. 4.1. The second definition relies on a bond-breaking correlation function to detect changes in the environment of individual particles. It is used for visualisation purposes only. At time $t = 0$, we compute the number n_i and the identity of particle i's neighbours. Two particles i and j are considered as neighbours at time 0 if $r_{ij}/\sigma_{ij} < 1.485$, which corresponds to the first minimum in the total rescaled pair correlation function

$$\tilde{g}(x) = \frac{1}{N\rho}\left\langle \sum_{\substack{i,j=1\\ i\neq j}}^{N} \delta(r_{ij}/\sigma_{ij} - x) \right\rangle, \tag{VI.8}$$

with ρ the density, $r_{ij} = |\boldsymbol{r}_i - \boldsymbol{r}_j|$ and σ_{ij} the interaction cross-diameter of particles i and j. At time $t > 0$, we define the bond-breaking correlation of particle i,

$$C_{\mathrm{B}}^{i}(t) = \frac{n_i(t|0)}{n_i}, \tag{VI.9}$$

as the fraction of remaining neighbours of particle i, with $n_i(t|0)$ the number of particles which were neighbours of particle i at time 0 and which are still its neighbours at time t. To avoid a spurious signal that we attribute to particles that lose their farthest neighbours because of thermal vibrations, we define the neighbours at time t with a slightly larger cutoff than at time 0, namely, $r_{ij}/\sigma_{ij} < 1.7$ [402]. At time 0, $C_{\mathrm{B}}^{i}(t) = 1$ by definition. Then, as the relaxation proceeds, the particles experience rearrangements which affect their local environment. In consequence, the particles which have relaxed lose their neighbours at the initial time and they have $C_{\mathrm{B}}^{i}(t) = 0$. Therefore, a particle i is considered as mobile at time t if $C_{\mathrm{B}}^{i}(t)$ is below a given threshold. This threshold is also discussed in Sec. 4.1. In particular, it is chosen so that the two alternative definitions of mobility give sets of mobile particles with a significant overlap and which are then consistent with each other.

Finally, we consider connected clusters of mobile particles. Two mobile particles at time t belong to the same cluster if their relative distance at this time in the inherent structure is smaller than 1.5, which corresponds to the first minimum in the total radial pair correlation function $g(r)$ (see Chap. IV).

2.4 Dictionary to confront experiment and simulation timescales

Thanks to the swap algorithm and the use of many initial configurations, we can measure two more decades of the increase in the structural relaxation time in computer simulations,

as compared to previous studies. In addition, we can prepare equilibrium configurations at very low temperatures. We have advocated that we are now able to directly compete with experiments and we detail this now. In particular, we explain how we transform simulation relaxation times τ_α into their experimental counterparts in seconds. Experimental measurements of the temperature evolution of τ_α in various glass-forming liquids show that at really high temperatures, the relaxation time is about 1 ps. As already mentioned before, the data in this high-temperature regime follow an Arrhenius law which extends over about 2 decades [287, 403], before the growth of the α-relaxation time when decreasing the temperature becomes super-Arrhenius. Thus, the relaxation time in a large number of experimental molecular liquids at the onset temperature $T_{\rm on}$ is about $\tau_{\rm on} \simeq 100$ ps, *i.e.*, 10^{-10} s. In simulations, we can also measure this onset temperature $T_{\rm on}$ and we find $T_{\rm on} = 0.2$ in $3d$. At this temperature, the α-relaxation time approximately equals $\tau_{\rm on} \simeq 3$ (or 3×10^2 MD steps).

Therefore, we use this value to set the dictionary between the simulations and the experiments. We express simulation times in units of $\tau_{\rm on}$ and we directly obtain the physical time in seconds by multiplying by 10^{-10}. For instance, conventional computer simulations (without the swap) are able to reach $\tau_\alpha/\tau_{\rm on} \simeq 10^4$-$10^5$, which represents a physical time of about 1 μs, hence a poor degree of supercooling with respect to experimental conditions. On the opposite, with the swap algorithm, we can measure the seven first decades of the increase in the relaxation time, namely, $\tau_\alpha/\tau_{\rm on} \simeq 10^6$-$10^7$. The latter corresponds to a physical time of about 1 ms, hence the title of this chapter. Finally, we later argue that we are able to prepare equilibrium configurations of relaxation time $\tau_\alpha/\tau_{\rm on} \simeq 10^{11}$ thanks to the swap algorithm, hence a physical time of 10 s. We recall that in experiments, the glass transition temperature is usually defined when the α-relaxation time reaches 100 s. As a consequence, we are in a position to study the equilibrium dynamics of a model glass-former for τ_α in the range $[10^{-11}, 10^1]$ s, such as experimental studies. We present our results in the next section.

3. Equilibrium correlation functions towards the glass transition

3.1 Time correlation functions

In Fig. VI.1 (a), we show the equilibrium self-intermediate scattering function $F_{\rm s}(t)$ at several temperatures. The curves for all the temperatures display the well-known two-step decay, with a first decrease to a plateau due to the ballistic motion at times $t \simeq \tau_{\rm on}$, which is followed by the structural relaxation that covers several orders of magnitude in time when the temperature is decreased over a small temperature window. At the largest temperature $T = 0.095$ for which we display the self-intermediate scattering function, the liquid already has a relaxation time of about 10^4, which corresponds to the longest time that is achievable without the swap algorithm. As a consequence, the combination of the swap algorithm and the "swarm" relaxation clearly enables us to surpass all previous studies of the dynamics of model glass-formers in computer simulations.

We note in Fig. VI.1 (a) that we are indeed able to measure the 6-7 first decades of glassy slowdown for temperatures $T \geq 0.0793$. We report in Fig. VI.1 (b) the value of the α-relaxation which is rescaled by its value at the onset temperature, and which grows as the temperature is decreased. A power law fit of the data $\tau_\alpha \propto (T - T_{\rm mct})^{-\gamma}$ [136] locates the mode-coupling crossover at $T_{\rm mct} = 0.095$ (with $\gamma \simeq 2.3$) but it obviously fails at fitting the data at lower temperatures. This is the manifestation of the fact that in finite dimensions, the mode-coupling

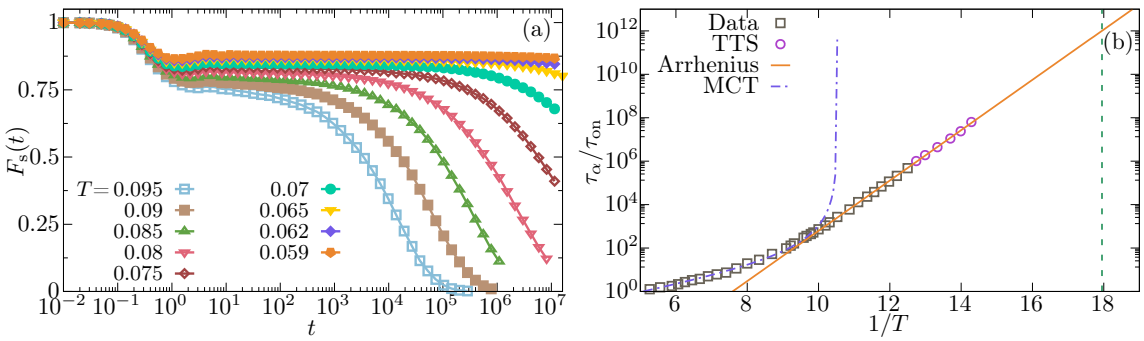

Fig. VI.1 | (a) Self-intermediate scattering function $F_s(t)$ versus time for different temperatures T which range from the mode-coupling crossover $T_{mct} = 0.095$ almost down to the experimental glass transition temperature T_g. A first decay to a plateau due to thermal vibrations is observed. At high-enough temperatures, we can observe the complete decorrelation with a second stretched exponential relaxation. At lower temperatures instead, the relaxation time exceeds the simulation window and only the beginning of the relaxation is observed. Errorbars are too small to be visible. (b) Rescaled α-relaxation time τ_α by its value τ_{on} at the onset temperature as a function of the inverse temperature $1/T$. This time has been directly measured when $F_s(\tau_\alpha) = e^{-1}$ (Data), or obtained via a time-temperature superposition (TTS) at low T when a sufficient decorrelation is observed. The dashed-dotted curve shows a power law fit to determine the location of the mode-coupling crossover and the straight line represents an Arrhenius fit which models the data well at low temperatures. The vertical dashed line marks the extrapolated laboratory glass transition temperature $T_g = 0.056$.

dynamical transition becomes a mere crossover. Below T_{mct}, and in the temperature range $0.0793 \leq T \leq 0.095$ in which we observe a sufficient decorrelation over the accessible time window, we can fit the second step of the relaxation in $F_s(t)$ by a stretched exponential of the form [32]

$$F_s(t) = F_0 e^{-(t/\tau)^\beta}, \tag{VI.10}$$

with F_0, τ and β fitting parameters. We find that τ varies by several orders of magnitude and it closely follows τ_α. On the opposite, the amplitude of the plateau F_0 slightly increases upon lowering the temperature while the stretching exponent $\beta \simeq 0.56$ turns out to be almost temperature independent. We use this property in order to extrapolate the relaxation at lower temperatures where the correlation function still significantly decorrelates but does not reach the threshold value to measure τ_α. We perform a time-temperature superposition (TTS) in which starting from high temperatures, we rescale both axes of Fig. VI.1 (a) in order to obtain a collapse of the data. This allows for an extrapolation of the relaxation time over 2 more decades when it is too large to be measured [404], see Fig. VI.1 (b).

Our results for τ_α (Data +TTS) are well-described by an Arrhenius behaviour $\tau_\alpha \propto e^{E_a/T}$, with E_a an activation energy ($E_a \simeq 2.67$), which yields the extrapolated laboratory glass transition temperature $T_g \simeq 0.056$ when $\tau_\alpha/\tau_{on} = 10^{12}$. In the following, we use this Arrhenius fit to extrapolate τ_α when it is too large to be measured. The Arrhenius trend is believed to represent a safe extrapolation of the relaxation time and consequently a lower bound of the actual relaxation time and of the extrapolated glass transition temperature [54].

Thus, in the range $0.059 \leq T \leq 0.095$, we are probing the dynamics below T_{mct} and almost down to T_g in a similar range as in experiments. In the next section, we directly confront with experiments by computing the relaxation spectrum of Eq. (VI.2).

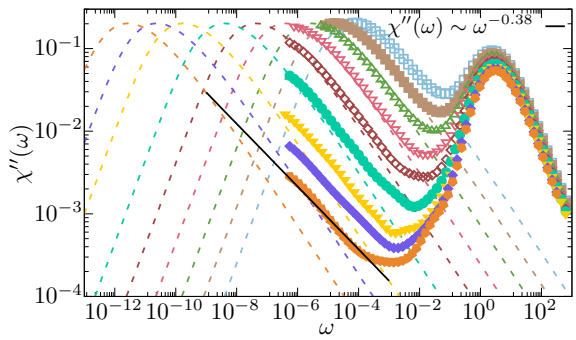

Fig. VI.2 | Relaxation spectra $\chi''(\omega)$ with respect to the angular frequency ω, as defined by Eq. (VI.2). For the two lowest temperatures, the spectrum has been computed after smoothing the curve of $F_s(t)$. A first high-frequency peak is observed for all the temperatures which corresponds to the first decay in $F_s(t)$ to its plateau value. At high temperatures, a second peak is observed, which stands for the second step of the relaxation in $F_s(t)$, see Fig. VI.1 (a). The dashed lines correspond to the α-peak prediction when $F_s(t)$ is modelled by a stretched exponential with a stretching exponent $\beta = 0.56$ and with τ_α which is extrapolated from the Arrhenius fit of Fig. VI.1 (b), see Eq. (VI.10). The straight line is a power law of the form $\omega^{-\sigma}$ with an exponent $\sigma = 0.38$ which approximates the data well. The color code is the same as in Fig. VI.1 (a). Errorbars are of order 4×10^{-4}.

3.2 Emergence of "excess wings" in the relaxation spectra near the glass transition

From $F_s(t)$, we can compute $\chi''(\omega)$ as an equivalent of the experimental dielectric loss, see Eq. (VI.2). The data from the different temperatures are shown in Fig. VI.2. For the two lowest temperatures, namely, $T = 0.059$ and $T = 0.062$, the data for $F_s(t)$ are noisy and weakly decreasing, and this leads to numerical artefacts in the computation of the relaxation spectrum. Therefore, for these two temperatures, we have smoothed the self-intermediate scattering function before computing the spectrum by using a smoothed cubic spline interpolation [405]. The spectra all have a first peak which is located at $\omega_{\rm on} \simeq 1/\tau_{\rm on}$ with a weak temperature dependence, and which accounts for the ballistic regime and the decrease in $F_s(t)$ to its plateau value. For temperatures $T \geq 0.09$, we detect a second peak at much lower frequency $\omega_\alpha \simeq 1/\tau_\alpha$ which corresponds to the structural relaxation and to the second step in the decay of $F_s(t)$. At lower temperatures however ($T \leq 0.085$), this α-peak is no longer present in the achievable frequency window. Still, the data systematically increase at low frequencies for all the temperatures, which indicates that relaxation processes are taking place.

As $F_s(t)$ is well-fitted by a stretched exponential [see Eq. (VI.10)] with a known value of β and τ_α which is extrapolated from the Arrhenius fit in Fig. VI.1 (b), we are able to predict the α-peak when it cannot be measured directly, and we plot it with dashed lines in Fig. VI.2. It behaves as a power law with exponents 1 and $-\beta$ at low and high frequencies respectively. This behaviour is similar to the empirical Cole-Davidson curve which is often used to fit the main peak in the experimental dielectric spectra [40] (see Chap. I). For $T \geq 0.075$, the low-frequency part of the spectrum is well approximated by the α-peak prediction which comes from the stretched exponential. However, at lower temperatures, we clearly see that the relaxation spectra systematically lie above the prediction from the stretched exponential fit. Instead, the signal shows a power law behaviour $\chi''(\omega) \sim \omega^{-\sigma}$ in the range $\omega \in [10^{-6}, 10^{-3}]$, with an exponent $0.34 \leq \sigma \leq 0.38$ which slightly increases with T, and which is much smaller than the stretching exponent β [we recall that the α-peak scales as $\chi''(\omega) \sim \omega^{-\beta}$ at high frequencies].

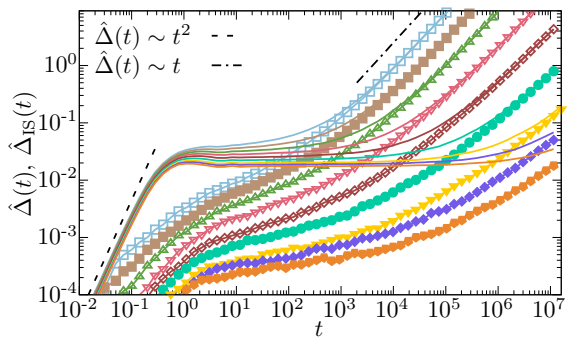

Fig. VI.3 | Mean-squared displacement in the normal dynamics $\hat{\Delta}(t)$ (full lines) and in the inherent structures $\hat{\Delta}_{\rm IS}(t)$ (full lines with symbols). The dashed and dashed-dotted lines respectively magnify the ballistic regime at microscopic times and the diffusive regime at larger times and high-enough temperatures. The mean-squared displacements for the normal dynamics and the inherent structures coincide in the diffusive regime. Instead, a sub-diffusive behaviour with a systematic growth is clearly visible in the time evolution of $\hat{\Delta}_{\rm IS}(t)$ in the plateau regime of the normal dynamics. The color code is similar to Fig. VI.1 (a). Errorbars are too small to be visible.

As a result, for temperatures close to $T_{\rm g}$, the spectra of glass-forming liquids are not merely composed of two peaks which stand for the microscopic motion at short times (large frequencies) and the structural relaxation at larger times (lower frequencies). At intermediate frequencies, there is an excess signal which is very similar to the experimental excess wing. We observe that this signal is one hundred times smaller than the main α-peak and that it covers a range of frequencies $\omega \in [10^{-6}, 10^{-3}]$ which corresponds to a range of physical frequencies $[10^4, 10^7]$ Hz. As a consequence, this excess signal has the same trend, frequency range and amplitude as excess wings which are observed in experiments. In Appendix A, we study the fate of the power law signal in our numerical spectra in the out-of-equilibrium dynamics of glasses of different stability to further confirm the similarity with experimental findings.

Consequently, Fig. VI.2 represents the first observation of excess wings in computer simulations of equilibrium model glass-formers to date. We stress that the wing becomes clearly visible only at temperatures $T \gtrsim T_g$, which explains why it has not been reported before in computer simulations of spherical particles. This observation strengthens the universal character of the excess wing but it also implies that there is no need for an extra degree of freedom to observe excess signals in the relaxation spectra, which is a key assumption for some of the models that try to account for the excess wings.

3.3 Sub-diffusive motion in the inherent structure mean-squared displacements

The processes which lead to the excess wing at intermediate frequencies correspond to processes at intermediate times which take place over several decades, when $F_{\rm s}(t)$ develops a plateau. They are thus masked by the vibrations of the particles but they are revealed once translating the data into the Fourier domain, via the time derivative in Eq. (VI.2). Another way of revealing these processes is to quench to the inherent states, as we explain now. In Fig. VI.3, we represent the mean-squared displacement (MSD) $\hat{\Delta}(t)$ (full lines). The data clearly show the ballistic regime at early times with $\hat{\Delta}(t) \sim t^2$. At large times, diffusion takes place for $T \geq 0.09$, with $\hat{\Delta}(t) \sim t$. At lower temperatures, the diffusive regime leaves the simulation

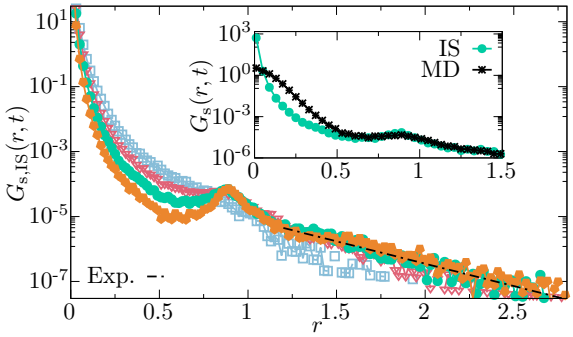

Fig. VI.4 | van Hove distribution of displacements in the inherent structures $G_{s,IS}(r,t)$ when $\hat{\Delta}_{IS}(t) = 1.5 \times 10^{-2}$. The dashed-dotted line is an exponential fit of the tail of the distribution. The inset shows a comparison of the van Hove distribution in the normal dynamics (MD) and in the inherent structures (IS) for $T = 0.07$. They agree at large displacements but the peak at $r = 0$ is significantly narrower and higher in the inherent structures because thermal vibrations are partially filtered. The color code is given in Fig. VI.1 (a).

window and we can only observe the beginning of the escape from the plateau. In Fig. VI.3, we also display the inherent structure mean-squared displacement (IS-MSD) $\hat{\Delta}_{IS}(t)$ with full lines and symbols (see Sec. 2). Both mean-squared displacements coincide at large times and in consequence the quenching protocol leaves unaffected the diffusive regime because the system has escaped from its initial structure. At intermediate times instead, $\hat{\Delta}_{IS}(t)$ is much smaller than $\hat{\Delta}(t)$ by 2 orders of magnitude. This large difference reveals that the main contribution to the MSD in the plateau regime represents vibrations of particles in the cages which are formed by their neighbours, without any significant change in the structure. The quenching protocol masks these vibrations partially, similarly to the computation of $\chi''(\omega)$ at the level of the time correlation function. In the plateau regime, and at all the temperatures down to T_g, we observe that $\hat{\Delta}_{IS}(t)$ systematically increases with a sub-diffusive behaviour [401]. We conclude that at these timescales which are much smaller than τ_α, not only the particles vibrate in their cages, but they also perform non-trivial displacements which lead to structural changes, as revealed by quenching the configuration into its inherent structure. At T_g, these processes occur as fast as $t \sim \tau_{on}$ and they continue up to the longest time we can simulate. This corresponds to a time regime and an amplitude similar to the excess wing.

We thus conclude from the two previous sections that going to the Fourier domain or to the inherent structures filters trivial the thermal vibrations of the particles in the cages which are formed by their neighbours. This emphasises that in the plateau regime of the time correlation functions, non-trivial processes occur and give rise to a wing in the relaxation spectra or to a sub-diffusive behaviour in the inherent structure mean-squared displacements. In the next section, we study the real-space organisation and the statistical properties of the particle motions which contribute to the relaxation much before the bulk.

4. Short-time relaxation much before the bulk

4.1 Dynamic heterogeneities and mobility classification

To have more intuition about the events which contribute to the relaxation and which occur much before the bulk, we analyse the dynamics at the single-particle level. In Fig. VI.4, we plot

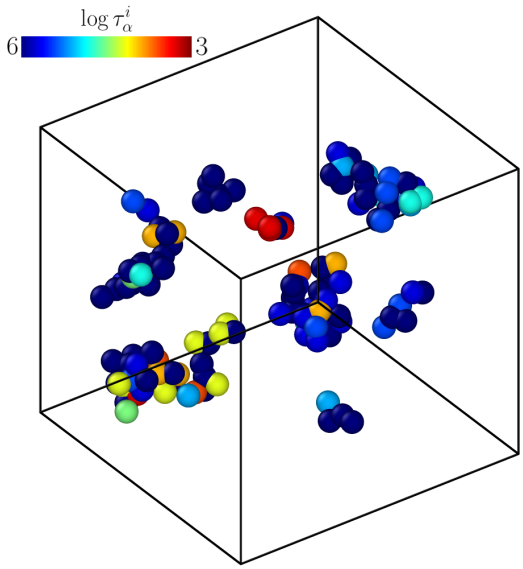

Fig. VI.5 | Snapshot which shows how the relaxation initiates in a $3d$ system of $N = 10000$ at a temperature $T = 0.07$ ($\tau_\alpha/\tau_{\rm on} = 6 \times 10^7$ or 6 ms in physical time). The snapshot is taken at a time $t = 10^6$ ($t/\tau_\alpha = 5 \times 10^{-3}$). Only the mobile particles (according to the bond-breaking criterion) which belong to clusters of size larger than 4 particles are represented. The particles are coloured according to the common logarithm of their relaxation time $\log \tau_\alpha^i = \ln \tau_\alpha^i / \ln 10$, *i.e.*, the first time t at which their bond-breaking correlation verifies $C_{\rm B}^i(t) < 0.55$. The diameter of the particles is set to 1.5 (distance criterion to belong to the same cluster) in order to more easily see the clusters. We observe that the birth of clusters is time-distributed on a logarithmic scale and that the clusters tend to grow in a hierarchical way as the relaxation proceeds.

the van Hove distribution of displacements in the inherent structures when $\hat{\Delta}_{\rm IS}(t) = 1.5 \times 10^{-2}$, which broadly corresponds to the beginning of the escape from the plateau in the normal mean-squared displacement. For all the temperatures, the distribution displays a strong peak around $r = 0$, which stands for the vibrations of the particles around the position they occupied at $t = 0$. At these timescales much smaller than τ_α, we already observe that the van Hove distribution is very broad. On the one hand, for temperatures $T \leq 0.07$, the distribution displays a secondary maximum for $r \simeq 0.9$ which stands for the particles that replace their neighbours: the location of the maximum approximately coincides with the position of the main peak in the total pair correlation function $g(r)$. On the other hand, the van Hove distribution shows an exponential tail which includes displacements that exceed the average inter-particle distance.

Consequently, as T decreases, the dynamic heterogeneities become more pronounced, even at very short timescales $t \ll \tau_\alpha$. A large majority of particles is immobile, these particles have small displacements (a fraction of their diameter) and they populate the high peak at $r = 0$ of $G_{\rm s,IS}(r,t)$. They coexist with a tiny fraction of mobile particles with displacements that can be larger than several times their diameter, and which corresponds to the second peak and the exponential tail in $G_{\rm s,IS}(r,t)$. In the following, we define mobile particles at time t as the particles with a displacement in the inherent structure larger than 0.8 at time t. The corresponding threshold for $C_{\rm B}^i(t)$ is 0.55. These mobile particles have escaped their initial position and they thus participate to the signal in the inherent structure mean-squared displacements and to the excess wing in the relaxation spectra. Their fraction at early times is very small as the tail and the second peak in $G_{\rm s,IS}(r,t)$ are both of much lower amplitude than the main peak at $r = 0$.

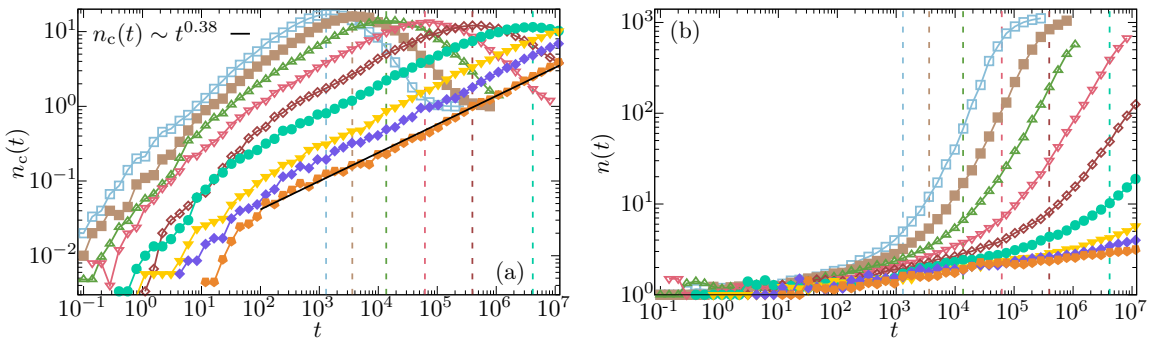

Fig. VI.6 | Spatio-temporal distribution of clusters of mobile particles. (a) Average number of clusters $n_c(t)$ of mobile particles (displacement in the inherent structure larger than 0.8). This number first grows with time before it reaches a maximum and it finally decreases towards 1 when all the particles have escaped from their initial position. At very low temperatures, the number of clusters grows as a power law with a similar exponent as the exponent of the excess wing, namely, 0.38 (straight line). (b) Average number of mobile particles $n(t)$ per cluster. The data increase and they reach the total number of particles N at late times. The vertical dashed lines mark the time t_c at which $n_c(t)$ is maximum for $0.07 \leq T \leq 0.095$. For both panels, the color code is the same and it is provided in Fig. VI.1 (a).

This fraction of mobile particles can be estimated by computing the area below the curve of the van Hove distribution for $r > 0.8$ and reads 0.8 % for $T = 0.059$ and $\hat{\Delta}_{\rm IS} = 1.5 \times 10^{-2}$, consistently with the amplitude of the excess wing and the inherent structure mean-squared displacement.

Now that we are able to identify the mobile particles which are responsible for the early relaxation, we analyse their distribution in both space and time in the next section to understand how the relaxation proceeds much before the bulk.

4.2 Birth and growth of independent clusters

We start by a qualitative analysis of a snapshot of a system of $N = 10000$ particles, see Fig. VI.5. For visualisation, we turn to the mobility definition which is based on the bond-breaking correlation. The snapshot is taken in the time and the temperature regimes for which there is a deviation between the numerical relaxation spectrum and its stretched exponential prediction, namely, $T = 0.07$ (which corresponds to an α-relaxation time of 6 ms) and $t/\tau_\alpha = 5\times10^{-3}$. We observe that at this time, the sample is populated by rare, localised and independent regions of mobile particles. We also observe that the birth of these clusters of mobile particles is distributed in time on a logarithmic scale. In other words, as the relaxation proceeds, new clusters appear independently throughout the simulation box. Indeed, in Fig. VI.5, the particles are colored according to the common logarithm[2] of the first time τ_α^i at which their bond-breaking correlation $C_{\rm B}^i$ is below 0.55. Some clusters are formed around red particles which relax as fast as $t = 10^3$ ($\tau_\alpha = 2 \times 10^8$), while others are only made of blue particles and they only appear two decades after. Finally, we note that the clusters are not of a single color but instead red particles are surrounded by yellow/green particles, themselves surrounded by blue particles. This suggests that the clusters also grow as the relaxation proceeds and this is the manifestation of dynamic facilitation in the system. In fact, the mobile particles tend to make their neighbours more

[2]We define the common logarithm of τ as $\log \tau = \ln \tau / \ln 10$ with $\ln \tau$ the natural logarithm of τ.

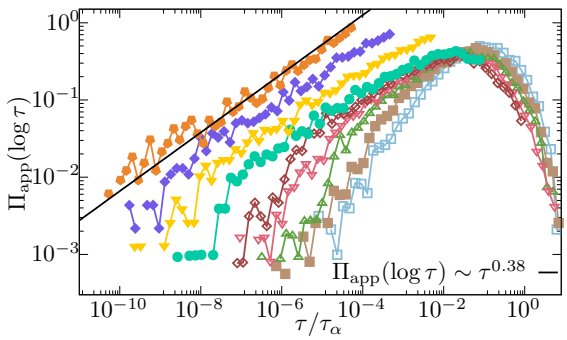

Fig. VI.7 | Distribution of the common logarithm of the appearance time of the clusters of mobile particles $\Pi_{\rm app}(\log\tau)$ up to an irrelevant normalisation factor. The mobile particles are defined by the fact that their displacement in the inherent structure is larger than 0.8. The data are plotted as a function of t/τ_α, where τ_α is directly measured or is extrapolated thanks to the Arrhenius fit in Fig. VI.1 (b). At very low temperatures, the distribution is well approximated by a power law $\Pi_{\rm app}(\log\tau) \sim \tau^{0.38}$ with the same exponent as the excess wing and the number of clusters (straight line). The color code is provided in Fig. VI.1 (a).

mobile at later times and in consequence mobility propagates throughout the sample.

At this stage, one can envision two different ways for the system to relax: (i) creation of new clusters of mobile particles or (ii) growth of the already born clusters. We now analyse the first process quantitatively, and we leave the second one for the next section. We come back to the system of $N = 1200$ with the mobility definition which is based on the displacements in the inherent structures. In Fig. VI.6, we show the average number of clusters $n_{\rm c}(t)$ and the average number of particles per cluster $n(t)$ as a function of time. The number of clusters first increases with time for all the temperatures while their average size midly grows from 1 to less than ten particles. This is the direct manifestation of the fact that rare localised regions of mobile particles appear independently in the sample. At later times instead, the number of clusters decreases towards 1 while their size reaches the total number of particles N in the system. Indeed, when $t \to +\infty$, the system is composed of a single cluster because all the particles have escaped from their initial position. As a result, the number of clusters reaches a maximum at $t = t_{\rm c}$ which is visible for $T \geq 0.07$ and which otherwise leaves the simulation time window. This time broadly corresponds to the time at which the average size of clusters starts to skyrocket. We have checked that these behaviours are not finite-size artefacts. The number of clusters is extensive in system size, which means that the absolute value of $n_{\rm c}(t)$ is proportional to the size N of the system, but the time and the temperature evolution is independent of the system size. Similarly, the average size of clusters $n(t)$ is independent of the system size at short times but it obviously scales linearly with N at later times, and its time evolution is also independent of N.

When the maximum in the number of clusters is reached at a time which is too large to be measured, we observe that $n_{\rm c}(t)$ grows as a power law, namely, $n_{\rm c}(t) \sim t^{0.38}$ with a similar exponent as the one of the excess wing in Fig. VI.2. On the opposite, the average size of clusters is very small in this regime, at most 7-8 particles. This suggests that the appareance of rare clusters rather than their growth is responsible for the signal at intermediate frequencies in the relaxation spectra (wings) or at intermediate times in the inherent structure mean-squared displacements. In addition, the fact that $n_{\rm c}(t)$ grows as a power law means that the appearance of the clusters is not characterised by a mere characteristic time but instead it is described by a distribution of timescales which covers several decades. This is what we directly check

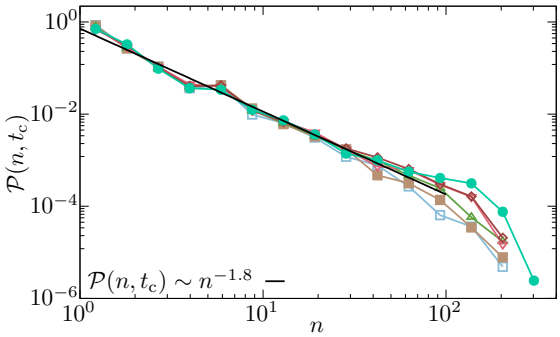

Fig. VI.8 | Distribution of cluster sizes (number of particles) $\mathcal{P}(n, t_c)$ at the time t_c where the number of clusters is maximum. The data are consistent with a temperature independent power law of exponent -1.8 which is cut at large cluster sizes because of finite-size effects. The color code is the same as in Fig. VI.1 (a).

by measuring the distribution of the common logarithm of the appearance time of the clusters $\Pi_{\text{app}}(\log \tau)$, see Fig. VI.7. For $T \leq 0.07$, we cannot measure the whole distribution which is thus determined up to an irrelevant normalisation constant.

At high temperatures, the distribution is already very broad and it covers about 6 orders of magnitude. The first clusters appear as early as $10^{-4}\tau_\alpha$ and they thus relax much before the bulk. The distribution peaks near $10^{-1}\tau_\alpha$, and it has a cutoff around $10^{1}\tau_\alpha$. As T is lowered, the distribution displays a power law tail for $\tau \ll \tau_\alpha$ over several decades with an almost constant exponent $\Pi_{\text{app}}(\log \tau) \sim \tau^{0.38}$. This distribution proves that the appearance of clusters is time-distributed but it also rationalises the behaviours which are observed in Fig. VI.2 and Fig. VI.6 (a). Indeed, the distribution of the common logarithm of the appearance time of clusters should be related to the number of clusters by the equality

$$\Pi_{\text{app}}(\log \tau) \sim \tau \frac{\mathrm{d}n_c}{\mathrm{d}t}(\tau), \tag{VI.11}$$

where the factor τ comes from the jacobian, namely, $\mathrm{d}\log \tau \propto \mathrm{d}\tau/\tau$. As a result, if $\Pi_{\text{app}}(\log \tau) \sim \tau^{0.38}$ then $n_c(t) \sim t^{0.38}$ which is consistent with the result in Fig. VI.6 (a). In addition, as the relaxation at short times is dominated by the growth of the number of clusters rather than that of their average size, it is reasonable to approximate the distribution in Eq. (VI.2) for $t \ll \tau_\alpha$ by the distribution of the appearance time of clusters. Then, a mere change of variables leads to $\chi''(\omega) \sim \omega^{-0.38}$ in agreement with Fig. VI.2. This demonstrates that the high-frequency power law in the relaxation spectrum and the sub-diffusive behaviour in the inherent structure mean-squared displacement close to T_g are the direct consequences of the relaxation of a sparse population of clusters which is characterised by a broad distribution of relaxation times.

So far, we have focused on the early stages of the relaxation. We explain in the next section how relaxation proceeds from these small clusters of mobile particles via dynamic facilitation.

5. Dynamic facilitation towards the α-relaxation

5.1 Mobility percolation

The way the sample fully relaxes relies on dynamic facilitation. This is already visible in the snapshot in Fig. VI.5 where we see that the clusters are composed of particles of different

relaxation times from the lowest at their core to the largest at their boundaries. This suggests that mobility propagates from neighbours to neighbours and that it gradually invades the system. This picture is also fully consistent with the results in Fig. VI.6. Indeed, the distribution of the appearance time of the clusters shows a cutoff for $t = 10\tau_\alpha$. However, at this time, the correlation function $F_\mathrm{s}(t)$ has not fully relaxed and it still equals about 0.1. This means that 10 % of the sample is still immobile. This suggests that at longer times, no new cluster of mobile particles appears but instead immobile regions are progressively invaded from their boundaries via dynamic facilitation. This is also consistent with the evolutions of the number and of the size of clusters. For $t > t_\mathrm{c}$ (where t_c stands for the location of the maximum in the number of clusters), $n_\mathrm{c}(t)$ decreases while $n(t)$ fastly grows, consistently with the fact that the clusters start to merge and that the mobility percolates in the system. This fact is directly demonstrated in Fig. VI.8 where we show the size distribution of clusters $\mathcal{P}(n,t)$ at the maximum in the number of clusters, namely, for $t = t_\mathrm{c}$. We observe that it follows a power law behaviour $\mathcal{P}(n,t_\mathrm{c}) \sim n^{-1.8}$ which is exponentially cut at large cluster sizes. The exponential cutoff is due to a finite-size effect (we have confirmed this point by running simulations with systems of size $N = 10000$) while the power law trend is indeed characteristic of the percolation transition, even though the exponent is different from the one of the random percolation [406]. This trend has also been found in previous studies of dynamic facilitation at higher temperatures [406–411]. We confirm here that it still holds at lower temperatures where the contrast between the mobile and immobile particles becomes clearer.

Our results are consistent with mobility percolation in the entire sample from rare regions of mobile particles to the entire bulk system. In the next section, we analyse the mechanisms which are responsible for dynamic facilitation or mobility percolation.

5.2 Multiple relaxations and mobility propagation

In order to quantify the role of facilitation in the dynamics, we compare this scenario to the opposite one in which we assume that the system relaxes because of the succession of independent events. We then define $x_\mathrm{m}(t) = N_\mathrm{m}(t)/N$ the average fraction of particles which are mobile (with the criterion on the displacement in the inherent structures) in the interval $[0,t]$, and $x_\mathrm{vm}(t) = N_\mathrm{vm}(t)/N$ the average fraction of particles which are mobile in both intervals $[0,t]$ and $[t,2t]$. If the dynamics could be described by the relaxation of independent events, then the probability to be mobile in both intervals would be the product of the probabilities to be mobile in each interval, *i.e.*, $x_\mathrm{vm}(t) = x_\mathrm{m}(t)^2$. Instead, larger values of $x_\mathrm{vm}(t)$ indicate that the particles can relax several times and that their motion is persistent and hence facilitated. One could argue that the fraction of very mobile particles can be over-estimated because of particles which move reversibly, namely, which come back at their initial position, and which do not participate to the relaxation. In order to take into account this effect, we also introduce the fraction $x_\mathrm{rev}(t) = N_\mathrm{rev}(t)/N$ of mobile particles in the range $[0,t]$ which come back to their initial position in the range $[t,2t]$. To decide whether a particle has performed a reversible motion, we look if its displacement in the inherent structures between 0 and $2t$ is such that $|\boldsymbol{r}_{\mathrm{IS},i}(2t) - \boldsymbol{r}_{\mathrm{IS},i}(0)| < 0.5$, which corresponds to the first minimum in the van Hove distribution of the displacements in the inherent structures, see Fig. VI.4.

We thus introduce the ratio

$$c(t) = \frac{x_\mathrm{vm}(t) - x_\mathrm{rev}(t) - x_\mathrm{m}(t)^2}{x_\mathrm{m}(t) - x_\mathrm{m}(t)^2}. \tag{VI.12}$$

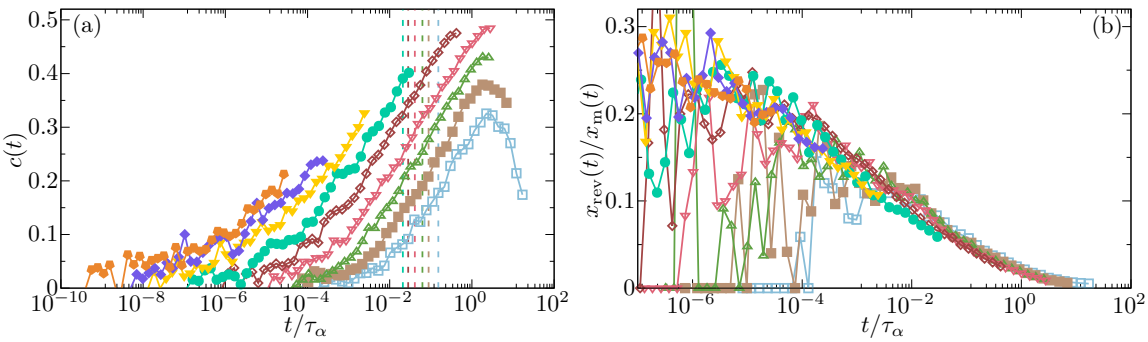

Fig. VI.9 | (a) Ratio $c(t)$ [see Eq. (VI.12)] as a function of time, where $x_{\rm m}(t)$ represents the fraction of particles which is mobile in the range $[0,t]$ (with the criterion on the displacement in the inherent structure), while $x_{\rm vm}(t)$ is the number of particles which are mobile in the two intervals $[0,t]$ and $[t,2t]$. Time is rescaled by τ_α which is directly measured from $F_{\rm s}(t)$ or which is deduced from the Arrhenius extrapolation in Fig. VI.1 (b). The data display a maximum for $t/\tau_\alpha \simeq 1$. The dashed lines mark the maximum in the number of clusters where mobility percolation sets in. (b) Probability for a particle to undergo a reversible motion as a function of t/τ_α. This probability is equal to the ratio $x_{\rm rev}(t)/x_{\rm m}(t)$, where $x_{\rm rev}(t)$ is the fraction of particles which are mobile in the range $[0,t]$ and which come back to their initial position in the range $[t,2t]$. The fraction of particles which move reversibly decreases as the relaxation proceeds and it plateaus for $t \ll \tau_\alpha$ with an enhanced probability to have a reversible motion as the temperature decreases. The color legend is similar for both panels and it is provided in Fig. VI.1 (a).

The numerator vanishes if the dynamics in the ranges $[0,t]$ and $[t,2t]$ are independent and if one assumes that the probability that a particle comes back to its initial position is negligible if the dynamics proceeds via independent events. The denominator is for normalisation purposes and it ensures that $c(t)$ lies between 0 and 1. The results are presented in Fig. VI.9 (a) versus t/τ_α. We note that $c(t)$ first increases with time, which means that the mobile particles which undergo irreversible motions in a given interval are also mobile irreversiblely in the next one with a higher and higher probability. This implies that the mobility is persistent in the system, in the sense that a mobile particle undergoes several relaxations. We also observe that $c(t)$ decreases and is likely to vanish when t becomes larger than typically several τ_α. This is because the displacements of the particles in the ranges $[0,t]$ and $[t,2t]$ become irreversible and uncorrelated in this case. As a result, $c(t)$ exhibits a maximum which turns out to be close to τ_α: the probability for a particle to be mobile in the interval $[t,2t]$ given it was mobile in the range $[0,t]$ is maximum. We finally remark that the full curve of $c(t)$ shifts to higher values when T decreases, which suggests that the dynamics is even more persistent when decreasing the temperature.

Even though reversible particle motions do not participate to the relaxation, they give indication on how particle motion proceeds. In Fig. VI.9 (b), we show the ratio of the fraction of very mobile particles which have a reversible motion to the fraction of mobile particles. This ratio thus corresponds to the probability for a particle to come back to its initial position in the range $[t,2t]$ given that it has escaped from it in the range $[0,t]$. We observe that this fraction consistently decreases with time. At short times, particles try to escape their initial position but this attempted relaxation is sometimes a failure and the particles come back to their initial cages. At later times instead, as the particles have multiplied trials to escape their cages and as other particles have already managed to relax, an irreversible relaxation becomes more probable (the probability for a particle to be immobile in the range $[t,2t]$ given it was mobile

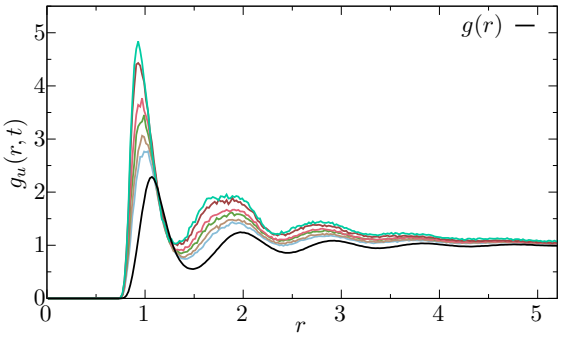

Fig. VI.10 | Displacement-weighted pair correlation function $g_u(r,t)$ for $t = t_c$ which corresponds to the location of the maximum in the number of clusters, hence to mobility percolation in the system. We represent the equilibrium pair correlation function $g(r)$ at $T = 0.07$ for comparison (it varies weakly with the temperature). The color code is similar to Fig. VI.1 (a).

in the range $[0, t]$ also decreases as the relaxation proceeds). For all the temperatures, and even though our data are noisy, we observe that the ratio $x_{\rm rev}(t)/x_{\rm m}(t)$ plateaus for $t \ll \tau_\alpha$, and the amplitude of the plateau increases as the temperature decreases, from 0.1 at $T = 0.095$ to 0.25 at $T = 0.059$. This suggests that the motion of the particles become increasingly reversible at short times as the temperature decreases and that the first dynamic events actually correspond to very frequent motions of the particles which rarely lead to an actual relaxation.

To explain why the dynamics becomes increasingly persistent as the temperature is lowered or as the relaxation proceeds, we look at a displacement-weighted pair correlation function $g_u(r,t)$ [412], namely,

$$g_u(r,t) = \frac{1}{N\rho u(t,0)u(2t,t)} \left\langle \sum_{i\neq j} u_i(t,0)u_j(2t,t)\delta(\boldsymbol{r} - \boldsymbol{r}_i(0) + \boldsymbol{r}_j(0)) \right\rangle, \tag{VI.13}$$

where the sums run over $i, j = 1 \ldots N$, where $u_i(t_2, t_1) = |\boldsymbol{r}_{{\rm IS},i}(t_2) - \boldsymbol{r}_{{\rm IS},i}(t_1)|$, and where $u(t_2, t_1) = \langle N^{-1} \sum_i u_i(t_2, t_1)\rangle$. The prefactor in Eq. (VI.13) ensures that $g_u(r,t)$ converges to 1 in the large-r limit (we recall that ρ is the average number density which is equal to 1). If the displacements in the ranges $[0, t]$ and $[t, 2t]$ are uncorrelated in space, then $g_u(r,t)$ should be similar to the conventional pair correlation function $g(r)$ at equilibrium at a temperature T [30]. Instead, positive correlations between displacements should lead to an enhanced displacement-weighted pair correlation function. In Fig. VI.10, we plot $g_u(r,t)$ for several temperatures and for $t = t_c$ where the number of clusters of mobile particles is maximum and where the mobility percolates in the system. The equilibrium pair correlation functions are also represented to assess the degree of correlation between the displacements of the particles. The correlation $g_u(r, t_c)$ shows a similar variation with the distance r as $g(r)$, with several extrema because of the underlying structure of the liquid. We note a shift in the position of the maxima in the displacement-weighted pair correlation function towards lower distances which stands for the fact that small particles are usually more mobile than the larger ones. We also clearly observe that $g_u(r, t_c)$ is much larger than the equilibrium pair correlation function at small distances. This means that there is a correlation between the fact that a particle is mobile in the range $[0, t]$ and that its neighbours become mobile in the range $[t, 2t]$. The maximum in $g_u(r, t_c)$ increases with decreasing the temperature, which indicates that the correlation between the displacements of the particles at unequal times increases as the temperature is lowered. The typical decay length

of $g_u(r, t_c)$ also seems to increase as T goes down (even though the linear size of the simulation box is moderate), which is indicative of a growing dynamic correlation length.

Overall, this indicates that the motion of the mobile particles becomes more and more persistent at low temperatures because the particles are able to make their neighbours mobile. This is consistent with the fact that the mobility is coarsening and transmitting from particles to their neighbours and in consequence that the dynamics is facilitated. The effect of facilitation is most important close to the peak in $c(t)$, namely, for $t \simeq \tau_\alpha$. In addition, the relative contribution of facilitation in the relaxation process grows when T is lowered as emphasised by the temperature evolution of the maximum in $c(t)$ or its value at $t = t_c$ where the mobility percolation settles.

Facilitation has already been discussed at length in the literature. Our quantification of facilitation is very reminiscent of several already reported measurements even though the latter were performed at much higher temperatures and they required more choices in the definition of mobile particles. In particular, we believe that our ratio $c(t)$ is close to the facilitation volume around an excitation which was introduced in Ref. [379]. This facilitation volume was found to be a non-monotonic function of time with a maximum whose amplitude was growing with decreasing the temperature. In addition, the results of Fig. VI.9 and Fig. VI.10 resemble previous analyses which were based on the measure of the probability distribution to find a mobile particle in the interval $[t, 2t]$ at a distance r from a particle which was mobile in the range $[0, t]$. A ratio was defined by comparing the integrated probability distribution to the expected one assuming no correlation in the displacements of the particles [381, 411].

6. Conclusions

6.1 Summary of the results

We summarise the main findings of this chapter. Thanks to the swap algorithm and long conventional molecular dynamics simulations, we have been able to access the equilibrium dynamics of deeply supercooled liquids over a large time window. Computer simulations are now in a position to directly compare with experiments while they have been at odds for several decades. Thanks to filtering procedures, we have managed to reveal that at very low temperatures the dynamics initiates from a weak population of diluted clusters whose waiting times are power law distributed. This is in contrast to the average correlation functions which display a plateau over several orders of magnitude. We have then seen how these small clusters facilitate their neighbourhood in a hierarchical manner to construct the structural relaxation [413]. The effect of facilitation seems more pronounced as the temperature is decreased. In Ref. [414], the effect of facilitation was instead found to become weaker as the glass transition was approached in a granular material. However, the analysis of Ref. [414] relied on tools which are very different from ours [415]. Trying to repeat this analysis in our system may be valuable in order to understand this seeming contradiction. The dynamics in other glass-formers may also be worth studying to assess the robustness of the evolution of facilitation with the temperature.

Moreover, we have shown that the short-time processes which take the form of small clusters are very reproducible, as shown by the evolution of the ratio $c(t)$ in Sec. 5. Indeed, as the dynamics is time-reversible, the ratio $c(t)$ also quantifies how the forward (from t to $2t$) and the backward (from t to 0) dynamic heterogeneities look similar and therefore how predictible

they are[3]. We first note that the predictability is maximum for times close to τ_α, in agreement with past studies [72]. But interestingly, below the mode-coupling crossover, the dynamics becomes reproducible at shorter and shorter timescales. This means that the first events which are responsible for the excess wing are increasingly predictible as T approaches T_g from above. Whether the events which account for the excess wing can be deduced from structural indicators, such as the ones in Ref. [373], is left for future work.

In the next section, we discuss the consequences of our results on the shape of the relaxation spectra.

6.2 Microscopic origin of the shape of the relaxation spectra

Our findings, which hold down to T_g, reveal that the dynamics can be described by two minimal ingredients, namely, dynamic heterogeneities at short times and subsequent facilitation. The first events appear independently throughout the sample while facilitation terminates the structural relaxation and it helps relaxing the slowest regions. Therefore, as far as the relaxation spectra are concerned, this suggests that what is called an "excess wing" is actually not an excess process but the very beginning of the α-relaxation. Instead, the α-peak stands for the relaxation of larger regions of the sample via dynamic facilitation. As a result, the α-peak is the one that should be rather considered to be in excess of an underlying broader distribution of timescales. Facilitation compresses the latter distribution by fastening all the slowest regions of the sample and this naturally leads to an excess α-peak. In Ref. [378], we have devised a minimal facilitated trap model to explain the shape of the relaxation spectra and to confirm the above scenario. It is minimal in the sense that it is only built on dynamic heterogeneities and dynamic facilitation. The system is composed of a collection of traps. Each trap is characterised by an energy $E > 0$ which is distributed according to a normalised distribution $\rho(E)$ and by a relaxation time which is exponentially-distributed and of mean $\propto e^{\beta E}$ (with β the inverse temperature), as in the original trap model [194, 416]. On top of this, we add facilitation in a mean-field way (see Ref. [417, 418] for a real space version). Whenever a trap relaxes, all the other trap energies are shifted by a random amount while leaving unchanged the equilibrium distribution $\mathcal{P}(E) \propto \rho(E)e^{\beta E}$ of energies. A new relaxation time is then computed for each trap from its new energy. These random energy kicks result in the diffusion of the traps in the energy space towards the most probable energy and thus in a faster relaxation. The spectrum of the trap model can be computed analytically without facilitation and it can be measured numerically when facilitation is implemented. We have found that the high-frequency range is unaffected while the low-frequency part is highly compressed. This results in a more compressed α-peak in the presence of dynamic facilitation.

We can also confront our numerical results to the collection of models which have already been introduced to describe the shape of the experimental dielectric spectra. First, we emphasise that the model under study in this chapter is a simple size-polydisperse glass-former of spherical particles. As a result, the coupling between the translation of the particles and an extra degree of freedom is not needed to account for the excess wing. Of course, such a coupling can exist and may lead to even richer spectra with additional processes which take the form of a β-peak at intermediate frequencies [419]. Instead, we have seen that the wing is due to small and localised regions of mobile particles in a sea of quiescent particles, as already predicted by Johari and

[3] As we simulate the equilibrium dynamics, the configuration at time t is an equilibrium configuration just like the initial configuration which is prepared with the swap algorithm.

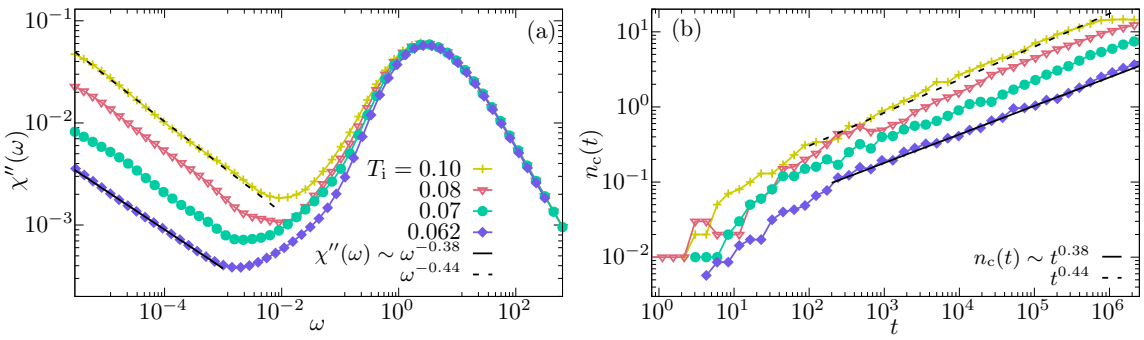

Fig. VI.11 | (a) Relaxation spectrum $\chi''(\omega)$ in systems which were equilibrated at a temperature T_i and subsequently aged at a temperature $T = 0.062$ during $t_w = 2 \times 10^6$. The curve for $T_i = 0.062$ corresponds to the equilibrium curve, see Fig. VI.2. The spectra shift to lower values for a fixed frequency $\omega \leq 10^{-3}$ when T_i is decreased in agreement with the rarefaction of short-time processes with increasing the glass stability. (b) Average number of clusters $n_c(t)$ of mobile particles (with the same definition as in Fig. VI.6). The number of localised regions of mobile particles at short times decreases for fixed time with increasing the stability, namely, with decreasing the initial temperature T_i. For both panels, the color legend is similar and it is given in panel (a).

Goldstein several decades ago [420–422]. However, the origin of these dynamic heterogeneities at much shorter times than the bulk relaxation time has not been investigated to discriminate between all the models which account for the excess wing and this is left for future work. The short-time processes are likely to be activated but studying their nature and their characteristics would be interesting. This could also allow for a more deeply understanding of the interplay between the dynamic facilitation theory [112] and the random first order transition theory [122, 144].

Appendix A - Suppression of the "excess wing" in stable glasses

Experiments on aging systems [384, 385, 423, 424] or ultrastable glasses [82, 425] suggest that the excess wings in the relaxation spectra are suppressed with increasing the stability of the sample: both their amplitude and the absolute value of the exponent in the power law decrease. To assess the influence of the glass stability on short-time processes, we have first prepared $n_s = 100$ equilibrium initial conditions via the swap algorithm at temperatures $T_i = 0.07$, 0.08, 0.10 close to and below the mode-coupling crossover. This variation in T_i allows for probing systems with different degrees of stability. The swap algorithm is then turned off and the configurations age at a temperature $T = 0.062$ during $t_w = 2 \times 10^6$ by using simulations in the canonical ensemble with a Nosé-Hoover thermostat. The aging time corresponds to about one week of simulation. We have restricted ourselves to sufficiently large t_w in order to shift the α-relaxation peak in the relaxation spectra outside the simulation window and in consequence to maximise the frequency range over which the excess wing can be observed. We have also checked that our measurements are not very sensitive to t_w in the small range of values of t_w that we can achieve with simulations of reasonable walltime (between one day and one week). After this aging procedure, we have measured the relaxation function $F_s(t)$ and computed the corresponding spectrum $\chi''(\omega)$ by using the methods which are described in Sec. 2: we have run conventional molecular dynamics simulations by starting from the aged configurations at $T = 0.062$.

The results are presented in Fig. VI.11. Fig. VI.11 (a) shows the relaxation spectra $\chi''(\omega)$. The curves shift towards lower values by one order of magnitude for a fixed frequency $\omega \leq 10^{-3}$ in the range of initial temperatures that we have investigated. In addition, the exponent of the power law which fits the signal at intermediate frequencies smoothly decreases from $\sigma = 0.44$ at $T_{\mathrm{i}} = 0.10$ to $\sigma = 0.38$ at $T_{\mathrm{i}} = 0.062$. Overall, this suggests that more stable glasses have weaker short-time processes and they are thus the slowest to relax, which result in a smaller excess wing. To understand the effect of glass stability, we show the number of clusters of mobile particles in Fig. VI.11 (b) (with the same definition as in Fig. VI.6). The data clearly show that the number of relaxation events is strongly suppressed with enhanced glass stability. In addition, the number of clusters of mobile particles grows as a power law with time with a similar exponent as the excess wing. These observations strengthen the connections we have made in Sec. 4 between the first rare and localised regions to relax and the excess wing in the relaxation spectra. We thus expect even more events at short timescales for very poorly annealed glasses [426, 427]. These events are fully irreversible and of non-equilibrium nature and they may lead to a secondary β-peak in the relaxation spectra.

VII Article: Stable glassy configurations of the Kob–Andersen model through the swap Monte Carlo algorithm

The swap Monte Carlo algorithm allows for the preparation of highly stable glassy configurations for a number of glass-formers, but it is inefficient for some models, such as the much studied binary Kob-Andersen (KA) mixture. This algorithm consists in exchanging the positions or equivalently the diameters of two randomly-chosen particles while respecting detailed balance. However, in binary models, such as the KA mixture, the swap of unequal species is almost always rejected because the difference in sizes is too large. Generalisations to the KA model have been developed recently where the swap algorithm can instead be very effective. These generalisations rely on the introduction of a small fraction of particles whose sizes interpolate between the sizes of the two types of particles in the binary mixture. In this chapter, we show that these models can be used to considerably enhance the stability of glassy configurations in the original KA model at no computational cost. We successfully develop several numerical strategies both in and out of equilibrium to achieve this goal and we show how to optimise them. We provide several physical measurements which indicate that the proposed algorithms considerably enhance mechanical and thermodynamic stability in the KA model, including a transition towards brittle yielding. Our results thus pave the way for future studies of stable glasses by using the KA model.

Outline

1 Introduction . . . 169
2 Models . . . 169
3 Reweighting equilibrium distributions . . . 171
3.1 General formalism . . . 171
3.2 Umbrella sampling simulations . . . 173
4 Annealing procedures to generate glassy Kob-Andersen configurations . . . 174
5 Enhanced stability of the annealed glassy Kob-Andersen configurations . . . 175
5.1 Inherent structure energies . . . 175
5.2 Fictive temperatures . . . 176
5.3 Relaxation timescales . . . 176
5.4 Calorimetric measurements . . . 177
5.5 Rheology . . . 178
6 Conclusions . . . 179

The work of this chapter is done in collaboration with A. D. S. Parmar. The results of this chapter have been published in Ref. [428].

1. Introduction

The swap Monte Carlo algorithm has become a powerful asset in the simulations of glass-forming liquids for a broad (but incomplete) class of model glass-formers [54, 55, 429]. It enables one to equilibrate supercooled liquids down to extremely low temperatures, even below the extrapolated glass transition temperature [182]. In other words it allows one to explore deeper regions of the free energy landscape in equilibrium configurations unlike other preparation protocols like gradual cooling.

The Kob-Andersen (KA) model is a binary mixture of Lennard-Jones particles which was devised to describe the generic physical properties of simple metallic glasses [430]. For this well studied model, the swap Monte Carlo algorithm is however inefficient as the swap of unlike species is almost always rejected [431]. Therefore, the simulation of the low-temperature properties of the KA model requires alternative methods, such as parallel tempering [432], simulations on graphic cards [401, 432], ghost particle insertion [433], Wang-Landau algorithm [434], transition path sampling [433, 435], physical vapor deposition [436], or oscillatory shear [437–439]. However, none of these attempts could provide the type of speedup that the swap Monte Carlo has provided in the models where it is efficient. There is thus a clear need to further develop computational algorithms to produce more stable glassy configurations of the KA model.

Recently, generalised versions to the KA model have been introduced. They are called KA_1 and KA_2 models, they are very similar to the original KA model, and for these models, the swap Monte Carlo algorithm is very efficient [440]. The strategy relies on introducing a small amount of additional species to the binary KA mixture to enhance the swap efficiency. This strategy is likely to allow for the investigation of properties of simple metallic glasses down to the experimental glass transition, but not for the KA model itself. In this chapter, we instead demonstrate that the production of very stable configurations within the KA_1 model can in turn be used to produce stable glassy configurations of the original KA model as well, for a modest computational effort. The KA model is the most studied glass model and a huge number of numerical tools have been developed for its analysis. Consequently, we aim at paving the way for future studies of stable glass physics within the KA model.

In this chapter, we first define the various glass models we consider in Sec. 2. In Sec. 3, we use histogram reweighting techniques to measure equilibrium properties of the KA model but we show that equilibrium properties of the KA model can be deduced from simulations of the KA_1 model only for temperatures at which the KA model can be directly simulated. We thus turn to non-equilibrium properties of KA glasses, as presented in Chap. I. In Sec. 4, we present two annealing procedures to prepare stable configurations of the KA model from configurations of the KA_1 model whose stability we directly quantify in Sec. 5. We finally conclude in Sec. 6.

2. Models

We consider mixtures of particles $i = 1 \dots N$ of different species which are characterised by a number $\omega_i \in [0, 1]$. The interaction potential between two particles i and j is

$$v(r_{ij}|\omega_i, \omega_j) = 4\varepsilon_{\omega_i\omega_j} \left[\left(\frac{\sigma_{\omega_i\omega_j}}{r_{ij}} \right)^{12} - \left(\frac{\sigma_{\omega_i\omega_j}}{r_{ij}} \right)^{6} \right], \tag{VII.1}$$

which depends on the distance r_{ij} between the two particles. It also involves the interaction strength $\varepsilon_{\omega_i\omega_j}$ and the cross-diameter $\sigma_{\omega_i\omega_j}$, which both depend on the types ω_i and ω_j of the

two particles. The potential is truncated and shifted to 0 at the cutoff distance $2.5\sigma_{\omega_i\omega_j}$.

We focus on two related models. The first one is the standard Kob-Andersen (KA) model [430] which is a 80:20 binary mixture of N_A particles of type A (with $\omega_i = 1$) and N_B particles of type B (with $\omega_i = 0$). The interaction parameters are: $\varepsilon_{AB}/\varepsilon_{AA} = 1.5$, $\varepsilon_{BB}/\varepsilon_{AA} = 1.0$, $\sigma_{AB}/\sigma_{AA} = 0.8$, and $\sigma_{BB}/\sigma_{AA} = 0.88$. Energies and lengths are expressed in units of ε_{AA} and σ_{AA} respectively, and the Boltzmann constant is set to unity. We denote by $\mathcal{H}_{\mathrm{KA}}[\boldsymbol{r}^N]$ the corresponding Hamiltonian of the KA model.

We also consider an extended version of the KA model (KA_1) by introducing a small fraction $\delta = N_C/(N_A + N_B)$ of particles of type C which interpolate continuously between A and B particles. More precisely, the C particles are characterised by a uniform distribution of $\omega_i \in]0, 1[$, while the A (resp. B) particles are still associated with the type $\omega_i = 1$ (resp. $\omega_i = 0$). The Hamiltonian of the KA_1 model is

$$\mathcal{H}_1[\boldsymbol{r}^N] = \frac{1}{2}\sum_{i\neq j} v(r_{ij}|\omega_i, \omega_j), \tag{VII.2}$$

where the sums run over all particles $i, j = 1 \ldots N$ with $i \neq j$, and where the additional interaction parameters are:

$$\begin{aligned} X_{1\omega_i} &= \omega_i X_{AA} + (1-\omega_i) X_{AB}, \\ X_{0\omega_i} &= \omega_i X_{AB} + (1-\omega_i) X_{BB}, \\ X_{\omega_i\omega_j} &= \omega_{ij} X_{AA} + (1-\omega_{ij}) X_{BB}, \end{aligned} \tag{VII.3}$$

with $X = \sigma, \varepsilon$ and with $\omega_{ij} = (\omega_i + \omega_j)/2$ [440]. We also define the Hamiltonian $\mathcal{H}_0[\boldsymbol{r}^N]$ the system would have if the C particles with $\omega_i \leq 0.2$ (resp. $\omega_i > 0.2$) were taken as B (resp. A) particles. Thus, $\mathcal{H}_0$ is the Hamiltonian of the corresponding KA model, which is given by Eq. (VII.2) where ω_i is replaced by $\omega_i' = 1 - \theta(1 - \omega_i/0.2)$ and where $\theta(x)$ is the Heaviside step function. Finally, we define

$$\mathcal{W}[\boldsymbol{r}^N] = \mathcal{H}_1[\boldsymbol{r}^N] - \mathcal{H}_0[\boldsymbol{r}^N] \tag{VII.4}$$

as the difference between the KA_1 and the KA energies for a given configuration of the KA_1 model.

We study the KA_1 model with $N_C = 5$, $N_A = 800$ and $N_B = 200$ (so that $\delta = 0.5$ %), at a number density $\rho = 1.2$ under periodic boundary conditions. The model is studied by using the swap Monte Carlo algorithm [54]. With probability $p = 0.2$, the identity of a randomly-chosen particle i is exchanged with the one of another randomly-chosen particle j. Otherwise, with probability $1 - p$, a standard translational move is performed in which the position $\boldsymbol{r}_i$ of a particle i is incremented by a random displacement $\delta\boldsymbol{r}_i$ which is drawn in a cube of linear size 0.15 around the origin [441]. The choice of p has been optimised in order to maximise the swap efficiency, *i.e.*, the ratio between the relaxation time of the system to the simulation walltime. Both moves are accepted according to the Metropolis rule [64, 293]. The position of the center of mass is held fixed.

Due to the large difference in diameters between the A and B particles, the swap moves are inefficient in the KA model [431], whereas the introduction of a small fraction of C particles makes the swap moves possible and results in a much faster relaxation [440]. The structural relaxation time τ_α of the system is defined as the time value at which the self-intermediate scattering function for the whole system, with a wave number which corresponds to the first

maximum in the total structure factor, decays to the value e^{-1} (see Chap. VI). The α-relaxation time is expressed in units of Monte Carlo (MC) steps, where 1 MC step corresponds to N attempted moves. The lowest temperature for which we can ensure equilibration in the KA model is $T \simeq 0.415$, whereas for the KA_1 we can reach $T \simeq 0.36$ for a comparable numerical effort of 10^8 Monte Carlo steps. In terms of τ_α, this represents a speedup factor of more than 10^2 over the standard KA model at the lowest temperature [440].

3. Reweighting equilibrium distributions

3.1 General formalism

The aim of this chapter is to access the low-temperature properties of the KA model from simulations of the KA_1 model only. We have seen in Chap. III that in computer simulations, a system can be forced to sample untypical regions of the phase space. This is usually done thanks to biased simulations, which rely on the umbrella sampling technique or which use external sources that are coupled to well chosen collective variables [293, 305, 442]. By looking at Eq. (VII.4), one can identify the KA_1 model as a biased version of the KA model, where an external field of amplitude equal to 1 has been coupled to the order parameter $\mathcal{W}$. Therefore, by using reweighting methods [294], we can potentially measure thermodynamic properties of the KA model without actually simulating it. As we are able to thermalise the KA_1 model to lower temperatures than the original KA model, we may be able to access low temperatures where only the KA_1 model can reach equilibrium.

In particular, we focus on the probability distribution of the energy in the standard KA model

$$P(E) = \langle \delta(E - \mathcal{H}_{\mathrm{KA}}) \rangle_{\mathcal{H}_{\mathrm{KA}}} = \frac{\int \mathrm{d}\boldsymbol{r}^N \delta(E - \mathcal{H}_{\mathrm{KA}}[\boldsymbol{r}^N]) e^{-\beta \mathcal{H}_{\mathrm{KA}}[\boldsymbol{r}^N]}}{\int \mathrm{d}\boldsymbol{r}^N e^{-\beta \mathcal{H}_{\mathrm{KA}}[\boldsymbol{r}^N]}}, \tag{VII.5}$$

with $\delta(x)$ the delta function and $\langle \cdots \rangle_{\mathcal{H}_{\mathrm{KA}}}$ the thermodynamic average at inverse temperature $\beta = T^{-1}$ for the Hamiltonian $\mathcal{H}_{\mathrm{KA}}$. We then rewrite Eq. (VII.5) by using quantities which are defined within the KA_1 model, namely,

$$P(E) = \frac{\int \mathrm{d}\boldsymbol{r}^N \delta(E - \mathcal{H}_0[\boldsymbol{r}^N]) e^{-\beta \mathcal{H}_1[\boldsymbol{r}^N] + \beta \mathcal{W}[\boldsymbol{r}^N]}}{\int \mathrm{d}\boldsymbol{r}^N e^{-\beta \mathcal{H}_1[\boldsymbol{r}^N] + \beta \mathcal{W}[\boldsymbol{r}^N]}} = \frac{\langle \delta(E - \mathcal{H}_0) e^{\beta \mathcal{W}} \rangle_{\mathcal{H}_1}}{\langle e^{\beta \mathcal{W}} \rangle_{\mathcal{H}_1}}, \tag{VII.6}$$

where now $\langle \cdots \rangle_{\mathcal{H}_1}$ stands for the thermodynamic average for the Hamiltonian $\mathcal{H}_1$. We have used Eq. (VII.4) and the fact that, by definition, $\mathcal{H}_0 = \mathcal{H}_{\mathrm{KA}}$.

By introducing $P^{(1)}_{\mathcal{W}}(W) = \langle \delta(W - \mathcal{W}) \rangle_{\mathcal{H}_1}$ the probability distribution of $\mathcal{W}$ in the KA_1 model, by using the trivial identity $e^{\beta \mathcal{W}} = \int \mathrm{d}W e^{\beta W} \delta(W - \mathcal{W})$ and the Kolmogorov definition of a conditional probability [443], Eq. (VII.6) can be written as

$$P(E) = \frac{\int \mathrm{d}W P^{(1)}_{\mathcal{H}_0|\mathcal{W}}(E|W) P^{(1)}_{\mathcal{W}}(W) e^{\beta W}}{\int \mathrm{d}W P^{(1)}_{\mathcal{W}}(W) e^{\beta W}}, \tag{VII.7}$$

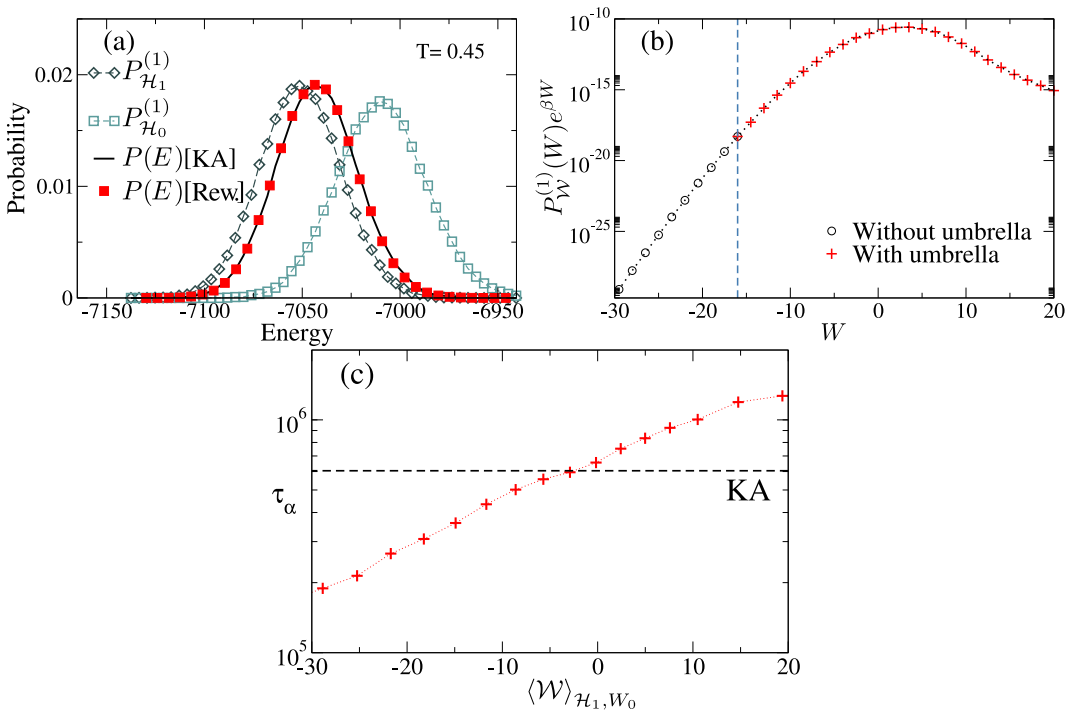

Fig. VII.1 | (a) Probability distributions $P^{(1)}_{\mathcal{H}_1}$, $P^{(1)}_{\mathcal{H}_0}$ of energies $\mathcal{H}_1$ and $\mathcal{H}_0$ in the extended Kob-Andersen (KA_1) system at $T = 0.45$ along with the reweighted probability distribution $P(E)$ [Rew.] of the energy for the Kob-Andersen (KA) model which is obtained from Eq. (VII.7). The probability distribution $P(E)$ has also been directly measured in the KA model [KA] to check the quality of the reweighting procedure. (b) Plot of $P^{(1)}_{\mathcal{W}}(W)e^{\beta W}$ with (red) and without (black) umbrella sampling. The vertical dashed line marks the limit of $\mathcal{W}$ in the unbiased Monte Carlo simulations of the KA_1 model. (c) Relaxation time τ_α of the system in the different umbrella simulations as a function of $\langle \mathcal{W} \rangle_{\mathcal{H}_1, W_0}$, the average value of $\mathcal{W}$.

where $P^{(1)}_{\mathcal{H}_0|\mathcal{W}}$ is the conditional probability of $\mathcal{H}_0$ given $\mathcal{W}$ in the KA_1 model. The two distributions in the right-hand side of Eq. (VII.7) can be measured in the course of a simulation of the KA_1 model and can be subsequently reweighted to obtain the probability distribution of the energy in the KA model in the left-hand side. Thus, in principle, the properties of the KA model can be obtained without ever performing a simulation of the KA model itself but by only working with the KA_1 model where the swap Monte Carlo works well.

In Fig. VII.1 (a), we show the distributions of $\mathcal{H}_1$ and $\mathcal{H}_0$ in the KA_1 model, for a temperature $T = 0.45$ for which the relaxation time of the KA model is $\tau_\alpha/\tau_{\mathrm{on}} \simeq 2 \times 10^2$, with $\tau_{\mathrm{on}} \simeq 3 \times 10^3$ the relaxation time at the onset temperature $T_{\mathrm{on}} \simeq 0.70$ of glassy behaviour (which corresponds to the appearance of a two-step decay in the time dependence of correlation functions). We also show $P(E)$ which is directly measured in the KA model to assess the validity of the reweighting procedure. The product $P^{(1)}_{\mathcal{W}}(W)e^{\beta W}$ plays a crucial role in the reweighting scheme as emphasised by Eq. (VII.7). However, as shown in Fig. VII.1 (b), this quantity exponentially increases without bounds in the range of $\mathcal{W}$ that is being explored in a direct simulation of the KA_1 model. This finding indicates that a direct application of Eq. (VII.7) is not possible with this set of data, as the tails of the distributions which are involved in the various integrands are not appropriately sampled. This limitation becomes increasingly difficult

to tackle when δ increases, which explains why we chose the smallest value $\delta = 0.5$ % that was studied in Ref. [440].

3.2 Umbrella sampling simulations

To overcome this sampling issue, we need to force the system to visit untypical larger values of $\mathcal{W}$. To this end, we use umbrella sampling techniques [293, 442], as already implemented in the study of glass-forming liquids in the Franz-Parisi setting, see Chap. III. We perform several simulations of the KA_1 model in parallel, and each simulation is run with a biased Hamiltonian of the form

$$\mathcal{H}_{1,W_0}[\boldsymbol{r}^N] = \mathcal{H}_1[\boldsymbol{r}^N] + \kappa(\mathcal{W}[\boldsymbol{r}^N] - W_0)^2, \tag{VII.8}$$

with $\kappa = 0.05$ the strength of the bias, in order to be able to sample values of the energy difference $\mathcal{W}$ around $W_0 \in [-17.5, 20]$. By combining the different umbrella simulations, we can extend the range over which $P^{(1)}_{\mathcal{H}_0|\mathcal{W}}$ and $P^{(1)}_{\mathcal{W}}$ are measured. The former remains identical when the phase space is sampled with the Hamiltonian $\mathcal{H}_{1,W_0}$. On the opposite, the latter is obtained by histogram reweighting as

$$P^{(1)}_{\mathcal{W}}(W) = \mathcal{Z}(W_0) P^{(1,W_0)}_{\mathcal{W}}(W) e^{\beta\kappa(W-W_0)^2}, \tag{VII.9}$$

with $P^{(1,W_0)}_{\mathcal{W}}$ the probability density of $\mathcal{W}$ with the bias and $\mathcal{Z}(W_0)$ an unknown normalisation constant [364]. For two consecutive values of W_0, the ratio of these normalisation constants can be estimated from the range of overlapping values of the biased probabilities [319, 320], without resorting to the heavy machinary of WHAM (as used in Chap. III) [294, 317, 318]. We first measure the unbiased probability distribution $P^{(1)}_{\mathcal{W}}$ which is well normalised. Then, for the umbrella simulations which sample a range of $\mathcal{W}$ which overlaps with the range of the unbiased distribution, we tune the normalisation constant $\mathcal{Z}(W_0)$ in order for $P^{(1)}_{\mathcal{W}}$ that is computed from Eq. (VII.9) to be "glued" so that it matches with the unbiased distribution on their mutual range. This procedure is eventually iterated for the successive umbrella simulations. Finally, the most accurate value is kept for each bin. In Fig. VII.1 (b), we show that $P^{(1)}_{\mathcal{W}}(W)\exp(\beta W)$ is now bounded with a maximum for $W \simeq 0$. This implies that the integrals in Eq. (VII.7) are dominated by configurations with $\mathcal{W} \simeq 0$, *i.e.*, KA-like configurations. After umbrella sampling, Eq. (VII.7) can now be numerically evaluated to obtain an accurate estimate of $P(E)$, see Fig. VII.1 (a).

We have shown that thermodynamic properties of the KA model can be computed from simulations of the KA_1 model, which can involve the efficient swap moves. However, these measurements rely on umbrella sampling simulations, and care must be taken that these biased simulations are all performed in equilibrium conditions. To ensure a proper sampling in the umbrella simulations, we measure the relaxation time τ_α as a function of $\langle\mathcal{W}\rangle_{\mathcal{H}_{1,W_0}}$, the average value of $\mathcal{W}$, see Fig. VII.1 (c). It turns out that τ_α increases from its value in the KA_1 model to its value in the KA model when $\langle\mathcal{W}\rangle_{\mathcal{H}_{1,W_0}} \simeq 0$, and it increases further for positive values. The biased KA_1 system visits KA-like configurations when $\langle\mathcal{W}\rangle_{\mathcal{H}_{1,W_0}} \simeq 0$, for which the swap algorithm is inefficient, despite the fact that the acceptance rate of swap moves is actually very high. This means that the frequently-accepted swap moves in the biased KA_1 model do not accelerate the equilibration when sampling KA-like configurations.

Therefore, the strategy devised here does work correctly, and numerical results for the KA model can be obtained without ever simulating it. However it can only be implemented at

sufficiently high temperatures, as one needs to achieve equilibration times close to the one of the KA model itself to implement the reweighting procedure. In other words, at equilibrium, we can measure $P(E)$ by using the KA_1 model only in a range of temperatures for which it can directly be measured in the KA model as well, as a continuous chain of equilibrium simulations which interpolate between the KA_1 and the KA models is needed. There is thus no computational advantage. In the next section, we see how we can use equilibrium stable KA_1 configurations to gain information about the KA model at low temperatures while relaxing the constraint to remain in equilibrium conditions.

4. Annealing procedures to generate glassy Kob-Andersen configurations

To produce useful results for the KA model by using only the KA_1 model, one needs to smoothly transform KA_1 data into KA ones. If this is done in fully equilibrium conditions, a bottleneck is necessarily encountered as the final steps involve being in equilibrium within a system close to the KA model. This is always problematic, as the swap Monte Carlo algorithm does not work well in this regime.

In this section, we again transform the KA_1 results (which benefit from the swap algorithm) into the KA ones (which do not), but we relax the constraint that the final configurations are at equilibrium. To this end, we develop two annealing procedures to smoothly transform in a finite amount of time very stable KA_1 configurations into KA ones. The hope is that the gain in stability in the first steps is not completely lost during the annealing procedure, and in consequence new regions in the free energy landscape of the KA model may be explored.

In method I, we perform simulations with the Hamiltonian $\mathcal{H}_{1,W_0}$ and we linearly increase the value of the bias W_0 up to $W_0 = 0$ (the system is then close to the KA model) in a total number of Monte Carlo steps t_{MC}. Initially, the value of W_0 is set to the instantaneous value of $\mathcal{W}$ in the initial configuration. We eventually switch the Hamiltonian to $\mathcal{H}_0$, which is equivalent to treating the final configuration as a genuine KA configuration. In this method, the KA_1 model is thus gradually biased by using the umbrella sampling Hamiltonian in Eq. (VII.8) towards the KA model.

In method II, we do not rely on umbrella sampling and we always use the unconstrained KA_1 Hamiltonian. We gradually convert the minority species C particles into A or B particles, and we therefore achieve the desired $\mathcal{H}_1 \to \mathcal{H}_0$ annealing. In practice, we run simulations with the Hamiltonian $\mathcal{H}_1$ and at each MC step, with probability $p_\omega = 1/50$, we pick up one C particle at random and we increase (resp. decrease) its type ω_i by a small increment $\mathrm{d}\omega$ if initially $\omega_i > 0.2$ (resp. $\omega_i \leq 0.2$). Otherwise, with probability $1 - p_\omega$, we perform translational or swap moves according to the procedure which is presented in Sec. 2. The increment $\mathrm{d}\omega$ is chosen so that after an average number of t_{MC} MC steps, the C particles are all converted into either A or B particles. We can then switch the Hamiltonian to $\mathcal{H}_0$, which is again equivalent to treating the final configuration as a genuine KA configuration.

In both methods, we transform the KA_1 configurations into the KA configurations at a constant temperature. More complicated annealing schemes could involve changing other parameters as well [444], but we remain at the least level of complexity for now. To compare the relative efficiency of all our schemes, we use a similar computational effort for all the configurations, which corresponds to a maximum simulation walltime of 2 weeks (about 10^8 Monte Carlo

steps). Even though the annealing methods may look artificial regarding other preparation protocols (like gradual cooling or aging), the only thing that matters is that a genuine amorphous KA glass is eventually obtained through the algorithm.

In order to implement our methods, we first prepare a series of equilibrium and glassy configurations of the KA_1 model for which equilibration is ensured down to $T = 0.36$. To produce glassy configurations at even lower temperatures, we quench several equilibrium configurations at $T = 0.36$ to a range of lower temperatures instantaneously, down to $T = 0.30$. Each of these glasses subsequently ages during $t_{\rm w} = 10^8$. The equilibrium (for $T \geq 0.36$) and aged (for $T < 0.36$) KA_1 configurations are then slowly annealed towards KA configurations by using methods I and II. We use annealing times $t_{\rm MC}$ from 9×10^5 to 7.5×10^7, to keep the longest simulations to at most 10^8 Monte Carlo steps and to ensure a fair comparison between all the protocols. To improve the statistics, we perform 30 independent simulations for each temperature.

As a result of the annealing methods, we obtain an ensemble of KA configurations at various temperatures, whose stability we can compare to direct simulations of the KA model over a similar preparation timescale. For the comparison with directly prepared KA configurations, we use either equilibrium configurations for $T \geq 0.415$ (lowest temperature for which the equilibration is ensured) while for $T < 0.415$, we quench equilibrium KA configurations at $T = 0.415$ down to the desired temperature instantaneously and we let them age for 10^8 Monte Carlo steps.

5. Enhanced stability of the annealed glassy Kob-Andersen configurations

In this section, we analyse the properties of the glassy KA configurations which are obtained thanks to methods I/II and we compare them to the standard aged KA glasses.

5.1 Inherent structure energies

Our first strategy to quantify the stability of the KA configurations is to quench them to $T = 0$ and to record the inherent structure (IS) energy per particle. In Fig. VII.2, we show the average energy of the IS per particle $e_{\rm IS}$ for (a) method I and (b) method II as a function of the inverse temperature for three different annealing rates, which correspond to $t_{\rm MC} = 9 \times 10^5$, 9×10^6 or 7.5×10^7 (and $\mathrm{d}\omega = 10^{-4}$, 10^{-5} or 1.2×10^{-6} for method II). For a given rate, we have checked the influence of the number of the C particles. We have found that for concentrations which are larger than $\delta = 0.5$ %, higher energy states are reached. This is why we only show results for $\delta = 0.5$ %. In addition, we clearly see that the lower annealing rates give lower IS energies at a fixed temperature.

As a matter of comparison, we show two additional data sets in Fig. VII.2. The first one represents the average IS energy of the KA_1 model for the set of initial conditions which have been described before. The second one corresponds to the IS energies which are directly obtained in the KA model, as explained in the previous section. The annealing data clearly lie above the data for the KA_1 model. This suggests that during the annealing procedure, some of the initial stability which is gained via the swap Monte Carlo algorithm is lost. However, the annealed states lie much below the IS energies of the KA configurations which are obtained by direct aging for a comparable numerical effort. Overall, this suggests that the annealing procedures I and II at small rates lead to more stable KA states with lower IS energies.

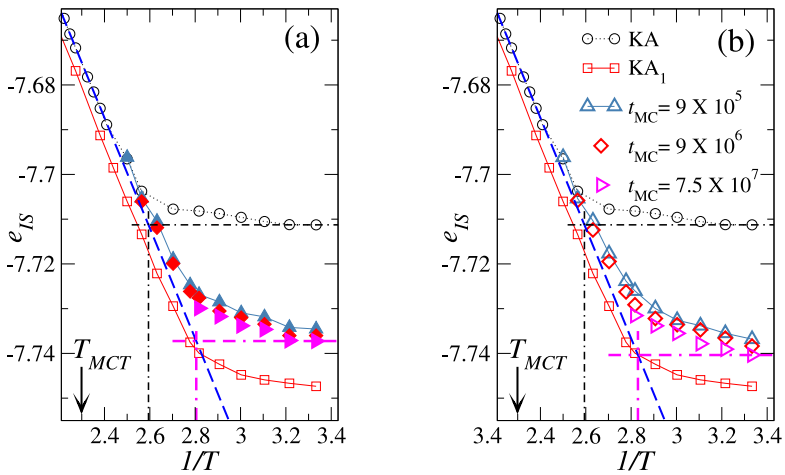

Fig. VII.2 | Average inherent structure energy per particle $e_{\rm IS}$ for the Kob-Andersen (KA) model, the extended Kob-Andersen ($\rm KA_1$) model along with the energies for KA configurations which are annealed by using (a) method I and (b) method II at different rates as a function of the inverse temperature T. The dashed blue line corresponds to $e_{\rm IS}^{\rm eq}(T) = a/T+b$ which fits the equilibrium data for the KA model (with a and b adjustable parameters). Fictive temperatures of aged or annealed KA configurations are determined via the intersection between the dashed-dotted horizontal lines and the straight line fit of the equilibrium data for the KA model. The legend is similar for the two panels and it is given in panel (b).

5.2 Fictive temperatures

To further quantify the stability of the annealed states, we estimate their fictive temperature $T_{\rm f}$. To this end, we fit the temperature evolution of the equilibrium IS energy of the KA model as $e_{\rm IS}^{\rm eq}(T) = a/T + b$ (with a, b fitting parameters), which is shown by the dashed blue line in Fig. VII.2 [188, 355].

We can then directly read-off the value of the fictive temperatures by the identification $e_{\rm IS} = e_{\rm IS}^{\rm eq}(T_{\rm f})$. This is shown with the black and purple dashed-dotted lines in Fig. VII.2. We find that in a direct KA simulation, the lowest IS energies correspond to $T_{\rm f} \simeq 0.386$, whereas the lowest IS energies for methods I and II give $T_{\rm f} \simeq 0.355$. The latter is within 18 % of the estimated experimental glass transition temperature for this system, namely, $T_{\rm g} \simeq 0.30$. These fictive temperature values confirm the enhanced stability of the annealed KA configurations.

5.3 Relaxation timescales

To determine the dynamic speedup which is gained by the above annealing protocols, we convert the obtained IS energies (or equivalently fictive temperatures) into an equilibrium relaxation timescale. To do this, we first need to extrapolate the equilibrium relaxation time $\tau_\alpha(T)$ of the KA model to lower temperatures, to infer relaxation timescales that are too large to be directly measured [404]. We use a parabolic fit of the temperature dependence of $\tau_\alpha(T)$ [188], namely, $\tau_{\alpha,\rm p}(T) = \tau_{0,\rm p} e^{J(1/T-1/T_{\rm p})^2}$ (with $\tau_{0,\rm p}$, J and $T_{\rm p}$ adjustable parameters). Consequently, for each value of the IS energy in Fig. VII.2, we determine the corresponding fictive temperature $T_{\rm f}$ (thanks to the method of the previous section), and we compute the extrapolated α-relaxation time $\tau_\alpha = \tau_{\alpha,\rm p}(T_{\rm f})$ from the parabolic fit. In Fig. VII.3, we display the parametric plot $\tau_\alpha(e_{IS})$ for IS energies at various temperatures, either by direct aging in the KA model or by annealing

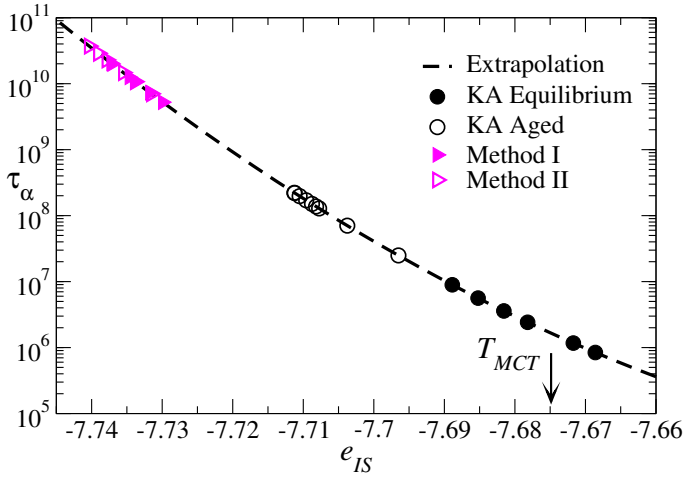

Fig. VII.3 | Parametric plot of the estimated relaxation time τ_α versus the average inherent structure (IS) energy per particle $e_{\rm IS}$. The dashed line combines the estimate of $\tau_\alpha(T)$ by using a parabolic fit with an affine dependence of $e_{\rm IS}$ with $1/T$. We can then report the IS energies which are obtained by direct aging in the Kob-Andersen (KA) model, or by annealing the extended Kob-Andersen (KA_1) model with methods I and II at the lowest annealing rate ($t_{\rm MC} = 7.5 \times 10^7$), and convert the IS energies into estimated relaxation times.

KA_1 configurations with the slowest annealing rate. The lowest IS energies which are obtained for the annealed configurations provide much larger estimates of the corresponding relaxation timescales, with a speedup factor of about 10^2 - 10^3. Therefore, we conclude that the speedup factor which is obtained for the KA_1 model with $\delta = 0.5$ % translates into a similar speedup for the original KA model, for an equivalent computational effort.

We recall that this very large speedup factor is obtained while keeping constant the total computational timescale for the preparation of the KA configurations. In other words, the speedup which is offered by the present algorithms is totally costless, unlike all the other methods which have been described in the introduction. We did not attempt to combine this approach to any other technique, such as parallel tempering, graphic cards, or longer simulation times. This would provide even more stable configurations, at the expense of increased computational time and, for some of these methods, a different scaling of the efficiency with system size.

5.4 Calorimetric measurements

We next perform calorimetric measurements, in order to study the stability of the generated glasses in the spirit of experiments on vapor-deposited ultrastable glasses [79, 445] (see Chap. I). The idea is to monitor the onset temperature T_0 at which the potential energy per particle $e(T)$ shows a brutal change of slope from its low-temperature glassy behaviour when the glass sample is heated at a constant rate. Note that this temperature is different from the onset temperature of glassy behaviour $T_{\rm on}$ which has been mentioned before, as T_0 is a non-equilibrium, rate-dependent quantity while $T_{\rm on}$ is measured at equilibrium.

In Fig. VII.4, we compare four different glasses at the same heating rate of 10^{-6}. The first one is obtained from an equilibrium configuration at $T = 1.36$ which is subsequently cooled at a constant rate of 10^{-7}. The second one represents a KA sample which is equilibrated at $T = 0.415$ and which is subsequently aged at $T = 0.36$ during $t_{\rm w} = 10^8$. Finally, the third and

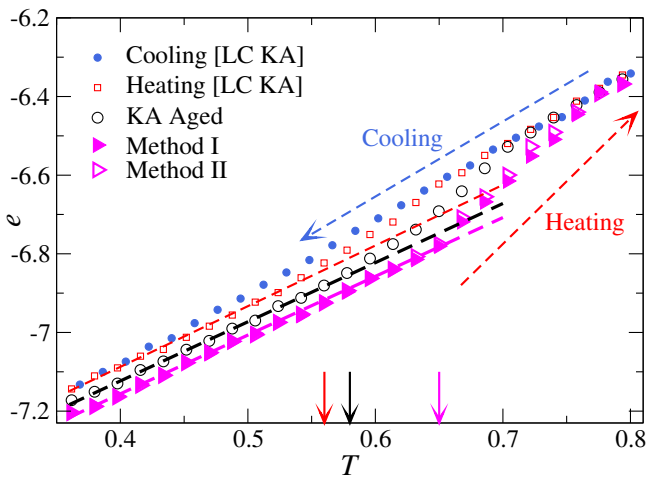

Fig. VII.4 | Potential energy per particle e of various glasses that are heated at a constant rate 10^{-6}: the liquid-cooled (LC KA) and the aged Kob-Andersen glasses show a relatively lower onset temperature T_0, as compared to the glasses which are generated by the two annealing methods I and II from the extended Kob-Andersen (KA_1) model. The onset temperatures T_0 are marked by arrows. For the liquid-cooled glass cooled at a constant rate 10^{-7}, the cooling curve is also displayed.

the fourth ones correspond to annealed samples which are prepared thanks to methods I/II at the same temperature $T = 0.36$ and the lowest annealing rate (with $t_{\rm MC} = 7.5 \times 10^7$). For the liquid-cooled glass, we estimate the onset temperature $T_0 = 0.56$. The well aged KA sample shows a moderately larger onset temperature, namely, $T_0 = 0.58$, while the two annealed glasses display a higher $T_0 = 0.65$, which again reflects the much larger kinetic stability which is reached by using our new annealing methods.

5.5 Rheology

We finally examine the stability of the annealed KA configurations against shear deformation. The stability of glassy configurations has recently been shown to qualitatively affect the nature of the yielding transition, with a sharp ductile-to-brittle transition with increasing the stability [85, 89, 446–448] (see also Chap. I). This transition is characterised by the emergence, in large-enough systems, of a macroscopic discontinuity in the stress-strain curves, which is accompanied by the formation of a macroscopic failure that takes the form of a system-spanning shear band. Despite scores of rheological studies of the KA model, this transition has not been observed in this model so far [448].

To study the rheology of stable KA configurations, we need to prepare larger configurations. We first produce very large KA/KA_1 samples by replicating 3^3 systems of $N = 1000/1005$ particles to obtain larger samples of $N = 27000/27135$ particles. These replicated systems are further aged for 10^6 MC steps at a temperature $T = 0.36$. The KA_1 samples are then annealed to KA configurations by using both methods I and II, with $t_{\rm MC} = 5 \times 10^4$, $p_\omega = 1/50$ and $d\omega = 5 \times 10^{-3}$. From these KA configurations, we perform a constant-volume athermal quasi-static shear protocol in the xz-plane with a strain increment $\Delta\gamma = 10^{-4}$ by using Lees-Edwards periodic boundary conditions. Each strain increment is followed by an energy minimisation by using the conjugate-gradient method.

In Fig. VII.5 (a), we present the stress-strain curves for three different samples for each

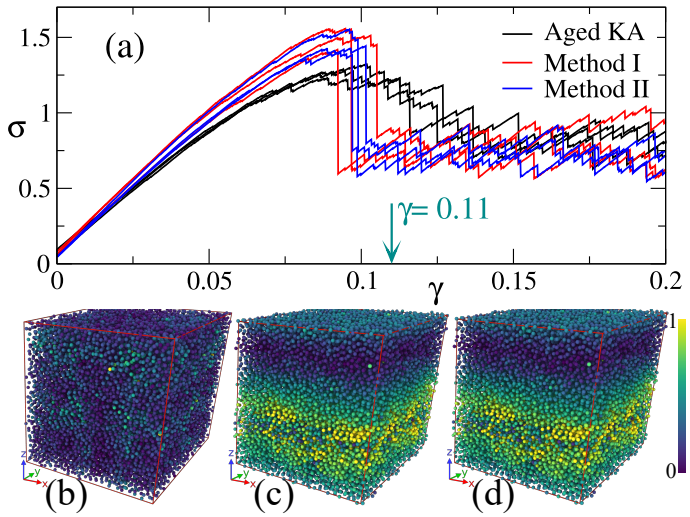

Fig. VII.5 | (a) Stress-strain curves for aged Kob-Andersen (KA) and annealed samples with methods I and II from the extended Kob-Andersen (KA_1) mixture. We report three independent loading curves for each case. The smooth stress overshoot of the aged KA glasses turns into a sharp stress drop for the stable annealed samples. Snapshots of the non-affine displacement between $\gamma = 0$ and $\gamma = 0.11$ for (b) a KA sample, (c) an annealed sample with method I and (d) an annealed sample with method II. The color of the particles encodes the absolute magnitude of their non-affine displacement in units of σ_{AA}.

of the three different preparation protocols (aged KA, methods I and II). In all cases, upon increasing the strain, we observe an elastic regime, a weakening due to small plastic events, a stress drop at the yielding transition, and finally a steady-state regime at large deformations. For the aged KA samples, the yielding transition after the stress overshoot is the result of several plastic events, which result in a modest stress drop and a relatively homogeneous strain field, see snapshot in Fig. VII.5 (b). The two annealing protocols provide KA samples with a much lower fictive temperature. This results in unique, sharp and macroscopic stress drops in the stress-strain curves of all the samples, which are associated with system-spanning shear bands that are formed within a single energy minimisation, and a highly heterogeneous plastic deformation field, see snapshots in Fig. VII.5 (c)-(d). The strong shear localisation at the yielding transition is correlated with the increased stability of the system [85, 89, 446–452], which further confirms that the proposed annealing methods produce highly stable KA glass configurations and complement other preparation protocols, like cycling shear at a finite temperature and a finite shear rate [437].

6. Conclusions

In this chapter, we have examined the possibility of using the speedup which is offered by the swap Monte Carlo algorithm in the extended Kob-Andersen (KA_1) model to access low energy states in the original Kob-Andersen (KA) model where swap moves are inefficient. An equilibrium method introduces a bottleneck with equilibration times that are as large as in the original KA model and therefore this method does not provide any significant speedup. We have however introduced two non-equilibrium annealing methods that produce very stable glassy configurations of the KA model at equivalent computational cost, with a speedup of about 2-3 orders of magnitude. The achieved glass states have a significantly lower inherent structure

energy than the one of the glasses which are obtained by direct aging in the KA model, they also have lower fictive temperatures, and calorimetric properties that indeed correspond to an enhanced kinetic stability.

The behaviour under shear of the glassy configurations which are obtained thanks to our new protocol is also consistent with an enhanced stability as compared to aged configurations. In particular, our results demonstrate that brittle yielding can now be analysed in computer simulations of metallic glasses as well as in experiments, and especially in the KA model which is one of the most studied models. More precisely, we have demonstrated that the behaviour of KA glasses can turn from ductile to brittle by tuning the degree of annealing of the configuration before shearing. This result was first shown in size-polydisperse soft sphere systems [85] (see Chap. I), and now in the KA model which mimics metallic glasses with a small number of components. As a consequence, this new possibility opens interesting research avenues to understand, for instance, the correlation between the deformation in the brittle regime and different structural indicators, such as the ones which were studied in Ref. [373], but also locally favoured structures which are well documented in the KA model [363, 453]. In addition, within the KA model, the influence of the attractive interaction forces between the particles on the yielding behaviour could be investigated, by a direct comparison with a purely repulsive model, namely, a model of particles which interact via the Weeks-Chandler-Andersen (WCA) potential [454]. These attractive forces are known to affect the equilibrium behaviour of glass-forming liquids quantitatively [455] and experiments suggest that the rheology of attractive glasses is also quantitatively different from their repulsive counterparts [456].

We have thus developed a computationally cheap method to produce KA glassy configurations that are very stable, although being out of equilibrium, and which belong to regions of the landscape that cannot be accessed by direct simulations of the KA model. Unlike parallel tempering, transition path sampling, or ghost insertion method, the methods which are proposed here scale very well with system size, and they are conceptually very simple. The present algorithm thus out-performs these more complicated algorithms. This strategy is generic, and it can be implemented in other glass-formers with a small number of components. In addition, combining the annealing methods with a parallel tempering scheme or graphic card simulations would allow for the production of even more stable systems. These would prove useful for further investigations of physical properties of highly stable metallic glasses by using the well studied KA model.

VIII | Conclusions and perspectives

Outline

1 The thermodynamics of constrained glass-forming liquids . . . 181
1.1 Conclusions . . . 181
1.2 Perspectives . . . 182
2 The dynamics of supercooled liquids close to their glass transition . . . 183
2.1 Conclusions . . . 183
2.2 Perspectives . . . 184
3 The properties of the non-equilibrium glass phase . . . 184
3.1 Conclusions . . . 184
3.2 Perspectives . . . 184

This work has addressed several questions regarding the concept of metastable state which is central in the mean-field theory of the glass transition and its finite-dimensional version, namely, the random first order transition theory. Supercooled liquids and glasses are believed to evolve in very rugged free energy landscapes with an exponentially large number of minima which control their low-temperature properties from the thermodynamic and the dynamic points of view. As a result, supercooled liquids and glasses share similarities with other current research topics, *e.g.*, jamming [457] or machine learning [458].

1. The thermodynamics of constrained glass-forming liquids

1.1 Conclusions

In Chap. I, we have first reviewed the concept of metastable states at the mean-field level. Their number sharply becomes exponential in the system size below the mode-coupling (dynamical) transition temperature, it decreases with decreasing then temperature and eventually gets sub-exponential in the system size at the Kauzmann transition temperature where a genuine thermodynamic phase transition to an ideal glass phase occurs. In Chap. II, we have then reviewed the Franz-Parisi construction in which one considers a supercooled liquid whose overlap or similarity with a quenched reference configuration of the same supercooled liquid is linearly coupled to a field ϵ. In this setting, the existence of metastable states directly translates into a thermodynamic first order phase transition line from a delocalised phase of low overlap to a localised phase of higher overlap which emerges from the random first order transition point at $T = T_{\mathrm{K}}$ and $\epsilon = 0$ and which ends in a critical point at a higher temperature $T = T_{\mathrm{c}}$ and a finite field $\epsilon = \epsilon_{\mathrm{c}}$ in the phase diagram (ϵ, T) of glass-forming liquids.

In Chap. III, we have performed computer simulations in $2d$ and $3d$ by using importance sampling techniques and reweighting schemes to study the fate of the phase diagram (ϵ, T).

Thanks to an original finite-size scaling analysis, we have revealed that the phase transition and the critical point which are predicted at the mean-field level survive the introduction of finite-dimensional fluctuations in $3d$ and are ruled by the physics of the random-field Ising model (RFIM). In $2d$ instead, any transition is smeared out in the thermodynamic limit because the disorder destroys long-range order. Overall, our study reveals that mean-field results are robust in finite dimensions despite the fact that metastable states are no longer well defined in physical dimensions. This also strengthens the connection between glass-forming liquids and the RFIM which has been reported in different contexts.

In Chap. IV, we have studied the role of the tolerance length in the definition of the overlap, *i.e.*, the small displacement of the particles which is authorised to consider that two liquid configurations are similar and that they belong to the same "metastable state". We have shown, within the hypernetted chain approximation of liquid-state theory, that the dynamical transition and the Kauzmann transition are independent of the tolerance length which defines the overlap but the whole phase diagram of constrained supercooled liquids for finite ϵ does depend on it, in particular the location of the first order transition between the delocalised and localised phases and the associated critical endpoint. The latter result has been confirmed thanks to computer simulations. From a practical point of view, a clever choice of the coarse-graining length could push the critical point and the first order phase transition higher in temperature to more easily sample them. From a more conceptual point of view, the variation of the phase diagram with the coarse-graining length gives information about the structure of the coarse-grained free energy landscape. In particular, the definition of "metastable states" in finite dimensions depend on the tolerance length in the definition of the overlap and so do the configurational entropy and the point-to-set length.

In Chap. V, we have studied the spatial fluctuations of the Franz-Parisi potential by biasing the local overlap between a configuration of a model glass-forming liquid and a reference configuration of the same liquid with a field. We have shown large spatial fluctuations of the field in order to localise a given patch of a liquid close to the reference configuration, namely, to force a large local overlap. The measure of these spatial fluctuations thus represents a quantitative assessment of the "self-induced" disorder in glass-forming liquids. We believe that the distribution of the localising field accounts for the spatial fluctuations of the local configurational entropy and also of the local surface free energy penalty due to the mismatch in density profiles between the constrained cavity when close to the reference configuration and the free exterior. We have finally paved the way towards a quantitative assessment of the correlation between these thermodynamic local fluctuations with structural indicators of the reference configurations and the dynamic propensity when measuring the bulk equilibrium or melting dynamics from the reference configurations.

1.2 Perspectives

We have presented the first finite-size scaling analysis of the constrained thermodynamics of supercooled liquids in the quenched Franz-Parisi setting. Repeating the complete analysis for different model glass-formers would be interesting as the existence and the location of the phase transitions in constrained supercooled liquids are expected to depend on the strength of the "self-induced" disorder. The comparison of different liquids could further confirm the relation between glass-forming liquids and the RFIM but also could allow for a quantitative comparison of the effective disorder in different glass-formers. This measure of "self-induced" disorder could

eventually be related to other properties of the equilibrium supercooled liquid or of the glass phase. For instance, more intrinsically-disordered liquids are expected to be strong with an Arrhenius-like increase of the α-relaxation time when decreasing the temperature while less intrinsically-disordered liquids may display a super-Arrhenius behaviour [207]. In addition, we have already reported in Chap. I that the yielding behaviour of glasses depends on the stability of the initial state which behaves as an effective source of disorder [85]. It could be interesting to compare models of different intrinsic disorder for a fixed kinetic stability.

Considering the pinning case could also be interesting: a fraction of particles c is pinned to its position in an equilibrium configuration at a temperature T_0 which can be equal to the temperature of the constrained liquid or which can be held fixed [246]. The pinning protocol shares similarities with the Franz-Parisi setting, in particular the existence of phase transitions in the plane (c, T) and of a critical point which should also be in the universality class of the RFIM [250]. However, the nature of the first order transition line is different: it is a random first order transition rather than a conventional first order transition. Our study could potentially inspire work in this direction too.

Our work has also raised questions regarding the measure of the configurational entropy or the point-to-set length in finite dimensional systems. From our comparison between mean-field calculations and computer simulations, we expect that both quantities depend on the observable which is used. In particular, when they are computed from the overlap and the Franz-Parisi potential, they may vary with the tolerance length which is involved in the definition of the overlap. Investigating this dependence in a systematic way would be valuable to reinforce our understanding of these quantities but also of the definition of the metastable states in finite dimensions.

Finally, we have been able to go beyond the bulk behaviour of supercooled liquids in order to assess the local fluctuations of the field to localise a given region of the liquid close to a reference configuration (hence to assess local fluctuations of the configurational entropy). In the random first order transition theory, the regions of higher configurational entropy (or localising field) are expected to be faster to relax. As a consequence, assessing the connections with the dynamics could be interesting through the iso-configurational ensemble construction. In particular, one could ask whether these local thermodynamic fluctuations are predictive of the dynamics and over which timescales and lengthscales. This is a direction of study that we are currently investigating.

2. The dynamics of supercooled liquids close to their glass transition

2.1 Conclusions

In Chap. VI, we have for the first time studied the dynamics of supercooled liquids close to their glass transition temperature by using computer simulations. We have been able to compute relaxation spectra which are similar to what is usually measured in experiments. We have shown that the excess wing which appears in the spectra close to the glass transition temperature directly originates from dynamic heterogeneities at very short times with respect to the bulk relaxation time. These heterogeneities are formed by rare and small clusters of mobile particles. The appearance time of these clusters is power law distributed on several decades and this directly accounts for the existence of excess wings in the relaxation spectra. The relaxation of the bulk then proceeds via mobility percolation in the entire system from these

initially relaxed regions. Mobility invasion relies on dynamic facilitation with mobile particles which undergo multiple relaxations but also which help their neighbours relaxing.

2.2 Perspectives

Our work has provided a clear description of how relaxation proceeds at low temperatures in bulk supercooled liquids. But the nature of the first events which populate the excess wing remains elusive. They are likely activated but their characterisation could be valuable. For instance, what is their activation (free) energy? Are they simple events which are performed by individual particles and which correspond to barrier crossings or are they already complicated and collective processes? We have shown that the first relaxation events should be increasingly predictible as the temperature is decreased, consequently are their locations related to static properties which are encoded in the structure of the initial configuration?

Another line of questions concerns the relative role of facilitation as the temperature is decreased. In particular, our results are in contradiction with the findings of Ref. [414] which indicate that the effect of facilitation decreases as the temperature is decreased while activation becomes more important. However, this difference might be explained by the fact that the analysis of Ref. [414] relies on very different tools from ours. The investigation of several models of glass-forming liquids at very low temperatures could help solving this paradox and clarifying the temperature evolution of the facilitation processes.

3. The properties of the non-equilibrium glass phase

3.1 Conclusions

In Chap. VII, we have studied an extended version of the Kob-Andersen model in which the swap algorithm is efficient to go deeper in the free energy landscape, contrary to the original model. We have shown that some equilibrium properties of the original model can be computed from simulations in the extended model, but this can only be achieved at temperatures at which we can directly simulate the Kob-Andersen model, hence decreasing the interest of the method. However, if we relax the requirement to remain at equilibrium, we have shown that annealing schemes allow for transforming stable equilibrium configurations of the extended Kob-Andersen model into glassy configurations of the original model which are more stable than configurations that are obtained by direct aging for equivalent simulation walltimes. The stability of the new generated Kob-Andersen glasses has been revealed by several indicators, including lower inherent structure energies and fictive temperatures, brittle yielding and higher non-equilibrium onset temperatures upon heating.

3.2 Perspectives

The Kob-Andersen model represents the archetypal computer model of metallic glasses with a few number of components. Computer simulations have been mostly unsuccessfull to produce stable metallic glasses so far or they require advanced simulation techniques, but we have filled this gap. In consequence, properties of stable metallic glasses are now reachable in the context of numerical studies, for instance brittle yielding or melting. In addition, as the Kob-Andersen is the most studied model of glasses, many different properties are largely documented in the litera-

ture. For instance, locally favoured structures have been reported, but also the non-perturbative effects of the attractive component of the interaction potential between the particles have been scrutinised. The non-equilibrium behaviour of stable glasses could thus be confronted with these properties.

IX Résumé en français

Outline

1 Motivations 186
2 Résumé des résultats obtenus 189
2.1 Thermodynamique contrainte des liquides surfondus 189
2.2 Dynamique d'équilibre des liquides proches de leur transition vitreuse 191
2.3 Propriétés hors d'équilibre des verres 192

1. Motivations

Dans le Chap. I et le Chap. II, nous présentons le contexte de recherche de la thèse. Nous commençons par la phénoménologie de la transition vitreuse puis nous introduisons la théorie champ moyen qui décrit le comportement vitreux des verres de spin avec désordre gelé et depuis plus récemment les liquides surfondus (refroidis sous leur point de fusion sans cristalliser) en dimension infinie. Finalement, nous décrivons les premiers éléments d'une théorie de la transition vitreuse en dimension finie s'appuyant sur des concepts champ moyen connue sous le nom de théorie RFOT (*Random First Order Transition*).

Nous commençons par rappeler les principaux éléments factuels associés à la transition vitreuse. Cette dernière concerne une grande variété de matériaux caractérisés par une croissance significative (au moins exponentielle) de leur temps de relaxation ou de leur viscosité lorsqu'un paramètre de contrôle (typiquement la température) est diminué sur un faible intervalle. Lorsque le temps de relaxation $\tau_\alpha(T)$ excède le temps typique de l'expérience ou de la simulation, le système tombe hors d'équilibre et forme un matériau solide amorphe, c'est-à-dire un verre. Il n'existe pas de définition rigoureuse de la température de transition vitreuse, car cette dernière dépend du protocole (par exemple la vitesse de refroidissement du liquide) et du temps typique d'observation. Seule une définition empirique et pragmatique peut être donnée, et on choisit usuellement $\tau_\alpha(T_\mathrm{g}) = 10^2$ s (sachant que le temps de relaxation à haute température est de l'ordre de 10^{-12} s à 10^{-10} s).

Non seulement le temps de relaxation augmente de façon significative, mais la dépendance temporelle des fonctions de corrélation à l'équilibre évolue à mesure que la température diminue. Ces dernières, notamment la fonction de corrélation des fluctuations de densité (fonction de diffusion intermédiaire), passent d'une relaxation exponentielle sur une échelle de temps de l'ordre d'1 ps à haute température à une relaxation en deux étapes à plus basse température avec une première relaxation partielle vers un plateau sur une échelle de temps de l'ordre de 1 ps suivie par une seconde relaxation structurelle α dont le temps de relaxation varie sur plusieurs ordres de grandeur à mesure que la température diminue. La seconde relaxation devient également de plus en plus étirée à mesure que la température diminue. Il en est de même des spectres de

relaxation qui sont reliés aux fonctions de corrélation par le théorème de fluctuation-dissipation à l'équilibre. À haute température, les spectres sont constitués d'un seul pic assimilable à une Lorentzienne à environ 100 GHz. À plus basse température, les spectres montrent deux pics, un à hautes fréquences correspondant à la première étape de la relaxation sur un temps microscopique, suivi par un second pic α qui se décale vers les basses fréquences à mesure que la température diminue et qui s'élargit. Proche de la température de transition vitreuse T_{g}, le spectre de relaxation s'enrichit encore davantage avec l'émergence d'un signal à fréquences intermédiaires entre le pic microscopique et le pic α (*excess wing*). Ce signal est dit en excès, car si on modélise le pic α par une fonction de relaxation usuelle (Cole-Davidson ou Havriliak-Negami), le signal à fréquences intermédiaires se situe au-dessus de la modélisation. Ce signal aux fréquences intermédiaires n'apparaît que proche de la transition vitreuse et n'a été observé que dans des expériences qui manquent d'une résolution à l'échelle élémentaire (nanoscopique pour les verres structuraux). Ainsi, il n'existe pas de consensus quant à son origine.

La transition vitreuse est une transition dynamique, mais il est légitime de se demander si elle n'est pas due à une transition thermodynamique sous-jacente, avec un temps de relaxation qui divergerait à une température inférieure à la température de transition vitreuse expérimentale dont la définition est purement empirique. Il y a 70 ans, Kauzmann a mis en évidence que l'entropie d'excès représentant la différence entre l'entropie du liquide surfondu et l'entropie du cristal à la même température variait de façon significative et s'annulait à une température en dessous de la température de Kauzmann $T_{\mathrm{K}} < T_{\mathrm{g}}$. Cette entropie d'excès a par la suite été interprétée comme étant une entropie de configuration quantifiant le logarithme du nombre d'« états amorphes » accessibles au liquide dont l'annulation suggère l'existence d'une transition de phase thermodynamique vers une phase où un seul état amorphe est possible, celui du verre idéal. Même si cette interprétation de l'entropie d'excès n'est pas rigoureuse, elle a motivé de nombreux travaux théoriques aboutissant à la théorie champ moyen de la transition vitreuse dans laquelle cette « crise entropique » se produit de façon exacte.

La théorie champ moyen des liquides surfondus décrit la thermodynamique et la dynamique des liquides en dimension infinie. L'étude de la dynamique montre que le temps de relaxation augmente en loi de puissance à basse température et diverge à une température finie dite de transition dynamique T_{d}. Sous cette température, l'espace des phases se scinde en un nombre exponentiellement grand de composantes appelées états métastables et dans lesquelles le liquide reste piégé indéfiniment. Pour $T < T_{\mathrm{d}}$, le temps de relaxation du liquide est véritablement infini, l'espace des phases ne peut pas être exploré de manière ergodique et les états métastables sont donc rigoureusement définis. Physiquement, ces états métastables correspondent à un ensemble de configurations caractérisées par un même profil de densité moyen. En champ moyen, les états métastables contrôlent la dynamique, la thermodynamique et les propriétés hors d'équilibre des verres. Le logarithme de leur nombre, l'entropie de configuration, peut être calculé exactement, et devient positif de façon discontinue à $T = T_{\mathrm{d}}$. Il décroît quand la température diminue jusqu'à atteindre une seconde température dite de transition statique et notée T_{K} en lien avec les travaux de Kauzmann où l'entropie de configuration s'annule. À cette température, il se produit en champ moyen une véritable transition de phase thermodynamique de la phase liquide à la phase vitreuse idéale. Un bon paramètre d'ordre de cette transition est le degré de similarité ou le recouvrement (*overlap*) entre configurations d'équilibre du liquide, qui saute de façon discontinue à $T = T_{\mathrm{K}}$ d'une valeur proche de 0 à une valeur proche de 1 quand la température diminue.

Une fois le bon paramètre d'ordre obtenu, il est naturel de définir l'énergie libre de Landau associée. Cette dernière décrit le coût en énergie libre des fluctuations du recouvrement entre

le liquide et une configuration de référence de même liquide, moyenné sur les configurations de référence. Dans le contexte de la transition vitreuse, cette fonction de grande déviation s'appelle le potentiel de Franz-Parisi (FP). Toute la thermodynamique des systèmes vitreux est alors élégamment décrite par l'évolution en température du potentiel de FP. À $T = T_{\mathrm{K}}$, celui-ci a deux minima de même profondeur correspondant à des valeurs de recouvrement entre configurations d'équilibre proches de 0 et de 1. Le premier décrit le liquide et le second le verre idéal. Quand $T > T_{\mathrm{K}}$, le minimum de haut recouvrement devient métastable vis-à-vis du liquide. La différence entre les deux minima pour $T_{\mathrm{d}} < T < T_{\mathrm{K}}$ représente le coût en énergie libre pour localiser le liquide proche de la configuration de référence et est donc égal par définition à l'entropie de configuration multipliée par la température. Le minimum secondaire du potentiel de FP disparaît en un point col pour $T = T_{\mathrm{d}}$ reflétant la disparition des états métastables. Néanmoins, le potentiel de FP reste non convexe jusqu'à une température $T_{\mathrm{c}} > T_{\mathrm{d}}$. Finalement, por $T > T_{\mathrm{c}}$, le potentiel de FP est convexe avec un seul minimum correspondant à un faible recouvrement entre configurations d'équilibre et décrivant la phase liquide.

La théorie champ moyen de la transition vitreuse donne un cadre complet pour décrire les liquides surfondus. En particulier, elle indique que la transition vitreuse dynamique s'accompagne d'une signature thermodynamique, mais qui est inaccessible à l'équilibre. Cependant, en couplant le recouvrement entre configurations d'équilibre à un champ ϵ, il est possible de stabiliser la phase de haut recouvrement (vitreuse) à haute température. Les résultats de calculs champ moyen montrent qu'une ligne de transition de phase du premier ordre dans le plan (ϵ, T) émerge de la transition vitreuse thermodynamique en champ nul ($\epsilon = 0$ et $T = T_{\mathrm{K}}$) et s'achève par un point critique à plus haute température et à champ non nul $(\epsilon_{\mathrm{c}}, T_{\mathrm{c}})$. Cette température critique correspond à la température à laquelle le potentiel de FP devient strictement convexe. En particulier, elle se trouve dans un régime accessible à l'équilibre ($T_{\mathrm{c}} > T_{\mathrm{d}}$) et est la conséquence directe d'une crise entropique à plus basse température. Ainsi, la thermodynamique contrainte de liquides surfondus rend observable en champ moyen les modifications non triviales du paysage d'énergie libre.

La description théorique des liquides en dimension finie est nettement plus ardue que la théorie champ moyen. Cela vient du fait que les états métastables ne sont plus définis de façon rigoureuse dans ce cas : leur durée de vie est finie et leur extension spatiale est limitée. Cela implique notamment que la transition dynamique est évitée en dimension finie et l'ergodicité est restaurée probablement jusqu'à $T = T_{\mathrm{K}}$ grâce à des processus activés qui permettent au liquide de s'échapper des états métastables. Le liquide pour $T < T_{\mathrm{d}}$ est alors schématiquement décrit par une mosaïque de sous-éléments de taille typique égale à la longueur de corrélation statique (*point-to-set*), chaque portion du liquide étant dans un état métastable bien défini. Cette longueur statique $\xi_{\mathrm{PTS}}(T)$ décrit l'extension spatiale de l'ordre amorphe dans un liquide. Elle croît à mesure que la température diminue et diverge à $T = T_{\mathrm{K}}$ si la crise entropique survit à l'introduction des fluctuations inhérentes à la dimension finie. Par conséquent, l'entropie de configuration n'est rigoureusement définie que pour des échelles de longueur inférieures à $\xi_{\mathrm{PTS}}(T)$ et fluctue probablement spatialement dans le liquide. Certaines régions sont alors caractérisées par une entropie de configuration locale plus faible et sont donc susceptibles d'avoir un recouvrement plus grand avec la configuration de référence. Ainsi, ces fluctuations spatiales de l'entropie de configuration représentent un champ aléatoire couplé au recouvrement. La description de la thermodynamique des systèmes vitreux en dimension finie nécessite donc de bâtir une théorie des champs du recouvrement entre configurations d'équilibre et qui tient compte du désordre auto-induit. Des premières avancées ont été faites dans cette direction ces dernières

années. Notamment, il est attendu de nombreuses analogies avec le modèle d'Ising en champ aléatoire (RFIM).

Le travail de cette thèse participe à l'effort de définir et d'étudier les propriétés des états métastables, ainsi que de déterminer leur pertinence dans la thermodynamique et la dynamique des liquides surfondus en dimension finie par le prisme des simulations numériques et des calculs analytiques. La description des résultats obtenus est l'objectif de la section suivante.

2. Résumé des résultats obtenus

2.1 Thermodynamique contrainte des liquides surfondus

Dans le Chap. II, nous étendons les études analytiques du p-spin sphérique, un modèle champ moyen de verre de spin dont la thermodynamique et la dynamique sont similaires à celles des liquides structuraux, avec l'existence d'une transition dynamique et d'une transition statique associées à des non-convexités du potentiel de FP. Nous considérons la possibilité d'échantillonner les configurations de référence à une température T_0 fixée et différente de la température T du liquide pour calculer le recouvrement du liquide. Nous montrons une diversité de diagrammes des phases (ϵ, T) quand le recouvrement entre le liquide à température T et la configuration de référence préparée à T_0 est couplé linéairement à un champ ϵ, et nous mettons notamment en évidence que la ligne de transition de phase du premier ordre et le point critique pour $\epsilon > 0$ se produisent à plus haute température quand T_0 est choisie entre T_d et T_K. Ces résultats seront utilisés dans le chapitre suivant afin de faciliter l'étude de la thermodynamique contrainte des liquides surfondus en dimension finie par les simulations numériques. Par la suite, nous allons au-delà du comportement moyen et nous étudions analytiquement les fluctuations du potentiel de FP. Nous montrons que pour toute valeur de T_0, le point critique contraint $(\epsilon_\mathrm{c}(T_0), T_\mathrm{c}(T_0))$ est décrit par la classe d'universalité du RFIM et nous montrons comment le désordre effectif varie avec la température de la configuration de référence.

Dans le Chap. III, nous étudions le diagramme des phases (ϵ, T) d'un liquide surfondu modèle en dimensions $d = 2, 3$ par le biais de simulations numériques. Les résultats sont en majorité obtenus pour une température T_0 prise suffisamment basse afin de déplacer tous les éléments potentiellement intéressants du diagramme des phases à plus haute température. Ces configurations sont facilement générées à l'aide de l'algorithme du *swap* récemment développé et qui permet d'équilibrer des liquides surfondus à des températures inférieures à la température de transition vitreuse expérimentale (correspondant à une augmentation du temps de relaxation microscopique de 12 ordres de grandeur par rapport à sa valeur à plus haute température où le comportement vitreux commence à se manifester). Les résultats pour le cas $T = T_0$ sont également présentés en annexe. Pour explorer le diagramme des phases (ϵ, T) et pour calculer avec précision les propriétés thermodynamiques des liquides surfondus contraints, nous utilisons des techniques d'échantillonnage avancées, à savoir l'échantillonnage parapluie (*umbrella sampling*) et la repondération d'histogrammes (*histogram reweighting*), qui permettent de déterminer les propriétés d'équilibre pour $\epsilon > 0$ par le biais de simulations à $\epsilon = 0$ seulement. Ceci est motivé par le fait que proche d'un point critique et d'une transition de phase du premier ordre, l'exploration ergodique de l'espace des phases n'est plus garantie. Nous constatons que les modèles à la fois en dimensions $d = 2$ et $d = 3$ présentent la phénoménologie de la théorie champ moyen dans des systèmes raisonnablement petits. En particulier, le potentiel de FP est non convexe tandis que les isothermes du recouvrement en fonction du champ ϵ et les distributions

de probabilité du paramètre d'ordre deviennent bimodales à basses températures. Tout ceci est cohérent avec l'existence d'une transition de phase du premier ordre se terminant à un point critique à plus haute température. Cependant, en dimensions finies, d'importants effets de taille finie sont attendus à proximité d'une transition de phase du premier ordre ou d'un point critique. Ainsi, nous effectuons une analyse en taille finie (*finite size scaling*) approfondie et nous étudions l'évolution de la distribution de probabilité du paramètre d'ordre et des susceptibilités en fonction de la taille du système. Cela nous permet de démontrer l'existence dans la limite thermodynamique d'une ligne de transition du premier ordre en champ aléatoire pour ϵ fini terminée par un point critique dans la classe d'universalité du RFIM en $3d$. À l'inverse, le système à $2d$ ne présente aucune transition dans la limite thermodynamique, en cohérence avec la classe d'universalité du RFIM dont la dimension critique inférieure est égale à 2. Le comportement critique RFIM est confirmé par l'étude de la dynamique du liquide contraint en $3d$ au voisinage de son point critique, qui est compatible avec une relaxation activée. Les résultats de ce chapitre montrent donc que la théorie champ moyen et sa généralisation par la théorie statistique des champs est remarquablement robuste en dimensions finies. En particulier, ils impliquent l'absence d'une transition de Kauzmann en $2d$ à température finie alors qu'à $3d$ ils ne contredisent pas l'existence d'une transition vitreuse thermodynamique à $T_{\mathrm{K}} > 0$. Ce travail a donné lieu à une publication [283] et sera l'objet d'une seconde publication prochainement.

Dans le Chap. IV, nous étudions précisément la définition du paramètre d'ordre de la transition vitreuse thermodynamique, à savoir la similarité ou recouvrement entre configurations d'équilibre. Dans les liquides, la définition du recouvrement implique une longueur de tolérance a, généralement une fraction du diamètre moyen des particules, associée au déplacement typique autorisé pour considérer que deux configurations doivent appartenir au même « état métastable ». Dans le Chap. III, les simulations numériques ont été menées en choisissant une longueur de tolérance « raisonnable » mais aucune étude n'a été menée pour étudier systématiquement son influence sur les fluctuations du recouvrement entre configurations d'équilibre, et notamment sur les transitions statique à T_{K} et dynamique à T_{d} ainsi que sur le diagramme des phases (ϵ, T). Nous montrons d'une part que les positions des transitions dynamique et statique sont indépendantes de a. D'autre part, nous mettons en évidence que la ligne de transition de phase du premier ordre pour $\epsilon > 0$ et le point critique à $(\epsilon_{\mathrm{c}}, T_{\mathrm{c}})$ dépendent de façon non triviale de a. Les résultats de ce chapitre sont en premier lieu obtenus en champ moyen en utilisant une approximation de la théorie des liquides, à savoir l'approximation de la chaîne hyper-réticulée (HNC). Ils sont par la suite confirmés par des simulations numériques analogues à celles du Chap. III. Ils suggèrent notamment qu'une plage de valeurs de a inférieure à celle usuellement considérée maximise la température T_{c}. D'un point de vue pratique, cela permettra d'accélérer les simulations numériques pour l'étude de la thermodynamique contrainte des liquides dans le futur. D'un point de vue plus conceptuel, cela suggère l'existence d'une échelle de température supérieure à T_{d} sous laquelle l'effet des états métastables commence à se manifester. Ce travail a donné lieu à une publication [295].

Dans le Chap. V, nous allons au-delà de la thermodynamique moyenne des liquides surfondus et nous étudions les fluctuations du potentiel de FP décrites par la physique du RFIM. Cependant, contrairement à ce dernier, le désordre des liquides est auto-induit et plus difficile à quantifier. L'objectif de ce chapitre est de présenter une méthode numérique pour répondre à cet objectif. Elle consiste à coupler linéairement à un champ extérieur le recouvrement dans une cavité sphérique entre le liquide et une configuration de référence. Nous mettons en évidence d'importantes fluctuations spatiales du champ nécessaire pour localiser le liquide proche

de la configuration de référence localement, ou encore pour imposer un haut recouvrement local. Nous analysons les propriétés spatiales et statistiques de ces fluctuations et en particulier nous montrons qu'elles sont correctement décrites par une distribution de Gumbel généralisée caractérisée par une queue exponentielle à grandes valeurs de champ. Nous rationalisons cette dernière en expliquant que le champ nécessaire à la localisation représente non seulement le coût entropique pour être localisé proche de la configuration de référence, mais tient également compte d'un coût supplémentaire en énergie libre en raison de la différence des profils de densité entre l'intérieur de la cavité lorsqu'elle est confinée proche de la configuration de référence et son extérieur (analogue à un terme de tension de surface). Ce chapitre décrit un travail en cours et nous expliquons les investigations que nous sommes actuellement en train de mener. D'une part, nous proposons d'évaluer la corrélation entre ces fluctuations thermodynamiques locales et des propriétés structurelles locales de la configuration de référence. Dans un second temps, nous suggérons d'essayer de relier les fluctuations thermodynamiques que nous mesurons aux hétérogénéités dynamiques rencontrées universellement dans la dynamique d'équilibre des liquides surfondus en étudiant la dynamique de relaxation des fluctuations de densité à partir des configurations de référence.

2.2 Dynamique d'équilibre des liquides proches de leur transition vitreuse

Dans le Chap. VI, nous étudions la dynamique d'équilibre de liquides surfondus proches de leur transition vitreuse expérimentale sur une échelle de temps de 10 décades. Pour cela, nous combinons l'algorithme récent du *swap* à de longues simulations de dynamique moléculaire parallélisées. Alors que les fonctions de corrélation moyennes temporelles montrent un plateau qui s'étend sur plusieurs décades, le calcul des spectres de relaxation et du déplacement carré moyen dans les structures inhérentes donnent accès à des résultats plus riches. Les deux procédures révèlent des mouvements non triviaux à l'échelle de quelques particules et à des échelles de temps très courtes par rapport à la relaxation α. Ces processus donnent lieu à une loi de puissance dans les spectres de relaxation, analogue à ce qui est observé expérimentalement (*excess wing*). Son observation dans les simulations de liquides surfondus à l'équilibre est une nouveauté majeure. De manière équivalente, dans le déplacement carré moyen des structures inhérentes, les processus à temps courts contribuent à un comportement sous-diffusif. Nous révélons donc de fortes hétérogénéités dynamiques à temps très courts par rapport à τ_α qui nous permettent de distinguer les particules mobiles et immobiles. Une étude détaillée de la distribution spatio-temporelle de ces hétérogénéités révèle que la relaxation structurelle commence dans des régions diluées et localisées dont le temps d'apparition est distribué en loi de puissance. Cette dernière permet d'expliquer directement l'émergence d'une loi de puissance dans les spectres de relaxation ou d'un comportement sous-diffusif dans le déplacement carré moyen des structures inhérentes. Nous analysons par la suite la dynamique à des temps plus longs et nous montrons que la relaxation structurelle procède par facilitation dynamique à partir de ces régions initialement plus mobiles. En particulier, nous constatons que le mouvement des particules est persistant et corrélé entre voisins et que l'effet de la facilitation dynamique devient plus fort à mesure que l'on s'approche de la transition vitreuse. Globalement, nos résultats montrent que la relaxation structurelle dans les liquides surfondus peut maintenant être analysée dans des simulations numériques pour des températures proches de T_g. Ils révèlent principalement que la dynamique dans les liquides surfondus est le résultat de deux ingrédients minimaux, à savoir (i) des événements rares et distribués dans le temps, se produisant vraisemblablement par activation thermique et (ii) croissance des domaines qui ont relaxé par facilitation dynamique.

Le projet décrit dans ce chapitre a été mené en collaboration avec C. Scalliet et a donné lieu à une publication [378]. Il serait intéressant dans l'avenir de caractériser en détail les événements à temps courts responsables de la loi de puissance dans les spectres de relaxation (énergie d'activation, géométrie, nombre de particules impliquées, etc.).

2.3 Propriétés hors d'équilibre des verres

Dans le Chap. VII, nous étudions une généralisation récente du modèle binaire de Kob-Andersen (KA) qui est l'un des systèmes vitreux les plus employés en simulations. L'algorithme du *swap* qui a été mis à profit dans différents chapitres de cette thèse est très efficace pour les modèles dont les particules présentent une large dispersion de tailles et permet de générer des configurations d'équilibre à des températures plus basses que ce qu'il est possible de faire par des simulations numériques classiques. Il consiste à échanger aléatoirement le diamètre de deux particules choisies aléatoirement en respectant le principe de balance détaillée. Cependant, l'algorithme du *swap* est inefficace pour le modèle original de KA, car la différence de tailles entre les deux types de particules composant le mélange binaire est trop grande. Dans les généralisations du modèle de KA, l'algorithme du *swap* peut au contraire être très efficace. Ces généralisations reposent sur l'introduction d'une faible fraction de particules dont les tailles sont intermédiaires entre les tailles des deux types de particules du mélange binaire. Dans ce chapitre, nous montrons que ces modèles peuvent être utilisés pour améliorer considérablement la stabilité de configurations vitreuses du modèle original de KA. Nous développons avec succès plusieurs stratégies numériques à la fois à l'équilibre et hors d'équilibre pour atteindre cet objectif. Nous menons ensuite plusieurs mesures pour montrer que les configurations générées sont bien plus stables que les verres obtenus directement à partir du modèle de KA par vieillissement. Nous étudions notamment le comportement des verres sous chauffage et sous cisaillement, et nous mettons en évidence une transition ductile-fragile lorsque la stabilité des verres augmente. Nos résultats ouvrent ainsi la voie à de futures études de verres stables utilisant le modèle de KA. Ce projet a été mené en collaboration avec A. D. S. Parmar et a donné lieu à une publication [428].

References

[1] P. G. Debenedetti and F. H. Stillinger, "Supercooled liquids and the glass transition", Nature **410**, 259 (2001).

[2] K. Chang, "The nature of glass remains anything but clear", The New York Times **182** (2008).

[3] P. W. Anderson, "Through the Glass Lightly", Science **267**, 1615 (1995).

[4] B. Diu, B. Roulet, C. Guthmann, and D. Lederer, *Éléments de physique statistique* (Hermann, 1989).

[5] N. W. Ashcroft and N. D. Mermin, *Solid state physics*, HRW international editions (Holt, Rinehart and Winston, 1976).

[6] C. Kittel, *Introduction to solid state physics* (John Wiley & Sons, 1976).

[7] J. C. Dyre, "Simple liquids' quasiuniversality and the hard-sphere paradigm", Journal of Physics: Condensed Matter **28**, 323001 (2016).

[8] J. Sethna, *Statistical mechanics: entropy, order parameters, and complexity* (Oxford University Press, 2021).

[9] H. B. Callen, *Thermodynamics and an Introduction to Thermostatistics* (American Association of Physics Teachers, 1998).

[10] A. Cavagna, "Supercooled liquids for pedestrians", Physics Reports **476**, 51 (2009).

[11] L. Berthier and G. Biroli, "Theoretical perspective on the glass transition and amorphous materials", Reviews of Modern Physics **83**, 587 (2011).

[12] P. G. Wolynes and V. Lubchenko, *Structural glasses and supercooled liquids: Theory, experiment, and applications* (John Wiley & Sons, 2012).

[13] G. Biroli and J. P. Garrahan, "Perspective: The glass transition", The Journal of chemical physics **138**, 12A301 (2013).

[14] F. Arceri, F. P. Landes, L. Berthier, and G. Biroli, "Glasses and aging: a statistical mechanics perspective", arXiv preprint arXiv:2006.09725 (2020).

[15] C. A. Angell, "Formation of glasses from liquids and biopolymers", Science **267**, 1924 (1995).

[16] M. D. Ediger, C. A. Angell, and S. R. Nagel, "Supercooled liquids and glasses", The Journal of Physical Chemistry **100**, 13200 (1996).

[17] G. L. Hunter and E. R. Weeks, "The physics of the colloidal glass transition", Reports on Progress in Physics **75**, 066501 (2012).

[18] P. N. Pusey and W. Van Megen, "Phase behaviour of concentrated suspensions of nearly hard colloidal spheres", Nature **320**, 340 (1986).

[19] O. Dauchot, G. Marty, and G. Biroli, "Dynamical heterogeneity close to the jamming transition in a sheared granular material", Physical Review Letters **95**, 265701 (2005).

[20] A. S. Keys, A. R. Abate, S. C. Glotzer, and D. J. Durian, "Measurement of growing dynamical length scales and prediction of the jamming transition in a granular material", Nature Physics **3**, 260 (2007).

[21] O. Dauchot, D. J. Durian, and M. van Hecke, "Dynamical heterogeneities in grains and foams", in *Dynamical Heterogeneities in Glasses, Colloids, and Granular Media* (Oxford University Press, 2011), pp. 203–228.

[22] L. Berthier, E. Flenner, and G. Szamel, "Glassy dynamics in dense systems of active particles", The Journal of Chemical Physics **150**, 200901 (2019).

[23] L. Berthier and J. Kurchan, "Lectures on non-equilibrium active systems", arXiv preprint arXiv:1906.04039 (2019).

[24] H. Frauenfelder, S. G. Sligar, and P. G. Wolynes, "The energy landscapes and motions of proteins", Science **254**, 1598 (1991).

[25] T. V. Stirbat, S. Tlili, T. Houver, J.-P. Rieu, *et al.*, "Multicellular aggregates: a model system for tissue rheology", The European Physical Journal E **36**, 1 (2013).

[26] L. Berthier and M. D. Ediger, "Facets of glass physics", Physics Today **69**, 40 (2016).

[27] F. Sausset, G. Biroli, and J. Kurchan, "Do solids flow?", Journal of Statistical Physics **140**, 718 (2010).

[28] L. Berthier and G. Biroli, "Glasses and Aging, A Statistical Mechanics Perspective on", in *Encyclopedia of Complexity and Systems Science*, edited by R. A. Meyers (Springer, 2009), pp. 4209–4240.

[29] J. Wuttke, W. Petry, and S. Pouget, "Structural relaxation in viscous glycerol: Coherent neutron scattering", The Journal of Chemical Physics **105**, 5177 (1996).

[30] J.-P. Hansen and I. R. McDonald, *Theory of simple liquids* (Elsevier, 1990).

[31] L. Berthier, D. Chandler, and J. P. Garrahan, "Length scale for the onset of Fickian diffusion in supercooled liquids", EPL (Europhysics Letters) **69**, 320 (2004).

[32] M. Fuchs, "The Kohlrausch law as a limit solution to mode coupling equations", Journal of Non-Crystalline Solids **172**, 241 (1994).

[33] M. P. Eastwood, T. Chitra, J. M. Jumper, K. Palmo, *et al.*, "Rotational relaxation in ortho-terphenyl: using atomistic simulations to bridge theory and experiment", The Journal of Physical Chemistry B **117**, 12898 (2013).

[34] L. Pardo, P. Lunkenheimer, and A. Loidl, "Dielectric spectroscopy in benzophenone: The β relaxation and its relation to the mode-coupling Cole-Cole peak", Physical Review E **76**, 030502 (2007).

[35] P. Lunkenheimer, A. Pimenov, B. Schiener, R. Böhmer, and A. Loidl, "High-frequency dielectric spectroscopy on glycerol", EPL (Europhysics Letters) **33**, 611 (1996).

[36] P. Lunkenheimer, M. Köhler, S. Kastner, and A. Loidl, "Dielectric Spectroscopy of Glassy Dynamics", in *Structural Glasses and Supercooled Liquids* (John Wiley & Sons, 2012), pp. 115–149.

[37] R. Kubo, "The fluctuation-dissipation theorem", Reports on Progress in Physics **29**, 255 (1966).

[38] B. Jakobsen, K. Niss, and N. B. Olsen, "Dielectric and shear mechanical alpha and beta relaxations in seven glass-forming liquids", The Journal of Chemical Physics **123**, 234511 (2005).

[39] R. Vallée, W. Paul, and K. Binder, "Single molecule probing of the glass transition phenomenon: Simulations of several types of probes", The Journal of Chemical Physics **127**, 154903 (2007).

[40] D. W. Davidson and R. H. Cole, "Dielectric relaxation in glycerol, propylene glycol, and n-propanol", The Journal of Chemical Physics **19**, 1484 (1951).

[41] S. Havriliak and S. Negami, "A complex plane analysis of α-dispersions in some polymer systems", Journal of Polymer Science Part C: Polymer Symposia **14**, 99 (1966).

[42] G. Williams and D. C. Watts, "Non-symmetrical dielectric relaxation behaviour arising from a simple empirical decay function", Transactions of the Faraday society **66**, 80 (1970).

[43] N. Menon and S. R. Nagel, "Evidence for a divergent susceptibility at the glass transition", Physical Review Letters **74**, 1230 (1995).

[44] K. S. Cole and R. H. Cole, "Dispersion and absorption in dielectrics I. Alternating current characteristics", The Journal of Chemical Physics **9**, 341 (1941).

[45] K. Ngai and M. Paluch, "Classification of secondary relaxation in glass-formers based on dynamic properties", The Journal of Chemical Physics **120**, 857 (2004).

[46] P. K. Dixon, L. Wu, S. R. Nagel, B. D. Williams, and J. P. Carini, "Scaling in the relaxation of supercooled liquids", Physical Review Letters **65**, 1108 (1990).

[47] R. L. Leheny and S. R. Nagel, "Dielectric susceptibility studies of the high-frequency shape of the primary relaxation in supercooled liquids", Journal of Non-Crystalline Solids **235**, 278 (1998).

[48] N. Menon, K. P. O'Brien, P. K. Dixon, L. Wu, *et al.*, "Wide-frequency dielectric susceptibility measurements in glycerol", Journal of Non-Crystalline Solids **141**, 61 (1992).

[49] C. Gainaru, R. Kahlau, E. A. Rössler, and R. Böhmer, "Evolution of excess wing and β-process in simple glass formers", The Journal of Chemical Physics **131**, 184510 (2009).

[50] M. D. Ediger, "Spatially heterogeneous dynamics in supercooled liquids", Annual Review of Physical Chemistry **51**, 99 (2000).

[51] L. Berthier, G. Biroli, J.-P. Bouchaud, and R. L. Jack, "Overview of different characterizations of dynamic heterogeneity", in *Dynamical Heterogeneities in Glasses, Colloids, and Granular Media* (Oxford University Press, 2011), pp. 68–109.

[52] L. Berthier, "Self-induced heterogeneity in deeply supercooled liquids", arXiv preprint arXiv:2010.12244 (2020).

[53] R. Richert, "Homogeneous dispersion of dielectric responses in a simple glass", Journal of Non-Crystalline Solids **172**, 209 (1994).

[54] A. Ninarello, L. Berthier, and D. Coslovich, "Models and algorithms for the next generation of glass transition studies", Physical Review X **7**, 021039 (2017).

[55] L. Berthier, E. Flenner, C. J. Fullerton, C. Scalliet, and M. Singh, "Efficient swap algorithms for molecular dynamics simulations of equilibrium supercooled liquids", Journal of Statistical Mechanics: Theory and Experiment **2019**, 064004 (2019).

[56] N. Lačević, F. W. Starr, T. Schrøder, V. Novikov, and S. Glotzer, "Growing correlation length on cooling below the onset of caging in a simulated glass-forming liquid", Physical Review E **66**, 030101 (2002).

[57] L. Berthier, G. Biroli, J.-P. Bouchaud, L. Cipelletti, *et al.*, "Direct experimental evidence of a growing length scale accompanying the glass transition", Science **310**, 1797 (2005).

[58] L. Berthier, "Revisiting the slow dynamics of a silica melt using Monte Carlo simulations", Physical Review E **76**, 011507 (2007).

[59] E. Flenner, M. Zhang, and G. Szamel, "Analysis of a growing dynamic length scale in a glass-forming binary hard-sphere mixture", Physical Review E **83**, 051501 (2011).

[60] S. Whitelam, L. Berthier, and J. P. Garrahan, "Dynamic criticality in glass-forming liquids", Physical Review Letters **92**, 185705 (2004).

[61] L. Berthier, "Time and length scales in supercooled liquids", Physical Review E **69**, 020201 (2004).

[62] A. Widmer-Cooper and P. Harrowell, "Predicting the long-time dynamic heterogeneity in a supercooled liquid on the basis of short-time heterogeneities", Physical Review Letters **96**, 185701 (2006).

[63] A. Widmer-Cooper, P. Harrowell, and H. Fynewever, "How reproducible are dynamic heterogeneities in a supercooled liquid?", Physical Review Letters **93**, 135701 (2004).

[64] M. P. Allen and D. J. Tildesley, *Computer simulation of liquids* (Oxford University Press, 2017).

[65] A. Widmer-Cooper, H. Perry, P. Harrowell, and D. R. Reichman, "Irreversible reorganization in a supercooled liquid originates from localized soft modes", Nature Physics **4**, 711 (2008).

[66] A. Widmer-Cooper, H. Perry, P. Harrowell, and D. R. Reichman, "Localized soft modes and the supercooled liquid's irreversible passage through its configuration space", The Journal of Chemical Physics **131**, 194508 (2009).

[67] R. L. Jack, A. J. Dunleavy, and C. P. Royall, "Information-theoretic measurements of coupling between structure and dynamics in glass formers", Physical Review Letters **113**, 095703 (2014).

[68] J. Paret, R. L. Jack, and D. Coslovich, "Assessing the structural heterogeneity of supercooled liquids through community inference", The Journal of Chemical Physics **152**, 144502 (2020).

[69] H. Tong and H. Tanaka, "Revealing hidden structural order controlling both fast and slow glassy dynamics in supercooled liquids", Physical Review X **8**, 011041 (2018).

[70] H. Tong and H. Tanaka, "Structural order as a genuine control parameter of dynamics in simple glass formers", Nature Communications **10**, 1 (2019).

[71] G. M. Hocky, D. Coslovich, A. Ikeda, and D. R. Reichman, "Correlation of local order with particle mobility in supercooled liquids is highly system dependent", Physical Review Letters **113**, 157801 (2014).

[72] L. Berthier and R. L. Jack, "Structure and dynamics of glass formers: Predictability at large length scales", Physical Review E **76**, 041509 (2007).

[73] W. Kob and J.-L. Barrat, "Aging effects in a Lennard-Jones glass", Physical Review Letters **78**, 4581 (1997).

[74] J.-P. Bouchaud, L. F. Cugliandolo, J. Kurchan, and M. Mézard, "Out of equilibrium dynamics in spin-glasses and other glassy systems", in *Spin glasses and random fields* (World Scientific, 1998), pp. 161–223.

[75] L. F. Cugliandolo, J. Kurchan, and L. Peliti, "Energy flow, partial equilibration, and effective temperatures in systems with slow dynamics", Physical Review E **55**, 3898 (1997).

[76] F. Corberi, L. F. Cugliandolo, and H. Yoshino, "Growing length scales in aging systems", in *Dynamical Heterogeneities in Glasses, Colloids, and Granular Media* (Oxford University Press, 2011), pp. 407–450.

[77] W. Kob, J.-L. Barrat, F. Sciortino, and P. Tartaglia, "Aging in a simple glass former", Journal of Physics: Condensed Matter **12**, 6385 (2000).

[78] C. Scalliet and L. Berthier, "Rejuvenation and memory effects in a structural glass", Physical Review Letters **122**, 255502 (2019).

[79] S. F. Swallen, K. L. Kearns, M. K. Mapes, Y. S. Kim, *et al.*, "Organic glasses with exceptional thermodynamic and kinetic stability", Science **315**, 353 (2007).

[80] K. L. Kearns, S. F. Swallen, M. D. Ediger, T. Wu, *et al.*, "Hiking down the energy landscape: Progress toward the Kauzmann temperature via vapor deposition", The Journal of Physical Chemistry B **112**, 4934 (2008).

[81] M. Ahrenberg, Y. Chua, K. Whitaker, H. Huth, *et al.*, "In situ investigation of vapor-deposited glasses of toluene and ethylbenzene via alternating current chip-nanocalorimetry", The Journal of Chemical Physics **138**, 024501 (2013).

[82] H. Yu, M. Tylinski, A. Guiseppi-Elie, M. Ediger, and R. Richert, "Suppression of β relaxation in vapor-deposited ultrastable glasses", Physical Review Letters **115**, 185501 (2015).

[83] L. Berthier, P. Charbonneau, E. Flenner, and F. Zamponi, "Origin of ultrastability in vapor-deposited glasses", Physical Review Letters **119**, 188002 (2017).

[84] L. Zhu, C. Brian, S. Swallen, P. Straus, *et al.*, "Surface self-diffusion of an organic glass", Physical Review Letters **106**, 256103 (2011).

[85] M. Ozawa, L. Berthier, G. Biroli, A. Rosso, and G. Tarjus, "Random critical point separates brittle and ductile yielding transitions in amorphous materials", Proceedings of the National Academy of Sciences **115**, 6656 (2018).

[86] M. D. Ediger, "Perspective: Highly stable vapor-deposited glasses", The Journal of Chemical Physics **147**, 210901 (2017).

[87] D. Bonn, M. M. Denn, L. Berthier, T. Divoux, and S. Manneville, "Yield stress materials in soft condensed matter", Reviews of Modern Physics **89**, 035005 (2017).

[88] A. Nicolas, E. E. Ferrero, K. Martens, and J.-L. Barrat, "Deformation and flow of amorphous solids: Insights from elastoplastic models", Reviews of Modern Physics **90**, 045006 (2018).

[89] M. Ozawa, L. Berthier, G. Biroli, and G. Tarjus, "Role of fluctuations in the yielding transition of two-dimensional glasses", Physical Review Research **2**, 023203 (2020).

[90] M. Ozawa, L. Berthier, G. Biroli, and G. Tarjus, "Rare events and disorder control the brittle yielding of amorphous solids", arXiv preprint arXiv:2102.05846 (2021).

[91] T. Nattermann, "Theory of the random field Ising model", in *Spin glasses and random fields* (World Scientific, 1998), pp. 277–298.

[92] I. Balog, G. Tarjus, and M. Tissier, "Criticality of the random field Ising model in and out of equilibrium: A nonperturbative functional renormalization group description", Physical Review B **97**, 094204 (2018).

[93] S. K. Nandi, G. Biroli, and G. Tarjus, "Spinodals with disorder: From avalanches in random magnets to glassy dynamics", Physical Review Letters **116**, 145701 (2016).

[94] D. Spasojević, S. Janićević, and M. Knežević, "Numerical evidence for critical behavior of the two-dimensional nonequilibrium zero-temperature random field Ising model", Physical Review Letters **106**, 175701 (2011).

[95] K. Dahmen and J. P. Sethna, "Hysteresis, avalanches, and disorder-induced critical scaling: A renormalization-group approach", Physical Review B **53**, 14872 (1996).

[96] S. Singh, M. D. Ediger, and J. J. De Pablo, "Ultrastable glasses from in silico vapour deposition", Nature Materials **12**, 139 (2013).

[97] K. L. Kearns, S. F. Swallen, M. Ediger, T. Wu, and L. Yu, "Influence of substrate temperature on the stability of glasses prepared by vapor deposition", The Journal of Chemical Physics **127**, 154702 (2007).

[98] G. Tarjus, S. A. Kivelson, Z. Nussinov, and P. Viot, "The frustration-based approach of supercooled liquids and the glass transition: a review and critical assessment", Journal of Physics: Condensed Matter **17**, R1143 (2005).

[99] R. L. Jack and L. Berthier, "The melting of stable glasses is governed by nucleation-and-growth dynamics", The Journal of Chemical Physics **144**, 244506 (2016).

[100] C. J. Fullerton and L. Berthier, "Density controls the kinetic stability of ultrastable glasses", EPL (Europhysics Letters) **119**, 36003 (2017).

[101] K. L. Kearns, M. Ediger, H. Huth, and C. Schick, "One micrometer length scale controls kinetic stability of low-energy glasses", The Journal of Physical Chemistry Letters **1**, 388 (2010).

[102] E. Flenner, L. Berthier, P. Charbonneau, and C. J. Fullerton, "Front-Mediated Melting of Isotropic Ultrastable Glasses", Physical Review Letters **123**, 175501 (2019).

[103] M. Avrami, "Kinetics of phase change. I General theory", The Journal of Chemical Physics **7**, 1103 (1939).

[104] L. Wang, L. Berthier, E. Flenner, P. Guan, and G. Szamel, "Sound attenuation in stable glasses", Soft Matter **15**, 7018 (2019).

[105] D. Khomenko, C. Scalliet, L. Berthier, D. R. Reichman, and F. Zamponi, "Depletion of two-level systems in ultrastable computer-generated glasses", Physical Review Letters **124**, 225901 (2020).

[106] T. Pérez-Castañeda, C. Rodríguez-Tinoco, J. Rodríguez-Viejo, and M. A. Ramos, "Suppression of tunneling two-level systems in ultrastable glasses of indomethacin", Proceedings of the National Academy of Sciences **111**, 11275 (2014).

[107] R. Zeller and R. Pohl, "Thermal conductivity and specific heat of noncrystalline solids", Physical Review B **4**, 2029 (1971).

[108] P. W. Anderson, B. Halperin, and C. M. Varma, "Anomalous low-temperature thermal properties of glasses and spin glasses", Philosophical Magazine **25**, 1 (1972).

[109] L. Wang, A. Ninarello, P. Guan, L. Berthier, *et al.*, "Low-frequency vibrational modes of stable glasses", Nature Communications **10**, 1 (2019).

[110] W. Kauzmann, "The nature of the glassy state and the behavior of liquids at low temperatures.", Chemical Reviews **43**, 219 (1948).

[111] F. P. Landes, G. Biroli, O. Dauchot, A. J. Liu, and D. R. Reichman, "Attractive versus truncated repulsive supercooled liquids: The dynamics is encoded in the pair correlation function", Physical Review E **101**, 010602 (2020).

[112] D. Chandler and J. P. Garrahan, "Dynamics on the way to forming glass: Bubbles in space-time", Annual Review of Physical Chemistry **61**, 191 (2010).

[113] M. Wyart and M. E. Cates, "Does a growing static length scale control the glass transition?", Physical Review Letters **119**, 195501 (2017).

[114] L. Berthier, M. Ozawa, and C. Scalliet, "Configurational entropy of glass-forming liquids", The Journal of Chemical Physics **150**, 160902 (2019).

[115] N. Goldenfeld, *Lectures on phase transitions and the renormalization group* (CRC Press, 2018).

[116] T. Kirkpatrick and P. Wolynes, "Connections between some kinetic and equilibrium theories of the glass transition", Physical Review A **35**, 3072 (1987).

[117] T. R. Kirkpatrick and D. Thirumalai, "p-spin-interaction spin-glass models: Connections with the structural glass problem", Physical Review B **36**, 5388 (1987).

[118] T. R. Kirkpatrick and D. Thirumalai, "Dynamics of the structural glass transition and the p-spin—interaction spin-glass model", Physical Review Letters **58**, 2091 (1987).

[119] T. Kirkpatrick and P. Wolynes, "Stable and metastable states in mean-field Potts and structural glasses", Physical Review B **36**, 8552 (1987).

[120] T. R. Kirkpatrick and D. Thirumalai, "Comparison between dynamical theories and metastable states in regular and glassy mean-field spin models with underlying first-order-like phase transitions", Physical Review A **37**, 4439 (1988).

[121] R. W. Hall and P. G. Wolynes, "The aperiodic crystal picture and free energy barriers in glasses", The Journal of Chemical Physics **86**, 2943 (1987).

[122] T. R. Kirkpatrick, D. Thirumalai, and P. G. Wolynes, "Scaling concepts for the dynamics of viscous liquids near an ideal glassy state", Physical Review A **40**, 1045 (1989).

[123] T. Kirkpatrick and D. Thirumalai, "Random solutions from a regular density functional hamiltonian: a static and dynamical theory for the structural glass transition", Journal of Physics A: Mathematical and General **22**, L149 (1989).

[124] J.-P. Bouchaud and G. Biroli, "On the Adam-Gibbs-Kirkpatrick-Thirumalai-Wolynes scenario for the viscosity increase in glasses", The Journal of Chemical Physics **121**, 7347 (2004).

[125] P. Charbonneau, J. Kurchan, G. Parisi, P. Urbani, and F. Zamponi, "Glass and jamming transitions: From exact results to finite-dimensional descriptions", Annual Review of Condensed Matter Physics **8**, 265 (2017).

[126] G. Parisi, P. Urbani, and F. Zamponi, *Theory of simple glasses: exact solutions in infinite dimensions* (Cambridge University Press, 2020).

[127] G. Szamel, "Simple theory for the dynamics of mean-field-like models of glass-forming fluids", Physical Review Letters **119**, 155502 (2017).

[128] P. C. Martin, E. Siggia, and H. Rose, "Statistical dynamics of classical systems", Physical Review A **8**, 423 (1973).

[129] H.-K. Janssen, "On a Lagrangean for classical field dynamics and renormalization group calculations of dynamical critical properties", Zeitschrift für Physik B Condensed Matter **23**, 377 (1976).

[130] T. Maimbourg, J. Kurchan, and F. Zamponi, "Solution of the dynamics of liquids in the large-dimensional limit", Physical Review Letters **116**, 015902 (2016).

[131] T. Castellani and A. Cavagna, "Spin-glass theory for pedestrians", Journal of Statistical Mechanics: Theory and Experiment **2005**, P05012 (2005).

[132] H. Frisch, N. Rivier, and D. Wyler, "Classical hard-sphere fluid in infinitely many dimensions", Physical Review Letters **54**, 2061 (1985).

[133] H. Frisch and J. Percus, "High dimensionality as an organizing device for classical fluids", Physical Review E **60**, 2942 (1999).

[134] A. Georges and J. S. Yedidia, "How to expand around mean-field theory using high-temperature expansions", Journal of Physics A: Mathematical and General **24**, 2173 (1991).

[135] A. Manacorda, G. Schehr, and F. Zamponi, "Numerical solution of the dynamical mean field theory of infinite-dimensional equilibrium liquids", The Journal of Chemical Physics **152**, 164506 (2020).

[136] W. Götze, *Complex dynamics of glass-forming liquids: A mode-coupling theory* (OUP Oxford, 2008).

[137] D. R. Reichman and P. Charbonneau, "Mode-coupling theory", Journal of Statistical Mechanics: Theory and Experiment **2005**, P05013 (2005).

[138] L. Janssen, "Mode-coupling theory of the glass transition: A primer", Frontiers in Physics **6**, 97 (2018).

[139] M. Mézard and G. Parisi, "Thermodynamics of glasses: A first principles computation", Journal of Physics: Condensed Matter **11**, A157 (1999).

[140] M. Mézard, "How to compute the thermodynamics of a glass using a cloned liquid", Physica A: Statistical Mechanics and its Applications **265**, 352 (1999).

[141] W. Appel and E. Kowalski, *Mathematics for Physics and Physicists* (Princeton University Press, 2007).

[142] Y. Singh, J. Stoessel, and P. Wolynes, "Hard-sphere glass and the density-functional theory of aperiodic crystals", Physical Review Letters **54**, 1059 (1985).

[143] T. Kirkpatrick and D. Thirumalai, "Random first-order phase transition theory of the structural glass transition", in *Structural Glasses and Supercooled Liquids* (John Wiley & Sons, 2012), pp. 223–236.

[144] G. Biroli and J.-P. Bouchaud, "The random first-order transition theory of glasses: a critical assessment", in *Structural Glasses and Supercooled Liquids: Theory, Experiment, and Applications* (John Wiley & Sons, 2012), pp. 31–113.

[145] A. Crisanti and H.-J. Sommers, "Thouless-Anderson-Palmer approach to the spherical p-spin spin glass model", Journal de Physique I **5**, 805 (1995).

[146] H. Rieger, "The number of solutions of the Thouless-Anderson-Palmer equations for p-spin-interaction spin glasses", Physical Review B **46**, 14655 (1992).

[147] A. J. Bray and M. A. Moore, "Metastable states in spin glasses", Journal of Physics C: Solid State Physics **13**, L469 (1980).

[148] S. Franz and G. Parisi, "Recipes for metastable states in spin glasses", Journal de Physique I **5**, 1401 (1995).

[149] F. H. Stillinger and T. A. Weber, "Hidden structure in liquids", Physical Review A **25**, 978 (1982).

[150] R. Monasson, "Structural glass transition and the entropy of the metastable states", Physical Review Letters **75**, 2847 (1995).

[151] G. Parisi and F. Zamponi, "Mean-field theory of hard sphere glasses and jamming", Reviews of Modern Physics **82**, 789 (2010).

[152] J. Kurchan, G. Parisi, and M. A. Virasoro, "Barriers and metastable states as saddle points in the replica approach", Journal de Physique I **3**, 1819 (1993).

[153] S. Franz and G. Parisi, "Phase diagram of coupled glassy systems: A mean-field study", Physical Review Letters **79**, 2486 (1997).

[154] M. Cardenas, S. Franz, and G. Parisi, "Constrained Boltzmann-Gibbs measures and effective potential for glasses in hypernetted chain approximation and numerical simulations", The Journal of Chemical Physics **110**, 1726 (1999).

[155] M. Cardenas, S. Franz, and G. Parisi, "Glass transition and effective potential in the hypernetted chain approximation", Journal of Physics A: Mathematical and General **31**, L163 (1998).

[156] S. Franz and G. Parisi, "Effective potential in glassy systems: theory and simulations", Physica A: Statistical Mechanics and its Applications **261**, 317 (1998).

[157] J. Kurchan, G. Parisi, P. Urbani, and F. Zamponi, "Exact theory of dense amorphous hard spheres in high dimension. II. The high density regime and the Gardner transition", The Journal of Physical Chemistry B **117**, 12979 (2013).

[158] G. Biroli and P. Urbani, "Liu-Nagel phase diagrams in infinite dimension", SciPost Physics **4**, 020 (2018).

[159] C. Scalliet, L. Berthier, and F. Zamponi, "Marginally stable phases in mean-field structural glasses", Physical Review E **99**, 012107 (2019).

[160] F. Krzakala and L. Zdeborová, "Following Gibbs states adiabatically—The energy landscape of mean-field glassy systems", EPL (Europhysics Letters) **90**, 66002 (2010).

[161] C. Rainone, P. Urbani, H. Yoshino, and F. Zamponi, "Following the evolution of hard sphere glasses in infinite dimensions under external perturbations: Compression and shear strain", Physical Review Letters **114**, 015701 (2015).

[162] P. Charbonneau, J. Kurchan, G. Parisi, P. Urbani, and F. Zamponi, "Fractal free energy landscapes in structural glasses", Nature Communications **5**, 1 (2014).

[163] S. Franz, G. Parisi, P. Urbani, and F. Zamponi, "Universal spectrum of normal modes in low-temperature glasses", Proceedings of the National Academy of Sciences **112**, 14539 (2015).

[164] M. Ozawa, G. Parisi, and L. Berthier, "Configurational entropy of polydisperse supercooled liquids", The Journal of Chemical Physics **149**, 154501 (2018).

[165] S. Franz, "Metastable states, relaxation times and free-energy barriers in finite-dimensional glassy systems", EPL (Europhysics Letters) **73**, 492 (2006).

[166] S. Franz, "First steps of a nucleation theory in disordered systems", Journal of Statistical Mechanics: Theory and Experiment **2005**, P04001 (2005).

[167] M. Dzero, J. Schmalian, and P. G. Wolynes, "Activated events in glasses: The structure of entropic droplets", Physical Review B **72**, 100201 (2005).

[168] M. Dzero, J. Schmalian, and P. G. Wolynes, "Replica theory for fluctuations of the activation barriers in glassy systems", Physical Review B **80**, 024204 (2009).

[169] J. S. Langer, "Statistical theory of the decay of metastable states", Annals of Physics **54**, 258 (1969).

[170] M. C. Angelini and G. Biroli, "Real space Migdal–Kadanoff renormalisation of glassy systems: recent results and a critical assessment", Journal of Statistical Physics **167**, 476 (2017).

[171] C. Cammarota, G. Biroli, M. Tarzia, and G. Tarjus, "Renormalization group analysis of the random first-order transition", Physical Review Letters **106**, 115705 (2011).

[172] S. Franz and G. Semerjian, "Analytical approaches to time-and length scales in models of glasses", in *Dynamical Heterogeneities in Glasses, Colloids, and Granular Media* (Oxford University Press, 2011), pp. 407–450.

[173] G. Biroli and C. Cammarota, "Fluctuations and shape of cooperative rearranging regions in glass-forming liquids", Physical Review X **7**, 011011 (2017).

[174] X. Xia and P. G. Wolynes, "Fragilities of liquids predicted from the random first order transition theory of glasses", Proceedings of the National Academy of Sciences **97**, 2990 (2000).

[175] G. Biroli, J.-P. Bouchaud, A. Cavagna, T. S. Grigera, and P. Verrocchio, "Thermodynamic signature of growing amorphous order in glass-forming liquids", Nature Physics **4**, 771 (2008).

[176] M. Mezard and G. Parisi, "Glasses and replicas", in *Structural Glasses and Supercooled Liquids: Theory, Experiment, and Applications* (John Wiley & Sons, 2012), pp. 151–191.

[177] K. H. Nagamanasa, S. Gokhale, A. Sood, and R. Ganapathy, "Direct measurements of growing amorphous order and non-monotonic dynamic correlations in a colloidal glass-former", Nature Physics **11**, 403 (2015).

[178] G. M. Hocky, T. E. Markland, and D. R. Reichman, "Growing point-to-set length scale correlates with growing relaxation times in model supercooled liquids", Physical Review Letters **108**, 225506 (2012).

[179] S. Yaida, L. Berthier, P. Charbonneau, and G. Tarjus, "Point-to-set lengths, local structure, and glassiness", Physical Review E **94**, 032605 (2016).

[180] L. Berthier, P. Charbonneau, and S. Yaida, "Efficient measurement of point-to-set correlations and overlap fluctuations in glass-forming liquids", The Journal of Chemical Physics **144**, 024501 (2016).

[181] L. Berthier, P. Charbonneau, D. Coslovich, A. Ninarello, *et al.*, "Configurational entropy measurements in extremely supercooled liquids that break the glass ceiling", Proceedings of the National Academy of Sciences **114**, 11356 (2017).

[182] L. Berthier, P. Charbonneau, A. Ninarello, M. Ozawa, and S. Yaida, "Zero-temperature glass transition in two dimensions", Nature Communications **10**, 1 (2019).

[183] A. Heuer, "Exploring the potential energy landscape of glass-forming systems: from inherent structures via metabasins to macroscopic transport", Journal of Physics: Condensed Matter **20**, 373101 (2008).

[184] M. Baity-Jesi, G. Biroli, and D. R. Reichman, "Revisiting the Concept of Activation in Supercooled Liquids", arXiv preprint arXiv:2103.07211 (2021).

[185] A. Cavagna, T. S. Grigera, and P. Verrocchio, "Mosaic multistate scenario versus one-state description of supercooled liquids", Physical Review Letters **98**, 187801 (2007).

[186] D. S. Fisher and D. A. Huse, "Equilibrium behavior of the spin-glass ordered phase", Physical Review B **38**, 386 (1988).

[187] A. Montanari and G. Semerjian, "Rigorous inequalities between length and time scales in glassy systems", Journal of Statistical Physics **125**, 23 (2006).

[188] Y. S. Elmatad, D. Chandler, and J. P. Garrahan, "Corresponding states of structural glass formers. II", Journal of Physical Chemistry B **114**, 17113 (2010).

[189] G. Adam and J. H. Gibbs, "On the temperature dependence of cooperative relaxation properties in glass-forming liquids", The Journal of Chemical Physics **43**, 139 (1965).

[190] M. Ozawa, C. Scalliet, A. Ninarello, and L. Berthier, "Does the Adam-Gibbs relation hold in simulated supercooled liquids?", The Journal of Chemical Physics **151**, 084504 (2019).

[191] C. Toninelli, M. Wyart, L. Berthier, G. Biroli, and J.-P. Bouchaud, "Dynamical susceptibility of glass formers: Contrasting the predictions of theoretical scenarios", Physical Review E **71**, 041505 (2005).

[192] P. Charbonneau and G. Tarjus, "Decorrelation of the static and dynamic length scales in hard-sphere glass formers", Physical Review E **87**, 042305 (2013).

[193] J. D. Stevenson, J. Schmalian, and P. G. Wolynes, "The shapes of cooperatively rearranging regions in glass-forming liquids", Nature Physics **2**, 268 (2006).

[194] C. Monthus and J.-P. Bouchaud, "Models of traps and glass phenomenology", Journal of Physics A: Mathematical and General **29**, 3847 (1996).

[195] X. Xia and P. G. Wolynes, "Microscopic theory of heterogeneity and nonexponential relaxations in supercooled liquids", Physical Review Letters **86**, 5526 (2001).

[196] G. Biroli, C. Cammarota, G. Tarjus, and M. Tarzia, "Random-field Ising-like effective theory of the glass transition. I. Mean-field models", Physical Review B **98**, 174205 (2018).

[197] G. Biroli, C. Cammarota, G. Tarjus, and M. Tarzia, "Random field Ising-like effective theory of the glass transition. II. Finite-dimensional models", Physical Review B **98**, 174206 (2018).

[198] J. P. Garrahan and D. Chandler, "Geometrical explanation and scaling of dynamical heterogeneities in glass forming systems", Physical Review Letters **89**, 035704 (2002).

[199] J. P. Garrahan and D. Chandler, "Coarse-grained microscopic model of glass formers", Proceedings of the National Academy of Sciences **100**, 9710 (2003).

[200] S. H. Glarum, "Dielectric relaxation of isoamyl bromide", The Journal of Chemical Physics **33**, 639 (1960).

[201] F. Ritort and P. Sollich, "Glassy dynamics of kinetically constrained models", Advances in Physics **52**, 219 (2003).

[202] J. P. Garrahan, P. Sollich, and T. Cristina, "Kinetically constrained models", in *Dynamical Heterogeneities in Glasses, Colloids, and Granular Media* (Oxford University Press, 2011), pp. 341–369.

[203] S. M. Bhattacharyya, B. Bagchi, and P. G. Wolynes, "Facilitation, complexity growth, mode coupling, and activated dynamics in supercooled liquids", Proceedings of the National Academy of Sciences **105**, 16077 (2008).

[204] S. M. Bhattacharyya, B. Bagchi, and P. G. Wolynes, "Bridging the gap between the mode coupling and the random first order transition theories of structural relaxation in liquids", Physical Review E **72**, 031509 (2005).

[205] P. G. Wolynes, "Spatiotemporal structures in aging and rejuvenating glasses", Proceedings of the National Academy of Sciences **106**, 1353 (2009).

[206] C. Rulquin, P. Urbani, G. Biroli, G. Tarjus, and M. Tarzia, "Nonperturbative fluctuations and metastability in a simple model: from observables to microscopic theory and back", Journal of Statistical Mechanics: Theory and Experiment **2016**, 023209 (2016).

[207] H. Tanaka, "Two-order-parameter description of liquids. I. A general model of glass transition covering its strong to fragile limit", The Journal of Chemical Physics **111**, 3163 (1999).

[208] S. Franz, G. Parisi, F. Ricci-Tersenghi, and T. Rizzo, "Field theory of fluctuations in glasses", The European Physical Journal E **34**, 1 (2011).

[209] L. Berthier and R. L. Jack, "Evidence for a disordered critical point in a glass-forming liquid", Physical Review Letters **114**, 205701 (2015).

[210] M. Mézard, G. Parisi, and M. Virasoro, *Spin glass theory and beyond: An Introduction to the Replica Method and Its Applications* (World Scientific, 1987).

[211] R. Vink, K. Binder, and H. Löwen, "Colloid–polymer mixtures in random porous media: finite size scaling and connected versus disconnected susceptibilities", Journal of Physics: Condensed Matter **20**, 404222 (2008).

[212] R. Vink, T. Fischer, and K. Binder, "Finite-size scaling in Ising-like systems with quenched random fields: Evidence of hyperscaling violation", Physical Review E **82**, 051134 (2010).

[213] L. Berthier, "Overlap fluctuations in glass-forming liquids", Physical Review E **88**, 022313 (2013).

[214] L. D. Landau and E. M. Lifshitz, *Course of theoretical physics* (Elsevier, 2013).

[215] A. Campa, T. Dauxois, and S. Ruffo, "Statistical mechanics and dynamics of solvable models with long-range interactions", Physics Reports **480**, 57 (2009).

[216] A. Campa, T. Dauxois, D. Fanelli, and S. Ruffo, *Physics of long-range interacting systems* (Oxford University Press, 2014).

[217] D. Ruelle, *Statistical mechanics: Rigorous results* (World Scientific, 1999).

[218] G. Biroli, C. Cammarota, G. Tarjus, and M. Tarzia, "Random-field-like criticality in glass-forming liquids", Physical Review Letters **112**, 175701 (2014).

[219] D. Sherrington and S. Kirkpatrick, "Solvable model of a spin-glass", Physical Review Letters **35**, 1792 (1975).

[220] J. R. de Almeida and D. J. Thouless, "Stability of the Sherrington-Kirkpatrick solution of a spin glass model", Journal of Physics A: Mathematical and General **11**, 983 (1978).

[221] A. Crisanti and H.-J. Sommers, "The sphericalp-spin interaction spin glass model: the statics", Zeitschrift für Physik B Condensed Matter **87**, 341 (1992).

[222] A. Barrat, S. Franz, and G. Parisi, "Temperature evolution and bifurcations of metastable states in mean-field spin glasses, with connections with structural glasses", Journal of Physics A: Mathematical and General **30**, 5593 (1997).

[223] P. Sollich, "The de Almeida–Thouless instability: when a 'simple'description of complexity is not enough", Journal of Physics A: Mathematical and Theoretical **49**, 421005 (2016).

[224] M. Mézard, G. Parisi, N. Sourlas, G. Toulouse, and M. Virasoro, "Replica symmetry breaking and the nature of the spin glass phase", Journal de Physique **45**, 843 (1984).

[225] G. Parisi, "The order parameter for spin glasses: a function on the interval 0-1", Journal of Physics A: Mathematical and General **13**, 1101 (1980).

[226] G. Parisi, "A sequence of approximated solutions to the SK model for spin glasses", Journal of Physics A: Mathematical and General **13**, L115 (1980).

[227] G. Parisi, "Infinite number of order parameters for spin-glasses", Physical Review Letters **43**, 1754 (1979).

[228] P. Charbonneau, J. Kurchan, G. Parisi, P. Urbani, and F. Zamponi, "Exact theory of dense amorphous hard spheres in high dimension. III. The full replica symmetry breaking solution", Journal of Statistical Mechanics: Theory and Experiment **2014**, P10009 (2014).

[229] S. Kirkpatrick and D. Sherrington, "Infinite-ranged models of spin-glasses", Physical Review B **17**, 4384 (1978).

[230] B. Derrida, "Random-energy model: Limit of a family of disordered models", Physical Review Letters **45**, 79 (1980).

[231] D. J. Gross and M. Mézard, "The simplest spin glass", Nuclear Physics B **240**, 431 (1984).

[232] A. Crisanti, H. Horner, and H.-J. Sommers, "The sphericalp-spin interaction spin-glass model: the dynamics", Zeitschrift für Physik B Condensed Matter **92**, 257 (1993).

[233] A. Barrat, "Quelques aspects de la dynamique hors d'equilibre des verres de spin", PhD thesis (Paris 6, 1996).

[234] H. Sompolinsky and A. Zippelius, "Relaxational dynamics of the Edwards-Anderson model and the mean-field theory of spin-glasses", Physical Review B **25**, 6860 (1982).

[235] L. F. Cugliandolo and J. Kurchan, "Analytical solution of the off-equilibrium dynamics of a long-range spin-glass model", Physical Review Letters **71**, 173 (1993).

[236] L. F. Cugliandolo and J. Kurchan, "On the out-of-equilibrium relaxation of the Sherrington-Kirkpatrick model", Journal of Physics A: Mathematical and General **27**, 5749 (1994).

[237] A. Barrat, R. Burioni, and M. Mézard, "Dynamics within metastable states in a mean-field spin glass", Journal of Physics A: Mathematical and General **29**, L81 (1996).

[238] W. H. Press, H. William, S. A. Teukolsky, A. Saul, *et al.*, *Numerical recipes 3rd edition: The art of scientific computing* (Cambridge University Press, 2007).

[239] S. Franz and J. Rocchi, "Large deviations of glassy effective potentials", Journal of Physics A: Mathematical and Theoretical **53**, 485002 (2020).

[240] M. Mézard and G. Parisi, "Statistical physics of structural glasses", Journal of Physics: Condensed Matter **12**, 6655 (2000).

[241] L. Berthier and D. Coslovich, "Novel approach to numerical measurements of the configurational entropy in supercooled liquids", Proceedings of the National Academy of Sciences **111**, 11668 (2014).

[242] G. Biroli, C. Rulquin, G. Tarjus, and M. Tarzia, "Role of fluctuations in the phase transitions of coupled plaquette spin models of glasses", SciPost Physics **1** (2016).

[243] J. P. Garrahan, "Transition in coupled replicas may not imply a finite-temperature ideal glass transition in glass-forming systems", Physical Review E **89**, 030301 (2014).

[244] A. Cavagna, I. Giardina, and G. Parisi, "An investigation of the hidden structure of states in a mean-field spin-glass model", Journal of Physics A: Mathematical and General **30**, 7021 (1997).

[245] C. Cammarota and G. Biroli, "Ideal glass transitions by random pinning", Proceedings of the National Academy of Sciences **109**, 8850 (2012).

[246] C. Cammarota and G. Biroli, "Random pinning glass transition: Hallmarks, mean-field theory and renormalization group analysis", The Journal of Chemical Physics **138**, 12A547 (2013).

[247] C. Cammarota, "A general approach to systems with randomly pinned particles: Unfolding and clarifying the random pinning glass transition", EPL (Europhysics Letters) **101**, 56001 (2013).

[248] G. Tarjus and M. Tissier, "Nonperturbative functional renormalization group for random field models and related disordered systems. I. Effective average action formalism", Physical Review B **78**, 024203 (2008).

[249] Y. Imry and S.-K. Ma, "Random-field instability of the ordered state of continuous symmetry", Physical Review Letters **35**, 1399 (1975).

[250] S. Franz and G. Parisi, "Universality classes of critical points in constrained glasses", Journal of Statistical Mechanics: Theory and Experiment **2013**, P11012 (2013).

[251] S. Franz and F. L. Toninelli, "A field-theoretical approach to the spin glass transition: models with long but finite interaction range", Journal of Statistical Mechanics: Theory and Experiment **2005**, P01008 (2005).

[252] S. Franz and F. L. Toninelli, "Kac limit for finite-range spin glasses", Physical Review Letters **92**, 030602 (2004).

[253] S. Franz and F. L. Toninelli, "Finite-range spin glasses in the Kac limit: free energy and local observables", Journal of Physics A: Mathematical and General **37**, 7433 (2004).

[254] J. D. Stevenson, A. M. Walczak, R. W. Hall, and P. G. Wolynes, "Constructing explicit magnetic analogies for the dynamics of glass forming liquids", The Journal of Chemical Physics **129**, 194505 (2008).

[255] E. Kierlik, P. Monson, M. Rosinberg, and G. Tarjus, "Adsorption hysteresis and capillary condensation in disordered porous solids: a density functional study", Journal of Physics: Condensed Matter **14**, 9295 (2002).

[256] C. Cammarota, A. Cavagna, I. Giardina, G. Gradenigo, *et al.*, "Phase-separation perspective on dynamic heterogeneities in glass-forming liquids", Physical Review Letters **105**, 055703 (2010).

[257] M. Newman and C. Moore, "Glassy dynamics and aging in an exactly solvable spin model", Physical Review E **60**, 5068 (1999).

[258] J. P. Garrahan, "Glassiness through the emergence of effective dynamical constraints in interacting systems", Journal of Physics: Condensed Matter **14**, 1571 (2002).

[259] J. P. Garrahan and M. Newman, "Glassiness and constrained dynamics of a short-range nondisordered spin model", Physical Review E **62**, 7670 (2000).

[260] R. L. Jack and J. P. Garrahan, "Phase transition for quenched coupled replicas in a plaquette spin model of glasses", Physical Review Letters **116**, 055702 (2016).

[261] R. M. Turner, R. L. Jack, and J. P. Garrahan, "Overlap and activity glass transitions in plaquette spin models with hierarchical dynamics", Physical Review E **92**, 022115 (2015).

[262] J. Villain, "Equilibrium critical properties of random field systems: new conjectures", Journal de Physique **46**, 1843 (1985).

[263] G. Tarjus and M. Tissier, "Random-field Ising and O (N) models: theoretical description through the functional renormalization group", The European Physical Journal B **93**, 1 (2020).

[264] N. G. Fytas and V. Martín-Mayor, "Universality in the three-dimensional random-field ising model", Physical Review Letters **110**, 227201 (2013).

[265] T. Schneider and E. Pytte, "Random-field instability of the ferromagnetic state", Physical Review B **15**, 1519 (1977).

[266] A. A. Pastor, V. Dobrosavljević, and M. L. Horbach, "Mean-field glassy phase of the random-field Ising model", Physical Review B **66**, 014413 (2002).

[267] J. Z. Imbrie, "Lower critical dimension of the random-field Ising model", Physical Review Letters **53**, 1747 (1984).

[268] M. Aizenman and J. Wehr, "Rounding of first-order phase transitions in systems with quenched disorder", Physical Review Letters **62**, 2503 (1989).

[269] A. Bray and M. Moore, "Scaling theory of the random-field Ising model", Journal of Physics C: Solid State Physics **18**, L927 (1985).

[270] G. Tarjus, I. Balog, and M. Tissier, "Critical scaling in random-field systems: 2 or 3 independent exponents?", EPL (Europhysics Letters) **103**, 61001 (2013).

[271] D. S. Fisher, "Scaling and critical slowing down in random-field Ising systems", Physical Review Letters **56**, 416 (1986).

[272] A. Young, "On the lowering of dimensionality in phase transitions with random fields", Journal of Physics C: Solid State Physics **10**, L257 (1977).

[273] A. Aharony, Y. Imry, and S.-k. Ma, "Lowering of dimensionality in phase transitions with random fields", Physical Review Letters **37**, 1364 (1976).

[274] G. Parisi and N. Sourlas, "Random magnetic fields, supersymmetry, and negative dimensions", Physical Review Letters **43**, 744 (1979).

[275] G. Tarjus and M. Tissier, "Nonperturbative functional renormalization group for random-field models: The way out of dimensional reduction", Physical Review Letters **93**, 267008 (2004).

[276] M. Tissier and G. Tarjus, "Supersymmetry and its spontaneous breaking in the random field Ising model", Physical Review Letters **107**, 041601 (2011).

[277] N. G. Fytas, V. Martín-Mayor, M. Picco, and N. Sourlas, "Restoration of dimensional reduction in the random-field Ising model at five dimensions", Physical Review E **95**, 042117 (2017).

[278] M. Schwartz, M. Gofman, and T. Natterman, "On the missing scaling relation in random field systems", Physica A: Statistical Mechanics and its Applications **178**, 6 (1991).

[279] M. Schwartz and A. Soffer, "Exact inequality for random systems: application to random fields", Physical Review Letters **55**, 2499 (1985).

[280] N. G. Fytas, V. Martín-Mayor, M. Picco, and N. Sourlas, "Phase transitions in disordered systems: the example of the random-field Ising model in four dimensions", Physical Review Letters **116**, 227201 (2016).

[281] P. C. Hohenberg and B. I. Halperin, "Theory of dynamic critical phenomena", Reviews of Modern Physics **49**, 435 (1977).

[282] I. Balog and G. Tarjus, "Activated dynamic scaling in the random-field Ising model: A nonperturbative functional renormalization group approach", Physical Review B **91**, 214201 (2015).

[283] B. Guiselin, L. Berthier, and G. Tarjus, "Random-field Ising model criticality in a glass-forming liquid", Physical Review E **102**, 042129 (2020).

[284] T. S. Grigera and G. Parisi, "Fast Monte Carlo algorithm for supercooled soft spheres", Physical Review E **63**, 045102 (2001).

[285] M. L. Ferrer, C. Lawrence, B. G. Demirjian, D. Kivelson, *et al.*, "Supercooled liquids and the glass transition: Temperature as the control variable", The Journal of Chemical Physics **109**, 8010 (1998).

[286] G. Tarjus, D. Kivelson, and P. Viot, "The viscous slowing down of supercooled liquids as a temperature-controlled super-Arrhenius activated process: a description in terms of frustration-limited domains", Journal of Physics: Condensed Matter **12**, 6497 (2000).

[287] B. Schmidtke, N. Petzold, R. Kahlau, M. Hofmann, and E. Rössler, "From boiling point to glass transition temperature: Transport coefficients in molecular liquids follow three-parameter scaling", Physical Review E **86**, 041507 (2012).

[288] G. J. Martyna, M. L. Klein, and M. Tuckerman, "Nosé–Hoover chains: The canonical ensemble via continuous dynamics", The Journal of Chemical Physics **97**, 2635 (1992).

[289] S. Nosé, "A unified formulation of the constant temperature molecular dynamics methods", The Journal of Chemical Physics **81**, 511 (1984).

[290] S. Nosé, "A molecular dynamics method for simulations in the canonical ensemble", Molecular Physics **52**, 255 (1984).

[291] W. G. Hoover, "Canonical dynamics: Equilibrium phase-space distributions", Physical Review A **31**, 1695 (1985).

[292] G. J. Martyna, M. E. Tuckerman, D. J. Tobias, and M. L. Klein, "Explicit reversible integrators for extended systems dynamics", Molecular Physics **87**, 1117 (1996).

[293] D. Frenkel and B. Smit, *Understanding molecular simulation: from algorithms to applications* (Elsevier, 2001).

[294] M. Newman and G. Barkema, *Monte Carlo methods in statistical physics* (Oxford University Press, 1999).

[295] B. Guiselin, G. Tarjus, and L. Berthier, "On the overlap between configurations in glassy liquids", The Journal of Chemical Physics **153**, 224502 (2020).

[296] T. Morita and K. Hiroike, "A new approach to the theory of classical fluids. I", Progress of Theoretical Physics **23**, 1003 (1960).

[297] K. Hiroike, "A New Approach to the Theory of Classical Fluids. II: Multicomponent Systems", Progress of Theoretical Physics **24**, 317 (1960).

[298] T. Morita and K. Hiroike, "A new approach to the theory of classical fluids. iii: General treatment of classical systems", Progress of Theoretical Physics **25**, 537 (1961).

[299] J.-M. Bomont, J.-P. Hansen, and G. Pastore, "An investigation of the liquid to glass transition using integral equations for the pair structure of coupled replicae", The Journal of Chemical Physics **141**, 174505 (2014).

[300] J.-M. Bomont, J.-P. Hansen, and G. Pastore, "Hypernetted-chain investigation of the random first-order transition of a Lennard-Jones liquid to an ideal glass", Physical Review E **92**, 042316 (2015).

[301] J.-M. Bomont, G. Pastore, and J.-P. Hansen, "Coexistence of low and high overlap phases in a supercooled liquid: An integral equation investigation", The Journal of Chemical Physics **146**, 114504 (2017).

[302] J.-M. Bomont, J.-P. Hansen, and G. Pastore, "Revisiting the replica theory of the liquid to ideal glass transition", The Journal of Chemical Physics **150**, 154504 (2019).

[303] G. M. Torrie and J. P. Valleau, "Monte Carlo free energy estimates using non-Boltzmann sampling: Application to the sub-critical Lennard-Jones fluid", Chemical Physics Letters **28**, 578 (1974).

[304] G. M. Torrie and J. P. Valleau, "Nonphysical sampling distributions in Monte Carlo free-energy estimation: Umbrella sampling", Journal of Computational Physics **23**, 187 (1977).

[305] J. Kästner, "Umbrella sampling", Wiley Interdisciplinary Reviews: Computational Molecular Science **1**, 932 (2011).

[306] L. Berthier, G. Biroli, D. Coslovich, W. Kob, and C. Toninelli, "Finite-size effects in the dynamics of glass-forming liquids", Physical Review E **86**, 031502 (2012).

[307] M. S. Challa, D. P. Landau, and K. Binder, "Finite-size effects at temperature-driven first-order transitions", Physical Review B **34**, 1841 (1986).

[308] K. Binder, "Finite size effects on phase transitions", Ferroelectrics **73**, 43 (1987).

[309] A. Cavagna, T. S. Grigera, and P. Verrocchio, "Dynamic relaxation of a liquid cavity under amorphous boundary conditions", The Journal of Chemical Physics **136**, 204502 (2012).

[310] N. D. Mermin, "Crystalline order in two dimensions", Physical Review **176**, 250 (1968).

[311] E. Flenner and G. Szamel, "Fundamental differences between glassy dynamics in two and three dimensions", Nature Communications **6**, 1 (2015).

[312] B. Illing, S. Fritschi, H. Kaiser, C. L. Klix, *et al.*, "Mermin–Wagner fluctuations in 2D amorphous solids", Proceedings of the National Academy of Sciences **114**, 1856 (2017).

[313] S. Vivek, C. P. Kelleher, P. M. Chaikin, and E. R. Weeks, "Long-wavelength fluctuations and the glass transition in two dimensions and three dimensions", Proceedings of the National Academy of Sciences **114**, 1850 (2017).

[314] K. Hukushima and K. Nemoto, "Exchange Monte Carlo method and application to spin glass simulations", Journal of the Physical Society of Japan **65**, 1604 (1996).

[315] A. M. Ferrenberg and R. H. Swendsen, "Optimized Monte Carlo data analysis", Computers in Physics **3**, 101 (1989).

[316] A. M. Ferrenberg and R. H. Swendsen, "Optimized Monte Carlo data analysis", Physical Review Letters **63**, 1195 (1989).

[317] S. Kumar, J. M. Rosenberg, D. Bouzida, R. H. Swendsen, and P. A. Kollman, "The weighted histogram analysis method for free-energy calculations on biomolecules. I. The method", Journal of Computational Chemistry **13**, 1011 (1992).

[318] S. Kumar, J. M. Rosenberg, D. Bouzida, R. H. Swendsen, and P. A. Kollman, "Multidimensional free-energy calculations using the weighted histogram analysis method", Journal of Computational Chemistry **16**, 1339 (1995).

[319] A. K. Hartmann, "Large-deviation properties of largest component for random graphs", The European Physical Journal B **84**, 627 (2011).

[320] A. K. Hartmann, P. Le Doussal, S. N. Majumdar, A. Rosso, and G. Schehr, "High-precision simulation of the height distribution for the KPZ equation", EPL (Europhysics Letters) **121**, 67004 (2018).

[321] J. D. Chodera, W. C. Swope, J. W. Pitera, C. Seok, and K. A. Dill, "Use of the Weighted Histogram Analysis Method for the Analysis of Simulated and Parallel Tempering Simulations", Journal of Chemical Theory and Computation **3**, 26 (2007).

[322] J. Kästner and W. Thiel, "Bridging the gap between thermodynamic integration and umbrella sampling provides a novel analysis method:"Umbrella integration"", The Journal of Chemical Physics **123**, 144104 (2005).

[323] M. S. Challa and J. Hetherington, "Gaussian ensemble: an alternate Monte Carlo scheme", Physical Review A **38**, 6324 (1988).

[324] M. S. Challa and J. Hetherington, "Gaussian ensemble as an interpolating ensemble", Physical Review Letters **60**, 77 (1988).

[325] L. Fernandez, V. Martin-Mayor, and D. Yllanes, "Tethered Monte Carlo: Computing the effective potential without critical slowing down", Nuclear Physics B **807**, 424 (2009).

[326] R. L. Vink, K. Binder, and H. Löwen, "Critical behavior of colloid-polymer mixtures in random porous media", Physical Review Letters **97**, 230603 (2006).

[327] G. Parisi and B. Seoane, "Liquid-glass transition in equilibrium", Physical Review E **89**, 022309 (2014).

[328] J. J. Potoff and A. Z. Panagiotopoulos, "Surface tension of the three-dimensional Lennard-Jones fluid from histogram-reweighting Monte Carlo simulations", The Journal of Chemical Physics **112**, 6411 (2000).

[329] R. Vink, J. Horbach, and K. Binder, "Critical phenomena in colloid-polymer mixtures: Interfacial tension, order parameter, susceptibility, and coexistence diameter", Physical Review E **71**, 011401 (2005).

[330] K. Binder, "Monte Carlo calculation of the surface tension for two-and three-dimensional lattice-gas models", Physical Review A **25**, 1699 (1982).

[331] A. A. Middleton and D. S. Fisher, "Three-dimensional random-field Ising magnet: Interfaces, scaling, and the nature of states", Physical Review B **65**, 134411 (2002).

[332] N. G. Fytas and V. Martín-Mayor, "Efficient numerical methods for the random-field Ising model: Finite-size scaling, reweighting extrapolation, and computation of response functions", Physical Review E **93**, 063308 (2016).

[333] A. Bruce and N. Wilding, "Scaling fields and universality of the liquid-gas critical point", Physical Review Letters **68**, 193 (1992).

[334] N. Wilding and A. Bruce, "Density fluctuations and field mixing in the critical fluid", Journal of Physics: Condensed Matter **4**, 3087 (1992).

[335] J. Houdayer and A. K. Hartmann, "Low-temperature behavior of two-dimensional Gaussian Ising spin glasses", Physical Review B **70**, 014418 (2004).

[336] O. Melchert, "autoScale. py-A program for automatic finite-size scaling analyses: A user's guide", arXiv preprint arXiv:0910.5403 (2009).

[337] S. Wansleben and D. Landau, "Monte Carlo investigation of critical dynamics in the three-dimensional Ising model", Physical Review B **43**, 6006 (1991).

[338] R. B. Pearson, J. L. Richardson, and D. Toussaint, "Dynamic correlations in the three-dimensional Ising model", Physical Review B **31**, 4472 (1985).

[339] Y. Parmar and J. Bhattacharjee, "Dynamic scaling, zero-temperature fixed point, and the random-field Ising model", Physical Review B **49**, 6350 (1994).

[340] L. Berthier, G. Biroli, J.-P. Bouchaud, and G. Tarjus, "Can the glass transition be explained without a growing static length scale?", The Journal of Chemical Physics **150**, 094501 (2019).

[341] A. T. Ogielski and D. A. Huse, "Critical behavior of the three-dimensional dilute Ising antiferromagnet in a field", Physical Review Letters **56**, 1298 (1986).

[342] S. Dierker and P. Wiltzius, "Random-field transition of a binary liquid in a porous medium", Physical Review Letters **58**, 1865 (1987).

[343] R. Valiullin, S. Naumov, P. Galvosas, J. Kärger, *et al.*, "Exploration of molecular dynamics during transient sorption of fluids in mesoporous materials", Nature **443**, 965 (2006).

[344] J. P. Sethna, K. Dahmen, S. Kartha, J. A. Krumhansl, *et al.*, "Hysteresis and hierarchies: Dynamics of disorder-driven first-order phase transformations", Physical Review Letters **70**, 3347 (1993).

[345] M. Mézard and G. Parisi, "The Bethe lattice spin glass revisited", The European Physical Journal B-Condensed Matter and Complex Systems **20**, 217 (2001).

[346] M. Mézard and G. Parisi, "A first-principle computation of the thermodynamics of glasses", The Journal of Chemical Physics **111**, 1076 (1999).

[347] M. Mézard and G. Parisi, "A tentative replica study of the glass transition", Journal of Physics A: Mathematical and General **29**, 6515 (1996).

[348] J.-M. Bomont, G. Pastore, and J.-P. Hansen, "Probing the pair structure of supercooled fluids by integral equations: Evidence for an equilibrium liquid-ideal glass transition?", EPL (Europhysics Letters) **105**, 36003 (2014).

[349] J. Van Leeuwen, J. Groeneveld, and J. De Boer, "New method for the calculation of the pair correlation function. I", Physica **25**, 792 (1959).

[350] S. Franz, H. Jacquin, G. Parisi, P. Urbani, and F. Zamponi, "Static replica approach to critical correlations in glassy systems", The Journal of Chemical Physics **138**, 12A540 (2013).

[351] J. A. Given and G. Stell, "Comment on: Fluid distributions in two-phase random media: Arbitrary matrices", The Journal of Chemical Physics **97**, 4573 (1992).

[352] E. Lomba, J. A. Given, G. Stell, J. J. Weis, and D. Levesque, "Ornstein-Zernike equations and simulation results for hard-sphere fluids adsorbed in porous media", Physical Review E **48**, 233 (1993).

[353] E. Pitard, M. Rosinberg, G. Stell, and G. Tarjus, "Critical behavior of a fluid in a disordered porous matrix: An Ornstein-Zernike approach", Physical Review Letters **74**, 4361 (1995).

[354] S. Franz, H. Jacquin, G. Parisi, P. Urbani, and F. Zamponi, "Quantitative field theory of the glass transition", Proceedings of the National Academy of Sciences **109**, 18725 (2012).

[355] S. Sastry, "The relationship between fragility, configurational entropy and the potential energy landscape of glass-forming liquids", Nature **409**, 164 (2001).

[356] S. Büchner and A. Heuer, "Potential energy landscape of a model glass former: Thermodynamics, anharmonicities, and finite size effects", Physical Review E **60**, 6507 (1999).

[357] G. Folena, S. Franz, and F. Ricci-Tersenghi, "Rethinking Mean-Field Glassy Dynamics and Its Relation with the Energy Landscape: The Surprising Case of the Spherical Mixed p-Spin Model", Physical Review X **10**, 031045 (2020).

[358] M. Ozawa and L. Berthier, "Does the configurational entropy of polydisperse particles exist?", The Journal of Chemical Physics **146**, 014502 (2017).

[359] G. Parisi, "Short-time aging in binary glasses", Journal of Physics A: Mathematical and General **30**, L765 (1997).

[360] N. Lačević, F. W. Starr, T. Schrøder, and S. Glotzer, "Spatially heterogeneous dynamics investigated via a time-dependent four-point density correlation function", The Journal of Chemical Physics **119**, 7372 (2003).

[361] S. Patinet, D. Vandembroucq, and M. L. Falk, "Connecting local yield stresses with plastic activity in amorphous solids", Physical Review Letters **117**, 045501 (2016).

[362] A. Barbot, M. Lerbinger, A. Hernandez-Garcia, R. García-García, *et al.*, "Local yield stress statistics in model amorphous solids", Physical Review E **97**, 033001 (2018).

[363] D. Coslovich and R. L. Jack, "Structure of inactive states of a binary Lennard-Jones mixture", Journal of Statistical Mechanics: Theory and Experiment **2016**, 074012 (2016).

[364] A. M. Ferrenberg and R. H. Swendsen, "New Monte Carlo technique for studying phase transitions", Physical Review Letters **61**, 2635 (1988).

[365] S. Bramwell, K. Christensen, J.-Y. Fortin, P. Holdsworth, *et al.*, "Universal fluctuations in correlated systems", Physical Review Letters **84**, 3744 (2000).

[366] E. J. Gumbel, "Les valeurs extrêmes des distributions statistiques", in Annales de l'institut Henri Poincaré, Vol. 5, 2 (1935), pp. 115–158.

[367] E. Bertin, "Global fluctuations and Gumbel statistics", Physical Review Letters **95**, 170601 (2005).

[368] J. M. Kosterlitz and D. J. Thouless, "Ordering, metastability and phase transitions in two-dimensional systems", Journal of Physics C: Solid State Physics **6**, 1181 (1973).

[369] S. Bramwell, P. Holdsworth, and J.-F. Pinton, "Universality of rare fluctuations in turbulence and critical phenomena", Nature **396**, 552 (1998).

[370] A. Noullez and J.-F. Pinton, "Global fluctuations in decaying Burgers turbulence", The European Physical Journal B-Condensed Matter and Complex Systems **28**, 231 (2002).

[371] Z. Racz and M. Plischke, "Width distribution for (2+ 1)-dimensional growth and deposition processes", Physical Review E **50**, 3530 (1994).

[372] S. T. Bramwell, T. Fennell, P. C. Holdsworth, and B. Portelli, "Universal fluctuations of the Danube water level: A link with turbulence, criticality and company growth", EPL (Europhysics Letters) **57**, 310 (2002).

[373] D. Richard, M. Ozawa, S. Patinet, E. Stanifer, *et al.*, "Predicting plasticity in disordered solids from structural indicators", Physical Review Materials **4**, 113609 (2020).

[374] S. S. Schoenholz, E. D. Cubuk, D. M. Sussman, E. Kaxiras, and A. J. Liu, "A structural approach to relaxation in glassy liquids", Nature Physics **12**, 469 (2016).

[375] T. Nattermann, "Interface roughening in random field models", in *Static Critical Phenomena in Inhomogeneous Systems* (Springer, 1984), pp. 359–376.

[376] J. D. Stevenson and P. G. Wolynes, "On the surface of glasses", The Journal of Chemical Physics **129**, 234514 (2008).

[377] R. Edelson and J. Krolik, "The discrete correlation function-A new method for analyzing unevenly sampled variability data", The Astrophysical Journal **333**, 646 (1988).

[378] B. Guiselin, C. Scalliet, and L. Berthier, "Microscopic origin of excess wings in relaxation spectra of deeply supercooled liquids", arXiv preprint arXiv:2103.01569 (2021).

[379] A. S. Keys, L. O. Hedges, J. P. Garrahan, S. C. Glotzer, and D. Chandler, "Excitations are localized and relaxation is hierarchical in glass-forming liquids", Physical Review X **1**, 021013 (2011).

[380] M. Isobe, A. S. Keys, D. Chandler, and J. P. Garrahan, "Applicability of dynamic facilitation theory to binary hard disk systems", Physical Review Letters **117**, 145701 (2016).

[381] M. Vogel and S. C. Glotzer, "Spatially heterogeneous dynamics and dynamic facilitation in a model of viscous silica", Physical Review Letters **92**, 255901 (2004).

[382] R. A. Denny, D. R. Reichman, and J.-P. Bouchaud, "Trap models and slow dynamics in supercooled liquids", Physical Review Letters **90**, 025503 (2003).

[383] P. Lunkenheimer, U. Schneider, R. Brand, and A. Loid, "Glassy dynamics", Contemporary Physics **41**, 15 (2000).

[384] U. Schneider, R. Brand, P. Lunkenheimer, and A. Loidl, "Excess wing in the dielectric loss of glass formers: A Johari-Goldstein β relaxation?", Physical Review Letters **84**, 5560 (2000).

[385] P. Lunkenheimer, R. Wehn, T. Riegger, and A. Loidl, "Excess wing in the dielectric loss of glass formers: further evidence for a β-relaxation", Journal of Non-Crystalline Solids **307**, 336 (2002).

[386] G. Diezemann, "A free-energy landscape model for primary relaxation in glass-forming liquids: Rotations and dynamic heterogeneities", The Journal of Chemical Physics **107**, 10112 (1997).

[387] G. Diezemann, U. Mohanty, and I. Oppenheim, "Slow secondary relaxation in a free-energy landscape model for relaxation in glass-forming liquids", Physical Review E **59**, 2067 (1999).

[388] M. Domschke, M. Marsilius, T. Blochowicz, and T. Voigtmann, "Glassy relaxation and excess wing in mode-coupling theory: The dynamic susceptibility of propylene carbonate above and below T_c", Physical Review E **84**, 031506 (2011).

[389] J. P. Sethna, J. D. Shore, and M. Huang, "Scaling theory for the glass transition", Physical Review B **44**, 4943 (1991).

[390] J. D. Stevenson and P. G. Wolynes, "A universal origin for secondary relaxations in supercooled liquids and structural glasses", Nature Physics **6**, 62 (2010).

[391] P. Viot, G. Tarjus, and D. Kivelson, "A heterogeneous picture of α relaxation for fragile supercooled liquids", The Journal of Chemical Physics **112**, 10368 (2000).

[392] R. Chamberlin, "Mesoscopic mean-field theory for supercooled liquids and the glass transition", Physical Review Letters **82**, 2520 (1999).

[393] R. V. Chamberlin, "Experiments and theory of the nonexponential relaxation in liquids, glasses, polymers and crystals", Phase Transitions: A Multinational Journal **65**, 169 (1998).

[394] R. Chamberlin, "Non-Arrhenius response of glass-forming liquids", Physical Review B **48**, 15638 (1993).

[395] J. C. Dyre and T. B. Schrøder, "Universality of ac conduction in disordered solids", Reviews of Modern Physics **72**, 873 (2000).

[396] L. Berthier and J. P. Garrahan, "Numerical study of a fragile three-dimensional kinetically constrained model", The Journal of Physical Chemistry B **109**, 3578 (2005).

[397] S. M. Malek, R. K. Bowles, I. Saika-Voivod, F. Sciortino, and P. H. Poole, ""Swarm relaxation": Equilibrating a large ensemble of computer simulations", The European Physical Journal E **40**, 1 (2017).

[398] R. Böhmer, R. Chamberlin, G. Diezemann, B. Geil, *et al.*, "Nature of the non-exponential primary relaxation in structural glass-formers probed by dynamically selective experiments", Journal of Non-Crystalline Solids **235**, 1 (1998).

[399] T. Blochowicz, C. Tschirwitz, S. Benkhof, and E. Rössler, "Susceptibility functions for slow relaxation processes in supercooled liquids and the search for universal relaxation patterns", The Journal of Chemical Physics **118**, 7544 (2003).

[400] T. B. Schrøder, S. Sastry, J. C. Dyre, and S. C. Glotzer, "Crossover to potential energy landscape dominated dynamics in a model glass-forming liquid", The Journal of Chemical Physics **112**, 9834 (2000).

[401] T. B. Schrøder and J. C. Dyre, "Solid-like mean-square displacement in glass-forming liquids", The Journal of Chemical Physics **152**, 141101 (2020).

[402] R. Yamamoto and A. Onuki, "Dynamics of highly supercooled liquids: Heterogeneity, rheology, and diffusion", Physical Review E **58**, 3515 (1998).

[403] B. Schmidtke, N. Petzold, R. Kahlau, and E. Rössler, "Reorientational dynamics in molecular liquids as revealed by dynamic light scattering: From boiling point to glass transition temperature", The Journal of Chemical Physics **139**, 084504 (2013).

[404] L. Berthier and M. D. Ediger, "How to "measure" a structural relaxation time that is too long to be measured?", The Journal of Chemical Physics **153**, 044501 (2020).

[405] P. Dierckx, "A fast algorithm for smoothing data on a rectangular grid while using spline functions", SIAM Journal on Numerical Analysis **19**, 1286 (1982).

[406] P. Chaudhuri, S. Sastry, and W. Kob, "Tracking heterogeneous dynamics during the α relaxation of a simple glass former", Physical Review Letters **101**, 190601 (2008).

[407] C. Donati, S. C. Glotzer, P. H. Poole, W. Kob, and S. J. Plimpton, "Spatial correlations of mobility and immobility in a glass-forming Lennard-Jones liquid", Physical Review E **60**, 3107 (1999).

[408] S. C. Glotzer, "Spatially heterogeneous dynamics in liquids: insights from simulation", Journal of Non-Crystalline Solids **274**, 342 (2000).

[409] E. R. Weeks, J. C. Crocker, A. C. Levitt, A. Schofield, and D. A. Weitz, "Three-dimensional direct imaging of structural relaxation near the colloidal glass transition", Science **287**, 627 (2000).

[410] F. W. Starr, J. F. Douglas, and S. Sastry, "The relationship of dynamical heterogeneity to the Adam-Gibbs and random first-order transition theories of glass formation", The Journal of Chemical Physics **138**, 12A541 (2013).

[411] Y. Gebremichael, M. Vogel, and S. Glotzer, "Particle dynamics and the development of string-like motion in a simulated monoatomic supercooled liquid", The Journal of Chemical Physics **120**, 4415 (2004).

[412] P. H. Poole, C. Donati, and S. C. Glotzer, "Spatial correlations of particle displacements in a glass-forming liquid", Physica A: Statistical Mechanics and its Applications **261**, 51 (1998).

[413] R. G. Palmer, D. L. Stein, E. Abrahams, and P. W. Anderson, "Models of hierarchically constrained dynamics for glassy relaxation", Physical Review Letters **53**, 958 (1984).

[414] R. Candelier, O. Dauchot, and G. Biroli, "Dynamical facilitation decreases when approaching the granular glass transition", EPL (Europhysics Letters) **92**, 24003 (2010).

[415] E. R. Weeks and D. Weitz, "Properties of cage rearrangements observed near the colloidal glass transition", Physical Review Letters **89**, 095704 (2002).

[416] J.-P. Bouchaud, A. Comtet, and C. Monthus, "On a dynamical model of glasses", Journal de Physique I **5**, 1521 (1995).

[417] C. Rehwald, O. Rubner, and A. Heuer, "From coupled elementary units to the complexity of the glass transition", Physical Review Letters **105**, 117801 (2010).

[418] C. Rehwald and A. Heuer, "How coupled elementary units determine the dynamics of macroscopic glass-forming systems", Physical Review E **86**, 051504 (2012).

[419] D. Fragiadakis and C. Roland, "Characteristics of the Johari-Goldstein process in rigid asymmetric molecules", Physical Review E **88**, 042307 (2013).

[420] M. Goldstein, "Viscous liquids and the glass transition: a potential energy barrier picture", The Journal of Chemical Physics **51**, 3728 (1969).

[421] G. P. Johari and M. Goldstein, "Viscous liquids and the glass transition. II. Secondary relaxations in glasses of rigid molecules", The Journal of Chemical Physics **53**, 2372 (1970).

[422] M. Goldstein, "The past, present, and future of the Johari–Goldstein relaxation", Journal of Non-Crystalline Solids **357**, 249 (2011).

[423] R. Wehn, P. Lunkenheimer, and A. Loidl, "Broadband dielectric spectroscopy and aging of glass formers", Journal of Non-Crystalline Solids **353**, 3862 (2007).

[424] P. Lunkenheimer, R. Wehn, U. Schneider, and A. Loidl, "Glassy aging dynamics", Physical Review Letters **95**, 055702 (2005).

[425] B. Kasting, M. Beasley, A. Guiseppi-Elie, R. Richert, and M. Ediger, "Relationship between aged and vapor-deposited organic glasses: Secondary relaxations in methyl-m-toluate", The Journal of Chemical Physics **151**, 144502 (2019).

[426] H.-B. Yu, R. Richert, and K. Samwer, "Structural rearrangements governing Johari-Goldstein relaxations in metallic glasses", Science Advances **3**, e1701577 (2017).

[427] H.-B. Yu, M.-H. Yang, Y. Sun, F. Zhang, *et al.*, "Fundamental link between β relaxation, excess wings, and cage-breaking in metallic glasses", The Journal of Physical Chemistry Letters **9**, 5877 (2018).

[428] A. D. Parmar, B. Guiselin, and L. Berthier, "Stable glassy configurations of the Kob–Andersen model using swap Monte Carlo", The Journal of Chemical Physics **153**, 134505 (2020).

[429] L. Berthier, D. Coslovich, A. Ninarello, and M. Ozawa, "Equilibrium sampling of hard spheres up to the jamming density and beyond", Physical Review Letters **116**, 238002 (2016).

[430] W. Kob and H. C. Andersen, "Testing mode-coupling theory for a supercooled binary Lennard-Jones mixture I: The van Hove correlation function", Physical Review E **51**, 4626 (1995).

[431] E. Flenner and G. Szamel, "Hybrid Monte Carlo simulation of a glass-forming binary mixture", Physical Review E **73**, 061505 (2006).

[432] D. Coslovich, M. Ozawa, and W. Kob, "Dynamic and thermodynamic crossover scenarios in the Kob-Andersen mixture: Insights from multi-CPU and multi-GPU simulations", The European Physical Journal E **41**, 62 (2018).

[433] F. Turci, C. P. Royall, and T. Speck, "Nonequilibrium phase transition in an atomistic glassformer: the connection to thermodynamics", Physical Review X **7**, 031028 (2017).

[434] R. Faller and J. J. de Pablo, "Density of states of a binary Lennard-Jones glass", The Journal of Chemical Physics **119**, 4405 (2003).

[435] R. L. Jack, L. O. Hedges, J. P. Garrahan, and D. Chandler, "Preparation and relaxation of very stable glassy states of a simulated liquid", Physical Review Letters **107**, 275702 (2011).

[436] I. Lyubimov, M. D. Ediger, and J. J. de Pablo, "Model vapor-deposited glasses: Growth front and composition effects", The Journal of Chemical Physics **139**, 144505 (2013).

[437] P. Das, A. D. Parmar, and S. Sastry, "Annealing glasses by cyclic shear deformation", arXiv preprint arXiv:1805.12476 (2018).

[438] N. V. Priezjev, "Molecular dynamics simulations of the mechanical annealing process in metallic glasses: Effects of strain amplitude and temperature", Journal of Non-Crystalline Solids **479**, 42 (2018).

[439] B. P. Bhowmik, V. Ilyin, and I. Procaccia, "Thermodynamic equivalence of cyclic shear and deep cooling in glass formers", Physical Review E **102**, 010603 (2020).

[440] A. D. Parmar, M. Ozawa, and L. Berthier, "Ultrastable metallic glasses in silico", Physical Review Letters **125**, 085505 (2020).

[441] L. Berthier and W. Kob, "The Monte Carlo dynamics of a binary Lennard-Jones glass-forming mixture", Journal of Physics: Condensed Matter **19**, 205130 (2007).

[442] G. Torrie and J. Valleau, "Monte Carlo study of a phase-separating liquid mixture by umbrella sampling", The Journal of Chemical Physics **66**, 1402 (1977).

[443] A. N. Kolmogorov and A. T. Bharucha-Reid, *Foundations of the theory of probability: Second English Edition* (Dover Publications, 2018).

[444] P. J. Van Laarhoven and E. H. Aarts, "Simulated annealing", in *Simulated annealing: Theory and applications* (Springer, 1987), pp. 7–15.

[445] K. Dawson, L. Zhu, L. A. Kopff, R. J. McMahon, *et al.*, "Highly stable vapor-deposited glasses of four tris-naphthylbenzene isomers", The Journal of Physical Chemistry Letters **2**, 2683 (2011).

[446] M. Singh, M. Ozawa, and L. Berthier, "Brittle yielding of amorphous solids at finite shear rates", Physical Review Materials **4**, 025603 (2020).

[447] W.-T. Yeh, M. Ozawa, K. Miyazaki, T. Kawasaki, and L. Berthier, "Glass stability changes the nature of yielding under oscillatory shear", Physical Review Letters **124**, 225502 (2020).

[448] H. Bhaumik, G. Foffi, and S. Sastry, "The role of annealing in determining the yielding behavior of glasses under cyclic shear deformation", arXiv preprint arXiv:1911.12957 (2019).

[449] F. Varnik, L. Bocquet, J.-L. Barrat, and L. Berthier, "Shear localization in a model glass", Physical Review Letters. **90**, 095702 (2003).

[450] Y. Shi and M. L. Falk, "Strain localization and percolation of stable structure in amorphous solids", Physical Review Letters **95**, 095502 (2005).

[451] J. Ketkaew, W. Chen, H. Wang, A. Datye, *et al.*, "Mechanical glass transition revealed by the fracture toughness of metallic glasses", Nature Communications **9**, 1 (2018).

[452] G. Kapteijns, W. Ji, C. Brito, M. Wyart, and E. Lerner, "Fast generation of ultrastable computer glasses by minimization of an augmented potential energy", Physical Review E **99**, 012106 (2019).

[453] D. Coslovich, "Locally preferred structures and many-body static correlations in viscous liquids", Physical Review E **83**, 051505 (2011).

[454] H. C. Andersen, J. D. Weeks, and D. Chandler, "Relationship between the hard-sphere fluid and fluids with realistic repulsive forces", Physical Review A **4**, 1597 (1971).

[455] L. Berthier and G. Tarjus, "Nonperturbative effect of attractive forces in viscous liquids", Physical Review Letters **103**, 170601 (2009).

[456] N. Koumakis and G. Petekidis, "Two step yielding in attractive colloids: transition from gels to attractive glasses", Soft Matter **7**, 2456 (2011).

[457] A. J. Liu and S. R. Nagel, "The jamming transition and the marginally jammed solid", Annu. Rev. Condens. Matter Phys. **1**, 347 (2010).

[458] M. Geiger, S. Spigler, S. d'Ascoli, L. Sagun, *et al.*, "Jamming transition as a paradigm to understand the loss landscape of deep neural networks", Physical Review E **100**, 012115 (2019).

États métastables dans des verres modèles

La mécanique statistique explique désormais les transitions de phase se produisant dans des substances simples à l'équilibre thermodynamique. Néanmoins, la transition vitreuse, observée universellement dès lors qu'un liquide est refroidi ou comprimé suffisamment rapidement pour éviter sa cristallisation, est toujours source d'intenses recherches. Dans l'approximation de champ moyen, le ralentissement des systèmes vitreux est la conséquence de l'émergence d'un paysage d'énergie libre rugueux avec un nombre exponentiellement grand de minima correspondant aux états métastables. Ces derniers dictent également les propriétés thermodynamiques des liquides surfondus ainsi que le comportement hors-équilibre des verres. Ils sont cependant mal définis au-delà du champ moyen : ils ont une durée de vie finie et une extension spatiale limitée. Le travail de cette thèse participe à l'effort de définir et de caractériser les états métastables en dimension finie par les simulations numériques et les travaux analytiques. Nous exploitons dans un premier temps la thermodynamique contrainte des liquides surfondus dans la construction de Franz et Parisi. La théorie champ moyen prédit que l'existence d'états métastables se manifeste par une ligne de transition de phase et un point critique dans un diagramme des phases étendu. Nous utilisons les simulations numériques et nous montrons que les résultats champ moyen survivent malgré l'introduction de fluctuations de dimension finie. Nous sommes capables de caractériser le point critique et d'en donner sa classe d'universalité ainsi que sa dimension critique inférieure. Nous étudions ensuite en détail la définition du paramètre d'ordre associé à cette transition analytiquement et numériquement pour orienter d'éventuelles futures études, mais également pour mieux comprendre la structure gros-grains du paysage d'énergie libre de verres modèles. Finalement, nous nous intéressons à la thermodynamique des liquides surfondus en présence d'une contrainte thermodynamique locale et nous révélons d'importantes fluctuations spatiales. Dans un second temps, nous étudions la dynamique des liquides surfondus proches de leur transition vitreuse en mettant à profit un algorithme récent pour générer des configurations d'équilibre de liquides modèles à très basses températures. Nous montrons que la dynamique de relaxation résulte de l'apparition distribuée de régions mobiles qui croissent par facilitation. Dans un troisième temps, nous étudions les propriétés de verres hors-équilibre, et nous mettons en place des protocoles numériques qui permettent de générer des verres beaucoup plus stables que ceux obtenus usuellement en simulations par vieillissement.

Mots-Clés : physique statistique des systèmes désordonnés, simulations numériques, théorie champ moyen, construction de Franz-Parisi, dynamique d'équilibre des liquides surfondus, transition vitreuse.

Metastable states in model glass-formers

Statistical mechanics now explains the phase transitions occurring in simple substances at equilibrium. However, the glass transition, which is universally observed when a liquid is cooled or compressed quickly enough to avoid crystallization is still a source of intense research. At the mean-field level, the slowing down of glassy systems is the consequence of the emergence of a rough free energy landscape with an exponentially large number of minima corresponding to metastable states. These metastable states also dictate the thermodynamic properties of supercooled liquids as well as the out-of-equilibrium behaviour of glasses. They are however ill-defined beyond mean-field: they have a finite lifetime and a restricted spatial extension. This work contributes to the effort of defining and characterising metastable states in finite dimensions thanks to numerical simulations and analytical calculations. Firstly, we consider the constrained thermodynamics of supercooled liquids in the construction put forward by Franz and Parisi. Mean-field theory predicts that the existence of metastable states manifests itself in a phase transition line and a critical point in an extended phase diagram. We use numerical simulations and we show that mean-field results survive despite the introduction of finite-dimensional fluctuations. We are able to characterise the critical point and we study its universality class along with its lower critical dimension. We then study the definition of the order parameter associated with this transition analytically and numerically in detail to guide any future work but also to better understand the coarse-grained structure of the free energy landscape of model glass-formers. We finally focus on the thermodynamics of supercooled liquids in the presence of a local thermodynamic constraint and we reveal significant spatial fluctuations. Secondly, we study the dynamics of supercooled liquids close to their glass transition by taking advantage of a recent algorithm to generate equilibrium configurations of model liquids at very low temperatures. We show that the relaxation dynamics results from the distributed appearance of mobile regions that grow thanks to dynamic facilitation. Thirdly, we study the properties of non-equilibrium glasses, and we implement computer methods that allow us to generate much more stable glasses than those usually obtained in aging simulations.

Keywords: statistical physics of disordered systems, numerical simulations, mean-field theory, Franz-Parisi construction, equilibrium dynamics of supercooled liquids, glass transition.